COUPLING EFFECTS OF CLT CONNECTIONS UNDER BI-AXIAL LOADING

by

Jingjing Liu

B.A.Sc., Tongji University, China, 2009

M.A.Sc. Tongji University, China, 2012

A THESIS SUBMITTED IN PARTIAL FULFILLMENT OF

THE REQUIREMENTS FOR THE DEGREE OF

DOCTOR OF PHILOSOPHY

in

THE FACULTY OF GRADUATE AND POSTDOCTORAL STUDIES

(Forestry)

THE UNIVERSITY OF BRITISH COLUMBIA

(Vancouver)

February 2019

The following individuals certify that they have read, and recommend to the Faculty of Graduate and Postdoctoral Studies for acceptance, the dissertation entitled:

Coupling effects of CLT connections under bi-axial loading

submitted by Jingjing Liu in partial fulfillment of the requirements for

the degree of Doctor of Philosophy

in Forestry

Examining Committee:

Frank Lam, Department of Wood Science

Supervisor

Terje Haukaas, Department of Civil Engineering

Supervisory Committee Member

Tony Yang, Department of Civil Engineering

Supervisory Committee Member

Stavros Avramidis, Department of Wood Science

University Examiner

Frank K. Ko, Department of Materials Engineering

University Examiner

Additional Supervisory Committee Members:

Supervisory Committee Member

Supervisory Committee Member

Abstract

This dissertation presents a study on the coupling effects of tension and shear force on CLT connections in mid-rise structures. Unlike the current simplified design assumption that CLT connectors only take either pure shear or pure tension force in the structures, this research first considers the significant interactions between tension and shear loads from two orthogonal directions for CLT connections through bi-axial loading experimental tests and numerical analysis.

Four sets of experimental tests were conducted: 1) AE 116 angle bracket connection tests under monotonic/cyclic tension loading with four levels of co-existent shear loads (0 kN, 20 kN, 30 kN, and 40 kN), 2) AE 116 angle bracket connection tests under monotonic/cyclic shear loading with four levels of co-existent tension loads (0 kN, 20 kN, 30 kN, and 40 kN), 3) HTT5 hold-down connection tests under monotonic/cyclic tension loading with three levels of co-existent shear loads (0 kN, 10 kN, and 20 kN), and 4) HTT5 hold-down connection tests under monotonic/cyclic shear loading with five levels of co-existent tension loads (0 kN, 20 kN, 30 kN, 40 kN and 60 kN). The specimens exhibited changes in strength and hysteresis behaviour under different configurations. Under bi-axial loading, different interactions between nails and surrounding wood embedment caused the coupling effect.

Based on the mechanisms of CLT connections under bi-axial loading, a pseudo-nail model was developed using a modified protocol-independent nail connection algorithm. Two key parameters, a gap size factor β, and an unloading stiffness degradation index γ, were implemented into the original algorithm to capture the unloading stiffness degradation and coupling effect of bi-axial loading. The developed model was able to capture all the characteristics of CLT connections, including strength degradation, reloading/unloading stiffness degradation, the pinching effect, and the coupling effect. Model parameters were calibrated for all 32 configurations from the tests, and

compared in terms of load carrying capacity and energy dissipation. Accurate agreements were reached. The results show that the proposed CLT connection model was able to predict the hysteresis behaviour of all nail-based connections.

Lay Summary

Under seismic activity, Cross Laminated Timber (CLT) connections in the structures take shear as well as tension loads. The current design methods have neglected this coupling interaction for simplification purposes. However, the recent rapid application of CLT technology has drawn the urgent need to attention to further understand the structural behaviour of connections in real cases for safer and more practical design. The research conducted bi-axial loading tests of typical CLT connections and developed corresponding numerical models. The test results showed that bi-axial loading changed the loading capacity and energy dissipation. As nail-based connectors, the nails in the connections pressed into the surrounding wood medium and formed gaps. In one-directional loading, the nails are able to travel freely in the gaps. But under bi-axial loading, the nails receive resistance in the gaps due to loading from the perpendicular direction. Based on this, a numerical model was developed considering this coupling effect which agreed well with the experimental results.

Preface

This research project was originally proposed by Professor Frank Lam, and completely conducted by Jingjing Liu. Two scientific articles have been published, and a further one has been submitted from this dissertation, in which Jingjing Liu is the lead author.

Chapter 3 was co-authored by Professor Frank Lam. Jingjing Liu was responsible for designing and performing its experimental tests, analyzing its results and preparing the manuscript. Professor Frank Lam provided guidance for the test design, and comments and revisions for the paper. The complete citation for the published article is, Liu, J., and Lam, F. (2018). "Experimental test of coupling effect on CLT angle bracket connections." *Eng.Struct.*, 171 862-873.

Chapter 4 was co-authored by Professor Frank Lam. Jingjing Liu was responsible for designing and performing the experimental tests, analyzing the results and preparing the manuscript. Professor Frank Lam provided guidance for the test design, and comments and revisions for the paper. The complete citation for the published article is, Liu, J., Lam, F. (2019). "Experimental test of coupling effect on CLT hold-down connections." *Eng.Struct.*, 178 586-602.

Chapters 5 and 6 were condensed into a single journal paper and co-authored by Professor Frank Lam, Professor Ricardo O. Foschi, and Dr. Minghao Li. Jingjing Liu was responsible for the model development, numerical simulation and preparation of the manuscript. Professor Frank Lam provided guidance for the model development, and comments and revisions for the paper. Professor Ricardo O. Foschi, and Dr. Minghao Li provided guidance for the model development. The article, titled, “Modeling coupling effect of CLT connections under bi-axial loading using pseudo-nail model with a nail connection algorithm” has been submitted as a journal paper.

Table of Contents

List of Tables

List of Figures

List of Symbols

a	global displacement vector
a^*	global displacement vector from previous step
A	area
d_s	a small lateral displacement
D	gap between nail and wood embedment
D_0	residual gap between nail and wood embedment from previous step
D_D	ductility ratio
D_{max}	displacement at the maximum compressive response
D_N	nail diameter
$D+$	positive gap value
$D-$	negative gap value
E	elastic modulus
$E_{d,i}$	dissipated energy in the i^{th} cycle
$E_{p,i}$	available potential energy in the i^{th} cycle
E_y	yielding strength
F	force
F_i	maximum force in the i^{th} cycle
F_{max}	maximum load
F_{Rx}	lateral resistance of connector
F_{Ry}	vertical resistance of connector

F_S	shear force
F_T	tension force
F_u	ultimate load
F_x	friction force
F_y	vertical support force
F_{yl}	yielding load
K_0	initial stiffness
K_{el}	initial stiffness of CLT connection
K_{pl}	plastic stiffness of CLT connection
K_{RL}	reloading stiffness
K_{UL}	unloading stiffness
L	length
L_N	nail length
M_R	turning moment
$p(w)$	reaction force from a given displacement w
Q_0	intercept of the asymptote at the maximum compressive response
Q_1	slope of the asymptote at the maximum compressive response
Q_2	postpeak decay factor
$Tol_{displacement}$	value of tolerant displacement
Tol_{force}	value of tolerant force
u_i	maximum displacement in the i^{th} cycle
v_{max}	maximum displacement

v_u	ultimate displacement
v_{yd}	yielding displacement
w	a given displacement
α	reloading degradation index
β	gap size factor
γ	unloading degradation index
Δ	displacement
ΔL	length change
ε	normal strain
θ	angle between steel cable and vertical direction
$\nu_{eq,i}$	ratio of $E_{d,i}$ to $E_{p,i}$
μ	coefficient for modulus of elasticity
σ	normal stress
ψ	out-of-balance vector
ψ^*	out-of-balance vector from previous step
$\nabla\psi$	corresponding tangential stiffness matrix
$\nabla\psi^*$	corresponding tangential stiffness matrix from the previous step

Acknowledgements

First, I would like to express my humble gratitude to my research supervisor, Professor Frank Lam, for his academic training and financial support. During the six years of my Ph.D. journey, he has taught me "how to fish" rather than simply "giving me that fish". He has cultivated my research skills with his admiring patience and profound knowledge on timber engineering. I am fortunate to have had him by my side during my personal growth. From him, I have acquired improved ways of performing, expressing empathy, and making better decisions. I have learned how to listen attentively, how to be down-to-earth and how to motivate myself. I will greatly benefit from his influence throughout my lifetime.

My gratitude is also extended to our lab stuff, George Li and Chao Zhang, who gave me so much help in conducting my experimental tests. I also wish to thank Professor Ricardo O. Foschi, Dr. Minghao Li, Professor Hyung-suk Lim, and Professor Zheng Li for helping me develop my numerical model. I further desire to show my appreciation towards my committee members, Professor Ricardo O. Foschi, Professor Stavros Avramidis, Professor Terje Haukaas, and Professor Tony Yang, who guided me in following the right approach.

I greatly enjoyed being a member of the TEAM group, and I wish to thank everyone for their friendship during my Ph.D. program, including: Xiaoyue Zhang, Xinlei Huang, Xin Nie, Siyao Ma, Yuan Li, Tzu-Hsien Shih, Dominik Horvat, P.K.M. Moniruzzaman, Yingyang Liu, Wancheng Gao, Professor Yong Xu, Hongming Li, Xing Zhang, Jing Zhang, Zhen Liang, Julian Asselstine, Giulia Natalini, Hengliang Dai, Rongrong Zhang, Kongyang Chen, and Xiaofeng Sun.

Finally, I express my deepest gratitude to my parents. I am thankful for their love, trust, support, and understanding, for them instilling into me so much power and courage.

I thank all the people who accompanied me on this journey, helping me to enjoy the experience, overcome any obstacles, and just being there for me.

I thank myself for accomplishing my Ph.D.`s requirements so that I can head out on a new journey.

Dedication

To

Kezhen Huang, Kehai Liu

my beloved mother and father

Chapter 1: Introduction

1.1 Problem description

Cross Laminated Timber (CLT) is an innovative building product first developed in Austria. It is fabricated by bonding timber boards together with structural adhesives to produce a solid timber panel with each layer oriented crosswise to the next. Alternating the grain directions of each layer reduces many weaknesses, such as the effects of in-plane shrinkage and swelling. Also, load may be transferred in more than one direction. Within the last 20 years, CLT production has spread to other parts of Europe and into North America and Asia. Among its attractive structural characteristics are its high dimensional stability, axial load capacity, and in-plane shear strength. Thanks to the maturing prefabrication technology, a single CLT panel can be as large as 18 m by 3 m by 0.5 m (height by width by depth) and can include three, five, seven, or more board layers. In the North American context, CLT structures exhibit competitive benefits for mid-rise buildings (six to 12 storey), including low density, fast installation, reduced waste, design versatility, thermal performance, effective cost, and environmental advantages, as compared with concrete and steel structures. Existing hypothetical studies even demonstrate the possibility of using it to construct taller wooden buildings up to 30 storey.

As an attractive structural material of relatively high dimensional stability and load capacity, CLT has been widely used for the walls and floors of structural systems. Experimental research has been carried out on the component and structural level to study its structural behaviour. The IVALSA Institute of the National Research Council at San Michelel all'Adige in Italy carried out the SOFIE project to investigate the performance and capacities of the X-LAM system, known now as CLT structures. The project included a series of lateral resistance performance tests on cross-laminated wooden panels (Ceccotti and Follesa, 2006), a shaking table

test of a three-storey CLT building (Ceccotti, 2008), and a seismic test on a 7-storey X-lam building performed on the E-Defense 3D shaking table in Japan (Ceccotti *et al.*, 2013). Those studies show that most CLT structural deformation takes place in the metal connectors rather than the wood, and is dominated by rocking and slip mechanisms. A typical design practice is that, angle brackets slip under loading and only take the shear force along the CLT wall, while hold-downs take all of the tension forces to the resist overturning moment. Under such assumptions, former researchers have tested CLT connections loaded in one direction (Popovski *et al.*, 2010), and presented the experimental performance of hold-downs, brackets, and half-lap joint connections under cyclic loading (Rinaldin *et al.*, 2013). These were tested in the shear and withdrawal directions to capture the main features of the behaviour of these CLT connections. Experiments were undertaken to evaluate how the structural characteristics of steel angle bracket connectors vary across a range of mass-produced and special connectors under shear loading (Tomasi and Smith, 2014). In those studies, the rocking and slip mechanisms were considered to be acting independently. However, recent research has proven that these two mechanisms behave jointly on the connectors. Under complex stress conditions, the shear behaviour and axial behaviour of the connectors are coupled, which had been neglected in previous simplified methods (Liu and Lam, 2016; Pozza *et al.*, 2018). Thus, the coupling effects of the lateral and vertical load on the CLT connections require investigation to gain a better understanding of the mechanism.

1.2 Research objectives

This PhD thesis investigates the structural mechanisms, and specifically the coupling effect of typical cross-laminated timber connections, angle brackets and hold-downs under bi-axial loading. Such research includes experimental tests, the development of mechanical models, and the validation of numerical analyses. The objectives are listed in details as below.

1) Experimental tests:

- Design an innovative experiment for typical CLT angle bracket and hold-down connections. Carry out monotonic and cyclic tests on the connections in shear, with different levels of constant force being applied simultaneously in tension. Carry out monotonic and cyclic tests of the connections in tension, with different levels of constant force being applied simultaneously in shear.
- Evaluate and analyze the test results in terms of the key mechanical characteristics, including strength, stiffness, ductility, strength/stiffness degradation, equivalent viscous damping, and energy dissipation, of those connections.

2) Numerical modeling:

- Determine the mechanisms of the CLT connections under bi-axial loading that consider the interactions of the loads in different directions on the CLT connectors.
- Develop a mechanically based "pseudo-nail" model that can fully address the coupling effects of the CLT connections under bi-axial loading based on the original algorithm HYST. The model will be able to capture all the characteristics of the CLT connections, including strength degradation, unloading and reloading stiffness degradation, the pinching effect and the coupling effect.
- Calibrate the model with CLT angle bracket and hold-down connection test results to analyze the hysteretic behaviour of CLT connections under bi-axial loading.

1.3 Thesis organization

The thesis is composed of seven chapters:

General information on the CLT's technological development will be given at the outset of Chapter 2. Then, the previous experimental research will be introduced, including tests on the

CLT`s structural and component levels. A followed-up section will describe the analytical and numerical studies on CLT connections both within the structures, and independent of them. The comparison of the results among those tests and analyses will be performed. Finally, the significance of the present research project will be highlighted.

In Chapter 3, a comprehensive report on the experimental test conducted on CLT angle bracket connections under bi-axial loading will be described. Detailed test configuration and loading procedures will be given. The failure mode, and load-displacement curves will be discussed. The main mechanical properties will be presented following the standard procedures. This chapter has been published as a journal paper by *Engineering Structures*.

In Chapter 4, a continuous experimental test on CLT hold-down connections under bi-axial loading will be described. The results and findings will be presented, following the same procedure as in Chapter 3. This chapter has been published as a journal paper by *Engineering Structures*.

In Chapter 5, the mechanisms of CLT connections under bi-axial loading will be analyzed based on the findings from experiments. An innovative mechanism-based “pseudo-nail” model, created using the modified algorithm, HYST, will be presented. This model can fully address the hysteresis behaviour of CLT connections under bi-axial loading, including strength degradation, unloading and reloading stiffness degradation, the pinching effect, and the coupling effect. The parameters of this model will be discussed.

In Chapter 6, the developed model will be validated by test results. The coupling effect of CLT connections under bi-axial loading will be further discussed in depth based on the model. Chapters 5 and 6 have been condensed into a single journal paper and submitted.

Chapter 7 will conclude the essential findings and address the limitations of the research. Recommendations for further study will be proposed.

Chapter 2: Background and Literature Review

2.1 CLT Introduction

Cross-laminated timber (CLT) is an innovative prefabricated solid engineered wood product. It was originally invented in Austria in the 1990s and has been increasingly gaining traction as a high-performance structural material. By the 2000s, CLT was recognized in Europe and widely used for single-family and multi-storey housing. In 2010, the North American wood industry implemented a plan to introduce generic CLT products in Canada and the United States. Nowadays, CLT has gradually become a popular material in North America in multi-storey structures.

CLT panels are typically used as load-carrying plate elements in structural systems such as walls, floors and roofs. These panels process high in-plane and out-of-plane strength and stiffness properties in both directions, giving them a a two-way action capability similar to a reinforced concrete slab. High dimensional stability allows for the prefabrication of wide and long floor slabs and single storey long walls.

CLT panels offer a solution for building designs with lateral loads such as those generated by winds or earthquakes. Shear transfer between adjacent panels is achieved through a variety of metal connector systems and plywood splines that are attached with screws or nails. The basic panel-to-panel connection can be established through half-lapped, single or double splines made with engineered wood products. Metal brackets, hold-downs and plates can be used to transfer shear and tension forces at those connections. Innovative types of connection systems can also be employed, including mechanical and carpentry connection systems. Dowel-type fasteners, such as nails, screws, and rivets, are commonly used in such connections.

In Canada, CLT is now included in the "Supplement to the National Building Code of Canada" (NBCC). The CSA-O86 Technical Committee has approved the adoption of CLT in the 2016 Supplement to the CSA-O86, which will form a part of the 2014 edition of the CSA-O86 that is referenced by the 2015 edition of the NBCC. The adopted package includes: 1) CLT as a structural member, 2) CLT connections, and 3) CLT as a lateral load resisting system. The Canadian Wood Council (CWC) and its partners are working on a code change proposal for raising the height of wood buildings to 12 storeys in the 2020 edition of NBCC.

To provide CLT design guidelines for the codes, it is essential to obtain greater knowledge of the structural performance of CLT buildings and connections through experimental tests and numerical studies.

2.2 Experimental studies

To investigate the behaviour of CLT structures and connections, several tests have been conducted to provide experimental data for further analyses.

2.2.1 CLT structure experiments

One of the first experiment studies on the structural performance of CLT walls was carried out at the University of Ljubljana, Slovenia (Dujič *et al.*, 2004) . In this study, 15 solid CLT walls with different anchorage details undertook monotonic and cyclic loading with several vertical load levels to study the influence of anchoring systems on the shear stiffness and strength of timber wall panels. Test results revealed that such wooden panels have relatively high shear stiffness and load-bearing capacity. The critical elements that govern the structural response are anchors connecting the panels with foundations and the local strength of the wood at the connections. The racking behaviour of the CLT walls is very sensitive to the magnitude of vertical loads and the

type of anchoring system used. The study also found that the lateral strength of CLT walls with weak anchorage are benefited by vertical gravity loads.

Following these initial tests, the same group conducted a series of tests on CLT panels. In 2006, the influence of vertical load and boundary conditions on CLT wall resistance was investigated through monotonic and cyclic loading tests (Dujic *et al.*, 2006). Three boundary conditions allowed wall deformations from cantilever to pure shear. Case A allowed the top of the wall to translate and rotate, Case B restrained its rotation, and Case C restrained both its vertical transition and rotation. The load carrying capacity of Case C is twice of that of Case A, depicting the significant impact of the boundary conditions on the lateral resistance of CLT walls.

Shaking table tests of full-scale CLT panels were conducted afterwards to obtain more information about the behaviour of their structural elements during an earthquake (Dujič and Žarnić, 2006; Hristovski *et al.*, 2012). The two specimens were parallel CLT walls with lateral walls to maintaining their stability. The walls were anchored to a concrete floor with angle brackets. Each specimen had attached a seismic mass of 9.6 t. Several earthquake records significant to Central and Southern Europe, and harmonic excitations, were applied to the specimens. The tests assessed the nonlinear behaviour of the CLT walls and demonstrated that the main sources of their non-linearity were their connections.

The group's final set of CLT wall tests studied the influence of openings (Dujic *et al.*, 2008). Cyclic tests were performed to obtain the hysteretic responses of two walls with and two without openings. The results revealed that the CLT panels with large openings had slightly lower shear stiffness, but their reduction in load-bearing capacity was negligible. Most of the failures were concentrated in their anchoring areas and in the corners surrounding the openings, with smashing and tearing of wood.

The SOFIE project in Italy, was further implemented as one of the most comprehensive studies on the seismic performance of CLT systems. CLT panel shear wall, and multiple full-scaled building system tests were conducted during this study.

The first CLT shear wall test series of this project included 14 wall tests employing four different configurations under cyclic loading (Lauriola and Sandhaas, 2006). These tests confirmed that the CLT panels used to construct the walls and floor slabs were very rigid and the connections optimized during the cyclic test series behaved very well in more realistic cases. All dissipation and ductility only depended on the design of the connections. The walls tested were able to exhibit good ductility and energy dissipation through localized damage at the connections. In addition to wall tests, pseudo-dynamic testing of a one-storey CLT building assembly was also carried out in this study. The one-storey specimen had a more realistic floor plan, with doors and windows. Three design variations with different opening sizes were tested. The results showed that the openings did not greatly affect the performance of the building and the behaviour of the wall under low magnitudes of shear force was due to the connections and not due to the wooden panel. Such building types are stiff but ductile, and shear deformation of the panel itself is negligible compared to that of the connections.

The second test in the SOFIE project was a 3-storey residential house shaking table test (Ceccotti, 2008). The building had a 7 m × 7 m plan and was 10 m in height with a pitched roof; it was presented in three different configurations and was constructed using typical connectors, angle brackets and hold-downs. Three different earthquakes at two increasing levels of peak ground were input as excitations. The building had minor repairs between tests but remained standing without permanent deformation after all tests. The results concluded that such CLT buildings were a self-centering construction systems. This study was the first table test on a CLT

building specimen with realistic dimensions and configuration. It highlighted the fact that the major damage of CLT buildings during earthquakes was concentrated at the connections, CLT walls and floors remained mostly elastic, and the building had significant uplift demands on its lower floor anchor system.

The SOFIE project conducted the largest CLT test to date, the seven-story CLT building shaking table test in Japan (Ceccotti *et al.*, 2013). The building had a total height of 23.5 m, a floor plan of 7.5 m × 13.5 m, and a total weight of 284 t. It was subjected to 10 earthquake ground motions with increasing intensity. During the tests, the building experienced some damage with considerable uplifts to its hold-down elements on its lower storeys. However, after the test, the building was able to return to its original position with negligible residual displacement. The natural frequency of the building decreased less than 25% at the end. The building demonstrated self-centering capabilities and high stiffness combined with sufficient ductility to avoid brittle failure.

In Canada, FPInnovations has conducted a series of experimental research studies on CLT structural performance. A cyclic test of 32 CLT shear walls, with different aspect ratios, openings, and panel combinations, was carried out by FPInnovations (Popovski *et al.*, 2010). The test provided a data set for follow-up CLT seismic research in North America. These tests addressed the contribution of inter-panel joints and metal brackets to the ductility of CLT walls.

To investigate the three-dimensional behaviour of CLT structures subjected to lateral loads, a two storey full-scale CLT model, 6.0 m × 4.8 m in plan with a height of 4.9 m, was tested under quasi-static monotonic and cyclic loading (Popovski *et al.*, 2014). Five push-over and cyclic tests were performed. The results indicated that not only did the walls parallel to the loading direction resist the lateral forces, but also the walls perpendicular to the loading direction contributed to the

overall building stiffness and resistance. The shear failure of the nails in the first storey brackets was the main failure mechanism noted, which resulted from the sliding and rocking of the CLT wall panels. The CLT house exhibited comprehensively integrity, stability, and lateral resistance.

In the United States, a NEES CLT Planning project is being conducted to develop seismically resilient, tall Cross-Laminated Timber (CLT) systems at an 8~20 storey height range that can be cost competitive built in the seismic regions of the U.S.; the plan is part of a vision to enable construction of the first greater than 10-storey CLT building in the U.S. by the year 2020 (CLT2020) (Pei *et al.*, 2014). A cyclic test was conducted for a CLT-based self-centering lateral force resistant wall component. Through post-tensioning, the wall was designed to resist reverse cyclic loads at large lateral drift, while maintaining the ability to recenter after an earthquake. The results concluded that single-storey rocking CLT walls can provide system recentering, energy dissipation, and strength with adequate performance-based design (Ganey, 2015). Another test has been completed for a deformable CLT floor diaphragm system. The entire project aimed to fill a void in the current seismic design procedure for multi-storey CLT buildings (Pei *et al.*, 2016) .

In addition to the above systematic CLT projects on panels and structures, many other notable efforts have been made.

Cyclic tests were carried out for 12 CLT walls using massive stiff panels and non-conventional high performance anchorage systems made by steel (Tavoussi *et al.*, 2008). The lateral performance of the walls turned out to be very similar among the specimens because the walls simply engaged the tie-down bar as a nearly rigid block.

In Japan, CLT walls made from *Sugi* wood, a locally available softwood species, were tested (Okabe *et al.*, 2012). The walls were tested under different levels of vertical load. Rocking deformation is the predominant behaviour for CLT walls, with the inter-panel connection failing

in shear and each individual panel engaging in its own rocking motion. Although the CLT material was different from that of the other studies, the observation was similar to the findings in the tests conducted in the other laboratories.

Another significant wall test was the one performed in Italy to verify the mechanical characteristics, hysteretic behaviour, and dissipative capacity of CLT walls (Pozza *et al.*, 2014). This work showed that, in CLT shear walls, dissipative capacity and ductility increased with the number of panels, i.e., with the number of steel connectors and fasteners used, advocating the use of CLT for constructing ductile shear walls. This research provided fundamental experimental data for many subsequent numerical analyses.

Two CLT two-storey timber shear wall systems were tested under vertical and lateral loads; this was to investigate how its shear wall system moves under loads to acquire further information towards an understanding of its load resistance mechanisms (Reynolds *et al.*, 2017). The study provided new knowledge on the deformation and load resistance of a common structural system using CLT: that of platform construction. The measured deformations of the two-storey shear wall systems showed that, under ultimate loading, the movement of the complete shear wall was dominated by rigid-body movement of the panels, and that the screwed half lap joint was effective in allowing the two panels to act compositely.

A cyclic test of CLT walls was conducted using an innovative connector subjected to "shear-tension" and "shear-compression" loading configurations (Polastri *et al.*, 2017) . The behavior of timber walls assembled by such connectors was reported.

The most up-to-date structural test is a shaking table test of an innovative two-storey structure made of cross-laminated timber panels; the assessment was performed through a series of seismic tests to determine how it would perform in an earthquake (Diego, 2017). The tests were

conducted at the Natural Hazards Engineering Research Infrastructure at the University of California`s San Diego (NEHRI@UCSD) site, which was funded by the National Science Foundation (NSF). The data collected will be used in the design of a new generation of wood-frame high-rise buildings following its release.

2.2.2 CLT connection experiments

As the key performance of CLT buildings under lateral loading is controlled mainly by their connections, many experimental studies on CLT wall-to-floor and wall-to-foundation connections have been conducted.

In 2005, the seismic behaviour of the CLT connections was tested at University of Ljubljana, Slovenia (Dujic and Zarnic, 2005). Cyclic tests were carried out for CLT connections with metal brackets loaded in tension and shear forces. Nails with a diameter of 4 mm and lengths of 40 mm and 60 mm were used to connect the angle brackets to the CLT panels to ensure a ductile failure mode. The use of the 60 mm long nails yielded to a ductile failure mode, while conversely, the use of the 40 mm long nails lead to a rather brittle behaviour, with failure occurring in the lowermost row of nails for the plug shear. This plug shear failure was a consequence of the nails not penetrating deeply enough into the middle layer of the wall. Hence, a recommendation was given to use nails or screws at least 60 mm in length to achieve a ductile failure mechanism and avoid brittle shear plug failure. This research also investigated the screwed connections between perpendicular panels; it employed five specimens with Φ8 mm screws 160 mm in length with 80 mm long threaded part that were cyclically tested under shear loading. The screws likewise exhibited ductile behaviour. Although too few specimens were tested to derive a final value, the results of this preliminary investigation provided a first approximation for the overstrength factor to be used in design of components with brittle failure.

The research project at the Technical University of Graz, Austria, consisted of a series of monotonic and cyclic tests on four types of angle brackets. At least three cyclic test repetitions were performed for each type (Flatscher and Schickhofer, 2011). The mechanical properties in terms of strength, stiffness, energy dissipation, ductility ratio, and strength degradation were calculated. The research results were reported in German and a broad database was created for connectors which are currently used in CLT construction.

One comprehensive CLT connection experiment conducted in Italy invloves a series of panel connection tests using 20 different screwed panel configurations (Gavric *et al.*, 2011). The types of metal connectors, screws and nails were equal or similar to the ones used in the SOFIE building. The number of fasteners in each configuration and the spacing between the fasteners was established in accordance with the reference building. The match between the properties of the X-Lam connections in the single connection experimental test program and between the full-scale SOFIE buildings enabled a better understanding of the cyclic behaviour of each connection in the SOFIE X-Lam buildings. In-plane monotonic and cyclic shear tests were performed on mechanical screwed connections between adjacent parallel wall-wall and floor-floor CLT panels. Monotonic and cyclic tests were carried out on orthogonally connected panels (wall-wall and wall-floor) subjected to shear and withdrawal load. Mechanical properties in terms of strength, stiffness, energy dissipation, ductility ratio and impairment of strength were evaluated. The overstrength factor, which is of great importance in capacity-based design, was also evaluated for the different types of connections tested. Two types of joints, the step and spline joint, were investigated, with the results showing that, the former one can perform at relatively high stiffness but with some failure modes being brittle, while the latter one can resist greater forces at higher displacement values. The withdrawal tests denoted the importance of screw head penetration.

Okabe *et al.* (2012) conducted a cyclic lateral load test of *Sugi* CLT, made by the most popular softwood in Japan. Two types of hold-down fastener were prepared which were certificated for Japanese timber construction. Shear performance between the bottom of the CLT wall and the sill, and vertical shear performance between the CLT wall-to-wall connections were also tested. This research provided experimental data for the structural performance of the CLT in Japan and proved its applicability.

A test program was conducted to investigate the performance of CLT connections subjected to simulated earthquake loads (Schneider *et al.*, 2012; Shen *et al.*, 2013). Two different brackets in combination with five types of fastener were tested under monotonic and cyclic loading protocols. An energy-based cumulative damage assessment model was calibrated with CLT connection test data. This study aimed to quantify the damage assessment and evaluation of connections in three-ply CLT panels under cyclic loading. Analysis of the test results showed that five of the six types of connections experienced failure when the average damage index, *D*, reached approximately 0.80; therefore, for the damage prediction model, complete failure of the connection was assumed to occur at this level. This is one of the few studies that attempted to quantify the damage of CLT connections.

An experimental investigation of the mechanical behaviour of a range of steel angle bracket connectors was carried out (Tomasi and Smith, 2014). These commercially manufactured and specially designed connectors were intended to resist horizontal shear force flow at CLT wall and foundation interfaces. Five types of proprietary angle brackets and two types specially designed by researchers were tested. Angle bracket connectors were attached to CLT panels by using two types of proprietary fasteners, Anker annular threaded nails, of 4 mm × 40 mm and 4 mm × 60 mm, respectively. The angle bracket was connected to the CLT panel with nails and then connected

to the vertical steel plate, representing a foundation, using one or two bolts. Both monotonic loading and fully reversed displacement controlled loading protocols were employed. The structural characteristics of the steel angle bracket connectors were evaluated. The research concluded that the behaviour of the CLT panel-to-foundation angle bracket connections was too complex to be predicted using simplified analytical methods. Therefore, test based studies are the only reliable means of determining the design capacities for particular types of angle bracket connections.

A laboratory test was carried out on a set of radiata pine CLT walls and hold-down connections taken into consideration both quasi-static monotonic and cyclic loading testing (Benedetti *et al.*, 2016). The CLT wall samples were 90 mm thick and, composed of three 30 mm thick layers of C16 grade radiata pine timber. WHT 540 hold-downs and different fastener combinations were experimentally analyzed. In terms of the connections, it was observed that the hold-downs on radiate pine CLT elements reached a lower loading capacity than those on other wood species, while no significant difference was observable in the parallel-to-grain capacity of angle brackets connections.

In addition to the traditional commercial connectors, several new connectors have also been invented and tested.

Two types of shear connectors used in floor elements to connect concrete beams and CLT panels were tested (Jacquier and Girhammar, 2012). The shear connectors consisted of a steel plate. The CLT panel was attached to the steel plate with screws. The main slip occurred between the CLT panel and steel plate. Shear tests were conducted on the specimens. The composite action, strength and stiffness increase were evaluated. The connectors exhibited desired ductile characteristics and can be recommended for use in composite floor elements. The main slip

occurred at the steel-timber interface. The slip modulus and ultimate capacity were satisfactorily high, providing a significant degree of composite action.

The CLT joints of a bonding system, the "Sherpa-CLT Connector", were designed and tested for CLT joints (Kraler *et al.*, 2014). The connector was designed to enable the joining of large-size massive timber elements for wall, roof and floor constructions, with intermittently fixed bonding materials at the construction joints so that a precise, airtight fitting could be achieved. The normal and shear forces were tested for the connectors.

An innovative angle CLT connection, called the XL-stub, was tested under one monotonic loading, three cyclic constant amplitude loadings and one cyclic loading at variable amplitudes (Latour and Rizzano, 2015). The proposed dissipative connector was designed to have the same stiffness and resistance as the classical hold-down. The results of the experimental analysis demonstrated an improvement in the hysteretic behaviour of the classical hold-down since it was designed to dissipate the energy in the flange plate, which has a shape similar to that usually employed for ADAS (added stiffness and damping) devices, rather than in the nails or screws.

A new energy dissipater was tested for cross-laminated timber (CLT) self-centering walls (Kramer *et al.*, 2015). The dissipater was fabricated following the concepts used in developing steel buckling restrained steel braces (BRB); it had a milled portion designed to yield and was enclosed within a grouted steel pipe. The connection was tested through a test sequence of displacement-controlled cycles. Three sets of tests were performed including: individual tension tests of the energy dissipaters, panel tension tests, and panel cyclic tests. The connection system showed little sign of fatigue from repeated use. The results attested to the robust yield behaviour and energy dissipation properties of the connection system. The design of the energy dissipater

needs to consider the effects of buckling, which should be controlled to ensure the predictability of the dissipater`s performance.

Another new CLT connection, called the X-bracket, was tested under cyclic loading (Scotta *et al.*, 2016). The connector was designed to provide an adequate level of dissipative capacity to the CLT structures. Compared to a commercial hold-down of almost the same strength and stiffness, the proposed connection achieved, on average, an approximately twice the ultimate displacement and a ductility value about eight-times larger. Compared to a commercial angle bracket of similar strength, it assured, on average, twice the ultimate displacement, a nine-fold ductility value and a four-fold elastic stiffness. It displayed higher performance than the traditional ones, in particular when loaded in shear, which testified that it can provide good ductility and dissipation capacities.

Thus, these above outlined tests provided the experimental data base for the numerical modeling of CLT connections and structures.

2.3 Numerical modeling

Analytical models, structural analyses and the numerical simulation of CLT shear walls, buildings, and connections have been studied based on the laboratory data acquired from the above experimental tests. Initially, numerical modeling was carried out on the structural level, considering the CLT connections as springs for simplification purposes. Later, the importance of those connectors' characteristics of was addressed and research on detailed connections modeling began.

The literature here includes two parts, CLT connection modeling in structures, and independent CLT connection modeling.

2.3.1 CLT connection modeling in structures

The earliest numerical modeling of CLT structures was numerical research conducted with shaking table tests of full-scale XLam buildings in Italy (Ceccotti, 2008). The research proposed constitutive models for hold-down connections and steel angles, implemented in the Drain 3DX computer program. In this model, non-linear symmetric springs were used to simulate angle brackets, and non-linear symmetric springs for hold-downs. The hysteresis models are shown in Figure 2.1. The modeling method reached satisfying global level prediction results for the building performance in the tests, but the modeling results for the connections were not sufficiently precise.

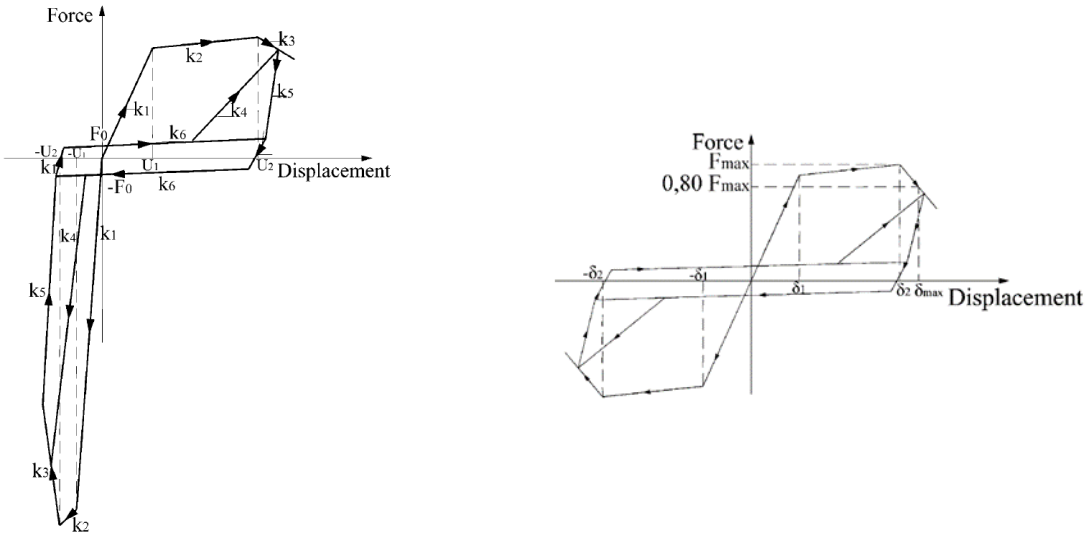

(a) (b)

Figure 2.1 Hysteresis Loops: (a) hold-down; (b) angle bracket (Ceccotti, 2008)

Later on, the dynamic behaviour of a 7-storey CLT building tested by shake table was predicted (Dujic *et al.*, 2010). Assumptions based on engineering judgment and rough static analyses were used to define the stiffness and load bearing capacity of mechanical connections. A mathematical model was developed in Program SAP2000 where modal and time history analyses were carried out. The model used longitudinal spring elements to simulate the behaviour of the

main mechanical connectors. The hysteresis loops are shown in Figure 2.2. Comparing the calculated and measured results, the research presents an approximate method for performing fully blind predictions.

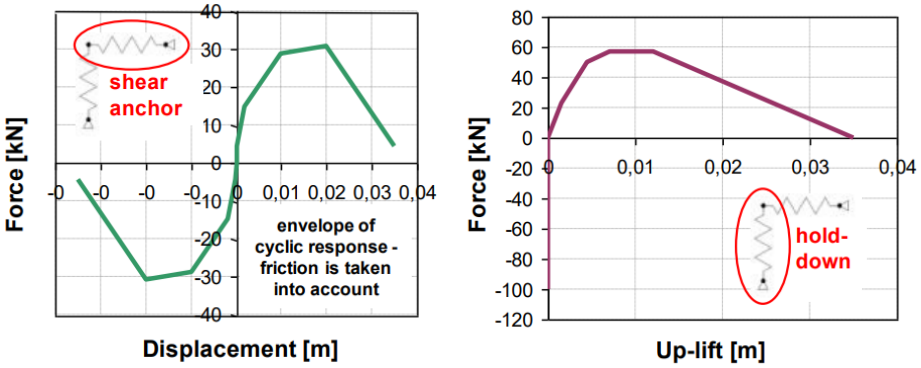

(a) (b)

Figure 2.2 Hysteresis Loops: (a) angle bracket; (b) hold-down (Dujic et al., 2010)

Fragiacomo *et al.* (2011) carried out a non-linear static analysis of a case study building. Non-linear springs were used to model the BMF105 brackets in SAP2000 based on the experimental curves of their mechanical properties. The paper addressed the importance of considering the overstrength factors of these connectors. It was suggested to determine the stiffness, strength and ductility of the steel brackets and screwed connections according to the procedure in Okabe *et al.* (2000), as shown in Figure 2.3. It was also recommended that more cyclic tests of metal bracket and hold-down connectors should be carried out for each configuration to derive more accurate values.

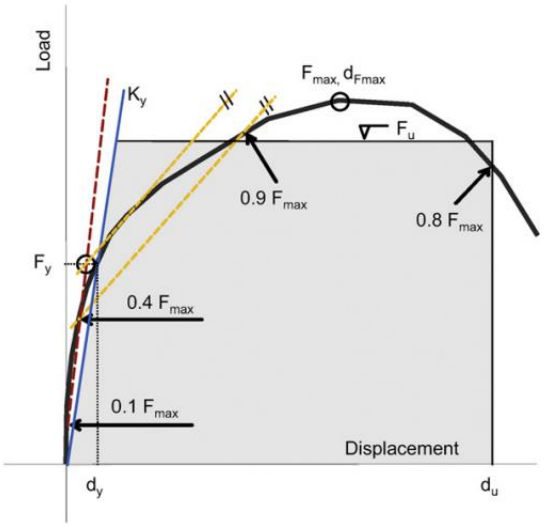

Figure 2.3 Stiffness, strength and ductility determination (Fragiacomo et al., 2011)

Pei *et al.* (2012) used a ten parameter hysteretic model commonly for wood connection modeling to simulate CLT walls. This model was proposed by Folz and Filiatrault (2002), shown in Figure 2.4. In this model, rather than matching the connectors' behaviour, the parameters of the connectors were calibrated by matching the entire wall model with the wall test results through iterations.

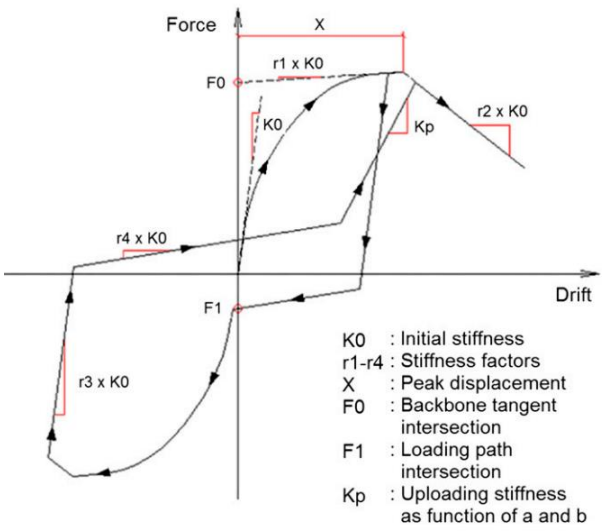

Figure 2.4 Hysteretic model commonly for wood connection modeling (Pei et al., 2012)

Hristovski *et al.* (2012) modelled a full-scale shaking table test of CLT panels systems and used inelastic constitutive relationships for the anchors. In the shear force-slip modeling, a bilinear envelope with a descending branch was adopted in both the positive and negative directions. The assumption was that the connection in the tangential direction could not support any shear force unless the absolute value of the actual slip were greater than that of the previously accumulated slip. In the vertical direction for the tension, the real working diagram was approximated with a linear elastic-plastic softening diagram, constructed according to the basic test under tension. For compression, the constitutive law was assumed to be linear elastic. Those computational constitutive relationships are shown in Figure 2.5.

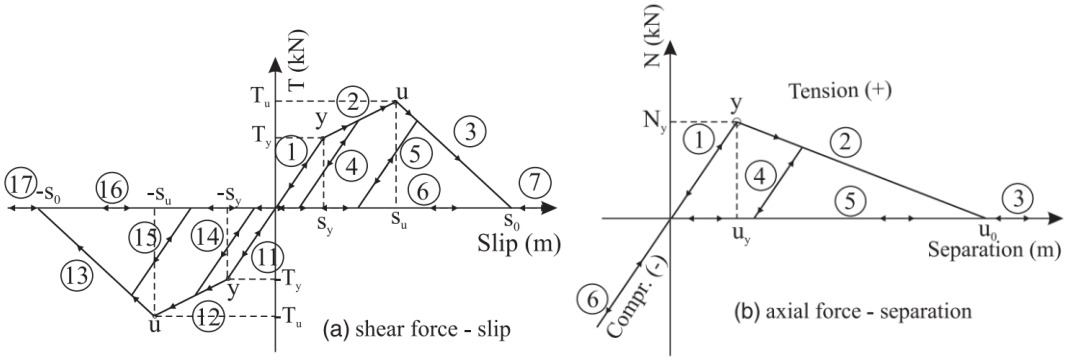

Figure 2.5 Hysteresis Loops: (a) shear force - slip; (b) axial force – separation (Hristovski et al., 2012)

Follesa *et al.* (2013) addressed the complexity of modeling an entire structure using the properties of mechanical fasteners and pointed out that in most cases, the only reliable design of a CLT building involves formulating a proper finite element model to analyze the CLT structure based on the available equations for the calculation of the connection slip modulus given in Eurocode 5. Thus, in this research, angle brackets and hold-downs were modelled in SAP2000 with truss elements. The section and material properties of the trusses were calculated through the equations in Eurocode 5 based on experimental results.

Liu and Lam (2014) simulated the seismic behaviour of mid-rise CLT shear walls with coupling beams. In this study, hold-downs and angle brackets were modelled as ZeroLength elements with Pinching4 material in OpenSees software. The Pinching4 model is composed by piecewise linear curves, which represents a "pinched" load-deformation relationship, and accounts for the stiffness and strength degradation under cyclic loading. The hysteresis law is shown in Figure 2.6. OpenSees provided an elastic No-tension material which could be applied to the additional ZeroLength elements to model the high compression stiffness at the base. This is the first research that adopted Pinching4 material for connections in CLT structural modeling.

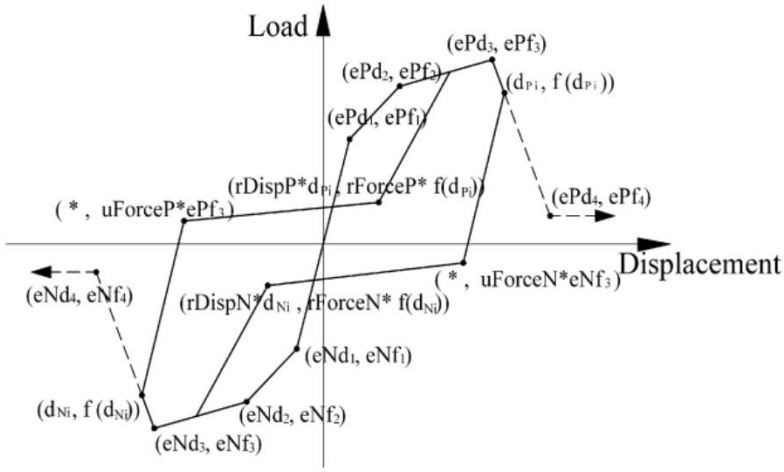

Figure 2.6 The Pinching4 model (OpenSeesWiki)

Gavric and Popovski (2014) proposed a design model for CLT shear walls and assemblies based on connection properties. The study pointed out the limitations of current design methods, which determine the resistance of CLT walls under lateral loads by a simple summary of the shear resistances of all the connectors at the bottom of the wall, while the uplift forces due to global overturning moments are taken by hold-downs in the corners of the building. The research addressed the problem that such simplified approaches did not take into account the fact that the kinematic behaviour of CLT walls under lateral loads is a combination of the rocking and sliding

of the entire panel. Consequently, all connectors at the bottom of the wall are subjected to a combination of shear and uplift loads. Thus, the paper proposed several kinematic models for CLT walls, as presented in Figure 2.7. The three models (D3, D4 and D5) took full uplift resistance of hold-downs and full shear and uplift resistance of all brackets into account. The last two models considered the shear-uplift interaction of the load carrying capacity in the brackets due to bi-axial loading with different shear-uplift interaction domains (circular and triangular). The newly developed models displayed a higher level of consistency, while the analytical model, D4, accounted for the sliding-uplift interaction in accordance with a circular domain; this model was proved to be the most suitable candidate for the future development of design procedures to determine resistance of CLT walls under lateral loads. The research addressed the great importance of studying the coupling effects of the shear and axial forces on the connections.

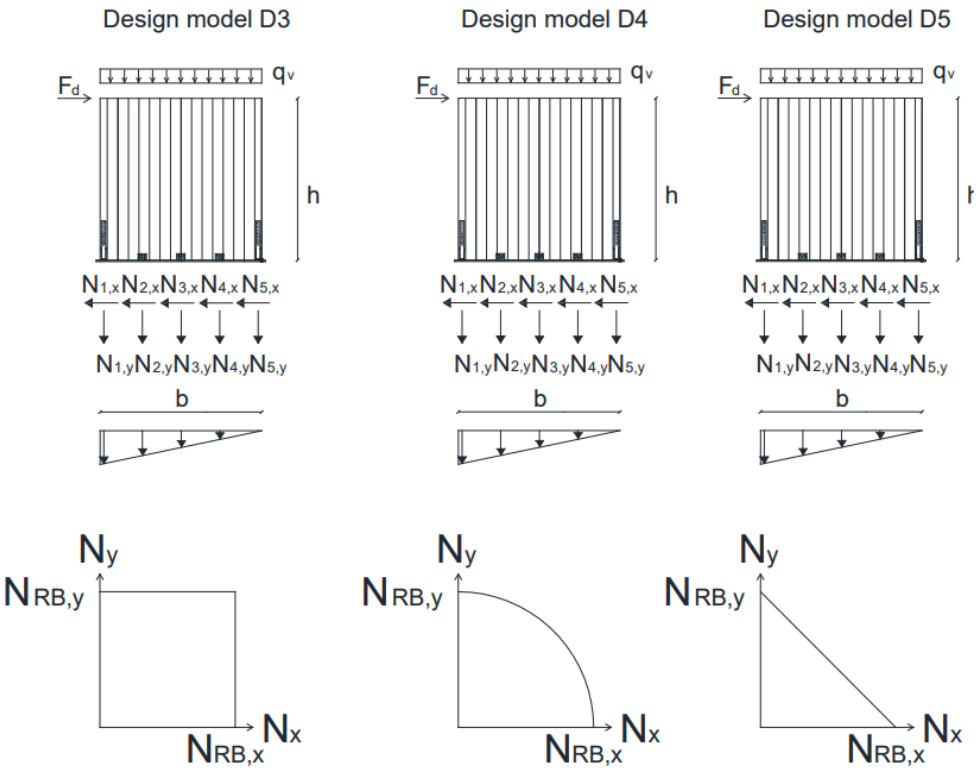

Figure 2.7 Kinematic models for CLT walls (Gavric and Popovski, 2014)

Based on the above analytical models, Gavric *et al.* (2015) developed models that take into account all the stiffness and strength components, including those in the weaker direction, of hold-downs and angle brackets. The model adopted a nonlinear approximating trilinear force-deflection relationship for CLT connectors, as shown in Figure 2.8. The study considered a reduction of their strength capacity due to the bi-axial loading of hold-downs and angle brackets using the shear-uplift interaction inequality from ETA -07/0055: $\left(F_x/F_{R,x}\right)^2+\left(F_y/F_{R,y}\right)^2\le 1$, where F_x and F_y = the shear and uplift forces in the connector; and $F_{R,x}$ and $F_{R,y}$ = the strength of the connectors in the shear and uplift direction. The model, taking into consideration the tension capacity of the connectors and an interaction plastic domain between the axial and shear capacity of the connectors, was proved to be accurate in terms of strength and deformability predictions, and was therefore proposed for nonlinear pushover analyses of CLT wall systems.

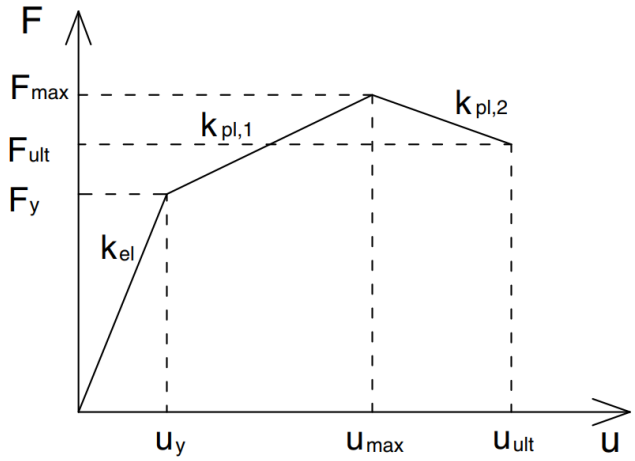

Figure 2.8 The trilinear force-deflection relationship for CLT connectors (Gavric et al., 2015)

To study CLT shear walls with more precise connection models, Li and Lam (2015) built a finite element wall program CLTWALL2D. The nonlinear spring properties were represented by a subroutine called HYST that is able to model the strength and stiffness degradation, and the

pinching effect commonly observed in timber connections. The parameters were calibrated by experimental data on CLT connections and embedded within the CLTWALL2D model. The study addressed the limitations of those multi-linear connection springs used in most commercial software packages since the load-deformation hysteresis of a typical timber connection shows high nonlinearity in the entire loading history, which can make it challenging to define a yielding point. The mechanics-based subroutine exhibited reasonably good agreement between the model predictions and test results. This model is also the base model of this dissertation. Thus, the details and further development of this model will be presented in Chapter 5.

Within the last two years, CLT structural behaviour has become a more essential focal point for research, and many findings have been published regarding the non-linear behaviour of connectors. However, most research to date has ceased from exploring the characteristics of CLT connections but used simplified method to predict the global performance of walls and structures.

Tamagnone *et al.* (2016) provided a simplified non-linear procedure for the seismic design of CLT wall systems using the same modeling method for the connections; the purposely-developed user subroutine for ABAQUS, mentioned earlier (Rinaldin *et al.*, 2013). The highlight of this method is that it gives the designer an indication on the failure mechanism in walls. Later on, the same connection modeling method was used for non-linear simulations of shaking-table tests on 3- and 7-storey CLT buildings (Rinaldin and Fragiacomo, 2016). The model somewhat fit the test results, yet it can still be observed that there is room for future improvement in the unloading branch and the model's robustness, as demonstrated in Figure 2.9.

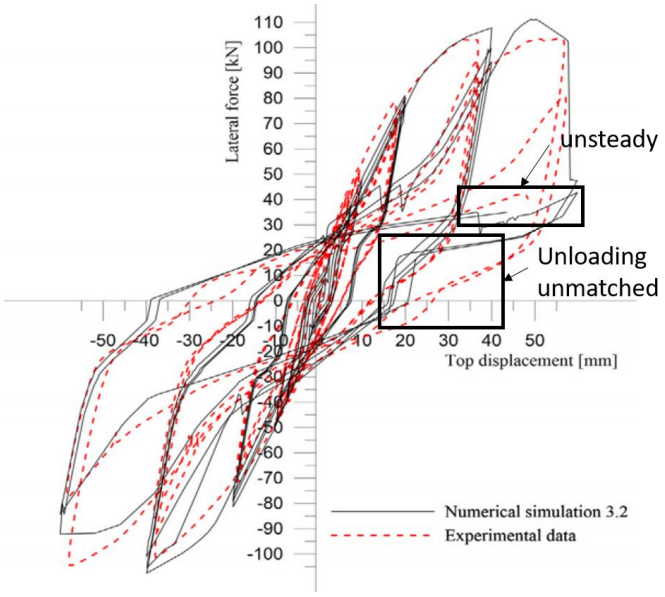

Figure 2.9 An experimental-numerical comparison of CLT walls (Rinaldin and Fragiacomo, 2016)

In a study on the seismic behaviour and design of an 8-storey CLT building, shear and uplift connectors were modelled using non-linear links and zero-length elements by means of the Hysteretic Material in OpenSees (Demirci *et al.*, 2017) , as shown in Figure 2.10.

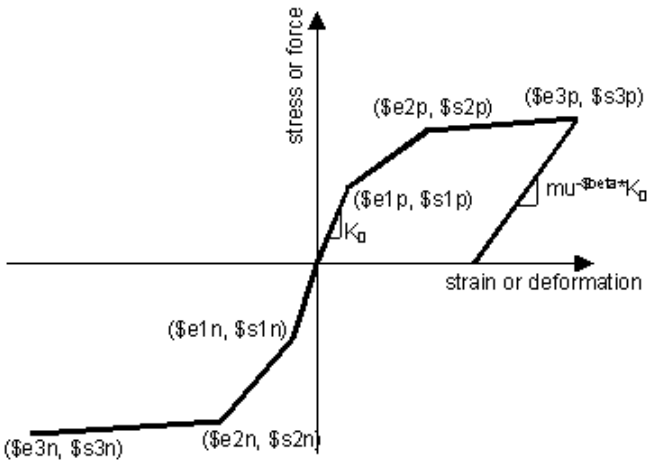

Figure 2.10 Hysteretic Material (OpenSeesWiki)

Nolet (2017) modelled the behaviour of multi-panel CLT walls under lateral loading with elastic-perfectly plastic curves for hold-downs. Much research has been conducted using the

connection models described earlier, particularly the Pinching4 material in OpenSees (Casagrande *et al.*, 2017; Shahnewaz *et al.*, 2017a; Shahnewaz *et al.*, 2017b; Tamagnone *et al.*, 2018).

It should be noted that the characteristics of connections under lateral loading are crucial to the performance of the entire structure. Without a deep understanding of their mechanism and accurate connection models, the simulation results cannot provide effective validation.

2.3.2 Independent CLT connection modeling

To better understand the structural behaviour of CLT connections, numerical studies on detailed CLT connections were carried out.

Rinaldin *et al.* (2011) proposed a numerical method providing a more accurate evaluation of the energy dissipation observed in previous experiments. Using this method, Rinaldin *et al.* (2013) modelled the CLT walls with connections using an advanced non-linear hysteretic spring to illustrate the cyclic behaviour of the connections in ABAQUS as an external subroutine. The advantage of these analytical models for connections in CLT structures (the brackets, hold-downs and connections between panels) is their allowance for the pinching effect, strength and stiffness degradation, which are features of great importance in the cyclic behaviour of timber structures. The piecewise linear laws used to model the angle bracket and hold-downs are outlined in Figure 2.11. A highlight of the model is that it also accounts for the shear and axial interactions on the connections. But the article concluded that these interactions are due to the influence of friction, not the complex loading status. It uses a shear-axial force domain to describe the interaction effects. Later, Izzi *et al.* (2018) used this model to study the influence of the boundary conditions (with vertical load applied to the top of the wall and friction to its base) and aspect ratio of the CLT panels.

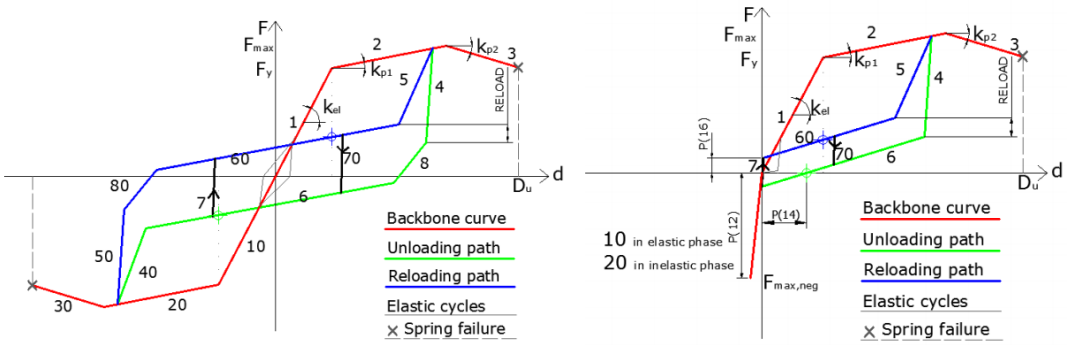

(a) (b)

Figure 2.11 Hysteresis Loops: (a) angle bracket; (b) hold-down (Rinaldin et al.,2013)

An energy-based cumulative damage assessment model was developed to focus on damage accumulation over time and the correlations of a computed damage index and to observe CLT connection damage (Schneider *et al.*, 2013). The research aimed to provide a means of numerically quantifying the damage resulting from earthquake loadings. In this study, the hysteretic response was calculated as an equivalent energy elastic-plastic (EEEP) curve based on empirical formulas. Although not sufficiently accurate, the model first provided a tool for considering the damage to various failure modes of CLT connections, which is able to capture stiffness and strength degradation. The hysteresis model is shown in Figure 2.12, and it is based on equations from Krätzig *et al.* (1989).

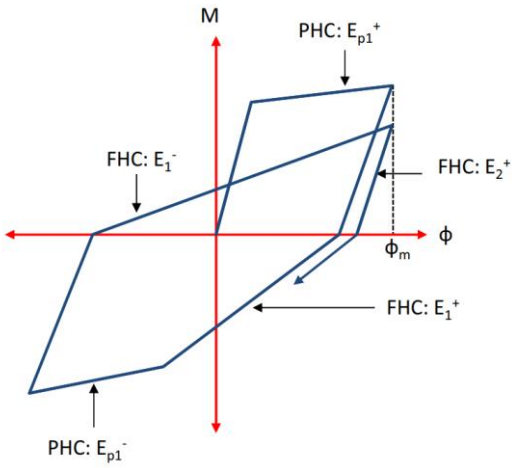

Figure 2.12 Equivalent energy elastic-plastic (EEEP) curve based on empirical formulas (Schneider et al., 2013)

Six connection combinations were modeled in a finite element program, using two methods to assess the load-displacement curves (Schneider *et al.*, 2015). The first method followed the American Society for Testing and Materials, accounting for the ductility ratio, elastic shear stiffness, and the EEEP-curve, while the second method adopted a SAWS model in OpenSees, as shown in Figure 2.13, following an energy-based accumulation principle with a damage index being calculated at each time step. The later one displayed greater accuracy in evaluating hysteretic models.

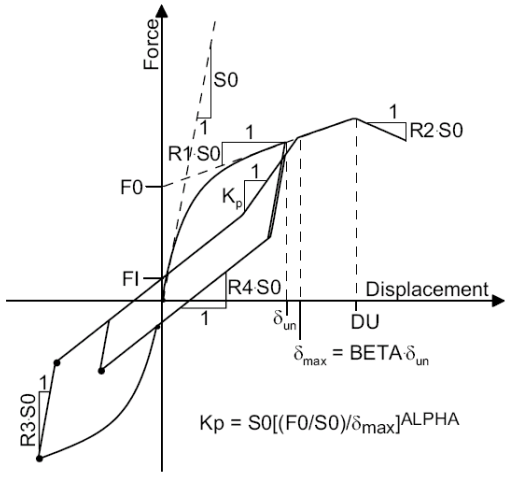

Figure 2.13 SAWS model (OpenSeesWiki)

Hassanieh *et al.* (2016) employed the Beam-on-Foundation model (BFM) to capture the behaviour of steel-CLT composite joints containing screws and bolts. The screws were modelled in OpenSees by a non-linear force-based beam-column element with distributed plasticity, as shown in Figure 2.14. The foundation behaviour was modelled by zero-length elements that used springs to connect the nodes on the beam (connector) to fixed supports. The model and adopted force-displacement relationships are shown in Figure 2.15. The model proved the efficiency of the Beam-Foundation Theory in modeling CLT connections. The monotonic analysis displayed great prediction capacity for the initial stiffness and yield strength of the connections. Further studies on cyclic and earthquake loading are required to investigate the damage and degradation of the CLT connections.

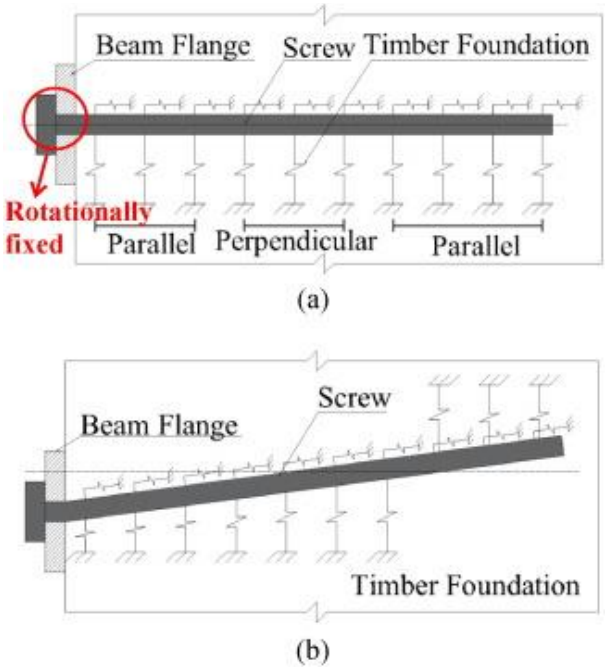

Figure 2.14 The Beam-on-Foundation model: (a) without deformation; (b) with deformation (Hassanieh et al., 2016)

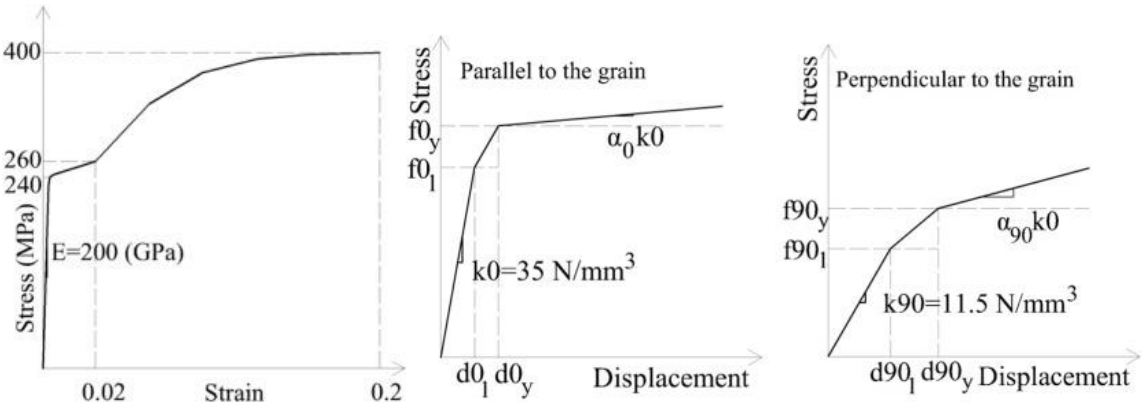

(a) (b) (c)

Figure 2.15 Force-displacement relationships: (a) steel; (b) wood parallel to the grain; (c) wood perpendicular to the grain (Hassanieh et al., 2016)

Pozza *et al.* (2017) proposed a new numerical model of CLT hold-down connections for coupled axial-shear actions. In order to consider axial-shear interaction, the research considered the constitutive law of the connection in one direction to be affected by the history of displacements occurring in the orthogonal direction, as shown in Figure 2.16. Further, the constitutive law adopted for the hysteretic behaviour is based on the model of a reinforced concrete joint, as shown in Figure 2.17 (Lowes *et al.*, 2003). The model provided a curve-fitting means to study the hysteretic behaviour of CLT connections under bi-axial loading.

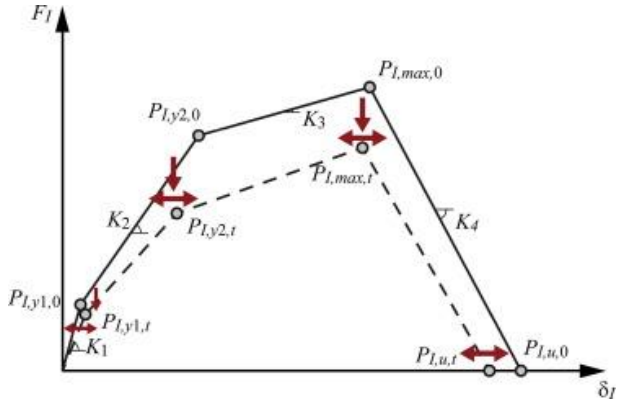

Figure 2.16 The constitutive law for the connections affected by the history of their displacements (Pozza et al., 2017)

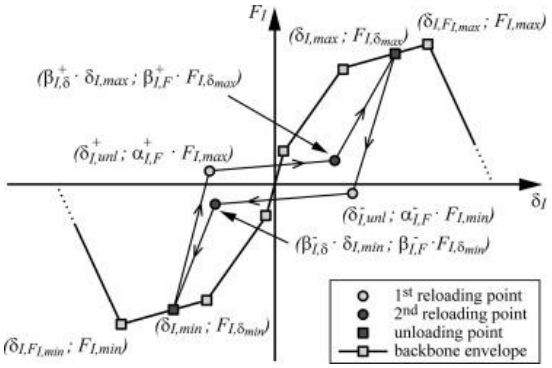

Figure 2.17 Hysteretic behaviour based on the model of a reinforced concrete joint (Lowes et al., 2003)

These curve-fitting methods, though possessing relevant accuracy in predicting behaviour, lack the potential for explaining the physical phenomena in the CLT connection tests. The above-mentioned finite-element methods, on the other hand, did not consider different types of loading conditions for CLT connections. These gaps demonstrate the urgent need to conduct research on the precise modelling of CLT connections under complex loading.

2.4 Summary

This chapter introduced background information and a literature survey on experimental test and numerical analyses of CLT connections.

Monotonic, cyclic, and shaking table tests of CLT structures and panels using metal connectors were reviewed first. These tests addressed the importance of the connections in CLT structural performance. Following this, the CLT connection tests were surveyed. Most of the limited experiments were conducted under uniaxial loading since the common assumption is that angle brackets take all of the shear forces, while hold-downs take all of the tension in CLT panels. There is, however, an absence of CLT connection tests under complex loading.

Numerical research on modeling CLT connections, both in structures and stand-alones, were introduced. In structural analyses, due to the high non-linearity in the complex CLT connections, springs with a simplified curve-fitting method were commonly adopted. Several

works addressed the need to consider the combined loading effect on metal connectors, and provided empirical formulas. Based on independent connection modeling by curve-fitting methods and finite-element methods, the full characteristics of CLT connections were outlined, including strength degradation, unloading and reloading stiffness degradation, and the pinching and coupling effects. However, most models lack the ability to assess all of these elements.

The above outlined studies failed to study the behaviour of CLT connections under complex loading, which would have obtained a more accurate understanding of CLT structural performance. Thus, for the purpose of this thesis, experimental tests on commonly used CLT connections, angle brackets and hold-downs, under bi-axial loading were conducted; furthermore, based on the test results, this research developed analytical and finite-element based numerical models for these connections demonstrating high accuracy and efficiency.

Chapter 3: Experimental Test of CLT Angle Bracket Connections under Bi-axial Loading

3.1 Introduction

Cross-Laminated Timber (CLT) is an attractive structural material with relatively high dimensional stability and load capacity; therefore, its use for walls and floors in massive timber structural systems is expanding. Much research on both the component and structural levels has recently been carried out to study CLT structural behaviour. A series of experimental tests on the structural performance of CLT walls was conducted at the University of Ljubljana, Slovenia, including monotonic and cyclic tests of CLT walls with different anchorage details (Dujič *et al.*, 2004), CLT walls with different vertical load and boundary conditions (Dujic *et al.*, 2006), and CLT walls with openings (Dujic *et al.*, 2008). The IVALSA Institute of the National Research Council at San Michelel all'Adige (Trento, Italy) carried out the SOFIE project to investigate the performance and capacities of the X-LAM system, known now as CLT structures. The project included a series of lateral resistance performance tests of cross-laminated wooden panels (Ceccotti and Follesa, 2006), a shaking table test of a three-storey CLT building (Ceccotti, 2008), and a seismic test on a seven-storey X-lam building on the E-Defense 3D shaking table in Japan (Ceccotti *et al.*, 2013). In Canada, FPInnovations and the University of British Columbia conducted a series of experimental research projects on the structural performance of CLT walls (Popovski *et al.*, 2010; Popovski and Gavric, 2015; Shahnewaz *et al.*, 2017). In the United States, a NEES CLT Planning project is ongoing to develop seismically resilient tall Cross-Laminated Timber (CLT) systems (Pei *et al.*, 2014; Ganey, 2015; Piazza *et al.*, 2015; Pei *et al.*, 2016).

Several notable experimental efforts on CLT structural behaviour have been performed in Germany (Flatscher and Schickhofer, 2011), Japan (Okabe *et al.*, 2012), Italy (Pozza *et al.*, 2014), and Chile (Benedetti *et al.*, 2016). These studies show that most deformation in CLT structures occurs with metal connectors rather than wood, and is dominated by the rocking and slip mechanisms. A typical design assumption is that, angle brackets will slip under loading and only take shear force along the CLT wall. Under such assumptions, former researchers tested CLT connections loaded in one direction (Rinaldin *et al.*, 2013; Schneider *et al.*, 2013). As well, the experimental performance of hold-downs, brackets, and half-lap joint connections under cyclic loading was investigated (Gavric *et al.*, 2011). Experiments were likewise undertaken to evaluate how the structural characteristics of steel angle bracket connectors vary across a range of mass produced and special connectors under shear loading (Tomasi and Smith, 2014). These connectors were tested in shear and withdrawal directions to capture the main features of the behaviour of these CLT connections.

In these studies, rocking and slip mechanisms were considered to be interacting independently. However, recent study has shown that those two mechanisms are acting jointly on the connectors. Under complex stress conditions, the shear behaviour and axial behaviour of angle brackets are coupled; this was neglected in the previous simplified methods (Liu and Lam, 2016; Pozza *et al.*, 2017). This chapter presents the results of the monotonic and cyclic tests on CLT angle bracket connections under bi-axial loading.

3.2 Experimental tests

This experiment aims to investigate the coupling effects of tension and shear forces on the angle brackets used in CLT structures. This section describes the associated setup, specimens and test procedures.

3.2.1 Description of the setup

An experiment was conducted for typical, commercially available CLT angle bracket connections. Steel base-panel connections were tested, representing the wall panels to foundations connection. Two sets of angle bracket connection tests were performed under bi-axial loading, as follows: 1) Set A: monotonic and cyclic tension loading with four levels of constant shear loads, and 2) Set B: monotonic and cyclic shear loading with four levels of constant tension loads. Figure 3.1 presents the configurations of the angle bracket connection tests.

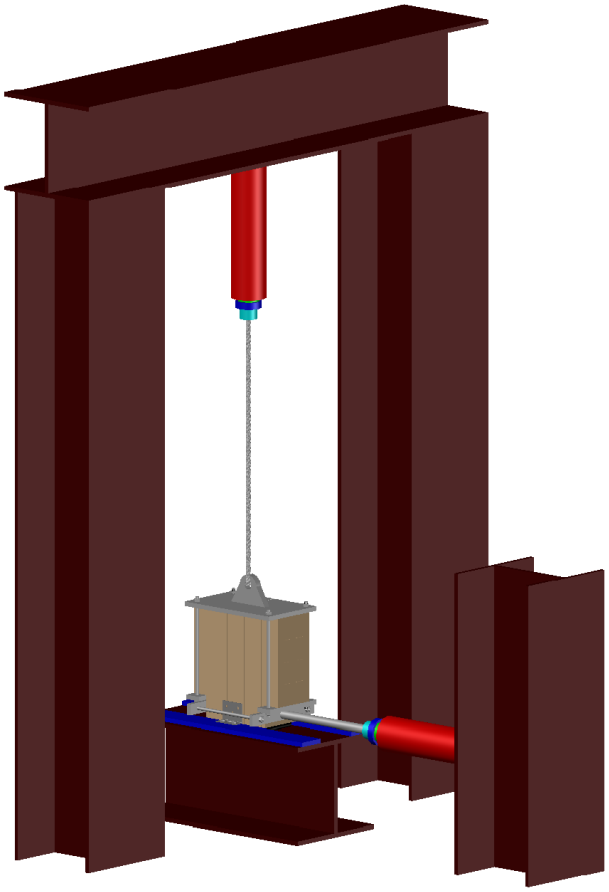

Figure 3.1 A 3D schematic drawing of the set-up

During bi-axial loading, the specimen slips due to the shear force, resulting in the tension force being loaded eccentrically. A long steel cable (1 m) was used to connect the load cell for the

purpose of maintaining tension with the specimen (Figure 3.2). With the horizontal displacement d_s of the specimen, the angle between the cable and the vertical direction θ would not exceed 5°, which minimizes the eccentricity effect. Thus, the tension load (F_T) can be considered as vertical throughout the test. The shear force (F_S) induced a turning moment, since it was located above the base of the specimen. Figure 3.3 shows the mechanisms for calculating the forces at the angle brackets.

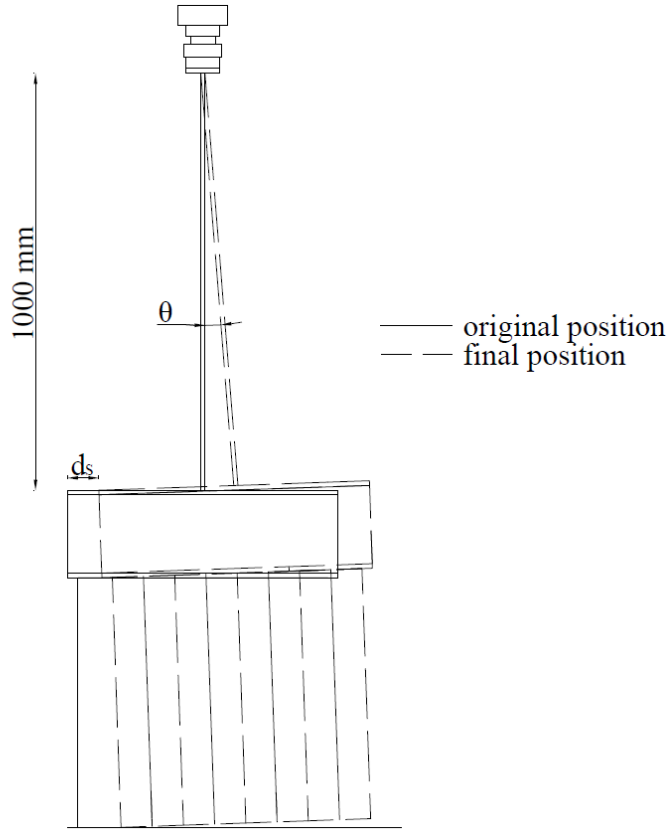

Figure 3.2 The deformation of the cable due to lateral displacement of the specimen

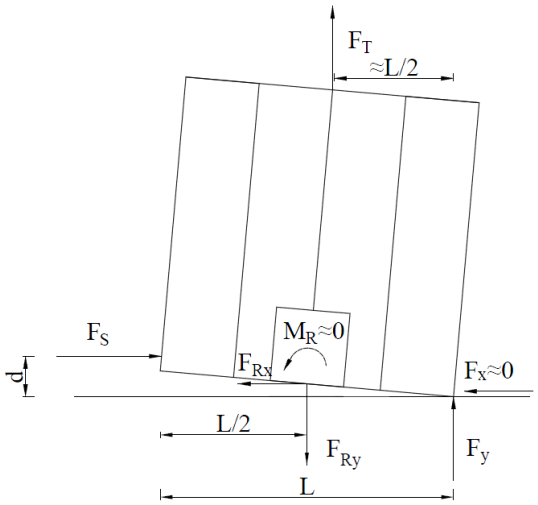

$$\begin{cases} F_S - F_{Rx} - F_x = 0 \\ F_T + F_y - F_{Ry} = 0 \\ F_S \cdot d + F_T \cdot L/2 - F_{Rx} \cdot d/2 - F_{Ry} \cdot L/2 - M_R = 0 \end{cases}$$

$$F_{Rx} = F_S, F_{Ry} = F_T + F_S \cdot d / L$$

Figure 3.3 The bi-axial loading mechanism

As shown in Figure 3.4 (a), the specimen was fixed to the steel base by angle brackets, using three M12 bolts on either side. Two actuators, denoted as LC1 and LC2, were acted on the specimen. LC1 was connected to the steel components constrained by the steel cable to the top of the CLT specimen, providing a constant tension load. LC2 was connected to the steel components constrained by steel plates to the bottom of the specimen, delivering monotonic and cyclic shear loads. Steel rollers were placed between the specimen and the steel base to prevent friction.

Figure 3.4 (b) illustrates one specimen fully set up for the experiment. On each side of the specimen, one linear potentiometer was installed to measure the specimen's vertical displacement. During the 40 kN vertical load test, such complex loading and slight eccentricity of the specimen can cause out-of-plane movement. This was avoided by connecting two rigid "L" shaped steel plates to the specimen with rollers. Figure 3.4 (c) shows how the bi-axial loading acted on the angle bracket connector: at the beginning of each test, a vertical tension load was applied to the connector; following achievement of the target tension load, the monotonic or cyclic shear load was delivered horizontally while maintaining the target tension load.

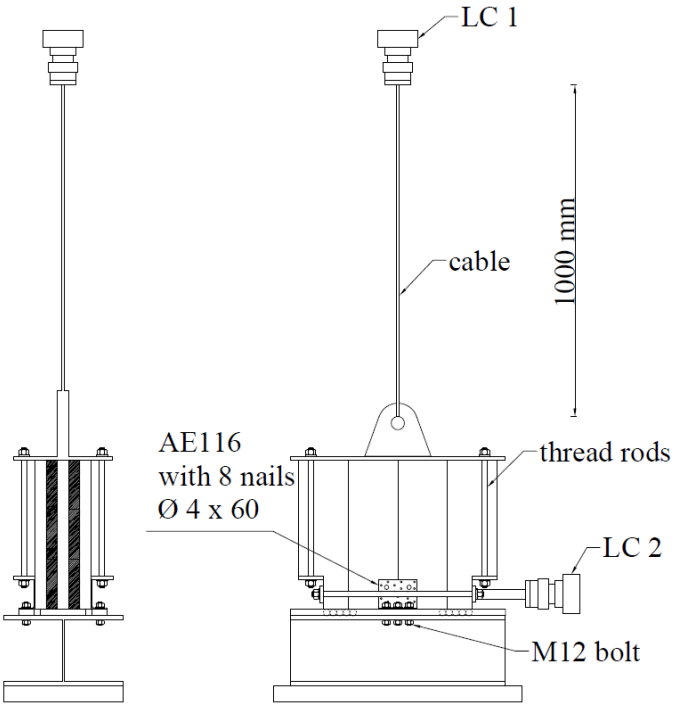
LC 1
cable
1000 mm
AE116
with 8 nails
Ø 4 x 60
thread rods
LC 2
M12 bolt

(a)


"L" shaped steel plate
linear potentiometer

(b)

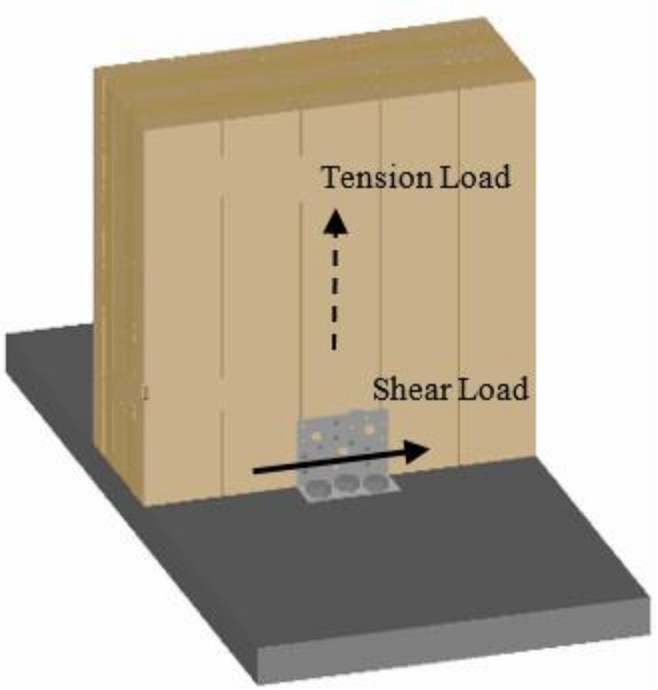

(c)

Figure 3.4 Test configurations of the angle bracket connections: (a) a front and side view drawing of the set-up; (b) a photo of the set-up; (c) bi-axial loading on the angle bracket connector

3.2.2 Specimens characteristics

The CLT panels were made of graded No. 1/2 SPF lumber with five layers. The thickness for each layer was 35 mm and the total thickness of the CLT panel was 175 mm. The dimensions of each CLT specimen were 450 mm × 600 mm; the layout is shown in Figure 3.5 (a). The specimens had a moisture content of 12% and they were stored and tested under controlled conditions at 50% RH and 20°C. The AE 116 (angle bracket) was tested using an 11 annular-ringed nail of 4 mm × 60 mm and 3 12 mm diameter bolts (8.8 grade). The photo and configuration for the AE 116 connector are shown in Figure 3.5 (b).

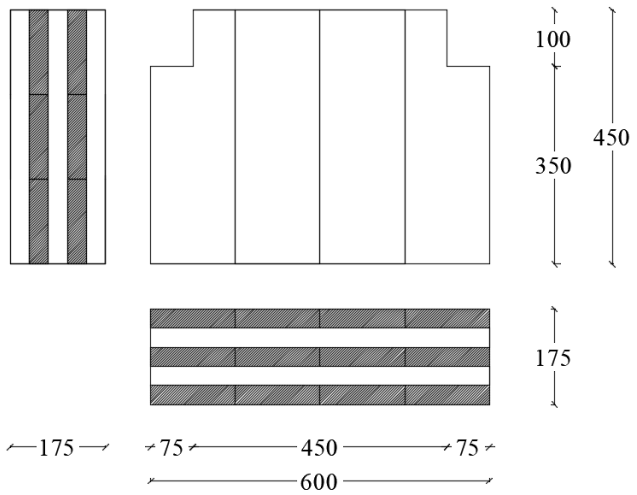

(a)

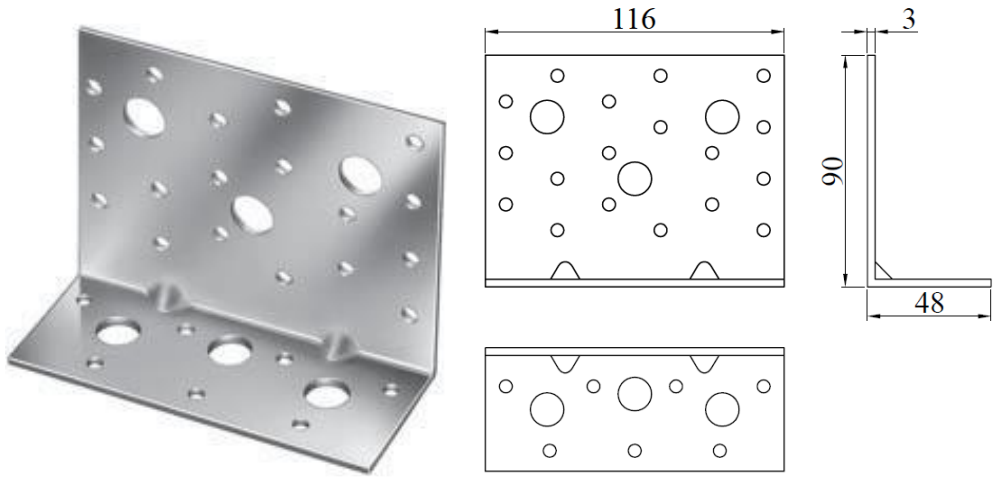

(b)

Figure 3.5 A CLT specimen and angle bracket: a) the layout of the CLT specimen; b) a photo and configuration of angle bracket

3.2.3 Test procedure

All shear tests were conducted using a reverse cyclic procedure with predefined yield values which varied between configurations, depending on the experimental yield values obtained from the monotonic tests.

In Set A, in the horizontal direction, constant shear load was first applied and maintained on the specimens up to the target value with the actuator being under load control. Then, in the perpendicular direction, monotonic or cyclic vertical displacement was applied subsequently. As shown in Figure 3.6 (a), monotonic tension tests were carried out under displacement control at a loading rate of 0.2 mm/s. Cyclic tension tests followed the modified procedure based on EN 12512 (CEN 2006) for the cyclic testing of joints made with mechanical fasteners, at an input displacement rate of 0.8 mm/s, so that a duration of each test did not exceed the time limit of 30 minutes.

In Set B, constant tension load was first applied and then maintained on the specimens in the vertical direction up to the target value with the actuator remaining under load control. Then, monotonic or cyclic lateral displacement was subsequently applied in the perpendicular direction. As shown in Figure 3.6 (b), the monotonic shear tests were carried out under displacement control at a loading rate of 0.2 mm/s. The cyclic shear tests followed the modified procedure based on EN 12512 (CEN 2006) for the cyclic testing of the joints made with mechanical fasteners; this was conducted at an input displacement rate of 0.8 mm/s, so that a duration of each test did not exceed the time limit of 30 minutes.

Set A Test Protocol	
Monotonic Loading Phase	Displacement rate 0.2 mm/s
Cyclic Loading Phase	Displacement rate 0.8 mm/s
No. of Cycle	Peak displacement (mm)
1	1
1	3
3	6
3	9
3	12
3	18

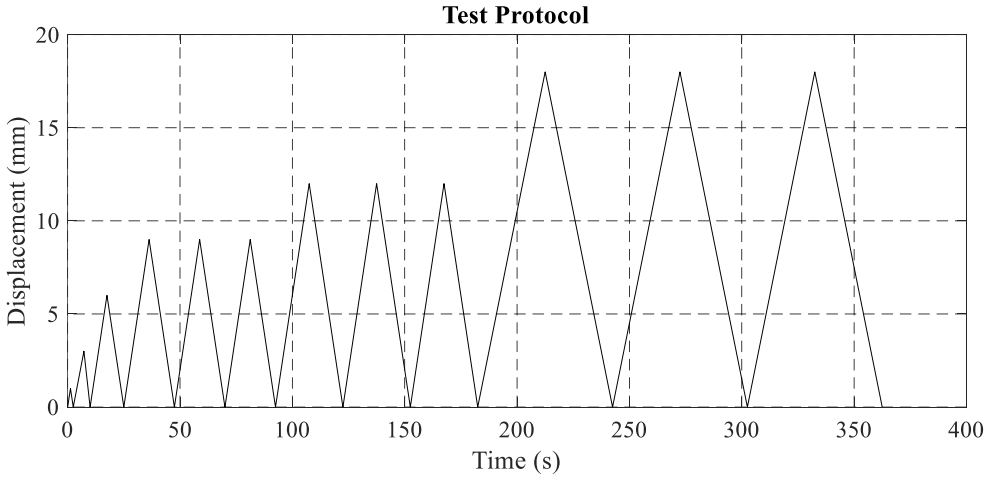

(a)

Set B Test Protocol	
Monotonic Loading Phase	Displacement rate 0.2 mm/s
Cyclic Loading Phase	Displacement rate 0.8 mm/s
No. of Cycle	Peak displacement (mm)
1	2
1	4
3	6
3	8
3	16
3	32

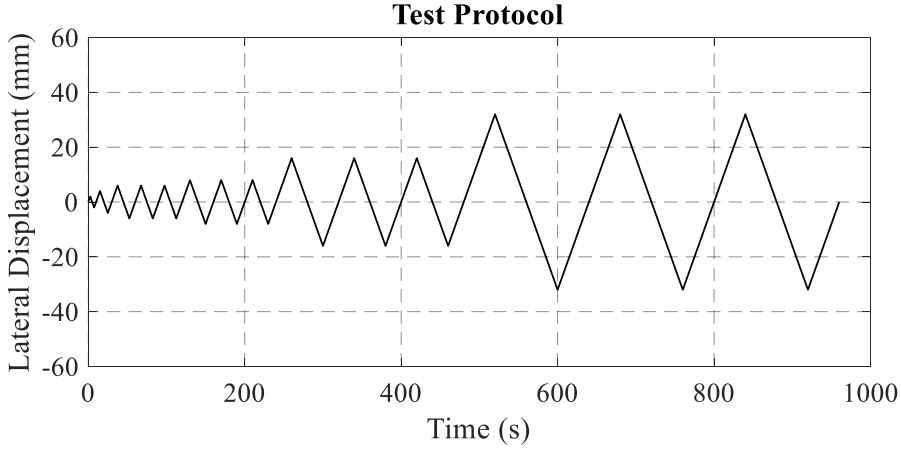

(b)

Figure 3.6 The test protocol: (a) Set A; (b) Set B

In order to evaluate the effects of the tension load on the shear behavior of the angle brackets, in Set A, the angle bracket connections were tested under monotonic/cyclic in-plane

tension loading with four levels of in-plane shear loads. The maximum shear capacity of AE116 was 62 kN; thus, four shear load levels (0 kN, 20 kN, 30 kN, and 40 kN) were selected. For each configuration, one monotonic and three/six cyclic tests were performed. For level 0 kN and 40 kN tension forces, three cyclic tests were conducted due to the stability of the performance at these levels. For level 20 kN and 30 kN, six cyclic tests were conducted.

In order to evaluate the effects of shear loading on the tension behavior of the angle brackets, in Set B, the angle bracket connections were tested under monotonic/cyclic in-plane shear loading with four levels of in-plane tension loads. The maximum tension capacity of AE116 was 76 kN; thus, four shear load levels (0 kN, 20 kN, 30 kN, and 40 kN) were selected. For each configuration, one monotonic and three/six cyclic tests were performed. For level 0 kN and 40 kN tension forces, three cyclic tests were conducted due to the stability of the performance at these levels. For level 20 kN and 30 kN, six cyclic tests were conducted to achieve more stable results.

In total, 44 tests were performed: 22 tests for Set A, and 22 tests for Set B. The specimens were named under the following rules: the first two letters "AB" denoted "angle bracket connection"; the following letter, "S" or "T", denoted "constant shear load" or "constant tension load" in one direction; the following number denoted the constant load value; the following letter "C" or "M" denoted "cyclic loading" or "monotonic loading" in the perpendicular direction; the number after "C" or "M" denoted the numbering of the specimen; and the last letter denotes the set number. For example, "ABS30C5A" represented Specimen No. 5 for cyclic tension loading with a co-existent shear load of 30 kN in Set A. A test matrix for the specimens is presented in Table 3.1.

Table 3.1 The test matrix for the angle bracket specimens

	Set A (constant shear force)			
	0	20 kN	30 kN	40 kN
Monotonic tension test	ABS0M1A	ABS20M1A	ABS30M1A	ABS40M1A
Cyclic tension test	ABS0C1A ABS0C2A ABS0C3A	ABS20C1A ABS20C2A ABS20C3A ABS20C4A ABS20C5A ABS20C6A	ABS30C1A ABS30C2A ABS30C3A ABS30C4A ABS30C5A ABS30C6A	ABS40C1A ABS40C2A ABS40C3A
	Set B (constant tension force)			
	0	20 kN	30 kN	40 kN
Monotonic shear test	ABT0M1B	ABT20M1B	ABT30M1B	ABT40M1B
Cyclic shear test	ABT0C1B ABT0C2B ABT0C3B	ABT20C1B ABT20C2B ABT20C3B ABT20C4B ABT20C5B ABT20C6B	ABT30C1B ABT30C2B ABT30C3B ABT30C4B ABT30C5B ABT30C6B	ABT40C1B ABT40C2B ABT40C3B

3.3 Test results

This section presents the test results of the 22 specimens under four different levels of constant shear forces, and the 22 specimens under four different levels of constant tension forces, including the failure modes and load-displacement curves.

3.3.1 Failure modes

In Set A, for different levels of constant shear load, the deformation shapes of the angle brackets varied at the maximum vertical displacement of 24 mm, as shown in Figure 3.7.As the co-existent shear load increased, the steel plate connected to the wood panel was significantly stretched.

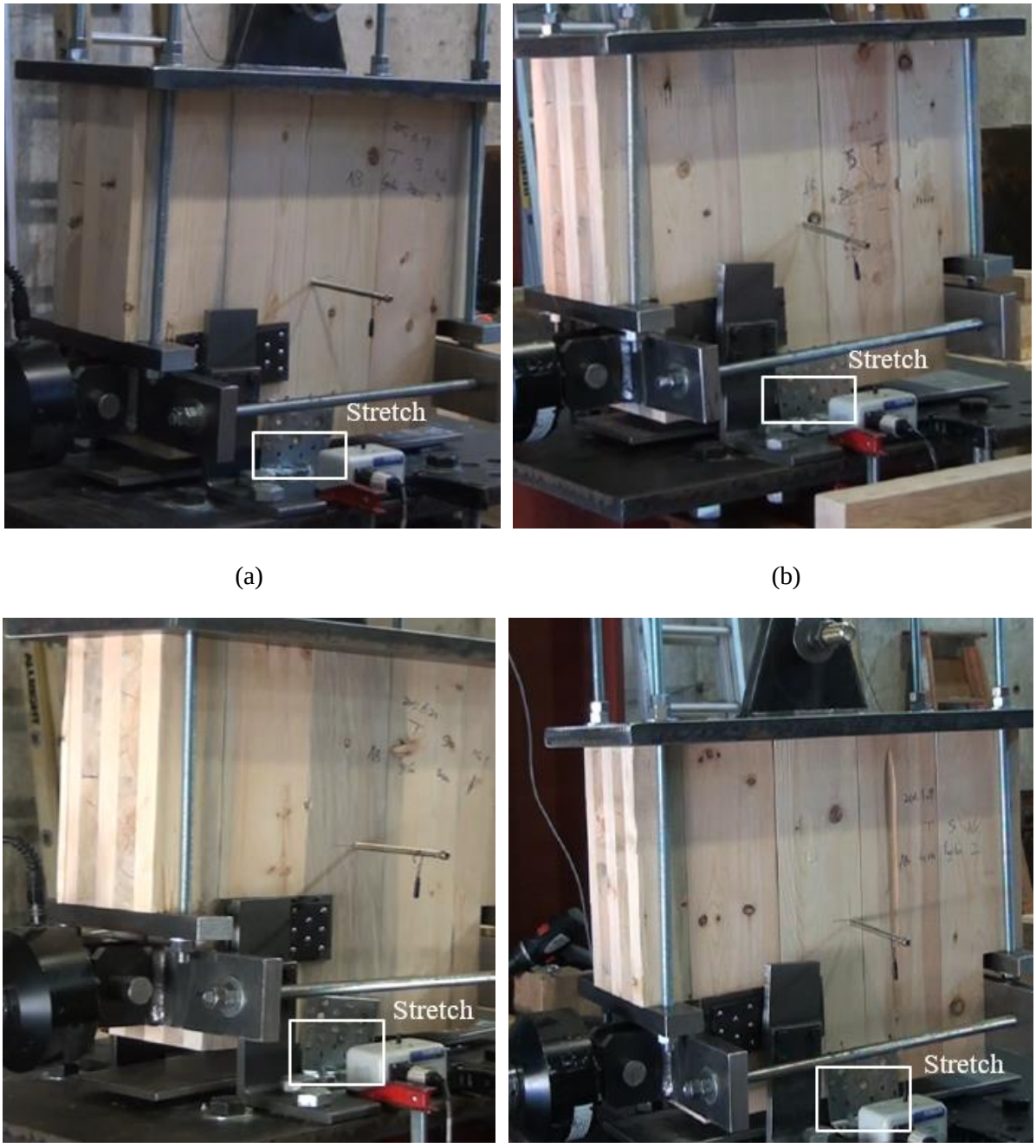

(a) (b)

(c) (d)

Figure 3.7 Deformation shapes of specimens at maximum lateral displacement for different levels of shear load: (a) 0 kN; (b) 20 kN; (c) 30 kN; (d) 40 kN

In Set B, for different levels of constant vertical load, the deformation shapes of the angle brackets at the maximum lateral displacement of 36 mm varied, as shown in Figure 3.8. In the

absence of tension load, the main deformation occurred at the site of interaction between the nails and the wood embedment. As the tension load increased, the steel plate connected to the wood panel was significantly stretched at the “L” corner. This is because the steel plate at this area bore the total tension load, while the upper part of the steel plate only partially took the tension load transferred from the nails. The steel plate connected to the steel base was constrained by the bolts. The outer sides were unable to move horizontally, but tipped upwards due to the uplift forces transferred through the adjacent steel part. Meanwhile, the greater co-existent axial load lead to more severe stretch of the upper part of the steel plate.

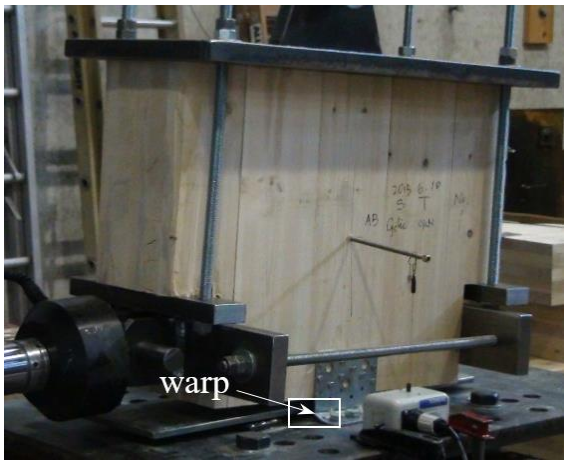

(a)

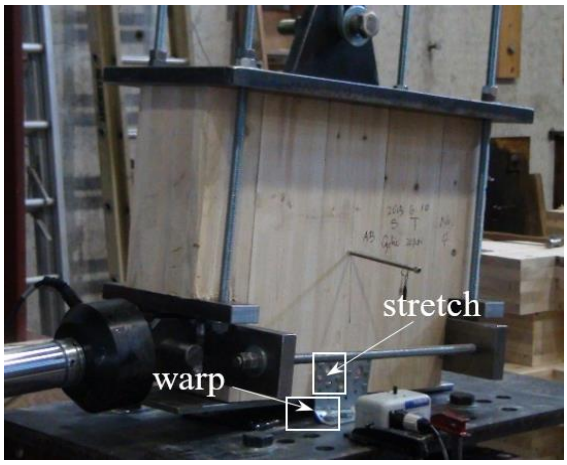

(b)

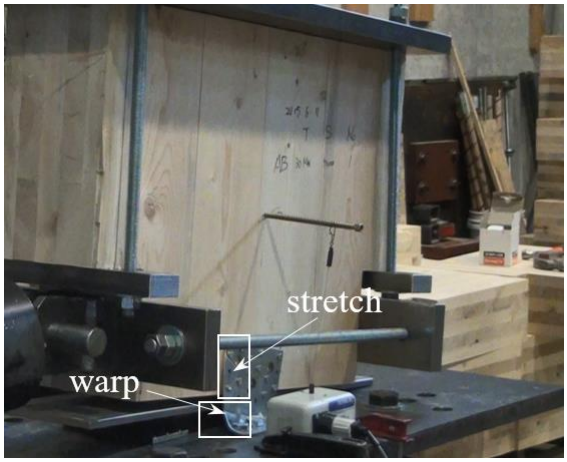

(c)

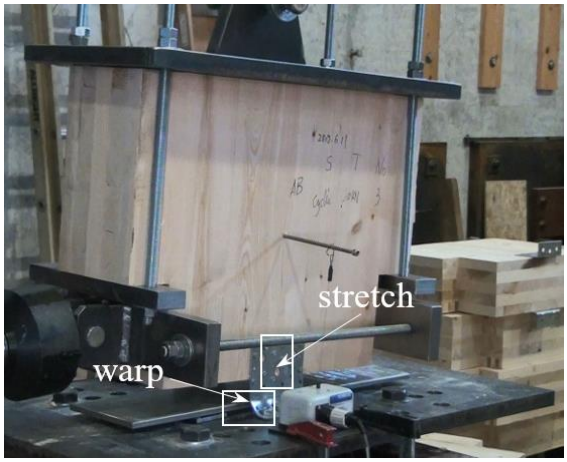

(d)

Figure 3.8 The deformation shapes of specimens at maximum lateral displacement for different levels of vertical load: (a) 0 kN; (b) 20 kN; (c) 30 kN; (d) 40 kN

The failure modes involved both brittle and ductile failures in Set A and Set B. For low co-existent load levels (Shear: 0 kN and 20 kN; Tension: 0 kN and 20 kN), most specimens failed due to the yielding of the nails connecting the angle brackets to the wood, as demonstrated in Figure 3.9 (a); this is considered as a ductile failure mode. When higher load levels were applied (Shear: 30 kN and 40 kN; Tension: 30 kN and 40 kN), the brittle failure modes, such as nail breakage, steel plate fracture, and localized wood crushing took place. Nail breakages occurred when the shear force on each nail equaled the shear capacity of its section (Figure 3.9 (b)). The steel plate around the bolts was torn due to stress concentration, thus, the cross-section of steel plate was reduced, leading to its fracture (Figure 3.9 (c)). Pressure was transmitted from nails to the wood embedment region, causing localized wood crushing when the pressure equaled its capacity. With one side of the nails embedded in the wood and the other side of the nails pulled out, significant torsion of the angle brackets' steel plate was observed (Figure 3.9 (d)).

(a) (b)

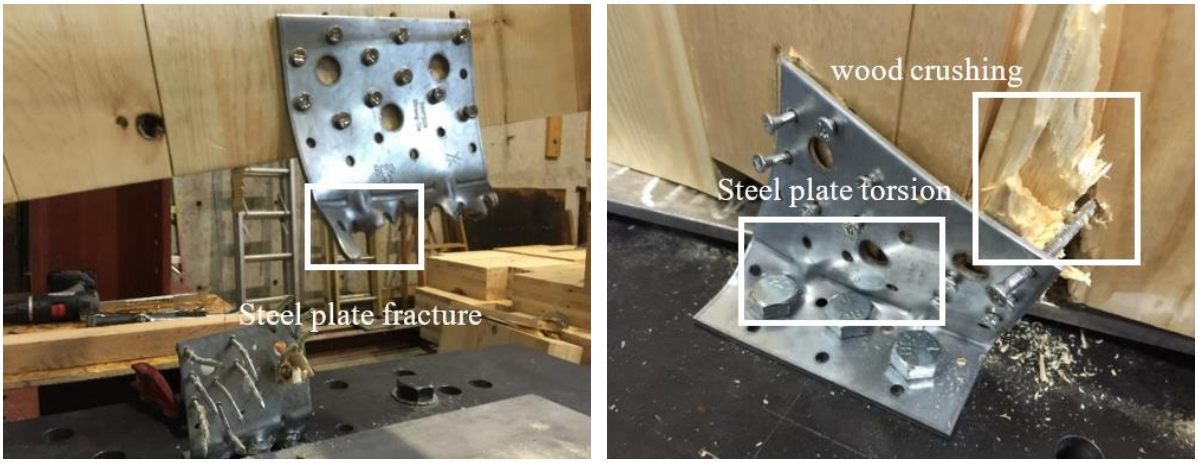

(c) (d)

Figure 3.9 Failure modes at the ultimate displacement: (a) nail yielding; (b) nail breakage; (c) steel plate fracture; (d) localized wood crushing and steel plate torsion

The failure modes for each specimen are summarized in Table 3.2. As the co-existent load increased, brittle failure bodes occurred more frequently.

Table 3.2 The failure modes of each angle bracket specimen

Failure mode	Specimen
Nail yielding	ABS0M1A, ABS0C1A, ABS0C2A, ABS0C3A, ABS20M1A, ABS20C1A, ABS20C2A, ABS20C3A, ABS20C6A, ABT0S1B, ABT0S2B, ABT0S3B, ABT0M1B, ABT20C1B, ABT20C2B, ABT20C3B, ABT20C4B, ABT20C6B, ABT30C2B, ABT30C4B, ABT30C6B
Nail breakage	ABS20C4A, ABS20C5A, ABS30C1A, ABT20C5B, ABT30C1B, ABT30C5B, ABT40C3B
Steel plate fracture	ABS30M1A, ABS30C2A, ABS30C4A, ABS30C5A, ABS40C2A ABT30C3B
Steel plate torsion	ABT20M1B, ABT30M1B
Wood crushing	ABS30C3A, ABS30C6A, ABS40M1A, ABS40C1A, ABS40C3A, ABT40M1B, ABT40C1B, ABT40C2B

3.3.2 Load-displacement curves

The lateral and axial relative displacements between the CLT panels and the steel plate, with their corresponding loads were recorded during each test to define the load-displacement curves.

For the vertical direction, the axial relative displacement between the CLT panel and the steel base was calculated by the axial displacement of the actuator deducting the elongation of the steel cable. This includes the deformation of nails, wood embedment and angle bracket plates. Since the cable was loose at the outset, a tension load of 1 kN was initially applied to tighten it. The elongation of the cable ΔL was calculated using the equation $\Delta L=F/EA$, in which, F is the tension load value from the actuator, E is the elastic modulus of steel, and A is the section area of the cable. Data from linear potentiometers D was only used to adjust and verify the axial relative displacement, as shown in Figure 3.10, since it combined both the vertical and horizontal displacements between the CLT panel and the steel plate.

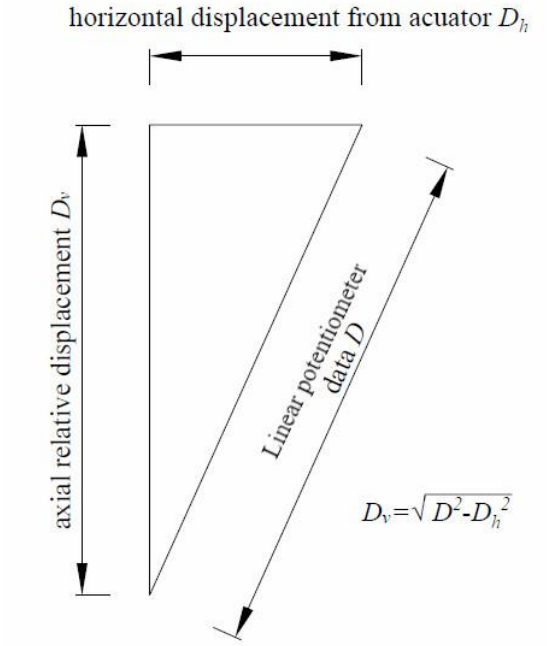

Figure 3.10 Calculation of the axial relative displacement using linear potentiometer data

For the horizontal direction, the shear displacement between the CLT plate and the steel base was represented by the movement of the actuator.

Figure 3.11 depicts the force-displacement curves at different levels of shear load for all specimens, including those used in the monotonic and cyclic tests in Set A. Since a steel cable was used to load the tension force, it could not carry reverse loading.

When no extra shear load was applied, in the monotonic test, the specimen undertook a maximum tension load of 75.6 kN at the displacement of 17.7 mm and an ultimate vertical displacement of over 23.3 mm in the vertical direction; the hysteresis loops for the three specimens in the cyclic tests were stable (Figure 3.11 (a)). For the 20 kN co-existent shear load, the maximum load maintained at 74.7 kN, and the ultimate shear displacement value was maintained at 22.4 mm; the hysteresis loops were comparably less stable among the specimens (Figure 3.11 (b)). For the 30 kN co-existent shear load, the maximum load dropped to 63.4 kN, and the ultimate shear displacement value dropped to 19.3 mm; the hysteresis loops became more scattered among the specimens (Figure 3.11 (c)). For the 40 kN co-existent shear load, the shear capacity from the monotonic testing was 50.9 kN, and the ultimate shear displacement decreased to 17.7 mm; it is worth noting that the shear capacity in the cyclic tests dropped significantly at the maximum vertical displacement of 18 mm, especially during the last few cycles. Meanwhile, severe strength degradation was observed (Figure 3.11 (d)). Two of the six specimens under cyclic tension loading failed at the amplitude of 18 mm before completing the first cycle.

The differences in the major mechanical characteristics were minor when vertical displacement fell below 10 mm. The tensile capacity of the connector decreased significantly when the additional shear force exceeded its elastic range (20 kN). At large displacements, the ductility of the connector dropped rapidly.

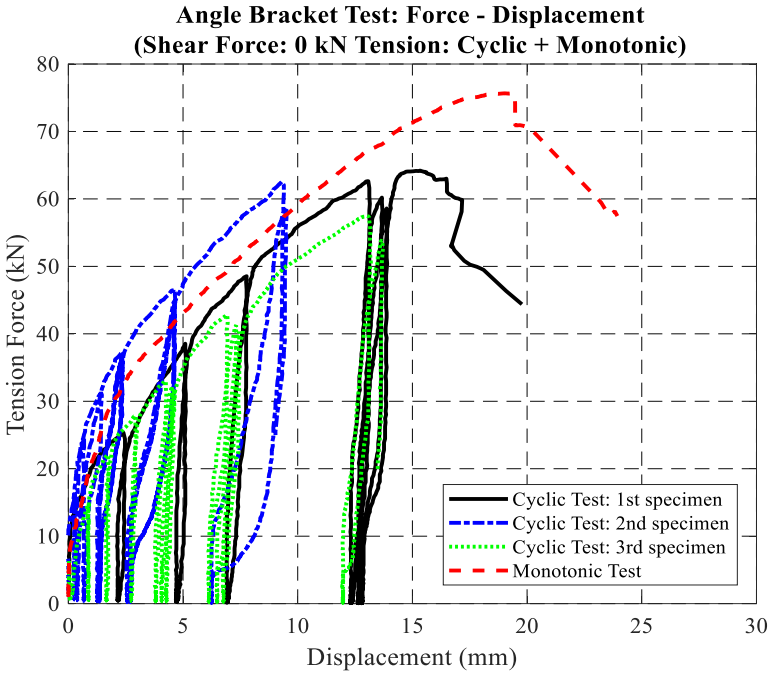
Angle Bracket Test: Force - Displacement
(Shear Force: 0 kN Tension: Cyclic + Monotonic)
Tension Force (kN)
Displacement (mm)
0
10
20
30
40
50
60
70
80
0
5
10
15
20
25
30
Cyclic Test: 1st specimen
Cyclic Test: 2nd specimen
Cyclic Test: 3rd specimen
Monotonic Test

(a)

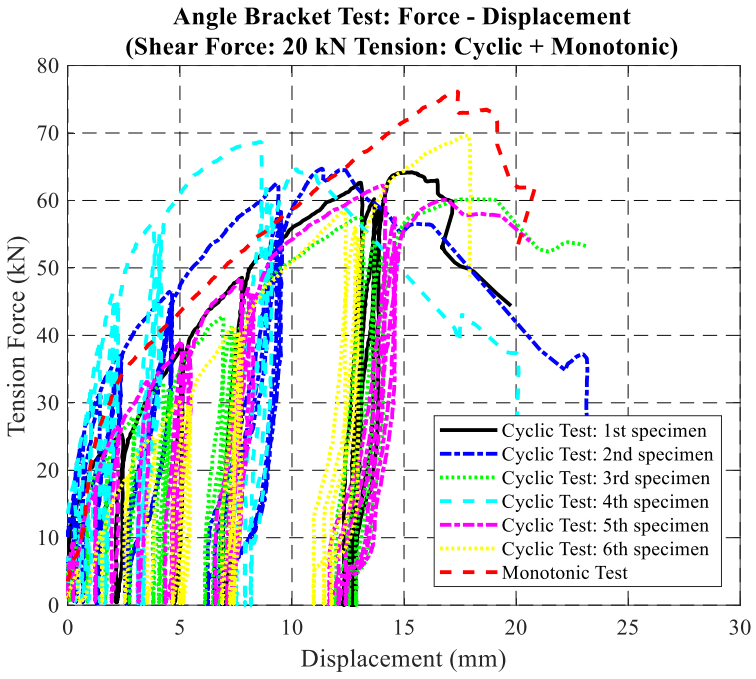
Angle Bracket Test: Force - Displacement
(Shear Force: 20 kN Tension: Cyclic + Monotonic)
Tension Force (kN)
Displacement (mm)
0
10
20
30
40
50
60
70
80
0
5
10
15
20
25
30
Cyclic Test: 1st specimen
Cyclic Test: 2nd specimen
Cyclic Test: 3rd specimen
Cyclic Test: 4th specimen
Cyclic Test: 5th specimen
Cyclic Test: 6th specimen
Monotonic Test

(b)

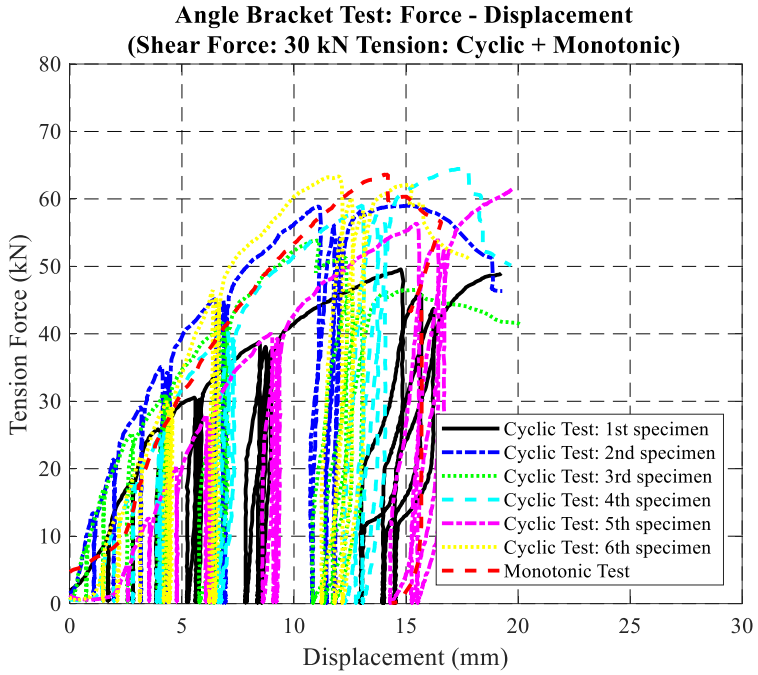

(c)

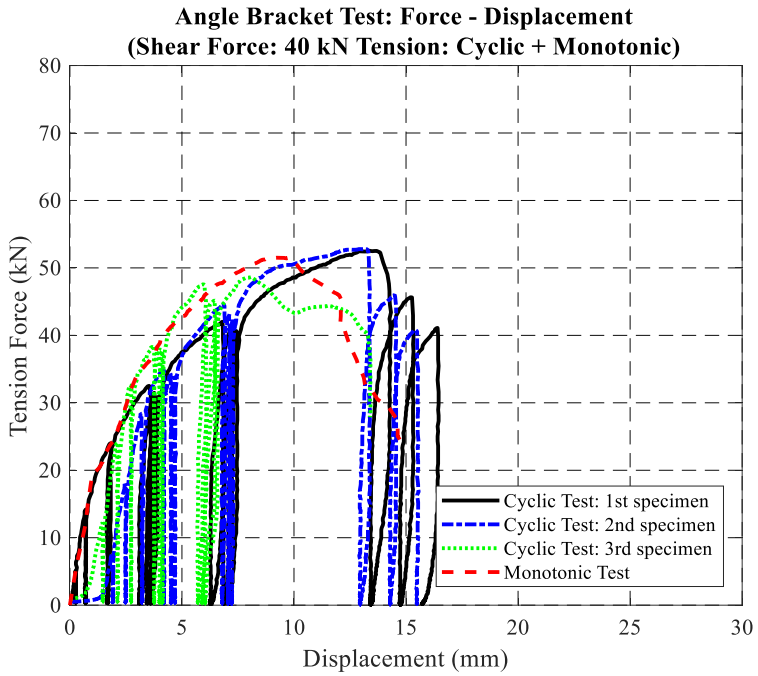

(d)

Figure 3.11 Force-displacement curves in Set A: (a) 0 kN; (b) 20 kN; (c) 30 kN; (d) 40 kN

Figure 3.12 depicts the force-displacement curves at different levels of tension load for all the specimens under monotonic and cyclic tests in Set B. When no additional tension load was applied, in the monotonic test, the specimen undertook a maximum shear load of 62.2 kN at a displacement of 41.0 mm and an ultimate shear displacement of over 60.0 mm; while for the cyclic test, the hysteresis loops for the three specimens remained stable (Figure 3.12 (a)). The pinching effect, strength and stiffness degradation were observed. The results verified the work performed by previous researchers (Gavric, 2013). For the 20 kN tension load, the maximum load applied reached 60.4 kN, but the ultimate shear displacement value dropped to 55.4 mm, which means a reduction in ductility; while the hysteresis loops become less stable and the pinching effect was weakened (Figure 3.12 (b)). For the 30 kN tension load, the shear capacity from the monotonic testing was 55.8 kN, which was around 10% less than that of the former two test sets, and the ultimate shear displacement decreased to 48.2 mm, showing a relatively low ductility; while for cyclic test, the specimens failed before the last cycle of cyclic loading, the hysteresis loop become increasingly more unstable, and the pinching effect disappeared at large shear deformations (Figure 3.12 (c)). For the 40 kN tension load, the specimen under monotonic loading could only take a maximum shear force of 52.6 kN and it failed in a brittle failure mode. All three specimens under cyclic shear loading failed at the amplitude of 32 mm before completing the first cycle. The hysteresis curves at the 24 mm amplitude exhibited almost no pinching effect (Figure 3.12 (d)).

The shear loads for the four figures at the maximum displacement for each cycle were very close. The shear loads at the 32 mm amplitude for all test configurations were around 45 kN; this may be due to the fact that the cyclic shear loading was conducted below the connections' maximum load capacities. The results show that a co-existent tension force of 40 kN decreased the maximum shear capacity of the connections and the initial stiffness of the connectors by 25% and

15%, respectively. As the tension force increased, the energy dissipation capacity of the connectors dropped significantly. Meanwhile, the pinching effect was mitigated because the gap between the nails and wood material was eliminated.

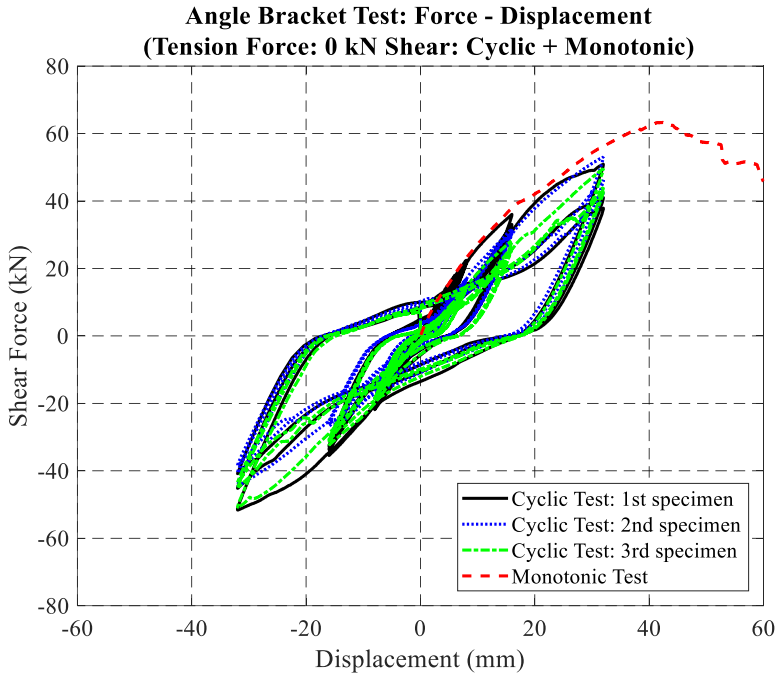

(a)

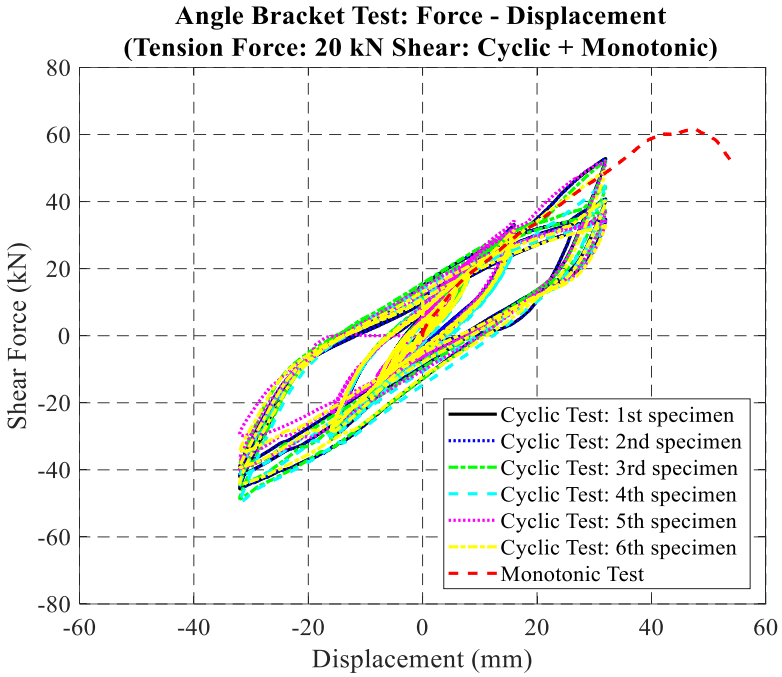
Angle Bracket Test: Force - Displacement
(Tension Force: 20 kN Shear: Cyclic + Monotonic)
Shear Force (kN)
Displacement (mm)
80
60
40
20
0
-20
-40
-60
-80
-60
-40
-20
0
20
40
60
Cyclic Test: 1st specimen
Cyclic Test: 2nd specimen
Cyclic Test: 3rd specimen
Cyclic Test: 4th specimen
Cyclic Test: 5th specimen
Cyclic Test: 6th specimen
Monotonic Test

(b)

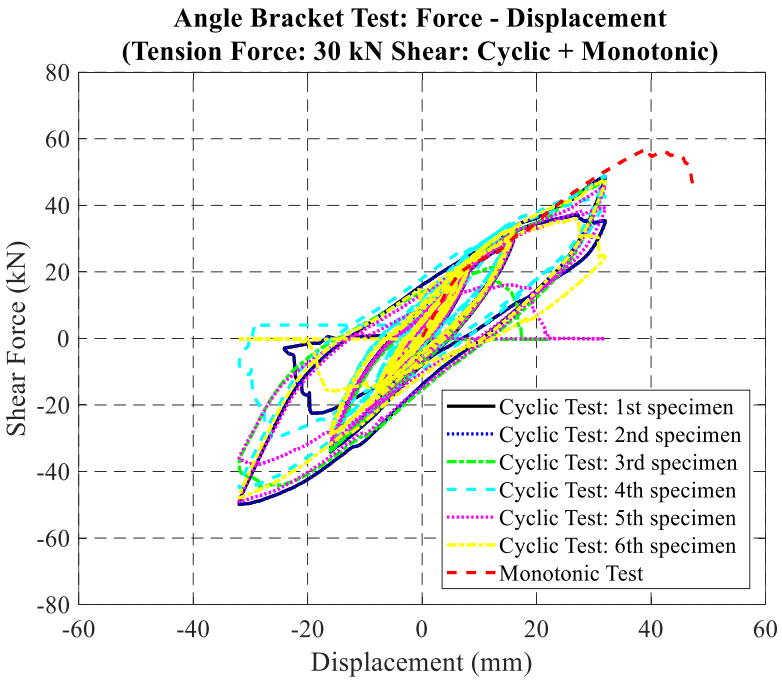
Angle Bracket Test: Force - Displacement
(Tension Force: 30 kN Shear: Cyclic + Monotonic)
Shear Force (kN)
Displacement (mm)
80
60
40
20
0
-20
-40
-60
-80
-60
-40
-20
0
20
40
60
Cyclic Test: 1st specimen
Cyclic Test: 2nd specimen
Cyclic Test: 3rd specimen
Cyclic Test: 4th specimen
Cyclic Test: 5th specimen
Cyclic Test: 6th specimen
Monotonic Test

(c)

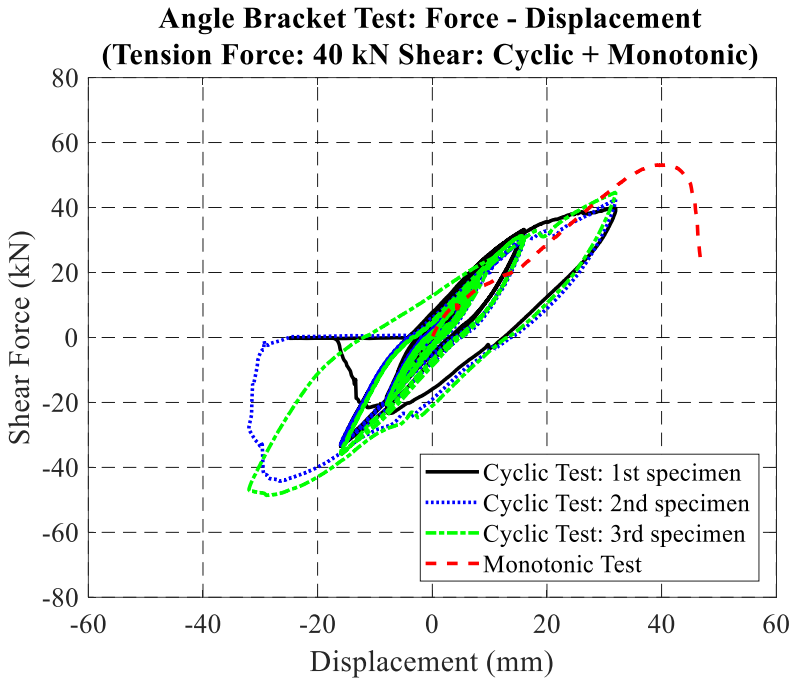

(d)

Figure 3.12 Force-displacement curves in Set B: (a) 0 kN; (b) 20 kN; (c) 30 kN; (d) 40 kN

The explanation for the change in hysteresis behaviour is as follow. Due to the co-existent force in the perpendicular direction, the nails in the angle bracket connections travelling in the gap encountered resistance. As shown in Figure 3.13 (a), when only shear force was applied, the nails could travel in the gap without resistance. However, the application of a co-existent tension force caused pressure on the nail shank from the surrounding wood embedment (Figure 3.13 (b)). This pressure provided lateral resistance to the nails in the gap during unloading. Furthermore, higher levels of co-existent force caused greater resistance during unloading.

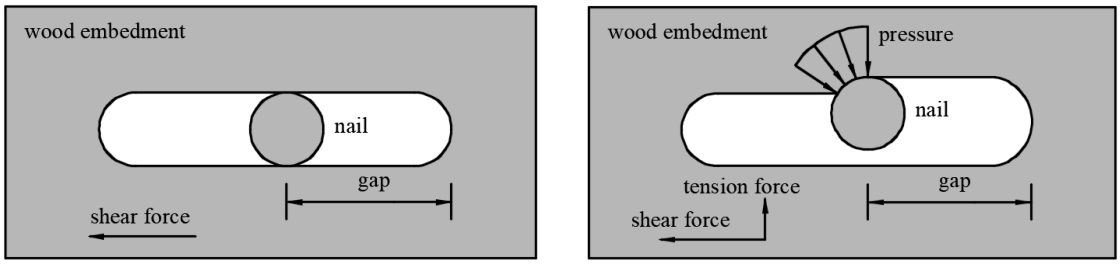

(a) (b)

Figure 3.13 A schematic section view of the nails in the wood embedment: (a) nail movement under shear force without co-existent tension load; (b) nail movement under shear force with co-existent tension load

3.4 Analyses of the results

The experimental results were analyzed based on the procedure described in EN 12512 (CEN 2006). The force and stiffness, equivalent viscous damping and strength degradation, and energy dissipation were evaluated accordingly.

3.4.1 Force and stiffness

The experimental test results were assessed in terms of strength, stiffness, and ductility, following the standard procedure from EN12512 (CEN 2006). Method "b" was used to define the elastic and post-elastic stiffness, yielding point and ultimate conditions.

Assessments of the mechanical properties include:

K_{el} and K_{pl} represent the initial stiffness and plastic stiffness; F_{yl} and v_{yd} signify the yielding load and yielding displacement; F_{max} and v_{max} denote the maximum load and maximum displacement; F_u and v_u signify the ultimate load and ultimate displacement; D_D signifies the ductility ratio (the ratio between the ultimate and yield displacement).

Table 3.3 provides the mechanical properties of the angle brackets under cyclic shear loading with co-existent axial load in Set A. The average values of K_{el} and F_{yl} in shear loading increased 7.8% and 1.3% from 0 kN to 20 kN, respectively, and then decreased 29.5% and 35.8%

from 20 kN to 40 kN， respectively. The average values of F_{max}, v_{max}, F_u, and v_u decreased 31.8%, 24.1%, 31.6%, and 24.0% from 0 kN to 40 kN. The co-existent shear force significantly weakened the tension capacity of the angle brackets.

Table 3.4 shows that the co-existent axial load weakened the mechanical properties of the angle brackets in Set B. The average values of K_{el}, F_{yl}, v_{yd}, F_{max}, v_{max}, F_u, and v_u decreased 13.1%, 17.2%, 10.6%, 16.2%， 7.1%， 16.2%， and 22.4% from 0 kN to 40 kN, respectively. The connections became less ductile with the increasing of the co-existent axial load. As well, increasing the co-existent axial load amplified the negative influence of the wood defects on the mechanical properties, thus, the coefficient of variation (CoV) of the values increased.

Table 3.3 Analyses of the experimental results of Set A according to EN 12512 (CEN 2006)

Mechanical property	0 kN (shear)		20 kN (shear)		30 kN (shear)		40 kN (shear)	
	Mean	CoV(%)	Mean	CoV(%)	Mean	CoV(%)	Mean	CoV(%)
K_{el}(kN/mm)	8.59	13.04	9.24	8.59	7.25	23.28	6.51	5.88
K_{pl}(kN/mm)	1.42	12.23	1.54	9.13	1.21	24.52	1.09	5.71
F_{yl}(kN)	37.67	2.60	38.14	21.20	25.97	12.40	24.49	15.62
v_{yd}(mm)	3.96	6.35	3.75	18.01	4.52	6.49	4.92	1.47
F_{max}(kN)	75.61	-	74.69	-	63.41	-	50.91	-
v_{max}(mm)	17.65	-	16.69	-	14.85	-	13.40	-
F_u(kN)	59.55	-	59.76	-	50.72	-	40.72	-
v_u(mm)	23.31	-	22.39	-	19.33	-	17.72	-
D_D	3.62	6.59	5.97	14.73	4.28	19.45	3.60	2.23

Table 3.4 Analyses of the experimental results of Set B according to EN 12512 (CEN 2006)

Mechanical property	0 kN (tension)		20 kN (tension)		30 kN (tension)		40 kN (tension)	
	Mean	CoV(%)	Mean	CoV(%)	Mean	CoV(%)	Mean	CoV(%)
K_{el}(kN/mm)	2.97	14.97	2.89	11.98	2.71	16.53	2.58	32.95
K_{pl}(kN/mm)	0.50	14.97	0.48	11.98	0.48	16.53	0.43	32.95
F_{yl}(kN)	35.41	23.29	32.98	19.45	34.20	5.91	29.33	27.65
v_{yd}(mm)	16.00	3.13	15.20	2.72	14.91	2.81	14.30	3.13
F_{max}(kN)	63.32	-	61.65	-	56.63	-	53.08	-
v_{max}(mm)	42.39	-	47.20	-	38.98	-	39.40	-
F_u(kN)	50.66	-	49.32	-	45.31	-	42.46	-
v_u(mm)	58.88	-	54.20	-	47.29	-	45.71	-
D_D	3.68	3.13	3.57	2.72	3.17	2.79	3.20	3.26

Figure 3.14 presents the tri-linear curves of the tests for Set A and Set B, following the procedure in EN 12512-b. These three lines represent the elastic branch up to the yielding point, the post-elastic hardening branch up to the maximum force, and the softening branch up to the failure level. This figure displays a more intuitive trend for the weakening effects of the co-existent axial load.

In Figure 3.14 (a), the trend shows that the co-existent shear load dramatically weakened the tension loading capacity. In Figure 3.14 (b), it shows that the co-existent tension load weakened the shear loading capacity.

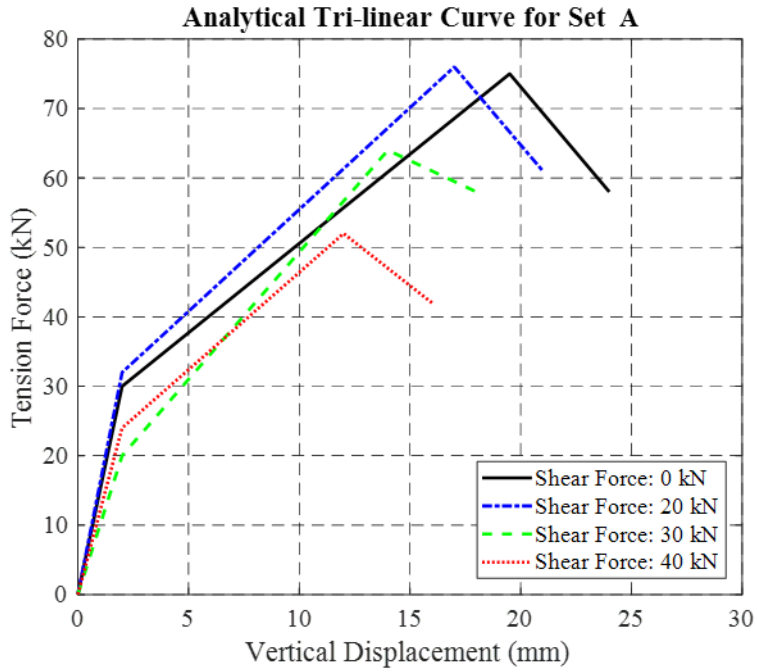

(a)

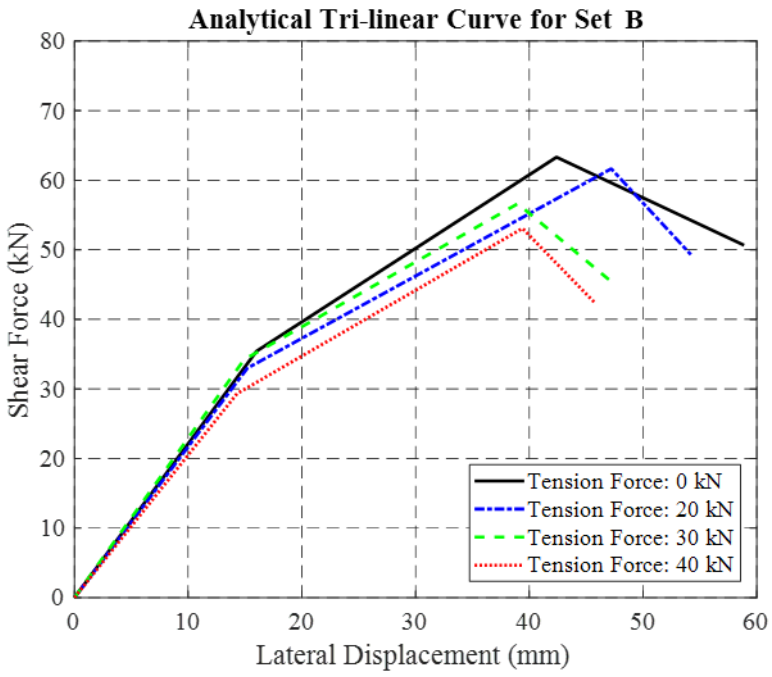

(b)

Figure 3.14 The analytical tri-linear curves: (a) the monotonic tension force - axial displacement relationship for Set A; (b) the monotonic shear force - lateral displacement relationship for Set B

3.4.2 Equivalent viscous damping and strength degradation

The equivalent viscous damping values for each cycle, and strength degradation values at the end of the 2nd and 3rd cycles of each shear displacement level were evaluated to assess the cyclic behaviour of the specimens.

The equivalent viscous damping ratio shows the hysteresis damping properties of the hold-down connections. The equivalent viscous damping ratio for the i^{th} cycle, $v_{eq,i}$ is defined as the ratio of the dissipated energy in the cycle, $E_{d,i}$, to the available potential energy in the cycle, $E_{p,i}$ multiplied by 4 π, $v_{eq,i} = \frac{E_{d,i}}{4\pi E_{p,i}}$. The available potential energy $E_{p,i}$ can be determined as

$E_{p,i} = 1/2 \cdot F_i \cdot u_i$, where F_i and u_i are the maximum force and maximum displacement attained in the i^{th} cycle.

Figure 3.15 (a) shows that in Set A, for a small amplitude (6 mm), the equivalent viscous damping values in the tension exhibit a decreasing trend with a corresponding increase of the co-existent shear load. But at the cycles for the amplitude of 12 mm, the specimens with a 40 kN co-existent shear load demonstrate a higher equivalent viscous damping of 16%, compared to 9% for those having a lower co-existent shear load (0 kN and 20 kN). One reason for this is the crushing of the wood embedment at this stage.

Figure 3.15 (b) shows that in Set B, for the first few cycles, the equivalent viscous damping values have a growing trend corresponding to the increases of the co-existent axial load. But at cycles of 16 mm amplitude, the specimens with a low co-existent axial load (0 kN and 20 kN) have a higher equivalent viscous damping of 25%, compared to 8% for those with high co-existent axial load (30 kN and 40 kN). Higher co-existent axial loads retain the equivalent viscous damping at a relatively low level, round 10% under all amplitudes.

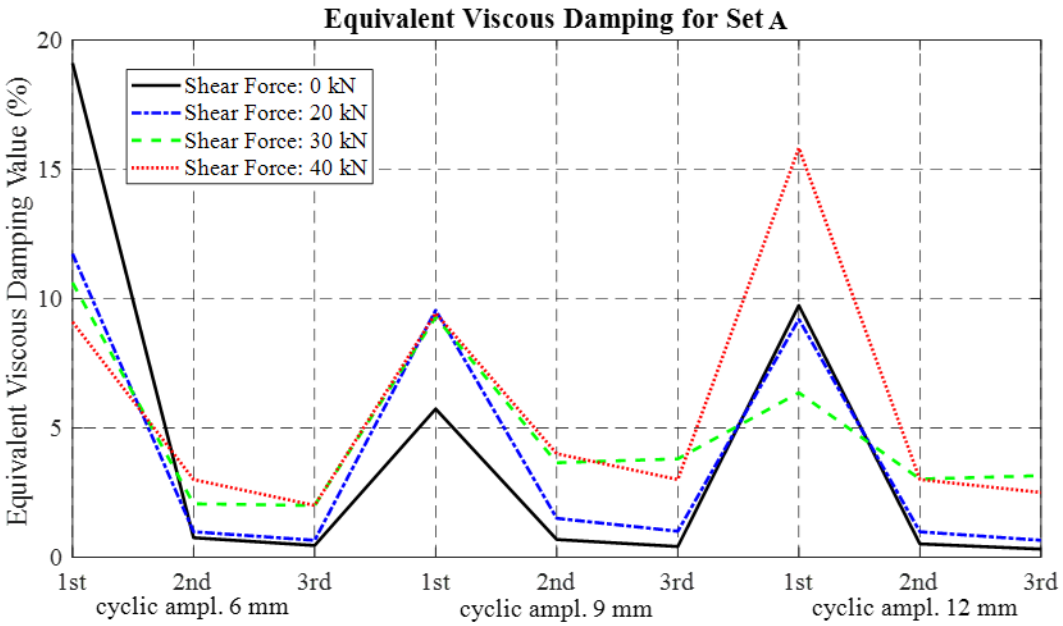

(a)

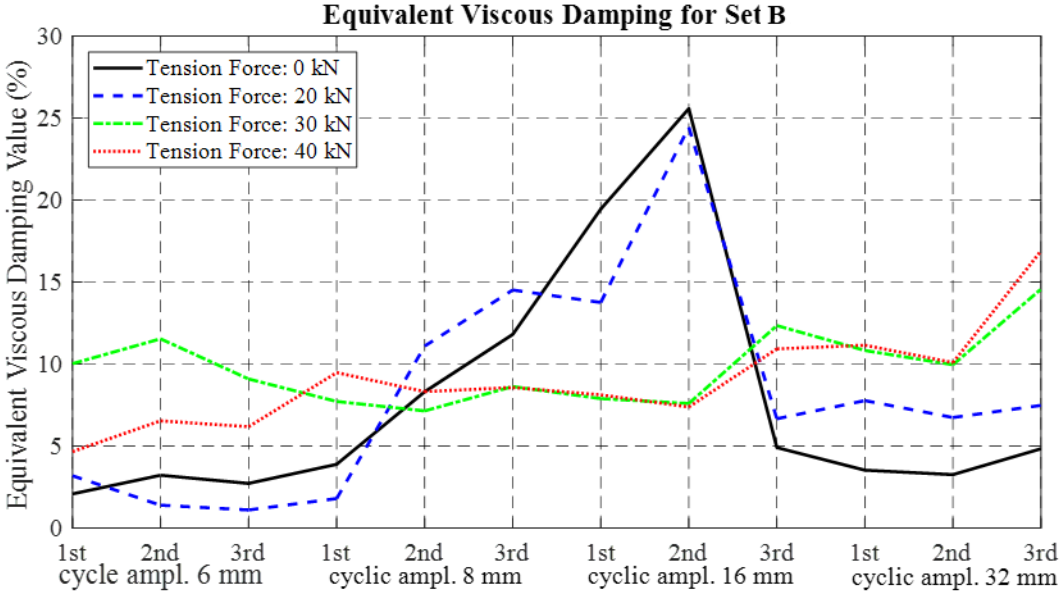

(b)

Figure 3.15 Equivalent viscous damping for each cycle: (a) Set A; (b) Set B

In terms of strength degradation, in Set A, amplitudes less than 12 mm failed to demonstrate any significant decrease in tension capacity (Figure 3.16 (a)). After this point, tension

capacity dropped rapidly under all circumstances. In Set B, below the medium displacement level of 16 mm, co-existent axial forces lowered the strength values by less than 15%, but at a large displacement (32 mm), the shear capacity dropped more than 60% due to co-existent axial forces (Figure 3.16 (b)).

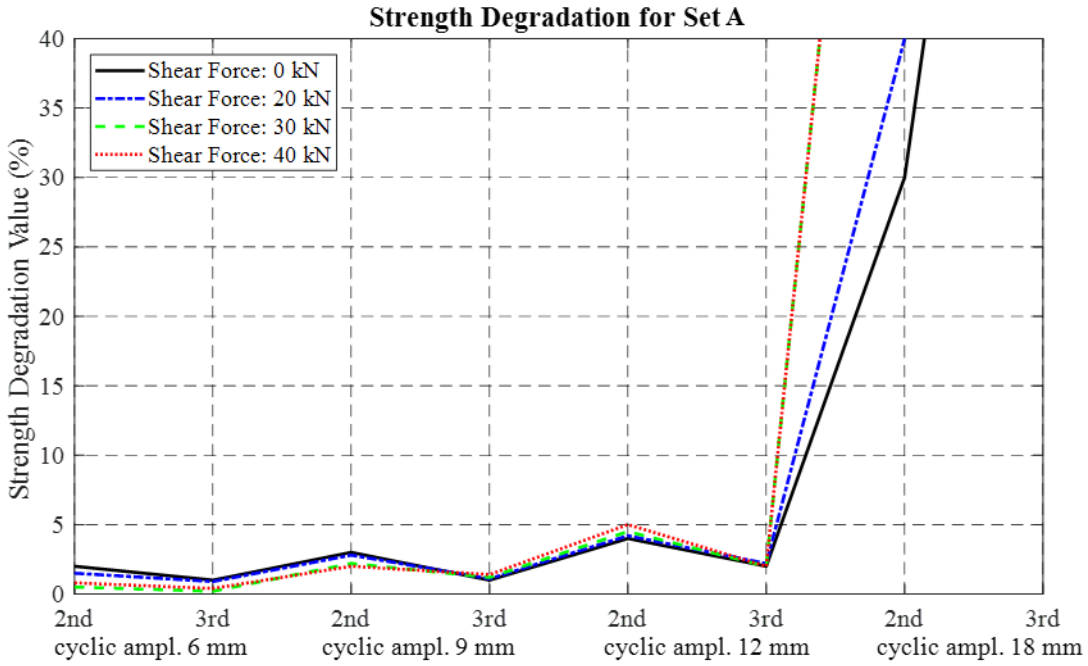

(a)

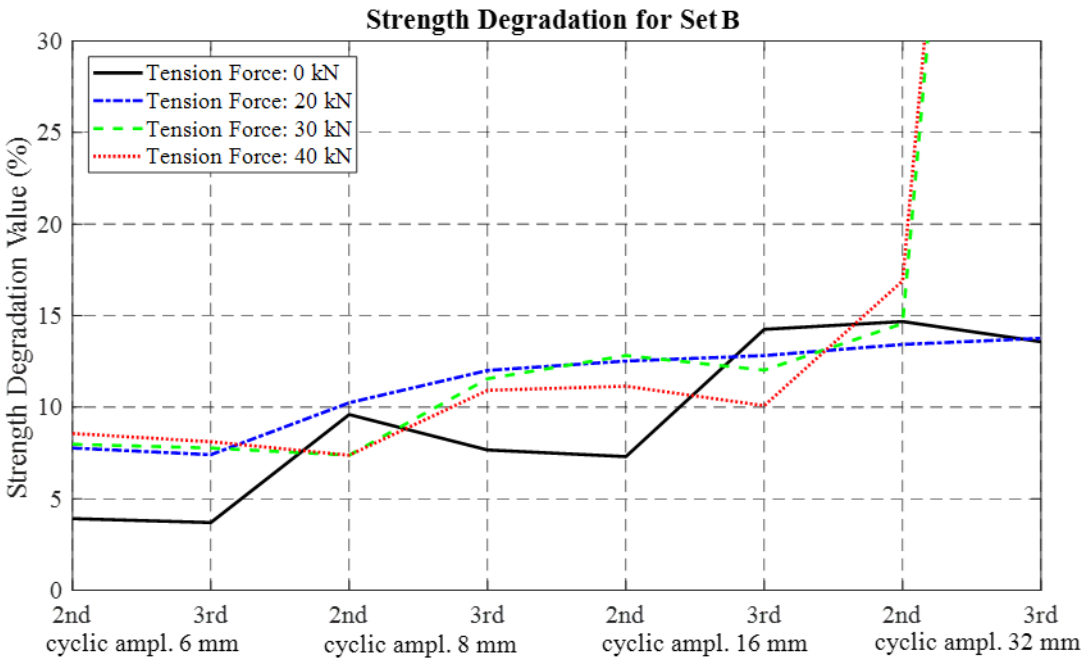

(b)

Figure 3.16 Strength degradation for the last two cycles: (a) Set A; (b) Set B

3.4.3 Energy dissipation

The energy dissipation for each test was divided into two parts, one for shear, and the other for tension loading. The energy dissipation values for cyclic shear/tension loading were calculated using the area of hysteresis loop for each cycle.

For Set A, the energy dissipated from cyclic tension loading for each cycle, constant shear loading for each cycle, and the cumulative total energy dissipation were plotted in Figure 3.17 (a), (b), and (c), respectively. As shown in Figure 3.17 (a), before the 11^{th} cycle (18 mm), the energy dissipated from the cyclic shear loading did not change significantly, with increases in the tension force. But at a large displacement value (18 mm), only the specimens under low tension force levels (0 kN and 20 kN), could still dissipate energy through cyclic tension loading, while the specimens under high tension force levels (30 kN and 40 kN) experienced failure. The constant

shear loading caused large lateral displacement, resulting significant energy dissipation compared to the cyclic tension loading, as shown in Figure 3.17 (b). For instance, the largest energy dissipation value for a cycle caused by cyclic tension loading was 321 kN·mm, but was 1050 kN·mm by constant shear loading. From Figure 3.17 (c), it can be observed that even under cyclic tension loading with constant shear loading, the energy dissipation was still dominated by shear force, which proved that angle brackets were more efficient in carrying shear load.

For Set B, the energy dissipated from cyclic shear loading, constant tension loading for each cycle, and the cumulative total energy dissipation were plotted in Figure 3.17 (d), (e), and (f), respectively. As co-existent axial load increased, the energy dissipation capacity from the shear loading dropped at large displacements (Figure 3.17 (d)). The energy dissipation value of tension loading was the co-existent axial load value multiplied by the vertical displacement of the specimen during each cycle, as shown in Figure 3.17 (e). This is the work performed by the tensile force. As the co-existent axial load increased, more energy was dissipated from the tension load. Prior to the 8^{th} cycle (8 mm), more energy was dissipated from the tension instead of the shear loading. Following the 9^{th} cycle (16 mm), more energy was dissipated from the shear loading. The total cumulated energy dissipation value was the combination of these two values above at each cycle, as shown in Figure 3.17 (f). The results show that the co-existent axial load decreased the energy dissipation capacity of the specimens. At large displacements, for instance, at the first cycle of the 32 mm amplitude, the total energy dissipation was 3350 kN·mm for the 0 kN axial load, and 2520 kN·mm for the 40 kN axial load. The energy dissipation had dropped by 24.8%.

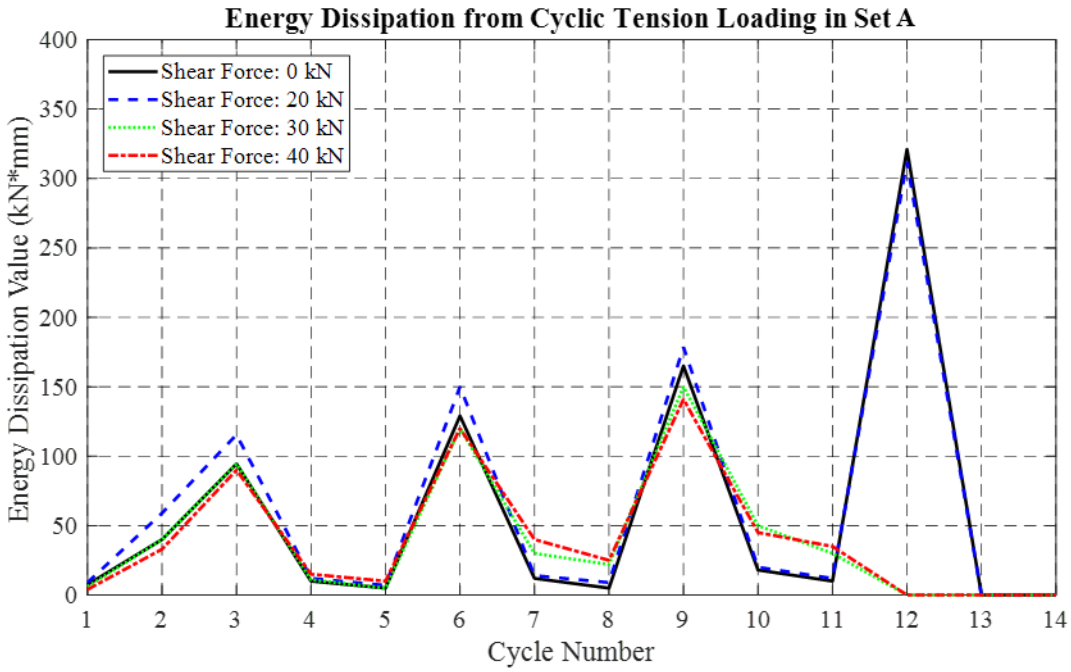
Energy Dissipation from Cyclic Tension Loading in Set A
Shear Force: 0 kN
Shear Force: 20 kN
Shear Force: 30 kN
Shear Force: 40 kN
Energy Dissipation Value (kN*mm)
Cycle Number
0
50
100
150
200
250
300
350
400
1
2
3
4
5
6
7
8
9
10
11
12
13
14

(a)

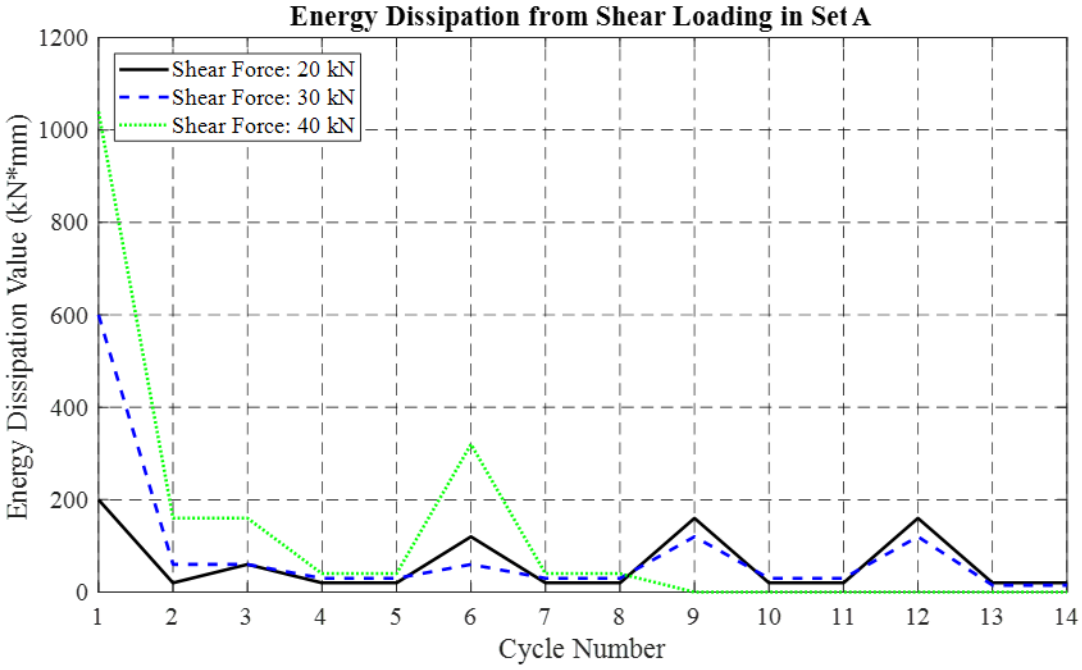
Energy Dissipation from Shear Loading in Set A
Shear Force: 20 kN
Shear Force: 30 kN
Shear Force: 40 kN
Energy Dissipation Value (kN*mm)
Cycle Number
0
200
400
600
800
1000
1200
1
2
3
4
5
6
7
8
9
10
11
12
13
14

(b)

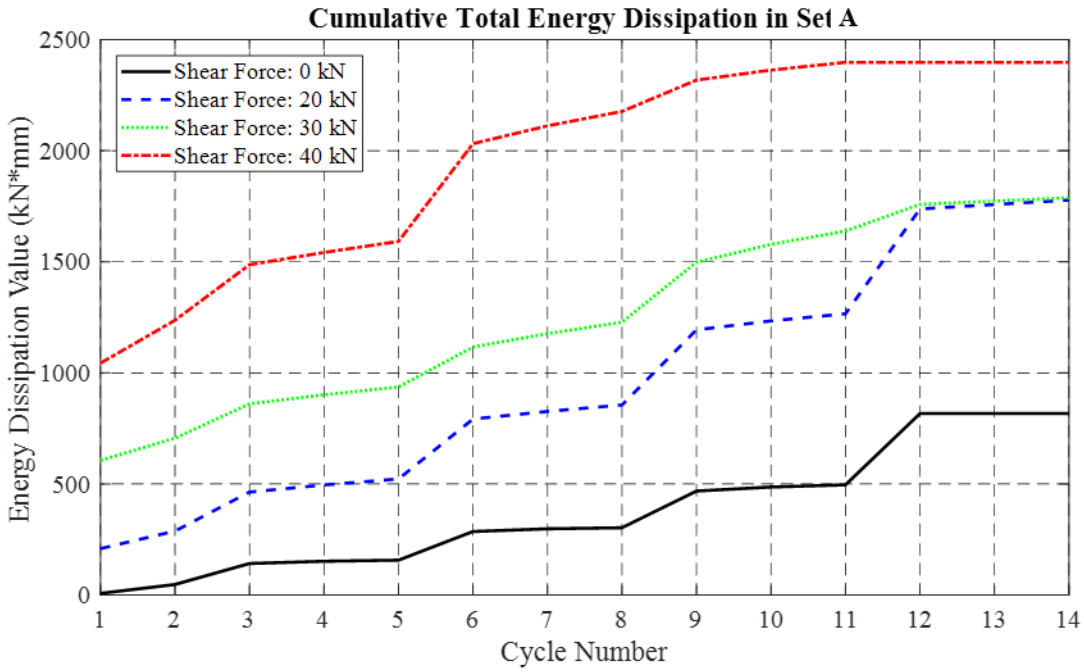
Cumulative Total Energy Dissipation in Set A
Shear Force: 0 kN
Shear Force: 20 kN
Shear Force: 30 kN
Shear Force: 40 kN
Energy Dissipation Value (kN*mm)
Cycle Number
0
500
1000
1500
2000
2500
1
2
3
4
5
6
7
8
9
10
11
12
13
14

(c)

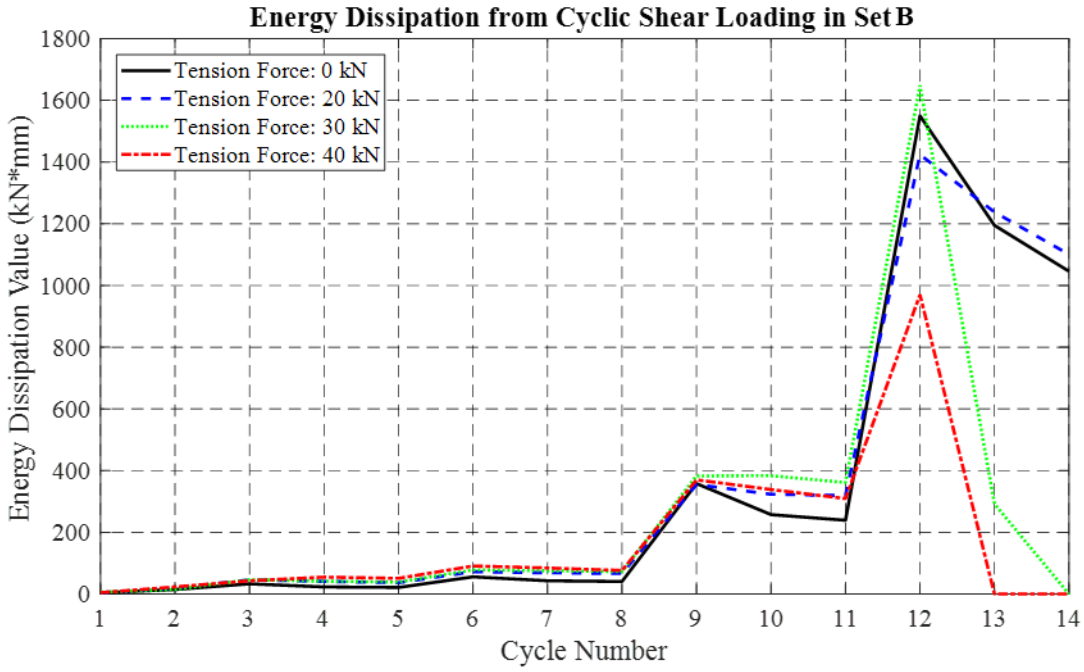
Energy Dissipation from Cyclic Shear Loading in Set B
Tension Force: 0 kN
Tension Force: 20 kN
Tension Force: 30 kN
Tension Force: 40 kN
Energy Dissipation Value (kN*mm)
Cycle Number
0
200
400
600
800
1000
1200
1400
1600
1800
1
2
3
4
5
6
7
8
9
10
11
12
13
14

(d)

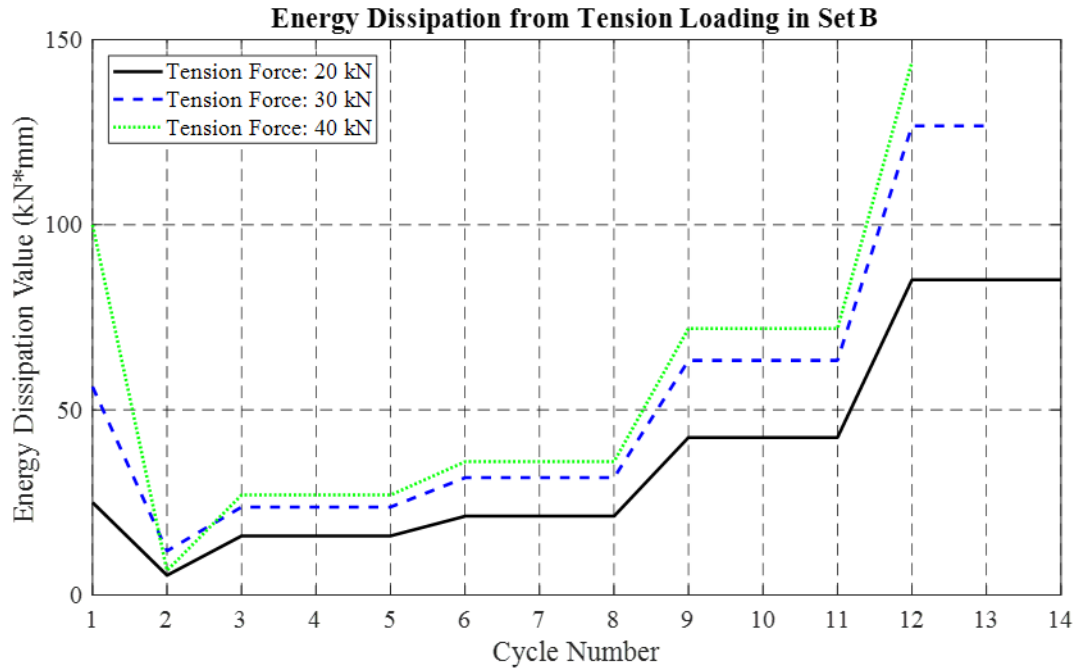

(e)

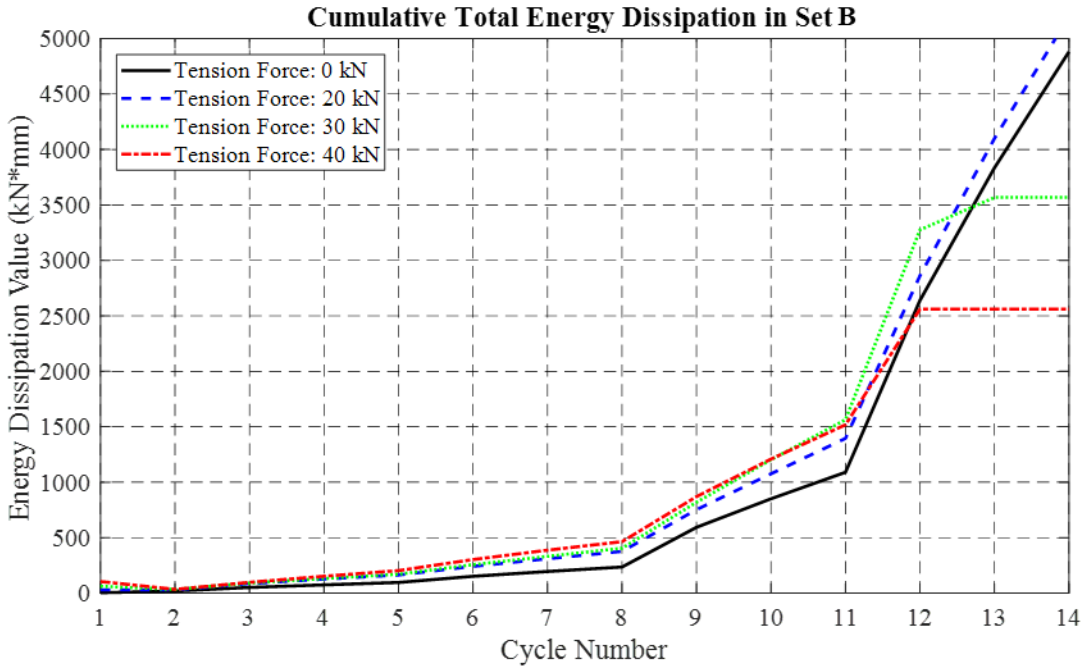

(f)

Figure 3.17 Energy dissipation plots: (a) energy dissipation from cyclic tension loading in Set A; (b) energy dissipation from shear loading in Set A; (c) cumulative total energy dissipation in Set A; (d) energy dissipation from

cyclic shear loading in Set B; (e) energy dissipation from tension loading in Set B; (f) cumulative total energy dissipation in Set B

3.4.4 Discussion on the coupling effect

The coupling effect was discussion in terms of two aspects, load and energy dissipation capacity.

To consider the coupling effects between shear load and tension load, for Set A, as shown in Figure 3.18 (a), shear force had a severe influence on the tension capacity. Co-existent shear load at the range of 0 kN ~ 20 kN increased the tension capacity at small to moderate amplitudes (6 mm, 9 mm, and 12 mm) since, in these circumstances, the shear load helped the nails carry more tension load by pressing them into the surrounding wood embedment; at a range of 20 kN ~ 40 kN, at those amplitudes, it decreased the tension capacity. It is noted that, at a large amplitude (18 mm), any applied co-existent shear load decreased the tension capacity. This is because the specimens had already been severely damaged by the cyclic tension loads.

For Set B, the shear forces at the end of each amplitude for the first cycle were plotted against different co-existent axial loads in Figure 3.18 (b). The figure shows that the co-existent axial load at the range of 0 kN ~ 20 kN had a negligible influence on the shear capacity at all amplitudes; at the range of 20 kN ~ 30 kN, it decreased the shear capacity at all amplitudes; but at the range of 30 kN ~ 40 kN, at the amplitude of 32 mm, it continued to decrease the shear capacity, while at amplitudes of 6 mm, 8 mm, and 16 mm, it increased the shear capacity. This is because, while the co-existent tension load weakened the shear strength of the specimen, it also pressed the nails into the surrounding wood embedment, which eliminated the gaps, thus, under relatively small amplitudes, it helped the nails carry greater shear loads. On the other hand, the shear capacities altered within a 10% range at amplitudes of 6 mm, 8 mm, and 16 mm under different

axial loads, while at the amplitude of 32 mm, the shear capacity dropped by 25%. This indicated the strong coupling effects between shear load and tension load under large displacements. Shear capacity was weakened by the presence of large co-existent tension forces.

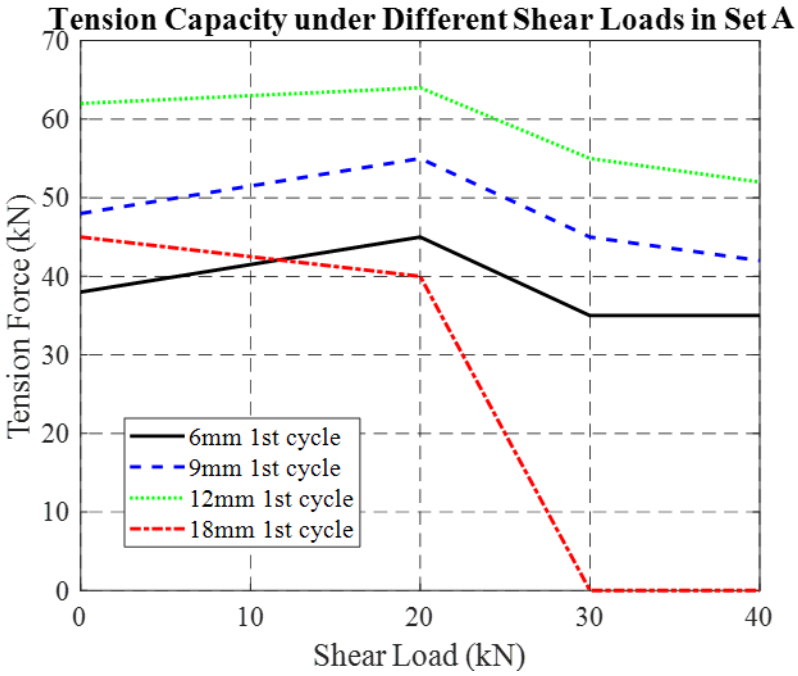

(a)

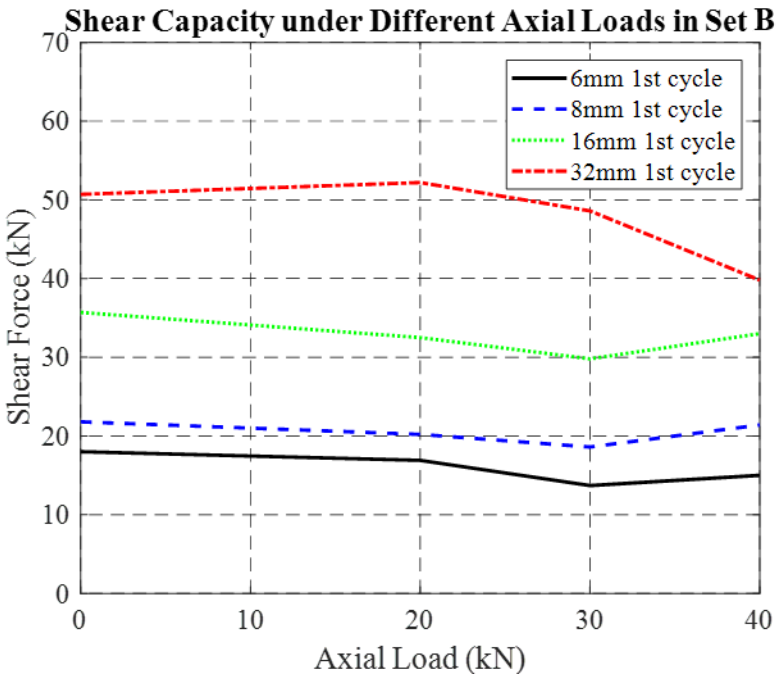

(b)

Figure 3.18 Coupling effect on load capacity at the first cycle of target cyclic displacement peaks: (a) tension capacity under different shear loads in Set A; (b) shear capacity under different axial loads in Set B

For the coupling effect on energy dissipation, for Set A, as shown in Figure 3.19 (a), the co-existent shear force helped increase the total energy dissipation at all levels. A larger co-existent shear force caused greater total energy dissipation. However, for a large amplitude (18 mm), the energy dissipated by large shear loads (30 kN and 40 kN) was weakened due to the damage from cyclic tension loading. By comparing Figure 3.19 (a) and (c), it was also found that, under the Set A loading protocol, the energy dissipation capacity of the angle brackets was much smaller than that under the Set B loading protocol - 2400 kN·mm for the former and 5100 kN·mm for the latter. This further proved the efficiency of angle brackets in carrying shear as opposed to tension force. In Figure 3.19 (b), it shows that the energy dissipated by cyclic tension loading was small as compared to that for co-existent shear loading. However, it can still be noticed that, under small

amplitudes (6 mm, 9 mm, and 12 mm), a larger shear load helped the energy dissipation from cyclic tension loading increase slightly, and under a large amplitude (18 mm), large shear loads (30 kN and 40 kN) decreased the energy dissipation from cyclic tension loading.

Figure 3.19 (c) gives the total energy dissipation at the end of each amplitude for the last cycle under different axial loads in Set B. The figure reveals that, at relatively small amplitudes (6 mm, 8 mm, and 16 mm), the total energy dissipation had a growing trend with the increasing co-existent axial load, while at a large amplitude (32 mm), it dropped by over 45%. This shows that the co-existent axial load had a severely negative influence on the energy dissipation capacity. Figure 3.19 (d) demonstrated that the energy dissipated from cyclic shear loading had similar results to that of the total energy dissipation, because the co-existent axial load played a small role in dissipating energy in Set B.

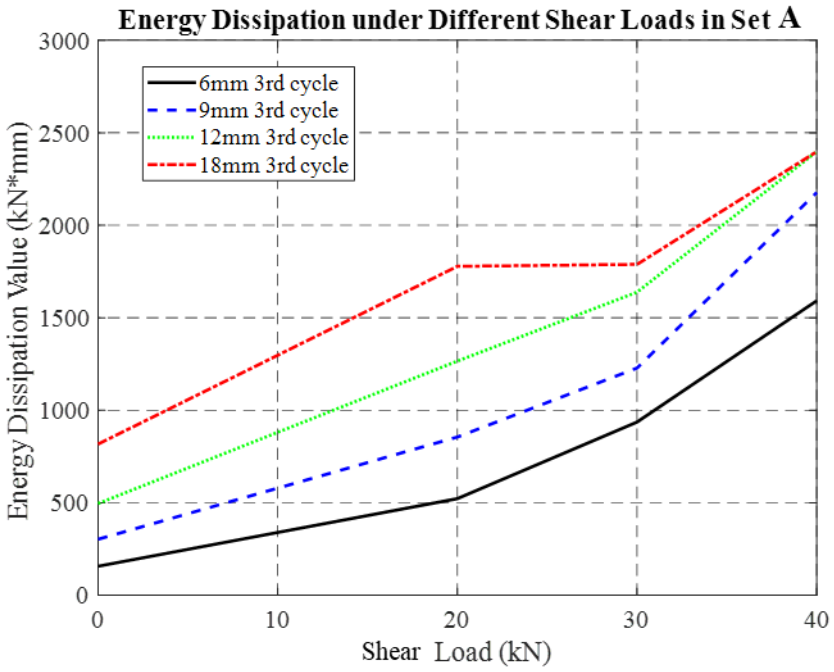

(a)

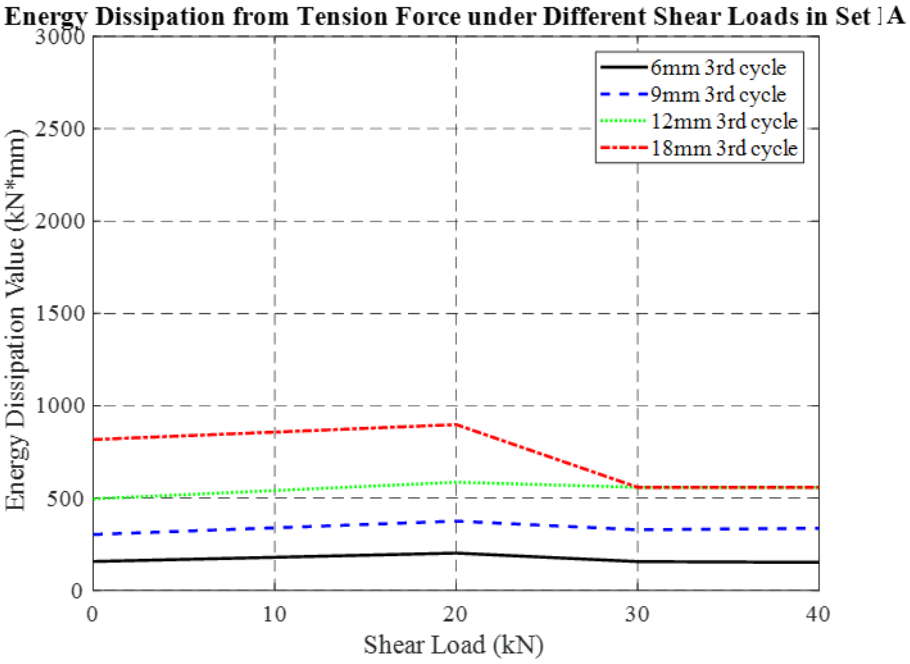
Energy Dissipation from Tension Force under Different Shear Loads in Set A
6mm 3rd cycle
9mm 3rd cycle
12mm 3rd cycle
18mm 3rd cycle
Energy Dissipation Value (kN*mm)
Shear Load (kN)
0
500
1000
1500
2000
2500
3000
0
10
20
30
40

(b)

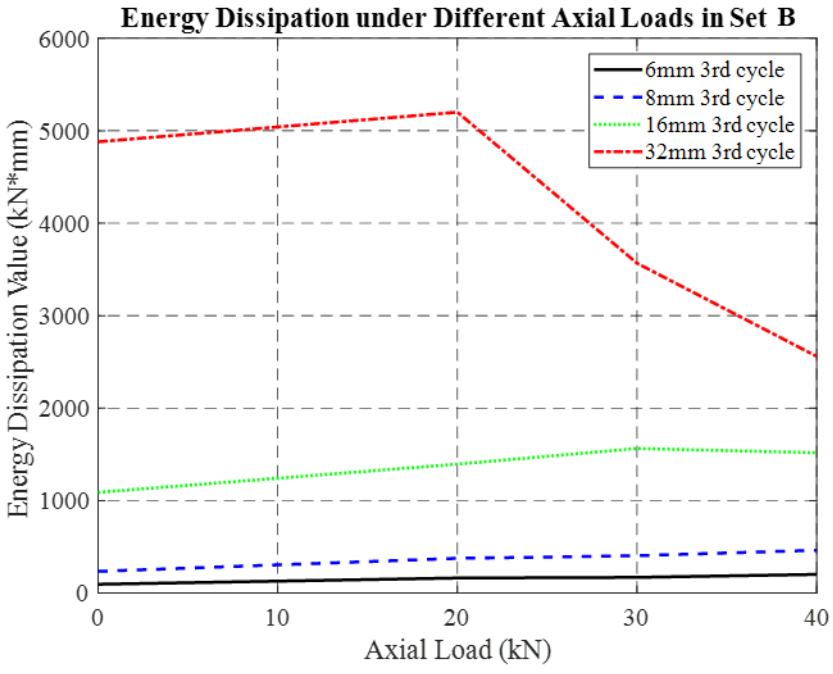
Energy Dissipation under Different Axial Loads in Set B
6mm 3rd cycle
8mm 3rd cycle
16mm 3rd cycle
32mm 3rd cycle
Energy Dissipation Value (kN*mm)
Axial Load (kN)
0
1000
2000
3000
4000
5000
6000
0
10
20
30
40

(c)

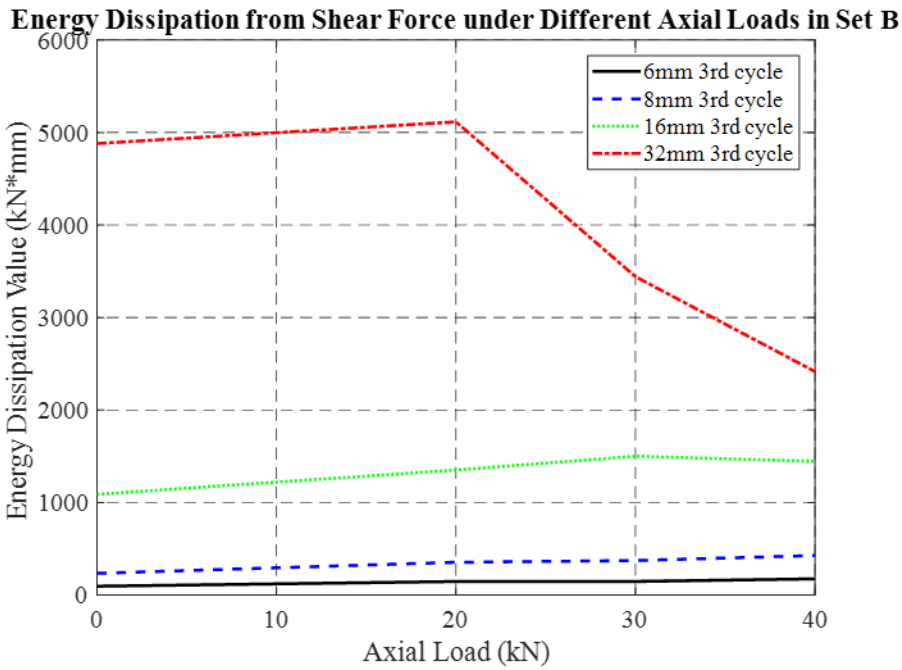

(d)

Figure 3.19 The coupling effect on energy capacity at the third cycle of the target cyclic displacement peaks: (a) energy dissipation under different shear loads in Set A; (b) energy dissipation from tension force under different shear loads in Set A; (c) energy dissipation under different tension loads in Set B; (d) energy dissipation from shear force under different tension loads in Set B

3.5 Summary

In this chapter, an innovative testing program was carried out to study the coupling effects of shear load and tension load for typical angle bracket CLT connections. In Set A, the specimens were tested under monotonic/cyclic shear loading with four levels of co-existent shear loads (0 kN, 20 kN, 30 kN, and 40 kN). In Set B, the specimens were tested under monotonic/cyclic shear loading with four levels of co-existent tension loads (0 kN, 20 kN, 30 kN, and 40 kN). The failure mode and load-displacement curve were also discussed. Important connection properties, such as stiffness, strength, strength impairment, ductility, overstrength, equivalent damping ratios, strength degradation, and energy dissipation were evaluated according to the EN 12512 procedure

(2006). The coupling effects on load capacity and energy dissipation capacity was likewise discussed. The results showed that the shear and tension behaviour of the angle brackets were strongly coupled. The following explanation for the hysteresis behaviour of angle bracket connections under bi-axial loading was proven: the nails in CLT connections had pressed into the surrounding wood embedment in both the horizontal and vertical directions, which caused different mechanisms from those involved in to one-directional loading.

For Set A, greater co-existent shear load also caused more brittle failure modes. The mechanical properties of the angle brackets in Set A were weakened by the co-existent shear load. The average values of K_{el}, F_{yl}, F_{max}, v_{max}, F_u, and v_u in shear decreased by 13.1%,17.1%, 31.8%, 24.1%, 31.6%, and 24.0% from 0 kN to 40 kN, respectively. Co-existent shear loads made the hysteresis loops of cyclic tension loading less stable and the connections less ductile. It maintained the tension capacity within 10% changes at small and moderate amplitudes (6 mm, 9 mm and 12 mm) but rapidly reduced the tension capacity to 0 at a large vertical amplitude (18 mm). Since the vertical deformation capacity of the angle bracket was small (20 mm), as compared to the horizontal deformation capacity (45 mm), the energy dissipation was dominated by the co-existent shear load. A Lager co-existent shear load caused greater energy dissipation. However, for a large amplitude (18 mm), the energy dissipated by large shear loads (30 kN and 40 kN) was weakened due to damage from cyclic tension loading.

For Set B, it was found that greater co-existent axial loads lead to more severe stretch of the angle brackets, and more brittle failure modes for the connections. Co-existent axial loads weakened the mechanical properties of the angle brackets. The average values of K_{el} , F_{yl}, v_{yd}, F_{max}, v_{max}, F_u, and v_u decreased by 13.1%, 17.2%, 10.6%, 16.2%，7.1%，16.2%，and 22.4% from 0 kN to 40 kN, respectively. In terms of hysteresis behaviour, the co-existent axial loads

decreased the stability, reduced the ductility, and weakened the pinching effect in cyclic shear loading. As the tension force increased, the shear capacity and energy dissipation capacity of the connectors dropped significantly. A large axial load level (40 kN) decreased the maximum shear capacity of the connections and initial stiffness of the connectors by 25% and 15%, respectively. Under a large lateral amplitude (32 mm), the co-existent axial load was able to cause an over 60% reduction in its shear loading capacity, and an around 25% reduction of its energy dissipation capacity. At relatively small amplitudes (6 mm, 8 mm, and 16 mm), the total energy dissipation had a growing trend with increasing co-existent axial loads, while at a large amplitude (32 mm), it dropped by over 45%. This shows that co-existent axial loads had a severely negative influence on the energy dissipation capacity. It was found that, while the co-existent tension load weakened the shear strength of the specimen at large amplitudes, it also pressed the nails into the surrounding wood embedment, which eliminated gaps. Thus, under relatively small amplitudes, this helped the nails to carry greater shear loads.

By comparing Set A and Set B, it was found that the energy dissipation capacity of the angle brackets was much smaller under Set A than Set B, which proved the efficiency of angle brackets in carrying shear loads rather than tension loads.

These conclusions addressed the importance of considering the coupling effects of tension and shear on angle brackets connections. The outcomes of the angle bracket tests were used to calibrate the numerical model in Chapter 6 for such connections to further study the coupling effects of bi-axial loading.

Chapter 4: Experimental Test of CLT Hold-down Connections under Bi-axial Loading

4.1 Introduction

Cross-Laminated Timber (CLT) is an attractive structural material with higher dimensional stability, axial load capacity, in-plane shear strength, as well as greater rigidity in comparison with traditional solid wood material. In structural systems, CLT panels are widely used as load bearing components such as walls and floors. Various crucial requirements in the structural behaviour of CLT must be addressed and incorporated into design guidelines for improved safety and efficiency. In the past decades, researchers have conducted a series of experimental studies on CLT structural performance on both the component level and structural level. One of the earliest such studies, carried out at the University of Ljubljana, Slovenia, involved monotonic and cyclic tests on CLT panels with different anchorage details, vertical load levels, and boundary conditions (Dujič *et al.*, 2004; Dujic *et al.*, 2006; Dujic *et al.*, 2008). These tests revealed that CLT panels have relatively a high shear stiffness and load-bearing capacity. The critical elements that govern their structural response are the anchors connecting the panels with the foundation. The study proved that the nonlinear behaviour of CLT walls and the main source of the non-linearity is the connections. Next, a systematical project to study the performance and capacities of CLT called SOFIE was conducted by the IVALSA Institute of the National Research Council at San Michelel all'Adige. This included a series of lateral resistance performance tests of CLT panels (Ceccotti and Follesa, 2006), a shaking table test of a three-storey CLT building (Ceccotti, 2008), and a shaking table test on a seven-storey CLT building (Ceccotti *et al.*, 2013). This project concluded that in CLT structures, most deformation and failure occurs at the metal connectors rather than the

wood. Also, rocking and slip are the major deformation mechanisms of the CLT panels. Later, FPInnovations and the University of British Columbia conducted the first series of experimental research projects in North America on the structural performance of CLT walls (Popovski *et al.*, 2010; Popovski and Gavric, 2015; Shahnewaz *et al.*, 2017). These tests provided a data set for follow-up North American seismic research on CLT. In the United States, a NEES CLT Planning project was undertaken to study the seismic resilience of tall Cross-Laminated Timber (CLT) systems (Pei *et al.*, 2014; Ganey, 2015; Piazza *et al.*, 2015; Pei *et al.*, 2016). Some other notable experimental efforts on CLT structural behaviour were also performed in Germany (Flatscher and Schickhofer, 2011), Japan (Okabe *et al.*, 2012), and Chile (Benedetti *et al.*, 2016) for different species of CLT. These test results further proved that CLT connections govern the deformation in any types of CLT panels.

In CLT structures, one typical design assumption is that, hold-downs will uplift under loading and only take the tension force to resist the overturning moment. Under such assumptions, tests were conducted on CLT hold-down connections loaded in one direction (Rinaldin *et al.*, 2013; Schneider *et al.*, 2013); in-plane monotonic and cyclic shear tests were performed on hold-down connections between adjacent parallel wall-wall and floor-floor CLT panels. Mechanical properties in terms of strength, stiffness, energy dissipation, ductility ratio, strength impairment, and overstrength factors were evaluated (Gavric *et al.*, 2011); a laboratory test was carried out to a set of radiata pine CLT walls and hold-down connections taking into consideration both quasi-static monotonic and cyclic loading. In terms of connection behaviour, it was observed that hold-downs on radiate pine CLT elements reached a lower load capacity than hold-downs on other wood species (Tomasi and Smith, 2014).

Recent studies showed that under horizontal loads, connections in CLT panels experience both shear loads and tension loads (Liu and Lam, 2016; Pozza *et al.*, 2017; Liu and Lam, 2018). More significantly, shear loads may weaken the axial loading capacity, taking into question the safety and rationality of current design methods. Pozza *et al.* (2018) studied axial-shear interactions on CLT hold-down connections. In this study, cyclic tension tests were conducted in the vertical direction following application of a lateral displacement. However, the specimens only undertook uniaxial tension forces during loading, whereas, for CLT panels under lateral loading in real scenarios, the connections resist both tension and shear forces simultaneously. In the tests of this Chapter, special setups were designed to concurrently capture shear and tension under bi-axial loading. A comprehensive investigation was conducted to consider the influence of axial forces on shear, and that of shear forces on tension. Besides load-carrying capacity and stiffness, this research also focused on the hysteresis behaviour which are more important for dynamic loading. Such coupling effect investigation through monotonic and cyclic tests of CLT hold-down connections under shear and tension load combinations provided a more profound understanding of hold-down behaviour under complex loadings.

4.2 Experimental tests

This experiment was designed to study the coupling effects of tension and shear forces on hold-down connections in CLT structures. The experiment setup, specimens and test procedures are described in this section.

4.2.1 Description of the experiment setup

Typical commercially available CLT hold-down connections were tested in this experiment. Steel base-panel connections represented the wall panel-to-foundation connections in real constructions. The connection tests were performed under bi-axial loading, as follows: 1) Set

C: monotonic and cyclic tension loading with three levels of constant shear loads; and 2) Set D: monotonic and cyclic shear loading with five levels of constant tension loads. Figure 4.1 displays the configurations of the hold-down connection tests.

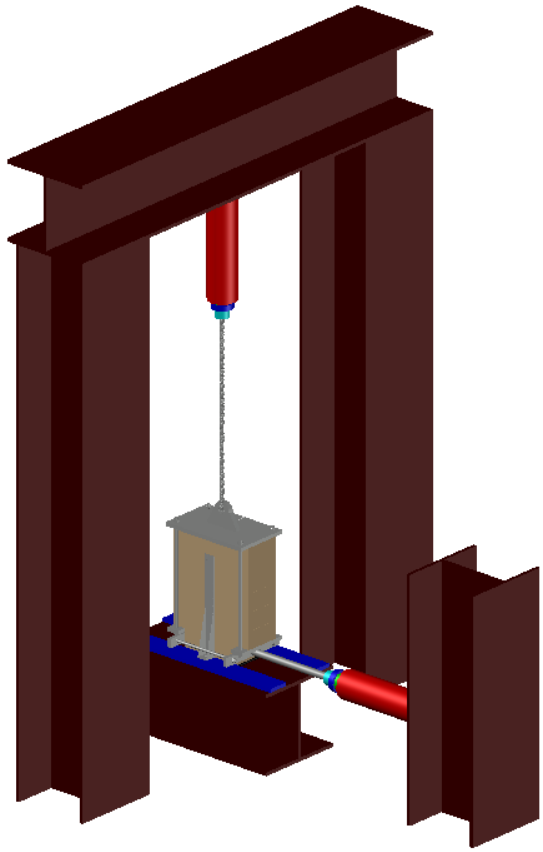

Figure 4.1 A 3D schematic drawing of the experiment setup

During the bi-axial loading, the specimen will slip due to the shear force. Thus, the tension force will be loaded eccentrically. To reduce such an eccentricity effect, a one-meter long steel cable was used to connect the vertical load cell with the specimen (Figure 4.2).

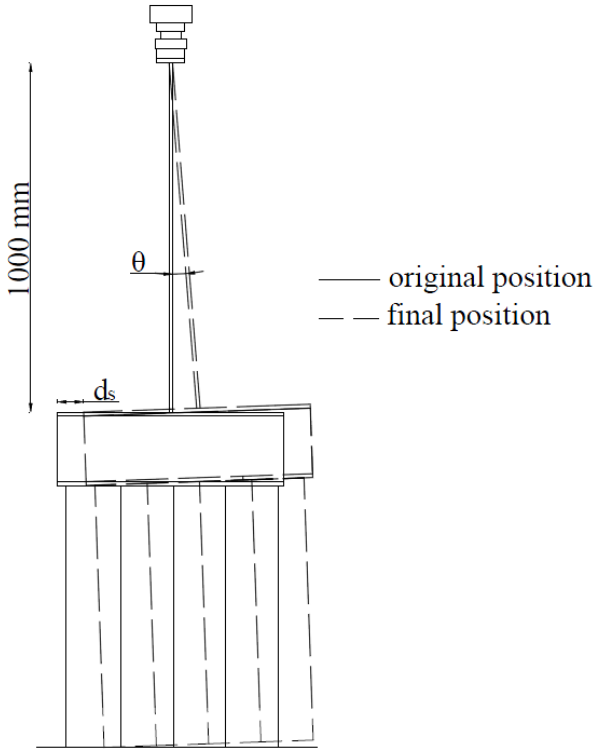

Figure 4.2 Rotation of the cable due to lateral displacement of the specimen

As illustrated in Figure 4.3 (a), the specimen was fixed to the steel base by hold-downs, using a 1 M16 bolt on either side. Two actuators, denoted LC1 and LC2, acted on the specimen. LC1 provided tension load through the steel cable, which was connected to the steel components constrained on the top of the CLT specimen. LC2 provided shear load through the steel components constrained at the bottom of the specimen. To prevent friction between the CLT panel and the steel base, steel rollers with a diameter of 10 mm were placed beneath the specimen.

The full setup of one specimen is presented in Figure 4.3 (b). A single linear potentiometer was installed on either side of the specimen to measure the relative displacement between the screw on the specimen and the steel base. Bi-axial loading and the slight eccentricity of the specimen may cause out-of-plane movement, which was avoided by using two rigid “L” shaped steel plates and roller plates to constrain it. Two sets of tests (Set C and Set D) were conducted

using the same setup. Figure 4.3 (c) shows how the bi-axial loading acted on the hold-down connector: for Set C, at the outset of each test, a shear load was applied to the connector, after the target shear load was reached, the monotonic or cyclic tension load was delivered while maintaining the target shear load; for Set D, at the start of each test, a tension load was applied to the connector, after the target tension load was reached, the monotonic or cyclic shear load was delivered while maintaining the target tension load. Since the specimens were moving in the other direction while constant force was being applied, the actual load on the specimens oscillated within a 5% range around the targeting values.

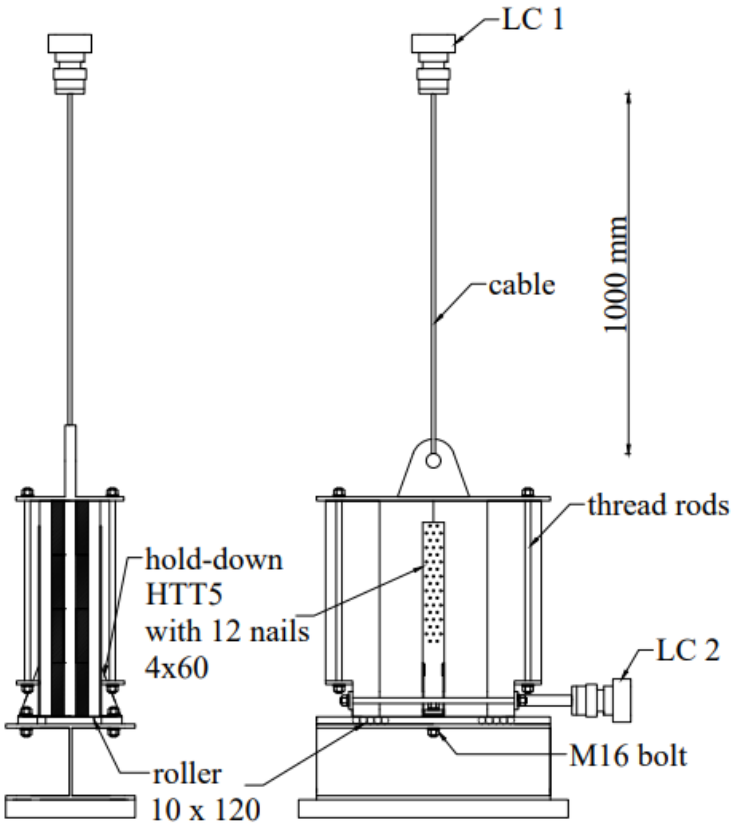

(a)

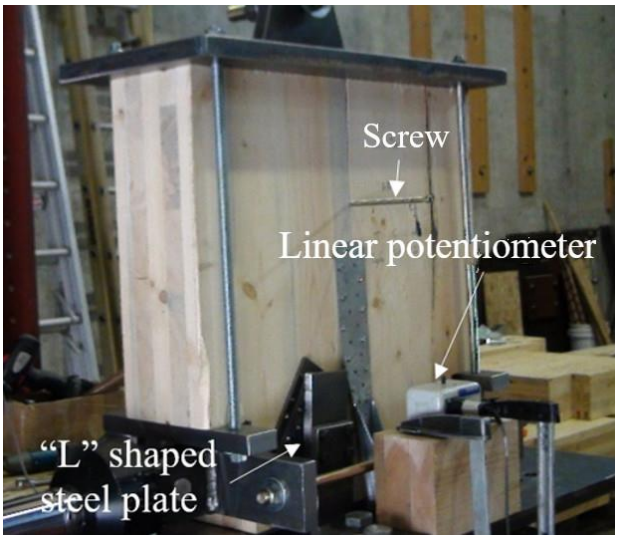

(b)

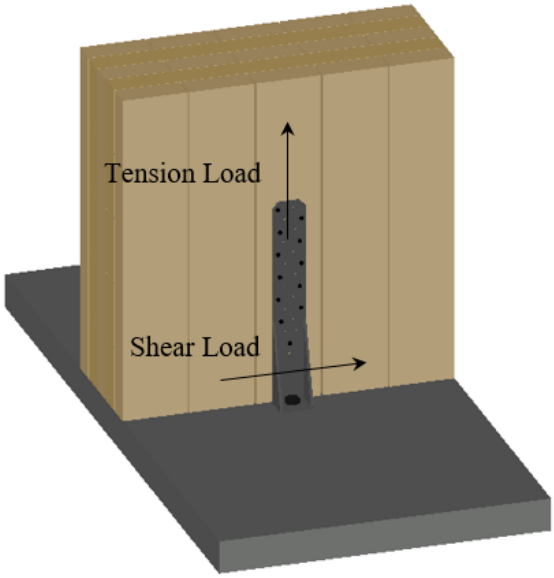

(c)

Figure 4.3 Test configurations of the hold-down connections: (a) front and side view drawing of the set-up; (b) photo of the set-up; (c) bi-axial loading on the hold-down connector

With the horizontal displacement d_s of the specimen, the rotation of the cable θ would not exceed 5°. Therefore, the tension load (F_T) can be considered to be a vertical load all along the test (Fig. 4). The turning moment (M_R) induced by the shear force (F_S) can be neglected since it was

located above the bottom of the specimen for less than 20 mm (d/2). As shown in Figure 4.4 (a), some rollers were placed under the specimen, thus, the friction F_x was considered to be 0. Since it was very difficult to record the actual lateral resistance and vertical resistance directly under bi-axial loading, using this setup, these values could be calculated through the mechanism shown in Figure 4.4 (b).

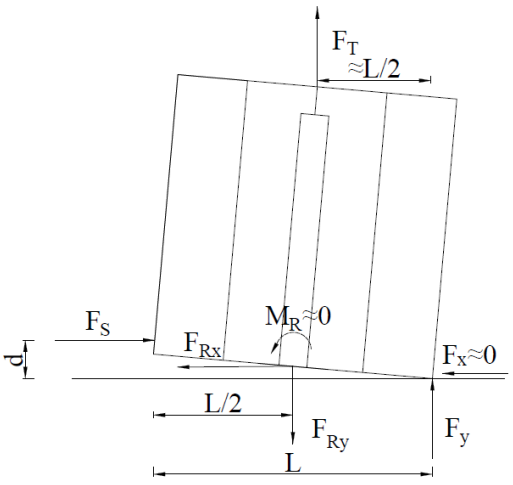

(a)

$$\begin{cases} F_S - F_{Rx} - F_x = 0 \\ F_T + F_y - F_{Ry} = 0 \\ F_S \cdot d + F_T \cdot L/2 - F_{Rx} \cdot d/2 - F_{Ry} \cdot L/2 - M_R = 0 \end{cases}$$

$F_{Rx} = F_S, F_{Ry} = F_T + F_S \cdot d / L$

F_{Rx} : *lateral resistance* F_{Ry} : *vertical resistance*

F_x : *friction* F_y : *vertical support force*

(b)

Figure 4.4 The bi-axial loading mechanism of a hold-down specimen: (a) force analysis; (b) calculations

4.2.2 Specimens characteristics

The CLT panels were of five layers and made from graded No. 1/2 SPF lumber. The thickness of each layer was 35mm, and the total thickness of the CLT panel was 175 mm. The dimensions of each CLT specimen were 600 mm × 600 mm and the layout is shown in Figure 4.5 (a). The specimens had a moisture content of 12%, and were stored and tested under controlled conditions at 50% RH and 20°C. As a commonly used hold-down device in the projects, the HTT5 (hold-down) was tested using 12 annular-ringed nail 4 mm × 60 mm and 1 16mm diameter bolt (8.8 grade). The configurations in (Gavric *et al.*, 2011), which was HTT5 tests for uniaxial loading,

were adopted for a comparison. The photo and configuration for the HTT5 connector are shown in Figure 4.5 (b).

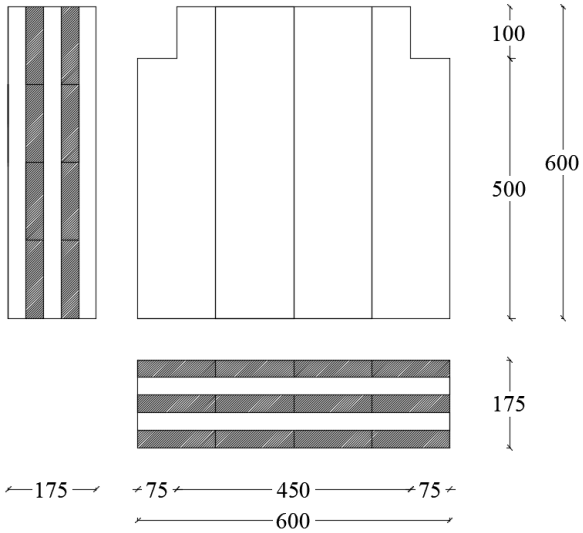

(a)

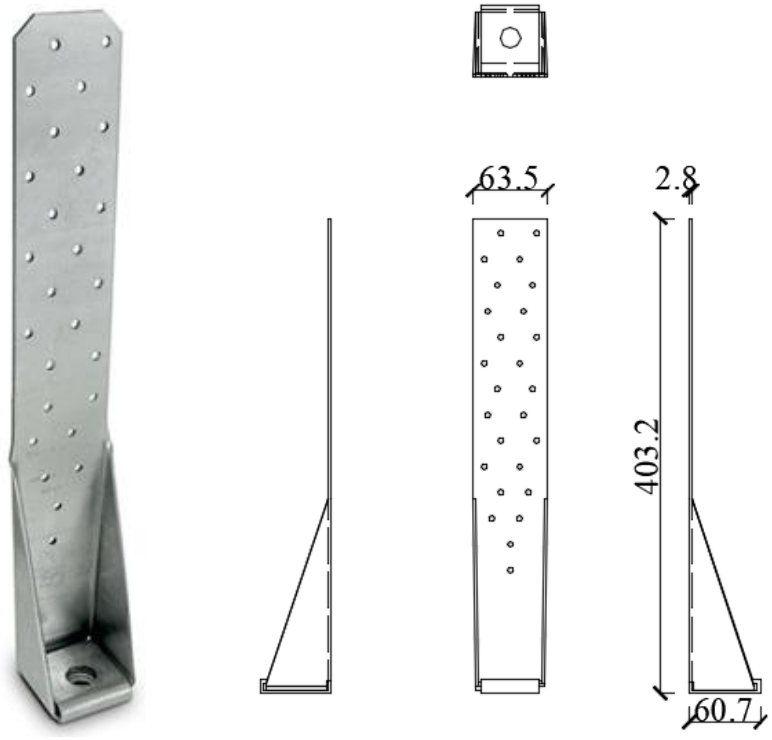

(b)

Figure 4.5 CLT specimen and hold-down: a) layout of the CLT specimen; b) photo and configuration of hold-down (all measured in mm)

4.2.3 Test procedure

Cyclic tests were conducted using reverse cyclic procedures with predefined yield values which varied between configurations, depending on the experimental yield values obtained from the monotonic tests.

In Set C, in the horizontal direction, constant shear load was first applied and then maintained on the specimens up to the target value with the actuator being under load control. Then, in the perpendicular direction, monotonic or cyclic vertical displacement was applied subsequently. As shown in Figure 4.6 (a), monotonic tension tests were carried out under displacement control at a loading rate of 0.2 mm/s. Cyclic tension tests followed the modified procedure based on EN 12512 (CEN 2006) for the cyclic testing of joints made with mechanical fasteners, at an input displacement rate of 0.8 mm/s, so that the duration of each test did not exceed the time limit of 30 minutes.

In Set D, in the vertical direction, constant tension load was first applied and maintained on the specimens up to the target value with the actuator being under load control. Then, in the perpendicular direction, monotonic or cyclic lateral displacement was applied subsequently. As shown in Figure 4.6 (b), monotonic shear tests were carried out under displacement control at a loading rate of 0.2 mm/s. Cyclic shear tests followed the modified procedure based on EN 12512 (CEN 2006) for the cyclic testing of joints made with mechanical fasteners, at an input displacement rate of 0.8 mm/s, so that the duration of each test did not exceed the time limit of 30 minutes.

Set C Test Protocol	
Monotonic Tension Loading Phase	Displacement rate 0.2 mm/s

Cyclic Tension Loading Phase	Displacement rate 0.8 mm/s
No. of Cycle	Peak displacement (mm)
1	1
1	2
1	4
1	6
3	8
3	12
3	16
3	24

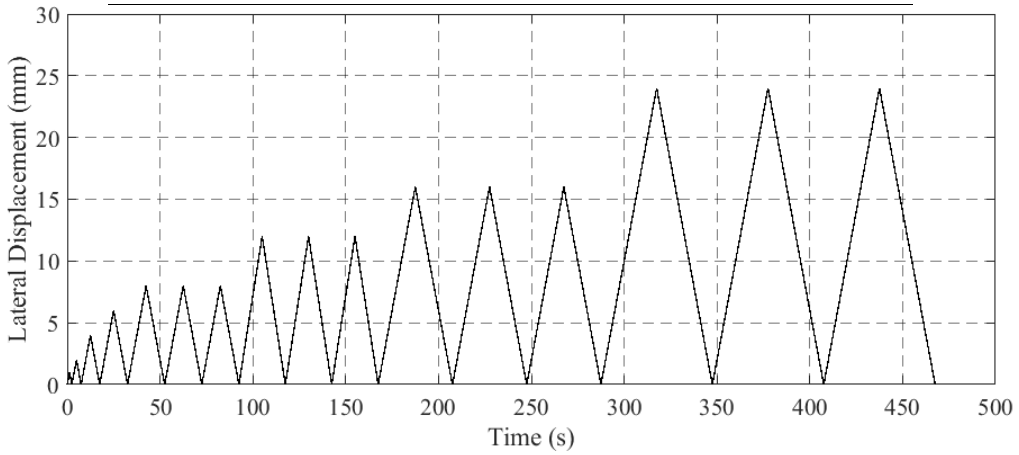

(a)

Set D Test Protocol	
Monotonic Shear Loading Phase	Displacement rate 0.2 mm/s
Cyclic Shear Loading Phase	Displacement rate 0.8 mm/s
No. of Cycle	Peak displacement (mm)
1	3
1	6
3	9
3	12
3	24
3	48

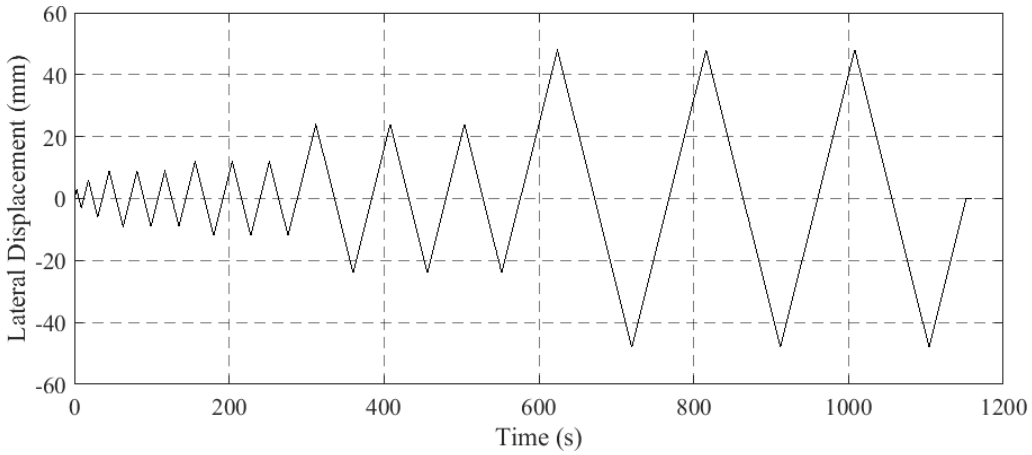

(b)

Figure 4.6 (a) Set C test protocol; (b) Set D test protocol

In order to evaluate the effects of shear loading on the tension behaviour of the hold-downs, in Set C, the hold-down connections were tested under monotonic/cyclic in-plane tension loading with three levels of in-plane shear loads. The maximum shear capacity of the HTT5 was 28 kN; thus, three shear load levels (0 kN, 10 kN, and 20 kN) were selected. The monotonic tests were conducted to determine the displacement magnitudes for the cyclic loading protocols and examine the load capacity. For each configuration, one monotonic and three/six cyclic tests were performed. For the level 0 kN shear force, three cyclic tests were conducted due to the stability of the performance at these levels. For force levels 10 kN and 20 kN, six cyclic tests were conducted.

In order to evaluate the effects of tension loading on the shear behaviour of the hold-downs, in Set D, the hold-down connections were tested under monotonic/cyclic in-plane shear loading with five levels of in-plane tension loads. The maximum tension capacity of the HTT5 was 80 kN, thus, five shear load levels (0 kN, 20 kN, 30 kN, 40 kN, and 60 kN) were selected. For each configuration, one monotonic and three/six cyclic tests were performed. For tension force levels 0

kN, 40 kN, and 60 kN, three cyclic tests were conducted due to the stability of the performance at these levels. For force levels 20 kN and 30 kN, six cyclic tests were conducted.

18 tests were performed for Set C and 26 tests for Set D. The specimens were named under the following rules: the first two letters "HD" denoted "angle bracket connection"; the following letter "S" or "T" denoted "constant shear load" or "constant tension load" in one direction; the following number denoted the constant load value; the following letter "C" or "M" denoted "cyclic loading" or "monotonic loading" in the perpendicular direction; the number after "C" or "M" denoted the numbering of the specimen; the final letter denoted the set. For example, "HDS20C3C" represented the No. 3 hold-down specimen for cyclic tension loading with a co-existent shear load of 20 kN in Set C. A test matrix for the specimens is outlined in Table 4.1.

Table 4.1 The test matrix for the hold-down specimens

	Set C (constant shear force)		
	0	10 kN	20 kN
Monotonic tension test	HDS0M1C	HDS10M1C	HDS20M1C
Cyclic tension test	HDS0C1C HDS0C2C HDS0C3C	HDS10C1C HDS10C2C HDS10C3C HDS10C4C HDS10C5C HDS10C6C	HDS20C1C HDS20C2C HDS20C3C HDS20C4C HDS20C5C HDS20C6C

	Set D (constant tension force)				
	0	20 kN	30 kN	40 kN	60 kN
Monotonic shear test	HDT0M1D	HDT20M1D	HDT30M1D	HDT40M1D	HDT60M1D
Cyclic shear test	HDT0C1D HDT0C2D HDT0C3D	HDT20C1D HDT20C2D HDT20C3D HDT20C4D HDT20C5D HDT20C6D	HDT30C1D HDT30C2D HDT30C3D HDT30C4D HDT30C5D HDT30C6D	HDT40C1D HDT40C2D HDT40C3D	HDT40C1D HDT40C2D HDT40C3D

4.3 Test results

This section presents the test results for the 18 specimens under three different levels of constant shear forces, and the 26 specimens under five different levels of constant tension force, including their failure modes and load-displacement curves.

4.3.1 Failure modes

In Set C, for different levels of constant shear load, the deformation shapes of the hold-downs varied at the maximum vertical displacement of 24 mm, as shown in Figure 4.7. As the shear load increased, the steel plate connected to the wood panel was significantly twisted right above the flanges since the shear stiffness along the hold-down changed abruptly at this weak area. The co-existent constant shear load intensified the torsion, while the cyclic axial load was observed as having little influence on the performance.

In Set D, for the different levels of constant axial load, the deformation shapes of the hold-downs at the maximum lateral displacement of 48 mm varied, as shown in Figure 4.8. Most deformation of the hold-downs occurred at the area above the flanges. The steel plate yielded due to the cyclic shear load and as the tension load increased, the steel at this area showed significant torsion and elongation.

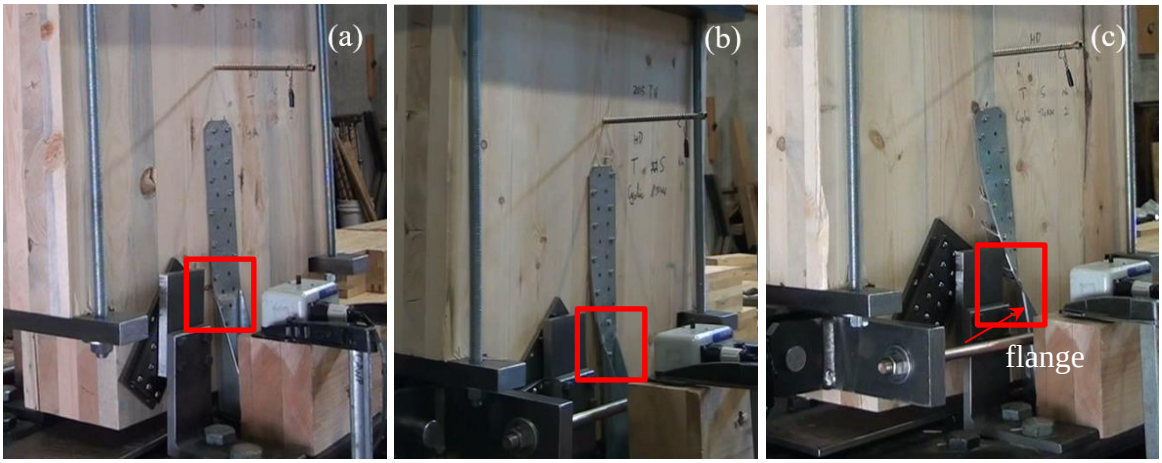

Figure 4.7 The deformation shapes for Set C specimens at the maximum vertical displacement for different levels of shear load: (a) 0 kN; (b) 10 kN; (c) 20 kN

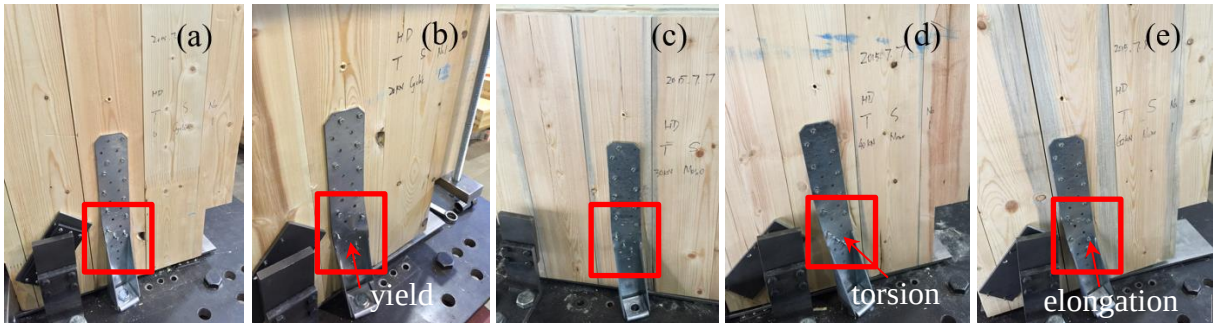

Figure 4.8 The deformation shapes for Set D specimens at the maximum lateral displacement for different levels of tension load: (a) 0 kN; (b) 20 kN; (c) 30 kN; (d) 40 kN; (e) 60 kN

The failure modes involved brittle failures and ductile failures in both Set C and Set D. For low co-existent load levels (Shear: 0 kN and 10 kN; Tension: 0 kN, 20 kN, and 30 kN), most specimens failed due to the yielding of the nails or steel plate, as shown in Figure 4.9 (a) and (b), which is considered as a ductile failure mode. When higher co-existent load was applied (Shear: 20 kN; Tension: 40 kN and 60 kN), the brittle failure modes, such as nail breakage, steel plate fracture, and localized wood crushing took place. Nail breakage generally occurred below the head of the nail when the shear force on each nail reached the shear capacity of its section (Figure 4.9 (c)). The steel plate was torn above the flanges and the nails were pulled out under the shear loading

(Figure 4.9 (d)). Cyclic shear loading may cause the weak cross-section of the steel plate to fracture from a high co-existent axial load (Figure 4.9 (e)). Pressure on the wood embedment area may cause localized wood crushing (Figure 4.9 (f)).

(a)

(b)

(c)

(d)

(e) (f)

Figure 4.9 The failure modes at the ultimate displacement: (a) nail yielding; (b) steel plate yielding; (c) nail breakage; (d) steel plate torsion; (e) steel plate fracture; (f) localized wood crushing

The failure modes of the specimens are summarized in Table 4.2. As the co-existent load increased, brittle failure bodes occurred more frequently.

Table 4.2 The failure modes of each specimen for hold-downs

Failure mode	Specimen
Nail yielding	HDS0C1C, HDS0C2C, HDS0C3C, HDS0M1C, HDS10C1C, HDS10C2C, HDS10C4C, HDS10M1C, HDT0C1D, HDT0C2D, HDT0C3D, HDT0M1D, HDT20C1D, HDT20C2D, HDT20C3D, HDT30C2D
Steel plate yielding	HDS10C3C, HDS10C5C, HDS10C6C, HDS20C3C, HDT20C4D, HDT20C5D, HDT20C6D
Nail breakage	HDT30C1D, HDT30C3D, HDT30C6D, HDT40C2D, HDT40C3D, HDT60C2D
Steel plate torsion and nail pullout	HDS20C1C, HDS20C2C, HDS20C4C, HDS20C5C, HDS20C6C, HDS20M1C, HDT20M1D, HDT30M1D, HDT40M1D, HDT60M1D
Steel plate fracture	HDT30C5D, HDT40C1D, HDT60C1D
Wood crushing	HDT30C4D, HDT60C3D

4.3.2 Load-displacement curves

The lateral and axial relative displacements between the CLT panels and the steel base, and the corresponding loads were recorded during all the tests to define the load-displacement curves. For the vertical direction, the axial relative displacement between the CLT panel and the steel base

was calculated by deducting the elongation of the steel cable from the axial displacement of the actuator. This included the deformation of nails, wood embedment and hold-down steel plates. A tension load of 1 kN was initially applied to tighten the cable. The elongation of the cable ΔL was calculated using the equation $\Delta L=FL/EA$, in which, F is the tension load value from the actuator, L is the total length of the steel cable, E is the elastic modulus of steel, and A is the section area of the cable. Data from the linear potentiometers was used to adjust and verify the axial relative displacement, as shown in Figure 4.10, since it included both the vertical and horizontal displacements between the CLT panel and the steel plate.

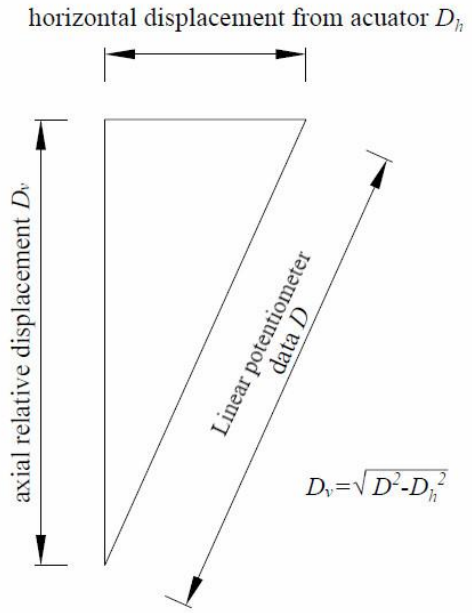

Figure 4.10 Calculation of the axial relative displacement using linear potentiometer data

For the horizontal direction, shear displacement between the CLT plate and the steel base was recorded through the horizontal actuator. Fig. 11 depicts the force-displacement curves in Set C at different levels of shear load for all the specimens, including monotonic and cyclic tests. Since a steel cable was used to load the tension force, it could not carry the reverse loading. During unloading, with residual deformations, the specimens only returned to the position of zero tension

force rather than zero vertical displacement. Thus, the actual vertical displacement protocol was different from the applied loading protocol.

When no extra shear load was applied, for the monotonic test, the specimen undertook a maximum tension load of 79.2 kN at the 18.7 mm displacement and an ultimate vertical displacement of over 22.3 mm; the hysteresis loops for the three specimens in the cyclic tests were stable (Figure 4.11 (a)). For the 10 kN co-existent shear load, the maximum load dropped to 75.9 kN, and the ultimate shear displacement value dropped to 19.6 mm; the hysteresis loops became more scattered among the specimens (Figure 4.11 (b)). For the 20 kN co-existent shear load, the shear capacity from the monotonic testing was 74.9 kN, and the ultimate shear displacement decreased to 16.5 mm; it is worth noting that the shear capacity in the cyclic tests dropped significantly, especially during the last few cycles at the maximum vertical displacement of 16 mm. At the same time, severe strength degradation was observed (Figure 4.11 (c)). Two of the six specimens under cyclic tension loading failed before finishing the first cycle of the amplitude of 16 mm.

Since the maximum shear force that can be loaded on the hold-downs was only 20 kN, co-existent shear load had a more negative effect on the ductility than the tension capacity and ultimate vertical displacement. According to the monotonic test, the ultimate lateral displacement was able to reach 80 mm. However, the hold-downs had been twisted severely at this stage. Hence, we selected 60 mm as the functional limit for the hold-downs in the cyclic tests.

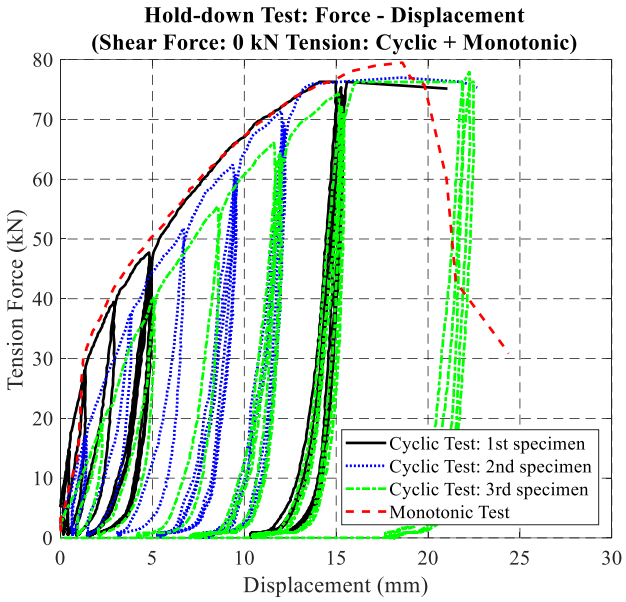
Hold-down Test: Force - Displacement
(Shear Force: 0 kN Tension: Cyclic + Monotonic)
Tension Force (kN)
Displacement (mm)
Cyclic Test: 1st specimen
Cyclic Test: 2nd specimen
Cyclic Test: 3rd specimen
Monotonic Test

(a)

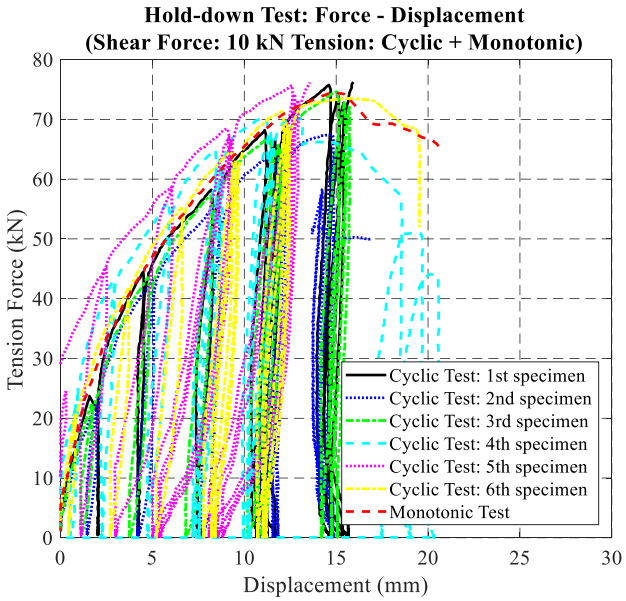
Hold-down Test: Force - Displacement
(Shear Force: 10 kN Tension: Cyclic + Monotonic)
Tension Force (kN)
Displacement (mm)
Cyclic Test: 1st specimen
Cyclic Test: 2nd specimen
Cyclic Test: 3rd specimen
Cyclic Test: 4th specimen
Cyclic Test: 5th specimen
Cyclic Test: 6th specimen
Monotonic Test

(b)

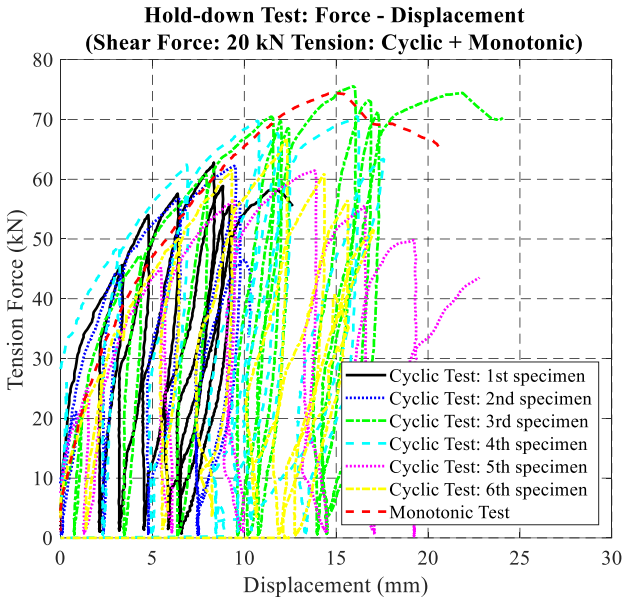

(c)

Figure 4.11 Force-displacement curves with constant shear load: (a) 0 kN; (b) 10 kN; (c) 20 kN

Figure 4.12 presents the force-displacement curves of the hold-down connections in Set D under shear monotonic and cyclic tests with five levels of co-existent tension load (0 kN, 20 kN, 30 kN, 40 kN, and 60 kN). The shear test for hold-downs with a 0 kN co-existent tension load had the same setting as that of the pure shear tests (Gavric, 2013). The results were compared and confirmed as similar. The hysteresis loops were very stable in the three specimens. The maximum shear force was 26.9 kN in the monotonic shear test. A significant pinching effect and strength degradation were observed, as shown in Figure 4.12 (a). For the 20 kN co-existent tension load, the maximum shear force was 25.5 kN in the monotonic shear test (Figure 4.12 (b)). The pinching effect was weakened compared to that of the 0 kN co-existent tension load. The mechanism was illustrated in Figure 4.13 through a section view of the nail moving in the surrounding wood embedment. As shown in Figure 4.13 (a), when no co-existent tension load was applied, the nail was able to move without horizontal resistance in the gap formed by the earlier displacement. With

the application of the co-existent tension load (Figure 4.13 (b)), additional pressure was introduced by the co-existent tension force on the contact surface between the nail and the surrounding wood embedment, resulting in additional lateral resistance. As observed from the hysteresis loops, the pinching effect was therefore mitigated. This is the principle of developing the numerical model for the coupling effects of CLT connections when considering reloading strength degradation, stiffness degradation, and unloading stiffness degradation. For the 30 kN co-existent tension load, the maximum shear force was 26.2 kN in the monotonic shear test (Figure 4.12 (c)). Some of the specimens showed a reduction in ductility. The second specimen had unstable results and did not finish the last cycle of the cyclic shear test at the 48 mm amplitude. For the 40 kN co-existent tension load, the maximum shear force was 25.1 kN in the monotonic shear test (Figure 4.12 (d)). The specimens failed to demonstrate a pinching effect when below the 24 mm amplitude. However, none of the specimens could finish the first cycle at the 48 mm amplitude in the cyclic shear tests. For the 60 kN co-existent tension load, the maximum shear force was 30 kN in the monotonic shear test (Figure 4.12 (e)). However, the performance of the specimens in the cyclic shear tests was poor. None of the specimens finished the last cycle at the 24 mm amplitude. This indicated that a high co-existent tension load significantly compromised the shear capacity of the hold-downs.

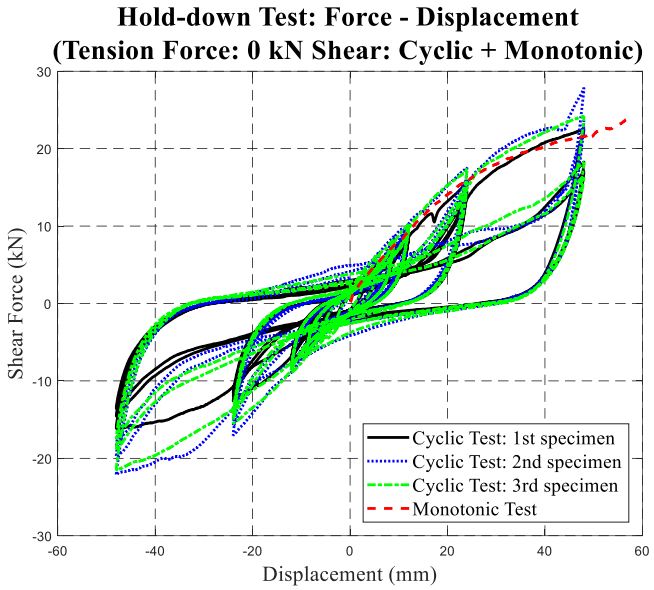
Hold-down Test: Force - Displacement
(Tension Force: 0 kN Shear: Cyclic + Monotonic)
Shear Force (kN)
Displacement (mm)
Cyclic Test: 1st specimen
Cyclic Test: 2nd specimen
Cyclic Test: 3rd specimen
Monotonic Test

(a)

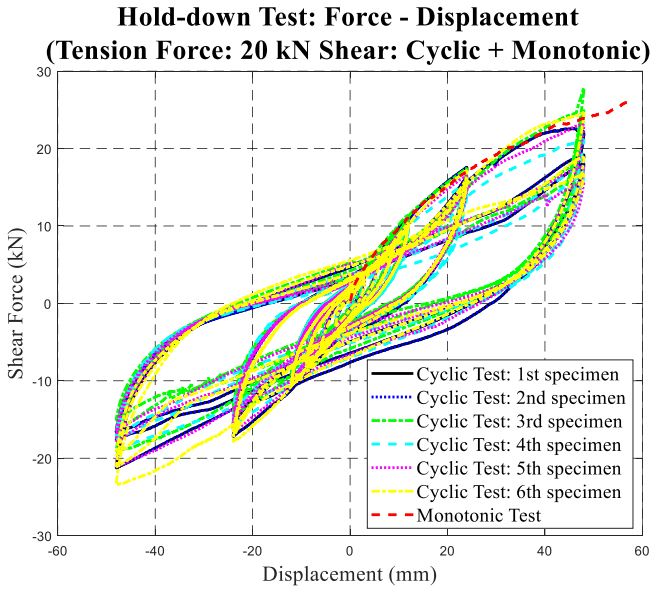
Hold-down Test: Force - Displacement
(Tension Force: 20 kN Shear: Cyclic + Monotonic)
Shear Force (kN)
Displacement (mm)
Cyclic Test: 1st specimen
Cyclic Test: 2nd specimen
Cyclic Test: 3rd specimen
Cyclic Test: 4th specimen
Cyclic Test: 5th specimen
Cyclic Test: 6th specimen
Monotonic Test

(b)

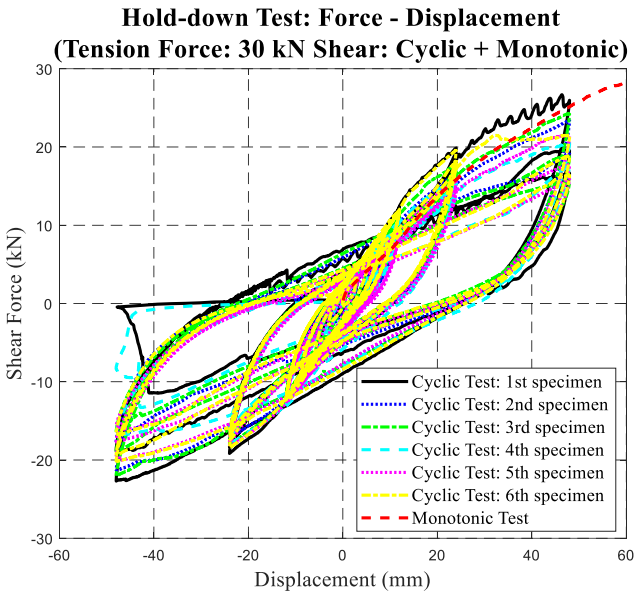
Hold-down Test: Force - Displacement
(Tension Force: 30 kN Shear: Cyclic + Monotonic)
Shear Force (kN)
Displacement (mm)
Cyclic Test: 1st specimen
Cyclic Test: 2nd specimen
Cyclic Test: 3rd specimen
Cyclic Test: 4th specimen
Cyclic Test: 5th specimen
Cyclic Test: 6th specimen
Monotonic Test

(c)

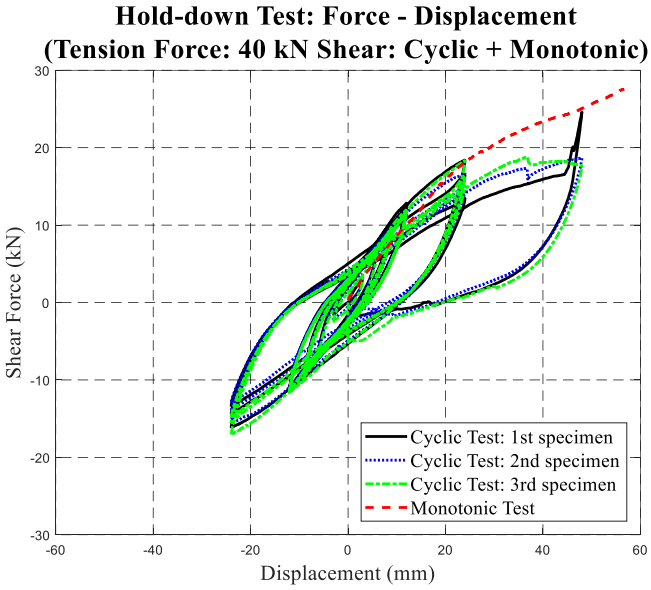
Hold-down Test: Force - Displacement
(Tension Force: 40 kN Shear: Cyclic + Monotonic)
Shear Force (kN)
Displacement (mm)
Cyclic Test: 1st specimen
Cyclic Test: 2nd specimen
Cyclic Test: 3rd specimen
Monotonic Test

(d)

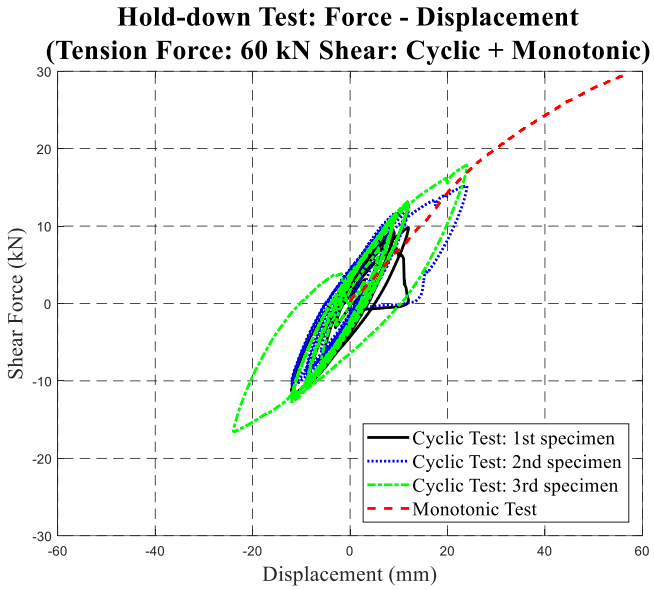

(e)

Figure 4.12 Force-displacement curves with different levels of constant tension load: (a) 0 kN; (b) 20 kN; (c) 30 kN; (d) 40 kN; (e) 60 kN

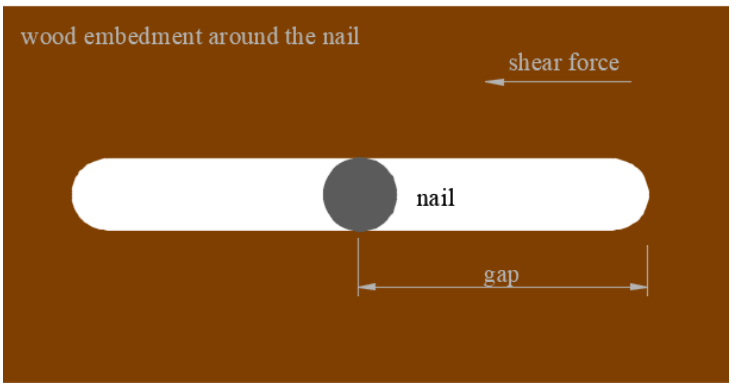

(a)

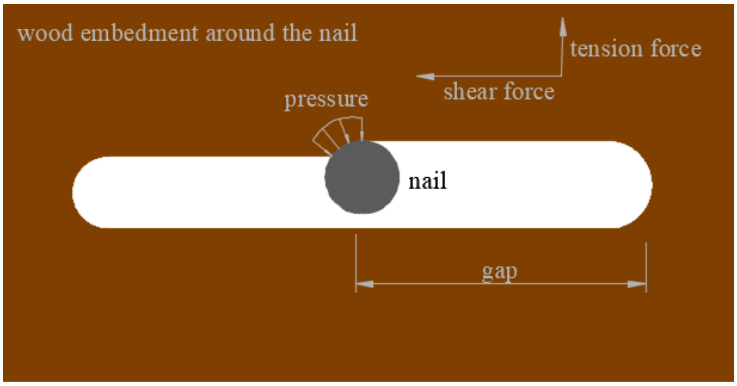

(b)

Figure 4.13 A schematic section view of the nails in the wood embedment: (a) nail movement under shear force in absence of a co-existent tension load; (b) nail movement under shear force with a co-existent tension load

4.4 Analyses of results

The experimental results of Set C and Set D were analyzed based on the procedure described in EN 12512 (CEN 2006). Strength and stiffness, equivalent viscous damping and strength degradation, and energy dissipation were evaluated accordingly.

4.4.1 Strength and stiffness

The experimental test results were assessed in terms of strength, stiffness, and ductility, following the standard procedure in EN12512 (CEN 2006), using method “b” to define elastic and post elastic stiffness, yielding point and ultimate conditions.

Assessments for the mechanical properties included the following details:

K_{el} and K_{pl} are initial stiffness and plastic stiffness; F_{yl} and v_{yd} represent yielding load and yielding displacement; F_{max} and v_{max} signify maximum load and maximum displacement; F_u and v_u represent ultimate load and ultimate displacement; D_D signifies ductility ratio (ratio between the ultimate and yield displacements).

Table 4.3 outlines the mechanical properties of the hold-downs in Set C under cyclic tension loading with a co-existent shear load, which weakened the axial loading capacity. The average values of K_{el} , F_{yl}, v_{yd}, F_{max}, v_{max}, F_u, and v_u in tension decreased by 19.7%, 5.8%, 2.9%, 5.4%, 11.6%, 12.9%, and 4.0% from 0 kN to 20 kN, respectively. Table 4.4 gives the mechanical properties of the hold-downs in Set D under cyclic shear loading with a co-existent axial load. The co-existent axial load strengthened the shear loading capacity at the elastic range. The average values of K_{el} and F_{yl} in shear increased by 55.2% and 43.4% from 0 kN to 60 kN, respectively. The average values of F_{max} and F_u increased by 25.3% and 20.3% from 0 kN to 30 kN, and then decreased by 12.1% and 16.6% from 30 kN to 60 kN.

Table 4.3 Analysis of the experimental results in Set C according to EN 12512 (CEN 2006)

Mechanical property	0 kN (shear)		10 kN (shear)		20 kN (shear)	
	Mean	CoV(%)	Mean	CoV(%)	Mean	CoV(%)
K_{el}(kN/mm)	13.61	31.56	11.82	25.09	10.93	19.71
K_{pl}(kN/mm)	2.27	30.14	1.97	22.52	1.82	17.63
F_{yl}(kN)	49.67	5.52	49.42	8.73	46.81	9.72
v_{yd}(mm)	3.79	7.00	3.92	8.95	3.68	8.81
F_{max}(kN)	79.20	-	75.88	-	74.94	-
v_{max}(mm)	18.70	-	19.60	-	16.54	-
F_u(kN)	68.16	-	60.80	-	59.37	-
v_u(mm)	22.30	-	21.51	-	21.40	-
D_D	5.90	7.17	5.49	9.36	5.70	9.53

Table 4.4 Analysis of the experimental results in Set D according to EN 12512 (CEN 2006)

Mechanical property	0 kN (tension)		20 kN (tension)		30 kN (tension)		40 kN (tension)		60 kN (tension)	
	Mean	Cov (%)	Mean	Cov (%)	Mean	Cov (%)	Mean	Cov (%)	Mean	Cov (%)

K_{el}(kN/mm)	0.67	2.43	0.77	16.31	0.88	15.10	1.02	7.10	1.04	9.62
K_{pl}(kN/mm)	0.11	2.54	0.13	16.54	0.14	14.89	0.17	7.19	0.17	9.89
F_{yl}(kN)	10.75	0.70	11.53	16.35	12.55	15.22	14.73	7.33	15.42	13.23
v_{yd}(mm)	16.00	3.13	15.00	2.72	15.18	4.35	14.18	8.55	15.12	7.63
F_{max}(kN)	26.93	-	32.54	-	33.75	-	32.63	-	29.67	-
v_{max}(mm)	80.00	-	80.00	-	80.00	-	80.00	-	55.20	-
F_u(kN)	26.93	-	32.54	-	33.75	-	32.63	-	29.37	-
v_u(mm)	80.00	-	80.00	-	80.00	-	80.00	-	64.09	-
D_D	5.02	3.34	5.37	2.89	5.67	7.79	5.67	8.88	4.23	11.43

Figure 4.14 outlines the tri-linear curves of the tests in Set C and Set D following the procedure in EN 12512-b using the mean values. In Figure 4.14 (a), these three lines represent the elastic branch up to the yielding point, the post-elastic hardening branch up to the maximum force, and the softening branch up to the tension failure. It shows that the co-existent shear load weakened the tension loading capacity, albeit to a lesser extent. In Figure 4.14 (b), those two lines symbolized the elastic branch up to the yielding point, and the post-elastic hardening branch up to the maximum force in shear. The specimens revealed strong ductility in shear and 80 mm was selected as an ending lateral displacement point. The trend shows that co-existent axial loading dramatically strengthened the shear loading capacity, disregarding cumulative damage. The cumulative effect will be discussed in Section 4.3.

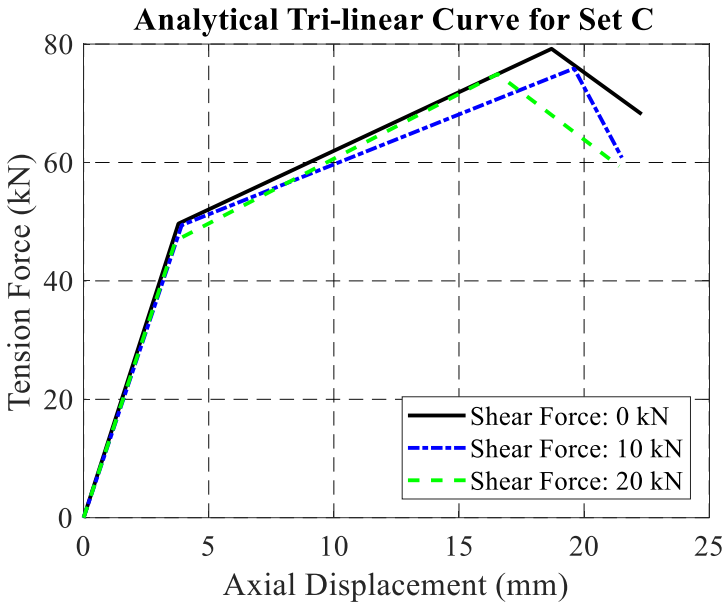

(a)

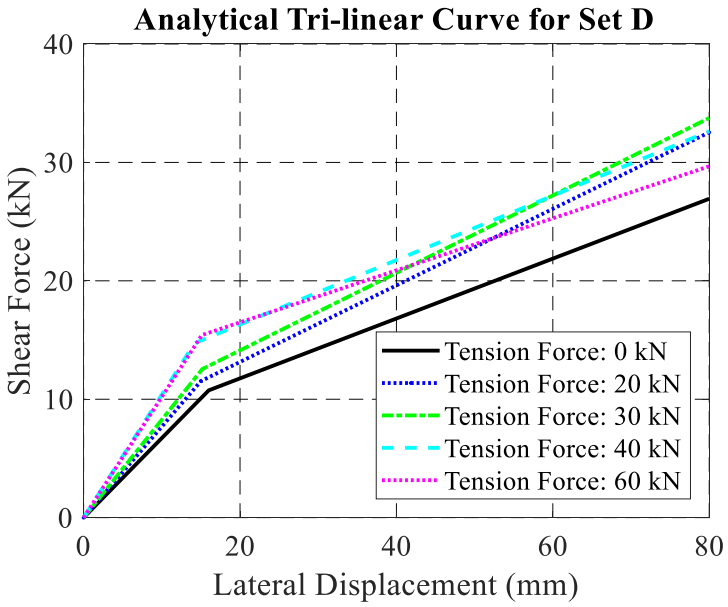

(b)

Figure 4.14 Analytical tri-linear curves: (a) the monotonic tension force - axial displacement relationship for Set C; (b) the monotonic shear force - lateral displacement relationship for Set D

4.4.2 Equivalent viscous damping and strength degradation

The equivalent viscous damping values for each cycle, and the strength degradation values at the end of the 2nd and 3rd cycles of each displacement level were evaluated to assess the cyclic behavior in the two sets, using data from a representative specimen in each group.

The equivalent viscous damping ratio shows the hysteresis damping properties of the hold-down connections. The equivalent viscous damping ratio for the i^{th} cycle $v_{eq,i}$ is defined as the ratio of the dissipated energy in the cycle $E_{d,i}$ to the available potential energy in the cycle $E_{p,i}$ multiplied by 4 π, $v_{eq,i} = \frac{E_{d,i}}{4\pi E_{p,i}}$. The available potential energy $E_{p,i}$ can be determined as $E_{p,i} = 1/2 \cdot F_i \cdot u_i$, where F_i and u_i are the maximum force and maximum displacement attained in the i^{th} cycle.

Figure 4.15 (a) shows that, in Set C, for small amplitudes (8 mm, 12 mm), the equivalent viscous damping values in tension revealed a growing trend with increases in co-existent shear loads. However, at cycles of the 16 mm amplitude, specimens with no co-existent shear load have higher equivalent viscous damping, at around 10%, as compared to the 7% values of those having co-existent shear loads (10 kN and 20 kN). Imposing of a co-existent shear load decreased the equivalent viscous damping of the hold-down connectors at large displacements. Figure 4.15 (b) reveals that, in Set D, for small amplitudes (9 mm and 12 mm), the equivalent viscous damping values in shear grew with increases in co-existent tension loads. Still, at amplitudes of 24 mm and 48 mm, the connectors rapidly lost their damping capacity under increases in co-existent tension loads. This is because the connectors were severely damaged at those amplitudes. Thus, larger co-existent tension loads accelerated the degree of failure.

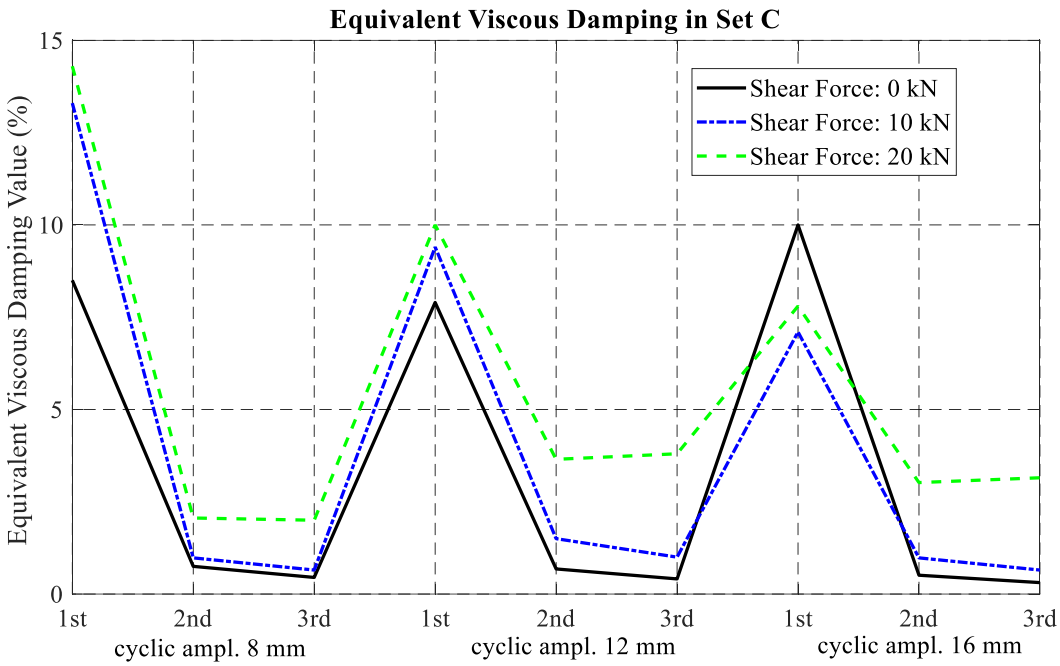

(a)

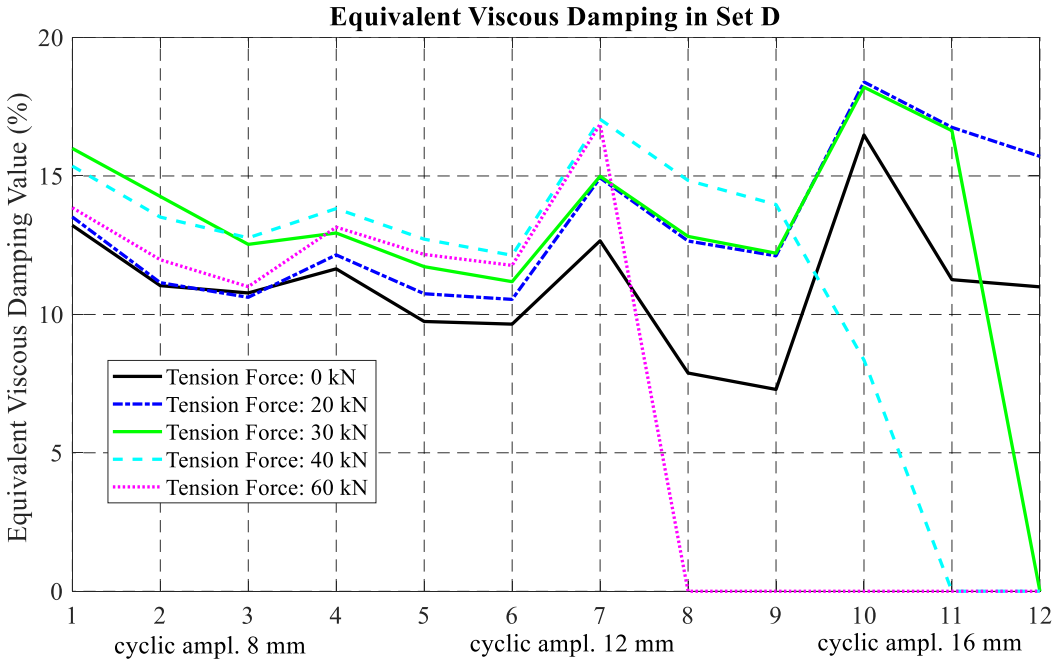

(b)

Figure 4.15 Equivalent viscous damping for each cycle: (a) Set C; (b) Set D

For strength degradation, in Set C, a 10 kN co-existent shear force had limited influence on the axial loading capacity, but a 20 kN co-existent shear force significantly decreased the axial capacity (Figure 4.16 (a)). At a large axial displacement (16 mm), the axial loading capacity dropped by 18% at the last cycle. At the 10 kN co-existent shear force level, the tension capacity remained the same. At the 20 kN co-existent shear force level, the tension capacity dropped 17.5%. Similar results were found by Pozza *et al.* (2018) that a small lateral displacement (7.5 mm) caused little axial-shear interaction in the hold-downs, but higher values of lateral displacement (30 mm) decreased the peak tension force by 25%. In Set D (Figure 4.16 (b)), the co-existent tension force began to have negative influence on shear loading capacity at larger lateral displacements (24 mm and 48 mm). The larger the co-existent tension force, the earlier the hold-down connectors lost their strength.

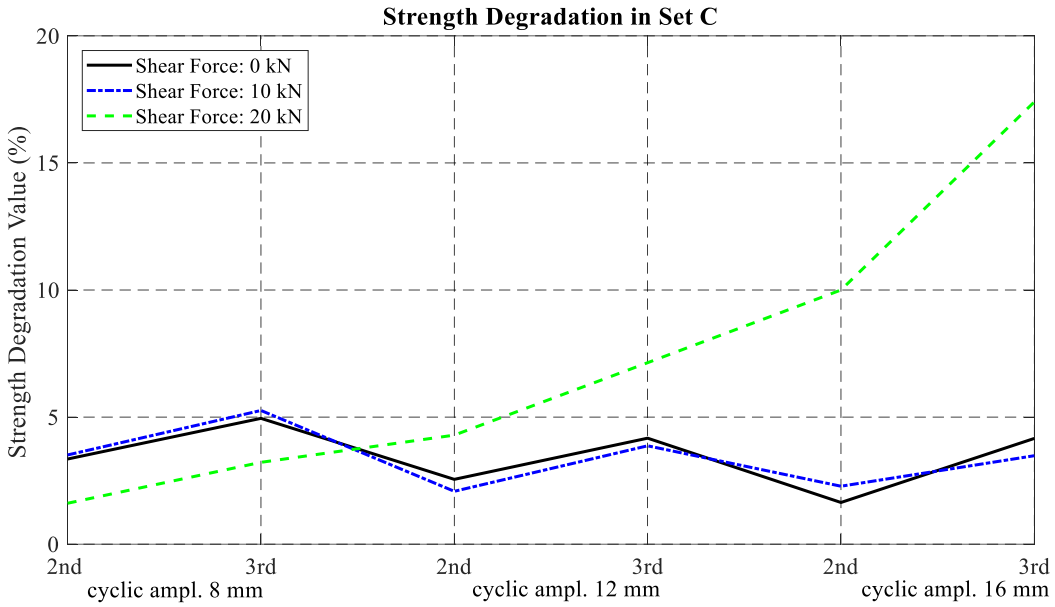

(a)

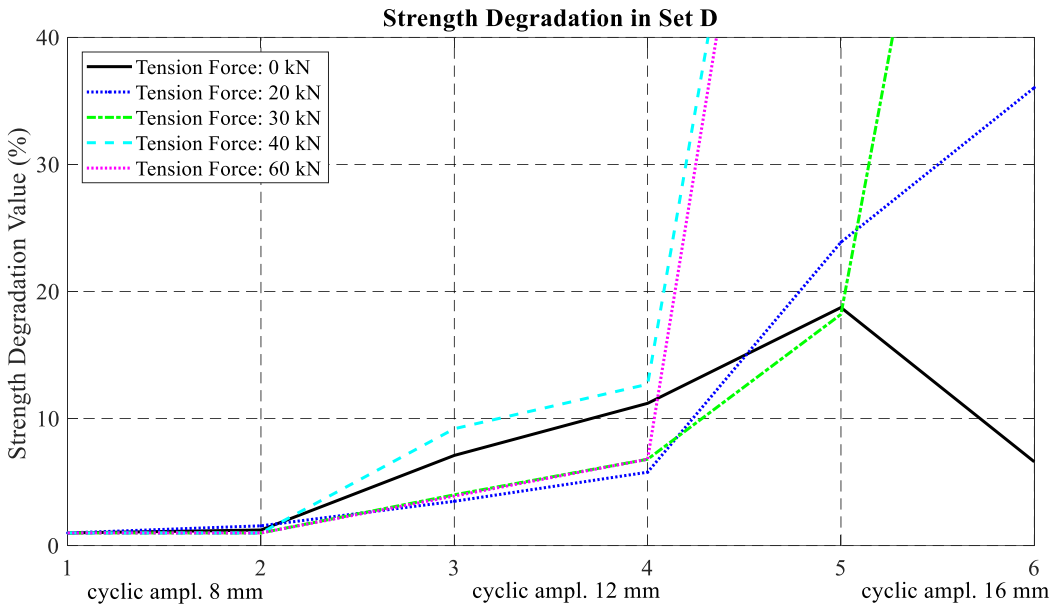

(b)

Figure 4.16 Strength degradation during the last two cycles

4.4.3 Energy dissipation

The energy dissipation for each test was considered from two parts, cyclic loading and co-existent constant loading. The energy dissipation value of cyclic loading was calculated by the area of the hysteresis loop in each cycle. The energy dissipation value of co-existent constant loading was the co-existent load value multiplied by the displacement of the specimen in the loading direction during each cycle.

For Set C, the energy dissipated from the cyclic tension loading, the constant shear loading for each cycle, and the cumulative total energy dissipation were plotted in Figure 4.17 (a), (b), and (c), respectively. Figure 4.17 (a) depicted that, with co-existent shear force, the hold-downs failed to dissipate energy at a large vertical amplitude of 16 mm. However, before this, the co-existent shear force strengthened the dissipation capacity in tension at smaller amplitudes. Figure 4.17 (b) indicated that the initial application of the co-existent shear force introduced comparably high

energy dissipation levels in shear, specially, 350 kN·mm for the 20 kN co-existent shear force. Afterwards, the energy dissipated from the co-existent shear force was minimal. The co-existent shear force strongly increased the cumulative total energy dissipation, from 1450 kN·mm to 2150 kN·mm, as shown in Figure 4.17 (c).

For Set D, the energy dissipated from cyclic shear loading, the constant tension loading for each cycle, and the cumulative total energy dissipation were plotted in Figure 4.17 (d), (e), and (f), respectively. All levels of co-existent tension force strengthened the dissipation capacity in shear prior to the amplitude of 12 mm (Figure 4.17 (d)). After arriving this amplitude, small co-existent tension forces (20 kN) were still able to strengthen the dissipation capacity in shear, but the energy dissipation capacity in shear dropped as the co-existent tension force increased. The greater the co-existent tension force, the sooner it reduced. For instance, the energy dissipation capacity in shear during the first cycle of the 48 mm amplitude dropped from 910 kN·mm to 460 kN·mm with a 40 kN co-existent tension force. With a 60 kN co-existent tension force, the energy dissipation capacity in shear decreased to 0 at the second cycle of the 24 mm amplitude. Figure 4.17 (e) indicated that an energy dissipation in tension of as high as 480 kN·mm was introduced when initially applying a co-existent tension force. Little energy was dissipated from the tension force afterwards, but during the last few cycles, the energy dissipation increased due to failure. As shown in Figure 4.17 (f), a moderate level of co-existent tension force (below 30 kN) actually increased the total energy dissipation capacity of the hold-downs in shear.

By comparing Figure 4.17 (c) and (f), the hold-downs can be observed as having better performance in dissipating energy in shear (4600 kN·mm) than in tension (2100 kN·mm). This is because they can undergo a much larger lateral displacement (over 80 mm) than vertical

displacement (less than 30 mm). Yet it is noted that hold-downs are generally used as tension resistant components because of their high strength rather than their ductility.

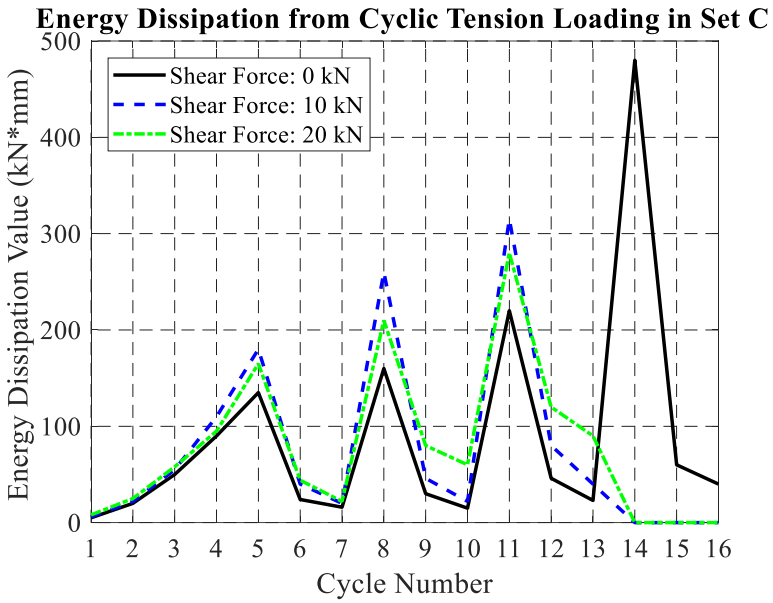

(a)

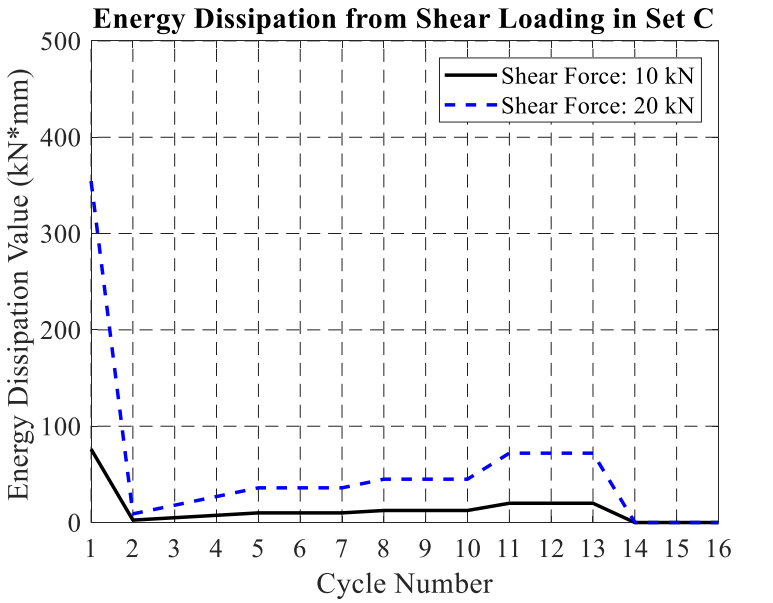

(b)

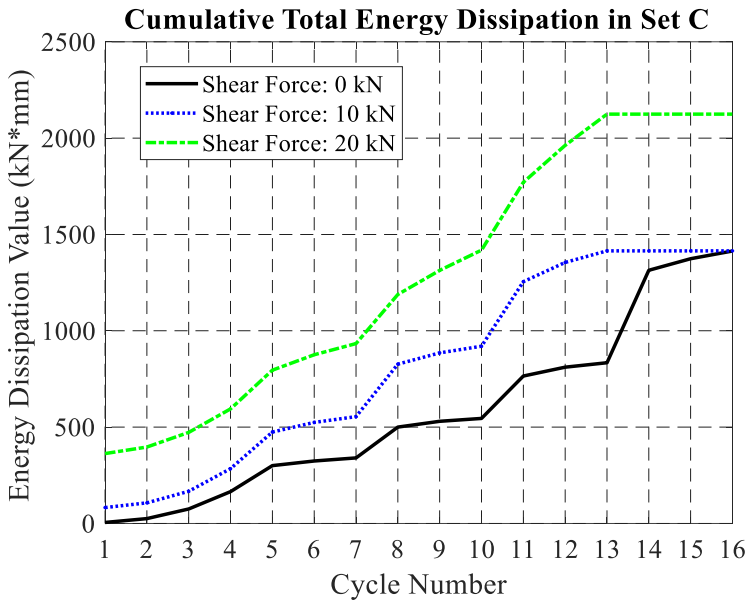
Cumulative Total Energy Dissipation in Set C
Shear Force: 0 kN
Shear Force: 10 kN
Shear Force: 20 kN
Energy Dissipation Value (kN*mm)
Cycle Number
0
500
1000
1500
2000
2500
1 2 3 4 5 6 7 8 9 10 11 12 13 14 15 16

(c)

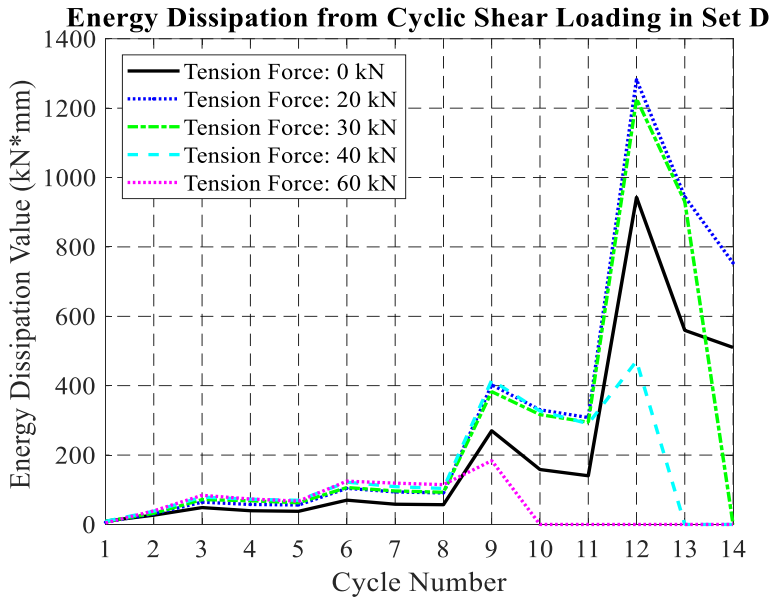
Energy Dissipation from Cyclic Shear Loading in Set D
Tension Force: 0 kN
Tension Force: 20 kN
Tension Force: 30 kN
Tension Force: 40 kN
Tension Force: 60 kN
Energy Dissipation Value (kN*mm)
Cycle Number
0
200
400
600
800
1000
1200
1400
1 2 3 4 5 6 7 8 9 10 11 12 13 14

(d)

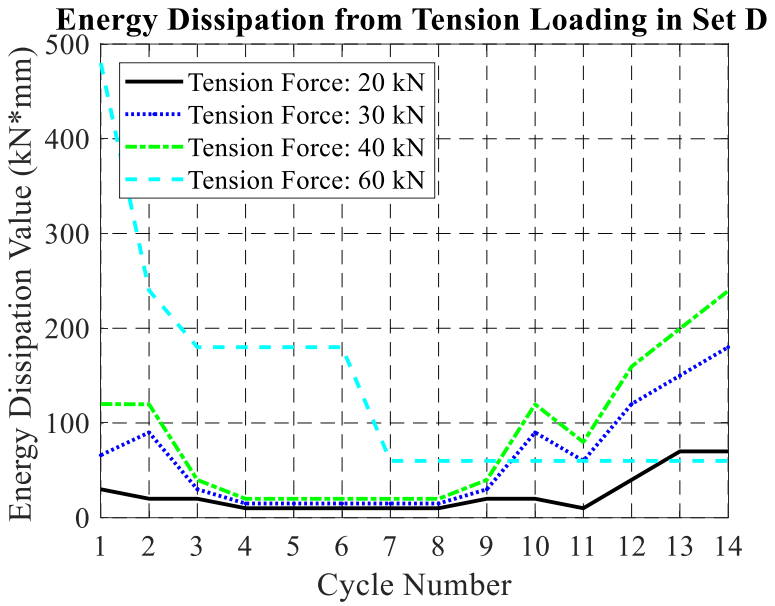

(e)

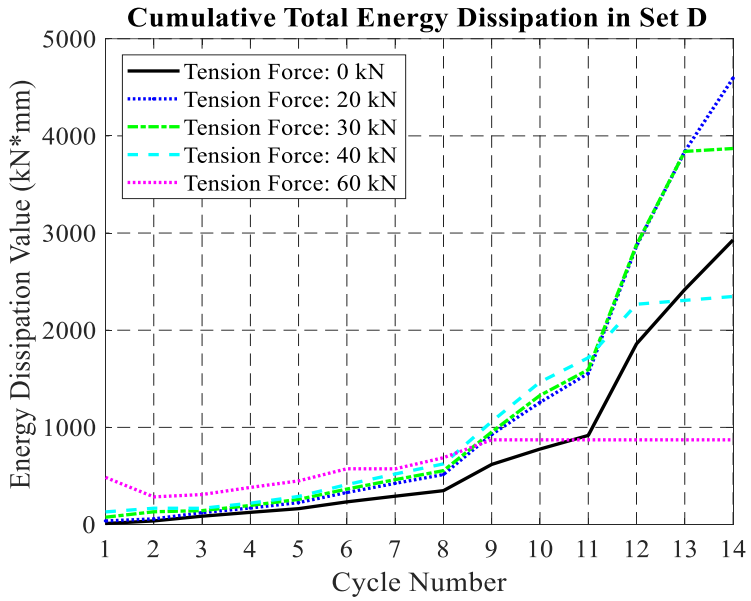

(f)

Figure 4.17 Energy dissipation plots: (a) energy dissipation from cyclic tension loading in Set C; (b) energy dissipation from shear loading in Set C; (c) cumulative total energy dissipation in Set C; (d) energy dissipation from cyclic shear loading in Set D; (e) energy dissipation from tension loading in Set D; (f) cumulative total energy dissipation in Set D

4.4.4 Discussion on coupling effect

The coupling effect is discussed from two aspects, load capacity and energy dissipation capacity.

To consider the coupling effect between shear load and tension load, for Set C, the tension forces at the end of each amplitude for the first cycle were plotted in Figure 4.18 (a) against different co-existent shear loads; for Set D, the shear forces at the end of each amplitude for the first cycle were plotted in Figure 4.18 (b) against different co-existent tension loads. From Figure 4.18 (a), it can be observed that the tension capacity had an increasing trend as the co-existent load in the vertical direction increased before the amplitude of 12 mm. At large vertical displacements (16 mm and 24 mm), co-existent shear loading weakened the tension capacity. A more severe weakening effect was observed with larger displacements. From Figure 4.18 (b), a similar but more obvious trend was found. The shear capacity increased at small lateral displacements (9 mm and 12 mm) along the increasing of co-existent tension force. At large lateral displacements (24 mm and 48 mm), the shear capacity dropped rapidly as co-existent tension increased. For instance, at the amplitude of 48 mm, the shear force dropped by 25% from 24 kN to 18 kN, when the co-existent shear force increased from 20 kN to 40 kN. An explanation for this trend is that, at small displacements, the hold-downs had not yet achieved their tension or shear capacity. Larger co-existent forces strengthened the contact between the nails and wood embedment, increasing the hold-downs' ability to undertake higher loads, whereas, at large displacements, the hold-downs had already reached their tension or shear capacity. Large co-existent forces weakened the nails and surrounding wood embedment, causing the load capacity to decrease.

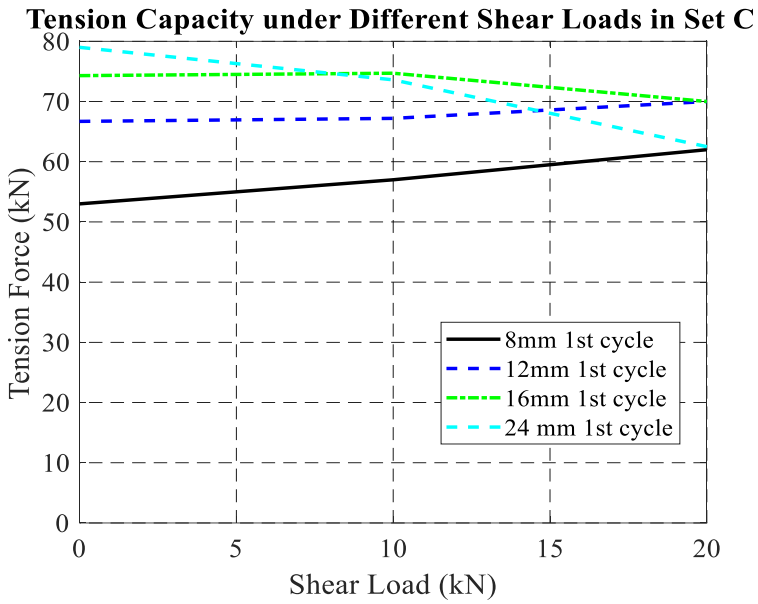

(a)

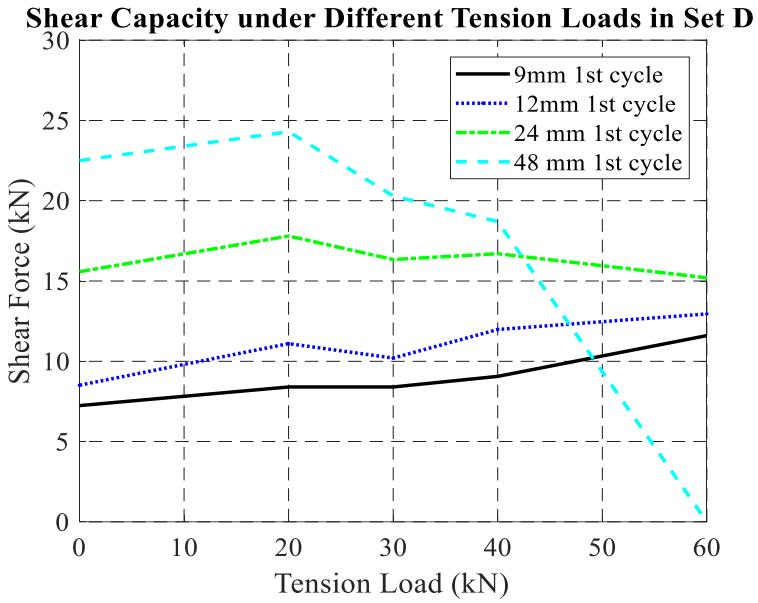

(b)

Figure 4.18 The coupling effect on load capacity during the first cycle of the target cyclic displacement peaks: (a) tension capacity under different shear loads in Set C; (b) shear capacity under different tension loads in Set D

To consider the coupling effect on energy dissipation, the total energy dissipation and energy dissipated from cyclic loading were plotted in Figure 4.19 for the two sets against the co-

existent load values. Figure 4.19 (a) shows that, in Set C, below the vertical amplitude of 16 mm, the total energy dissipation increased with increases in the co-existent shear load. With the co-existent shear load, the hold-downs failed to dissipate energy at larger amplitude (24 mm). Figure 4.19 (b) reveals that, between the 0 kN ~ 10 kN range, the co-existent shear load increased the energy dissipation from the tension force below the 16 mm amplitude. As the vertical displacement increased up to 16 mm, the strengthening effect became more obvious. One reason is that small co-existent shear force mitigated the gap between the nails and wood embedment to help the tension load dissipate energy. Then, at a larger amplitude (24 mm), the co-existent shear load altered to weaken the energy dissipation capacity from the tension force. This is because, at large amplitudes, the hold-downs began to fail. The higher co-existent shear load accelerated the failure of the connections, which decreased the accumulated energy dissipation. Between the 10 kN ~ 20 kN range, the co-existent shear load had little influence on the energy dissipation capacity from the tension force. As for Set D, Figure 4.19 (c) reveals that, at small lateral displacements (9 mm and 12 mm), as the co-existent tension load increased, the total energy dissipation likewise steadily increased. At the 0 kN ~ 20 kN range, the co-existent tension helped increase the total energy dissipation more significantly at larger amplitudes (24 mm and 48 mm). The reason for this is that, such co-existent tension loads strengthened the contact between the nails and wood embedment, which, in turn, enhanced the shear carrying capacity of the hold-downs. The hold-downs did not fail at the ends of the tests. Thus, more energy dissipation was accumulated at larger amplitudes. At the 20 kN ~ 60 kN range, the total energy dissipation dropped rapidly as the co-existent tension force increased, since such large co-existent tension loads caused the failure of the hold-downs. Figure 4.19 (d) is very similar to Figure 4.19 (c), revealing that, although a high co-existent tension

force was applied on the hold-downs, most of the energy was dissipated through the cyclic shear loading in Set D.

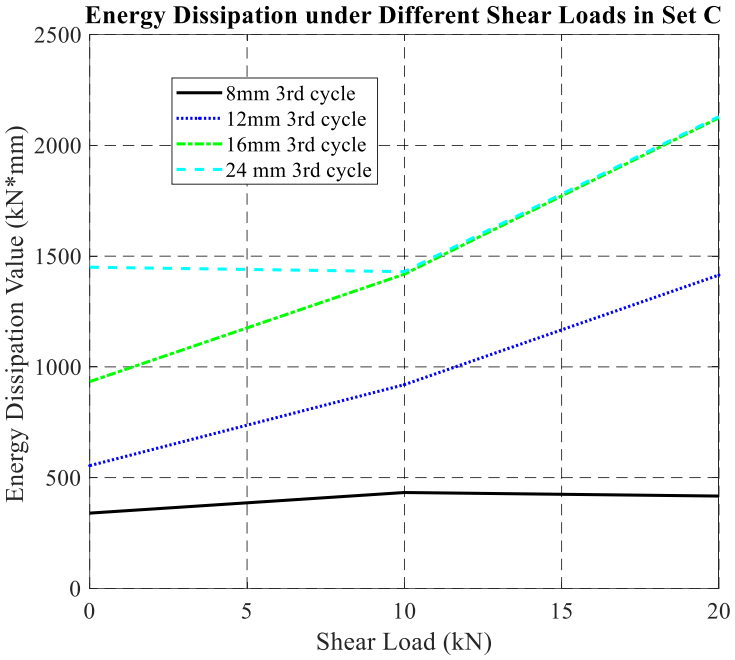

(a)

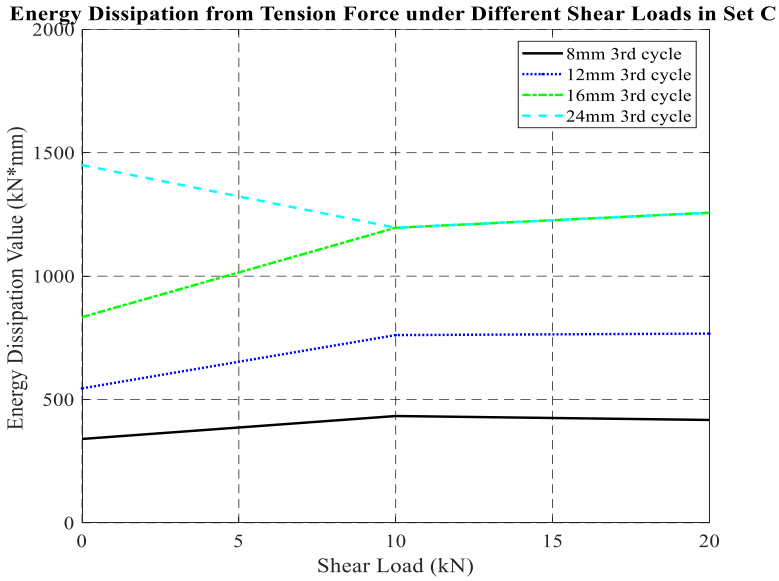

(b)

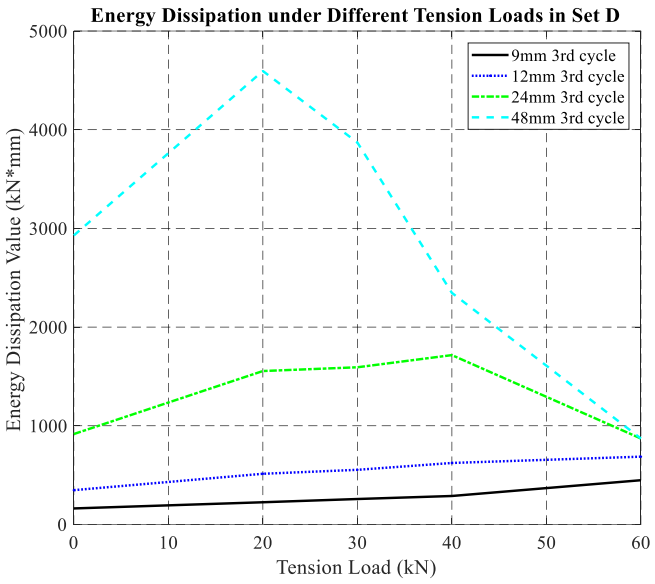

(c)

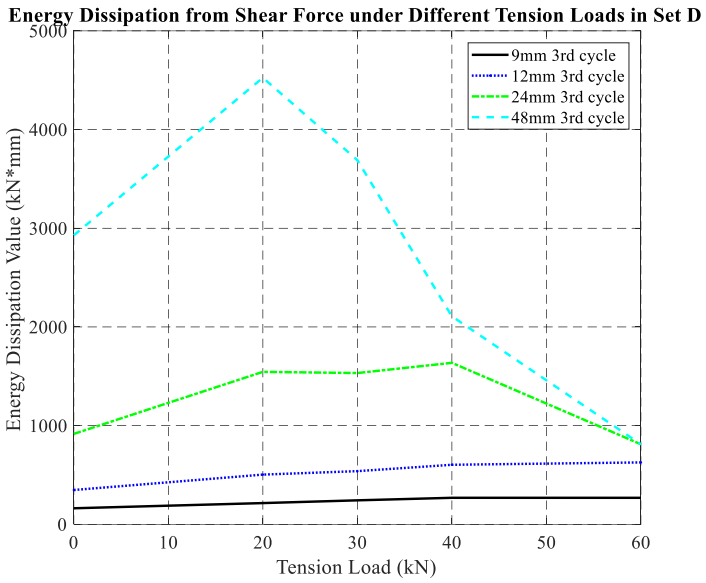

(d)

Figure 4.19 The coupling effect on energy capacity at the third cycle of the target cyclic displacement peaks: (a) energy dissipation under different shear loads in Set C; (b) energy dissipation from the tension force under different shear loads in Set C; (c) energy dissipation under different shear loads in Set D; (d) energy dissipation from the tension force under different shear loads in Set D

4.5 Summary

In this chapter, an innovative testing program was carried out to study the coupling effects of shear load and tension load on typical hold-down CLT connections. In Set C, the specimens were tested under monotonic/cyclic shear loading with three levels of co-existent shear loads (0 kN, 10 kN, and 20 kN). In Set D, the specimens were tested under monotonic/cyclic shear loading with five levels of co-existent tension loads (0 kN, 20 kN, 30 kN, 40 kN and 60 kN). The failure mode and load-displacement curve were discussed. Important connection properties, such as stiffness, strength, strength impairment, ductility, overstrength, equivalent damping ratios, strength degradation, and energy dissipation were evaluated according to the EN 12512 procedure (2006). The coupling effect on the load capacity and energy dissipation capacity was investigated. The results demonstrated that, generally, the co-existent shear force decreased the tension capacity, and the co-existent tension force decreased the shear capacity. Furthermore, the co-existent force significantly changed the hysteresis behaviour of the hold-downs under cyclic loading.

For Set C, a greater co-existent shear load caused more brittle failure modes, especially steel plate torsion and nail pullout. Co-existent shear load weakened the axial loading capacity. The average values of K_{el} , F_{yl}, v_{yd}, F_{max}, v_{max}, F_u, and v_u decreased by 19.7%, 5.8%, 2.9%, 5.4%, 11.6%, 12.9%, and 4.0% from 0 kN to 20 kN, respectively. A small co-existent shear load (10 kN) showed minor influence on the tension capacity. For a large co-existent shear load (20 kN), the shear capacity in the cyclic tests dropped significantly, especially for the last few cycles at the maximum vertical displacement of 16 mm (17.5%). At small displacements (below 16 mm), a small co-existent shear load (10 kN) increased the energy dissipation from the tension force since it mitigated the gap between the nails and wood embedment to help the tension load dissipate energy; a high co-existent shear load (20 kN) had little influence on the energy dissipation capacity

from the tension force. At a larger amplitude (24 mm), when the hold-downs were about to fail, the co-existent shear load altered to weaken the energy dissipation capacity from the tension force since it accelerated the failure of the connections.

For Set D, a greater co-existent tension load caused more brittle failure modes such as nail breakage. A co-existent axial load strengthened the shear loading capacity at small displacements (below 24 mm). The average values of K_{el} and F_{yl} in shear increased by 55.2% and 43.4% from 0 kN to 60 kN, respectively. The average values of F_{max} and F_u increased by 25.3% and 20.3% from 0 kN to 30 kN, and then decreased by 12.1% and 16.6% from 30 kN to 60 kN. This is because small co-existent forces (20 kN and 30 kN) improved the contact between the nails and surrounding wood embedment whereas large co-existent forces (40 kN and 60 kN) crushed the surrounding wood embedment, causing the load capacity to decrease. At large displacements (24 mm and 48 mm), the shear capacity dropped rapidly as the co-existent tension increased. The co-existent tension force helped increase the energy dissipation at small displacements (below 24 mm). Large co-existent tension forces (40 kN and 60 kN) decreased the energy dissipation at large displacements (24 mm and 48 mm).

An insightful finding is that, in the hold-down connections, the nails travelling in the gap within the wood embedment received resistance due to the co-existent force in the perpendicular direction under bi-axial loading, which changed the hysteresis behaviour and caused the coupling effect, including strength degradation, reloading stiffness degradation, and unloading stiffness degradation.

The bi-axial tests provided a more realistic way than uniaxial tests to understand the behaviour of hold-down connections in CLT structures under dynamic loading. This chapter gave a mechanism-based explanation for bi-axial behaviour. Based on the proposed principle, a finite-

element based numerical model, called pseudo-nail model, which employs a protocol-independent nail connection algorithm, was constructed, which can fully address the characteristics of CLT connections, including strength degradation, unloading and reloading stiffness degradation, the pinching effect and the coupling effect. The mechanism-based model will provide a more accurate means for studying the structural behaviour of CLT structures.

Chapter 5: Model Development of CLT Connections under Bi-axial Loading

5.1 Introduction

In the past decades, Cross-Laminated Timber (CLT) has been widely used in such load bearing components as walls and floors due to its high stability and loading capacity. Numerous experimental tests has been conducted on CLT structural performances (Dujič *et al.*, 2004; Dujic *et al.*, 2006; Ceccotti and Follesa, 2006; Dujic *et al.*, 2008; Ceccotti, 2008; Popovski *et al.*, 2010; Flatscher and Schickhofer, 2011; Okabe *et al.*, 2012; Ceccotti *et al.*, 2013; Pei *et al.*, 2013; Pei *et al.*, 2014; Popovski and Gavric, 2015; Ganey, 2015; Piazza *et al.*, 2015; Pei *et al.*, 2016; Shahnewaz *et al.*, 2017). These tests revealed that the connections anchoring CLT panels with foundations and walls are the critical elements that govern the structural response. The non-linearity of the connection is of key importance to design safe CLT structures. For such connections, one typical assumption is that, hold-downs take the tension force to resist the overturning moment, while angle brackets take the shear force to resist the lateral force. Under such assumptions, several CLT connections have been assessed through monotonic and cyclic tests, all only uniaxial loaded (Rinaldin *et al.*, 2013; Schneider *et al.*, 2013; Tomasi and Smith, 2014; Benedetti *et al.*, 2016).

However, recent tests of CLT panels under cyclic loading have demonstrated that both hold-downs and angle brackets undertake uplift and slip resistance (Gavric et al., 2011). Moreover, those forces are coupled on the connections, deteriorating their mechanical properties and seismic capacity, which questions the safety and rationality of the current design methods. To investigate such coupling effects, monotonic and cyclic tests of CLT connections have been conducted under co-existent shear and tension loads (Liu and Lam, 2016; Pozza *et al.*, 2017; Liu and Lam, 2018; Liu and Lam, 2019).

As for the numerical models, several approaches have been proposed to investigate the nonlinearity of the CLT connections under different loading protocols. The first approach is to consider the CLT connections as macro elements. Under this category, Folz and Filiatrault (2001) proposed a ten-parameter model which adopted a depredating backbone curve for strength and stiffness degradation. Lowes *et al.* (2004) simulated the hysteretic behaviour of the CLT assemblies using a model originally proposed for reinforced concrete beam-column joints to consider the pinching effect. Ceccotti *et al.* (2008) used semirigid elements with rotational and translational degrees of freedoms to model the CLT connections. This model was effective in predicting a structure's global response, but cannot fit the hysteretic behavior, strength impairment, and stiffness impairment for connections. To improve modeling accuracy, empirical models fitting the responses from specific loading protocols to experimental data were developed. Pozza *et al.* (2009) considered the steel connectors as a group of springs and dampers, using an equivalent damping coefficient to characterize the nonlinear behaviour of the springs. This model cannot take the degradation and post-peak softening into account. Fragiacomo *et al.* used multilinear elastic springs to model the connections in SAP2000 (Fragiacomo *et al.*, 2011; Fragiacomo and Rinaldin, 2011). This model is effective for monotonic nonlinear analysis but accurate cyclic characterization of the connections cannot be implemented. A more sufficient empirical model, Pinching4 material in OpenSees was used to study CLT connections in (Shen *et al.*, 2013; Liu and Lam, 2014; Zhang *et al.*, 2016) by calibrating the piecewise linear curves to fit the experimental data derived from connection tests. A finite-element based model was proposed by Rinaldin *et al.* (2013) to consider the CLT connections as nonlinear hysteretic multispring elements. The multispring has hysteretic behaviour, which differs for each degree of freedom, taking account of the nonlinear hysteretic behaviour, post-peak behaviour, strength and stiffness degradation,

pinching behaviour, interactions between the axial and shear resistance of the connectors, and influence of friction. Pozza *et al.* (2017) used this model to consider the coupled axial-shear effects of CLT connections. Those models have limitations and inherent uncertainties in their applicability to other protocols, and to seismic loading in particular. It is recognized that the shear wall response in cyclic loading depends on the test protocols. Although these models can be fit quite accurately into specific loops from cyclic loading, it remains questionable whether the fitted curves would provide a good representation of CLT connections under other loading protocols. Additionally, empirical models can be incorporated into applications but provide little aid in understanding the fundamental mechanisms of CLT connections under complex loading.

The second approach is using mechanism-based micro elements to consider the CLT connections. Because the behaviour of a CLT connection is mostly governed by that of the nail connections, the hysteretic responses from a CLT connection and a nail connection show strong similarities in terms of their strength/stiffness degradation and pitching effect. Hence, the CLT connections can be modelled as if it was a single nail connection, i.e, pseudo-nail (Gu and Lam, 2004). Using this pseudo-nail approach, Li and Lam (2009) studied diagonal-braced timber walls, Li *et al.* (2009) studied the seismic reliability of diagonal-braced walls and structural-panel-sheathed walls, and Li *et al.* (2014) studied the seismic performance of timber-steel hybrid structures. In this approach, the nonlinear behaviour of connections and walls is predicted through nonlinear analysis conducted at the fastener level using the HYST algorithm. As a finite-element detailed nail model, this algorithm can capture the hysteresis behaviour of timber connections using metal fasteners, based on the basic elastoplastic stress-strain relationship of the connector material and a simple presentation of the nonlinear behaviour of the wood embedment medium. This approach has the advantage of being based on the equivalent mechanical properties of the

nail fasteners, steel plates, and surrounding wood medium of a connection or wall, which helps in understanding the mechanisms under complex loading.

The original HYST algorithm was proposed and adopted to calculate the hysteretic behaviour of timber connections using metal fasteners (Foschi *et al.*, 2000). Li *et al.* (2011) modified this algorithm to improve its representation of strength and stiffness degradation. Key features of the improved algorithm include automatically tracking the formation of gaps between the nails and the wood, and the strength degradation and reloading stiffness degradation of the wood embedment. Later on, Lim *et al.* (2017) modified the algorithm and embedded a more mechanistically sound withdrawal model with consideration of the displacement compatibility between the movement of the nail and the resisting wood medium.

In this chapter, a gap size factor and an unloading stiffness degradation index were introduced into the HYST algorithm to fully address the hysteresis behaviour of CLT connections under bi-axial loading, providing sufficient explanation of the coupling effect. It first discussed the base models and the proposed model. Then a parameter study was followed.

5.2 Modeling approach

The CLT connections under bi-axial loading were simulated as pseudo-nail models using the HYST algorithm so as to take into account the coupling effect. As a micro-modeling approach, the pseudo-nail model has three parts: the nail, sheath, and wood embedment, which can represent the group of nails, steel plate of the hold-down/angle bracket, and CLT wood panel in the CLT connections, respectively. The HYST algorithm was modified to incorporate features to characterize the strength degradation, unloading stiffness degradation, reloading stiffness degradation, and pinching effect of typical timber connections. Details about the model and algorithms are described as below.

5.2.1 Pseudo-nail model

The shapes of the load deformation curve for individual nails and that of the connectors with fasteners have many similarities, which can be explained since the structural response of the CLT connections is governed by the characteristics of the nails. The effects of all the nail deformations are imposed together to exhibit an overall load-displacement curve for the CLT connections. Thus, it is possible to represent a CLT connection with a mechanics-based analog as a single pseudo-nail. Figure 5.1 (a) shows the nail connector model. Given a lateral force of F on the covering sheath, the head of the nail will have a displacement of Δ. As well, the shank of the nail experienced non-linear deformation within the surrounding wood embedment. Figure 5.1 (b) and (c) present angle bracket and hold-down connection as a pseudo-nail, respectively. The steel plate of the angle bracket/hold-down is considered as the equivalent sheath. All nails are grouped as one pseudo-nail and the CLT panel is considered as the equivalent wood embedment.

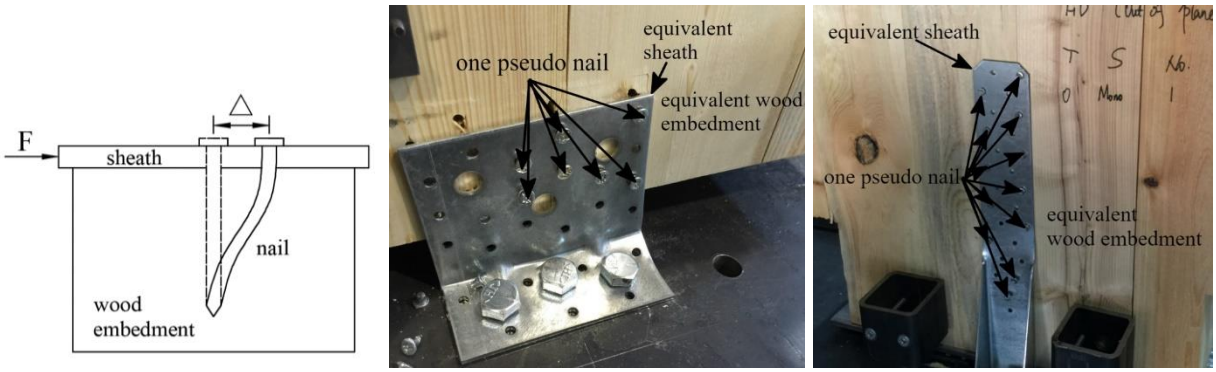

(a) (b) (c)

Figure 5.1 (a) the nail connector model; (b) the pseudo nail description of angle bracket connection; (c) the pseudo nail description of hold-down connection

5.2.2 Original HYST algorithm

The original HYST algorithm was used to calculate the nail connector model as shown in Figure 5.2.

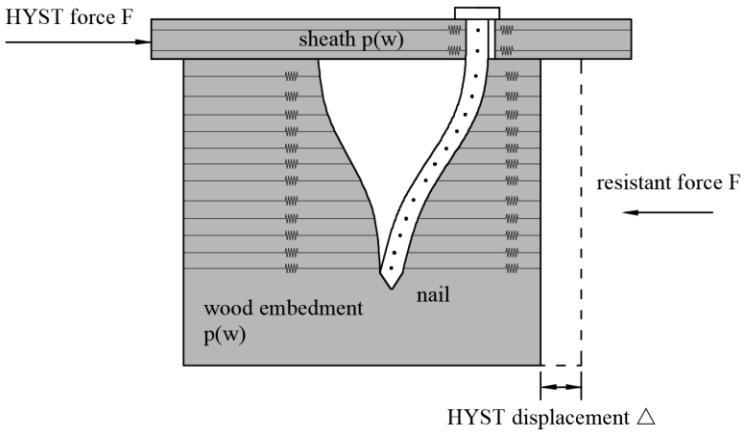

Figure 5.2 The schematics of the HYST nail connection model

In HYST, the nail shank is modelled as elastoplastic steel beam elements with strain hardening considered, with each of its nodes having five degrees of freedoms. The hysteresis of the beam element is shown in Figure 5.3. Normal stress ($\sigma(\varepsilon)$) changes linearly with normal strain (ε) at the modulus of elasticity (E) until it reaches either its positive or negative limits determined by the yield strength (σ_y), E, and coefficient μ. Then, the stress changes at a slope of μE until the direction of the strain alters. Since μ is close to zero, the positive and negative y-intercepts are considered to be $+\sigma_y$ and $-\sigma_y$. Accordingly, the stress corresponding to a strain ε is calculated following Eq. 5.1, where σ_0 and ε_0 are the stress and strain from the previous step.

$$\sigma(\varepsilon)=\begin{cases}\sigma_0 \quad \text{if} \quad \varepsilon-\varepsilon_0=0 \\ \min\begin{cases}\sigma_0+E(\varepsilon-\varepsilon_0)\\ \sigma_y+\alpha E\varepsilon\end{cases} \quad \text{if} \quad \varepsilon-\varepsilon_0>0 \\ \max\begin{cases}\sigma_0+E(\varepsilon-\varepsilon_0)\\ -\sigma_y+\alpha E\varepsilon\end{cases} \quad \text{if} \quad \varepsilon-\varepsilon_0<0\end{cases} \qquad \text{(Eq. 5.1)}$$

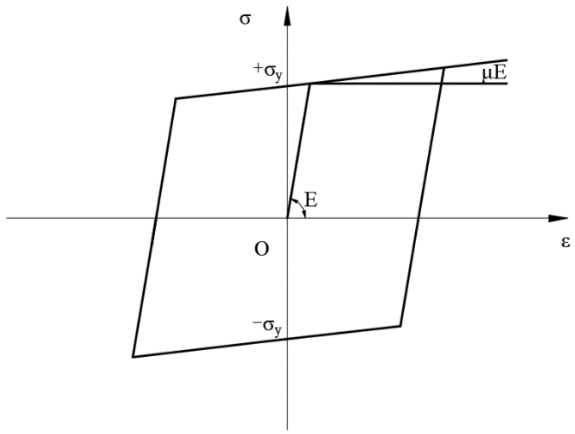

Figure 5.3 The hysteresis of the beam element

The wood embedment and covering sheath are both modelled as a bed of continuous, compression-only nonlinear springs of different properties, smeared along the nail shank. Given a HYST force, *F*, on the sheath, the wood embedment provides the resistant force *F* and the head of the nail bears a HYST displacement *Δ*. The relationship between the pressure *p(w)* and the deformation of the sheath and wood embedment *w* in the embedment properties in original HYST algorithm is presented in Figure 5.4.

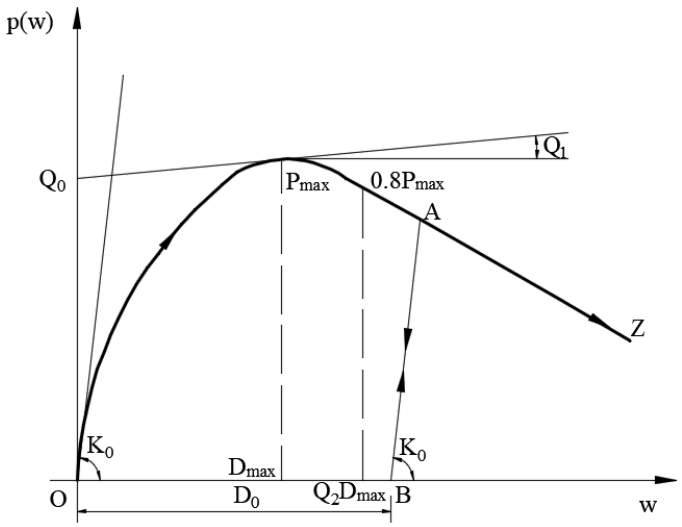

Figure 5.4 The embedment properties in the original HYST algorithm

The displacement *w* begins at *O* with an initial stiffness of K_0. It reaches the peak value P_{max} at D_{max} along the first exponential curve. After that, it follows the second exponential curve with a softening trend towards *Z*. When unloading from *A* to *B*, the unloading stiffness of the spring is the initial stiffness K_0. From *B* to *O*, the unloading stiffness of the spring is 0, which indicates that the spring does not provide resistance in the gap D_0. The nail shank is released from the embedment surface and travels through this gap. When reloading from *O* to *B*, the reloading stiffness of the spring is 0. The gap D_0 remains and the shank travels through it until it reaches the embedment again at *B*. From *B* to *A*, the reloading stiffness is also the initial stiffness K_0. After it reaches *A*, it continues to follow the backbone curves to *Z*. Table 5.1 provides descriptions of the five parameters to define this force-displacement relationship.

Table 5.1 Descriptions of the embedment property parameters in the original HYST algorithm

Parameter	Description
K_0	Initial stiffness
Q_0	Intercept of the asymptote at the maximum compressive response
Q_1	Slope of the asymptote at the maximum compressive response
Q_2	Postpeak decay factor
D_{max}	Displacement at the maximum compressive response

Using these five parameters, the force-displacement curve is represented in Eq. 5.2,

$$\begin{cases} p(w) = (Q_0 + Q_1 w)(1 - e^{-K_0 w/Q_0}) & \text{if } w \le D_{max} \\ p(w) = P_{max} e^{Q_3 (w - D_{max})^2} & \text{if } w > D_{max} \end{cases} \quad \text{(Eq. 5.2)}$$

where $P_{max} = (Q_0 + Q_1 D_{max})(1 - e^{-K_0 D_{max}/Q_0})$ and $Q_3 = \log(0.8)/[(Q_2 - 1.0)D_{max}]^2$.

For a node *j* along the nail subjected to the cyclic displacement history given in Figure 5.5 (a), when the node is transversely displaced by x_1, the wood embedment acquires the same displacement x_1. The corresponding response $p(x_1)$ at x_1 is obtained following the loading path in the wood embedment response-displacement relationship, as shown in Figure 5.5 (b). Then, as the

node moves inversely towards a transverse displacement of x_2, the compressed wood medium unloads following the dashed line with a slope of initial stiffness K_0. After the wood medium fully recovers, the embedment response reaches zero, resulting a residual gap D. Accordingly, the embedment response $p(x_2)$ at x_2 becomes zero. When the loading direction changes again and the point transversely displaces to x_3, the reloading of the wood medium begins from D until it reaches x_3. The embedment response $p(x_3)$ initially follows the dashed line before it reaches the embedment curve, whereupon it follows the embedment curves. The response of the wood medium under loading, unloading, and reloading is dependent on the residual gap D.

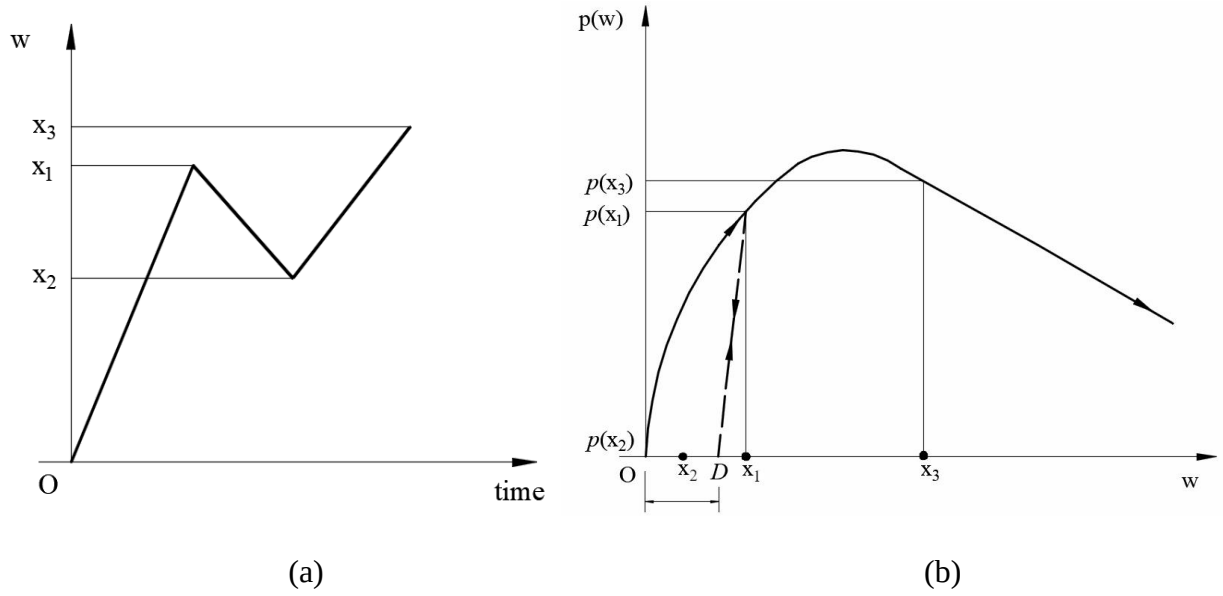

Figure 5.5 (a) cyclic displacement history; (b) the response-displacement relationship of wood embedment

Under cyclic loads, the residual gap D can be either positive or negative, depending on the loading direction at different points along the nail against the wood medium. Therefore, two residual gap values, $D+$ and $D-$, are assigned to each node. Figure 5.6 illustrates the positive and negative residual gaps associated with node j.

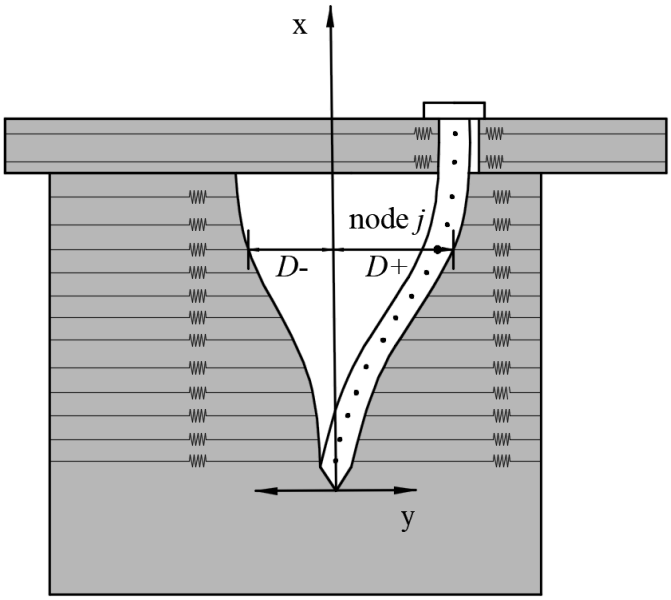

Figure 5.6 Positive and negative residual gaps associated with a point on a nail

The embedment response in terms of *p(w)*, *dp/dw*, and *D* are expressed in Eq. 5.3. In the algorithms, *D* represents the residual gap at the current loading step while D_0 represents the residual gap from the previous step.

$$
\begin{cases} p(w) = 0 \\ dp/dw = 0 \\ D = D_0 \end{cases} \qquad if \quad w < D_0
$$

$$
\begin{cases} p(w) = 0 \\ dp/dw = K \\ D = D_0 \end{cases} \qquad if \quad w = D_0
$$

$$
\begin{cases} p(w) = \min \begin{cases} P_1 = (Q_0 + Q_1 w)(1 - e^{-K_0 w/Q_0}) \\ P_2 = K_0 (w - D_0) \end{cases} \\ dp/dw = \begin{cases} Q_1(1 - e^{-K_0 w/Q_0}) + \dfrac{K_0 (Q_0 + Q_1 w) e^{-K_0 w/Q_0}}{Q_0} & if \ p(w) = P_1 \\ K_0 & if \ p(w) = P_2 \end{cases} \qquad if \quad D_0 < w < D_{\max} \\ D = w - p(w)/K_0 \end{cases}
$$

$$
\begin{cases} p(w) = \min \begin{cases} P_1 = P_{\max} e^{Q_3 (w - D_{\max})^2} \\ P_2 = K_0 (w - D_0) \end{cases} \\ dp/dw = \begin{cases} 2 P_1 Q_3 (w - D_{\max}) & if \ p(w) = P_1 \\ K_0 & if \ p(w) = P_2 \end{cases} \qquad if \quad w > D_{\max} \\ D = w - p(w)/K_0 \end{cases}
$$

(Eq. 5.3)

5.2.3 Modified HYST algorithm

The modified HYST algorithm by Li *et al.* (2011) had two key improvements: first, it reduced the degrees of freedom of the nodes from five to three, which accelerated the computational speed without sacrificing its accuracy; second, it revised the reloading assumption of the original HYST algorithm and added a reloading degradation index α to model the strength degradation and reloading stiffness degradation. With such features integrated, the modified HYST algorithm was enhanced to capture the hysteresis behaviour of the nail connections during cyclic loading.

In the modified HYST algorithm, the relationship between the pressure *p(w)* and the deformation of the sheath and wood embedment *w* in the embedment properties is shown in Figure 5.7.

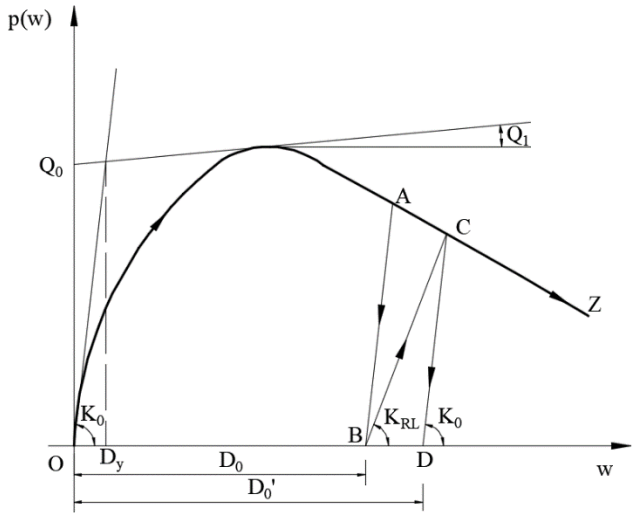

Figure 5.7 Embedment properties in the modified HYST algorithm

It is assumed that reloading from *B* to C follows another straight line with reduced stiffness K_{RL}. Subsequent unloading from *C* follows the original stiffness K_0 until *D* is reached, resulting in a new gap of magnitude D_0'. A reloading degradation index α is used to account for both the strength degradation and reloading stiffness degradation. The value of α is between 0 and 1. The reloading stiffness K_{RL}, which is related to the initial stiffness K_0 and the gap size D_0, is represented in Eq. 5.4,

$$\begin{cases} K_{RL} = K_0 & \text{if } D_0 \le D_y \\ K_{RL} = (D_y / D_0)^{\alpha} K_0 & \text{if } D_0 > D_y \end{cases} \qquad \text{(Eq. 5.4)}$$

where $D_y = Q_0 / (K_0 - Q_1)$, which corresponds to the yielding deformation given by the intersection of the original slope and the asymptote.

The embedment response in terms of *p(w)*, *dp/dw*, and *D* are expressed in Eq. 5.5. In the algorithms, *D* represents the residual gap at the current loading step while D_0, w_0, and P_0 represent the residual gap, displacement, and response from the previous step.

$$
\begin{cases}
p(w) = 0 \\
dp/dw = 0 \qquad\qquad if \quad w < D_0 \\
D = D_0
\end{cases}
$$

$$
\begin{cases}
p(w) = 0 \\
dp/dw = K \qquad\qquad if \quad w = D_0 \\
D = D_0
\end{cases}
$$

$$
\begin{cases}
p(w) = \begin{cases} P_0 + K_0(w - w_0) \;\; if \;\; p(w) > 0 \\ 0 \qquad\qquad\qquad if \;\; p(w) \le 0 \end{cases} \\
\qquad dp/dw = \begin{cases} K_0 \;\; if \;\; p(w) > 0 \\ 0 \quad if \;\; p(w) \le 0 \end{cases} \qquad\qquad if \quad D_0 < w < w_0 \\
\qquad D = w - p(w)/K_0
\end{cases}
$$

$$
\begin{cases}
p(w) = \min \begin{cases} P_1 = (Q_0 + Q_1 w)(1 - e^{-K_0 w/Q_0}) \\ P_2 = P_0 + (D_y/D_0)^{\alpha} K_0 (w - D_0) \end{cases} \\
dp/dw = \begin{cases} Q_1(1 - e^{-K_0 w/Q_0}) + \dfrac{K_0(Q_0 + Q_1 w)e^{-K_0 w/Q_0}}{Q_0} \quad if \;\; p(w) = P_1 \\ (D_y/D_0)^{\alpha} K_0 \qquad\qquad\qquad\qquad\qquad if \;\; p(w) = P_2 \end{cases} \qquad if \quad w > D_0 \;\; and \;\; w_0 < w < D_{\max} \\
\qquad D = w - p(w)/K_0
\end{cases}
$$

$$
\begin{cases}
p(w) = \min \begin{cases} P_1 = P_{\max} e^{Q_3 (w - D_{\max})^2} \\ P_2 = P_0 + (D_y/D_0)^{\alpha} K_0 (w - D_0) \end{cases} \\
dp/dw = \begin{cases} 2P_1 Q_3 (w - D_{\max}) \quad if \;\; p(w) = P_1 \\ (D_y/D_0)^{\alpha} K_0 \quad\;\; if \;\; p(w) = P_2 \end{cases} \qquad if \quad w > D_{\max} \\
\qquad D = w - p(w)/K_0
\end{cases}
$$

(Eq. 5.5)

5.2.4 Proposed HYST algorithm

From the CLT connection bi-axial loading experiments, it was found that, due to the co-existent force occurring in the perpendicular direction, the nails travelling through the gap encountered resistance. As shown in Figure 5.8 (a), when only shear force was applied, the nail could travel within the gap without resistance. But with the application of a co-existent tension force (Figure 5.8 (b)), pressure was placed on the nail shank from surrounding wood embedment. This pressure provided lateral resistance to the nail in the gap during unloading. Furthermore, a higher level of co-existent force caused increased resistance during unloading.

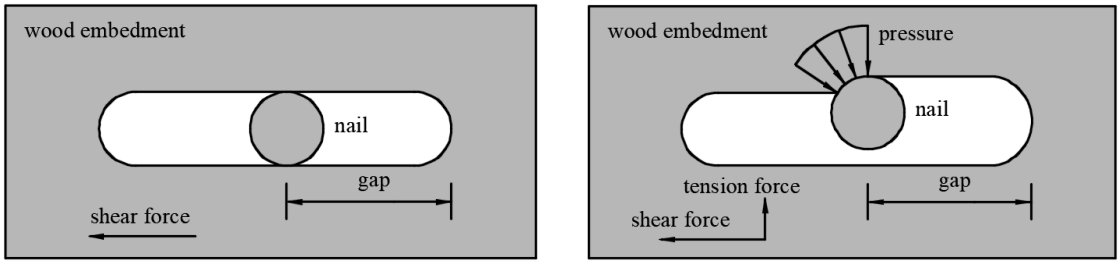

(a) (b)

Figure 5.8 A schematic section view of the nails in the wood embedment: (a) nail movement under shear force in the absence of a co-existent tension load; (b) nail movement under shear force with a co-existent tension load

To address such coupling effects, in the proposed HYST algorithm, a gap size factor β and an unloading stiffness degradation index γ were introduced into the modified HYST algorithm. The proposed algorithm was able to capture all features of the nail based connections under complex loading, including the strength degradation, reloading stiffness degradation, unloading stiffness degradation, and pinching effect.

In the proposed HYST algorithm, the relationship between the pressure *p(w)* and the deformation of the sheath and wood embedment *w* in the embedment properties is shown in Figure 5.9. It was noted that, in the CLT connections under bi-axial loading, the backbones of the force-

displacement curves also changed. This can be modelled by the change in the embedment property parameters for the equivalent wood embedment.

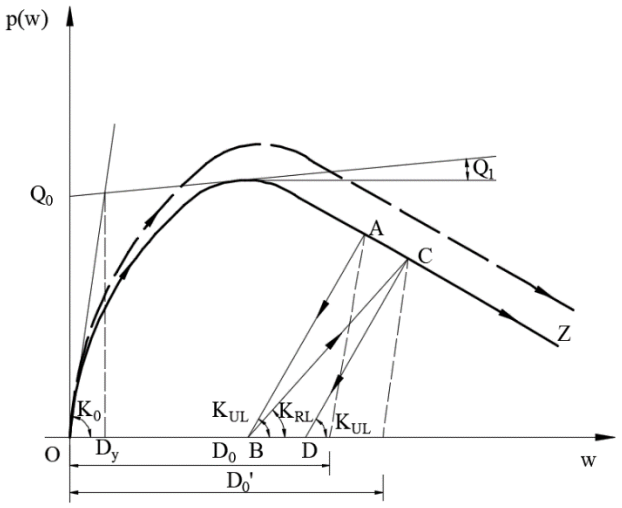

Figure 5.9 Embedment properties in the proposed HYST algorithm

When unloading from A, rather than following a straight line with an unloading stiffness of K_0 in the original HYST algorithm and modified HYST algorithm, the unloading curve follows another straight line with an unloading stiffness of K_{UL} until it reaches *B*. *B* is inside the gap D_0, which indicates the contribution of resistance during unloading. When reloading from *B*, the reloading stiffness K_{RL} is the same as that for the modified HYST algorithm. The proposed algorithm introduced a gap size factor β to indicate the position of *B*. The distance L_{OB} between *O* and *B* is calculated as $L_{OB} = \beta D_0$. An unloading degradation index γ is used to consider the unloading stiffness degradation. The value of γ is between 0 and 1. The unloading stiffness K_{UL}, which is related to the initial stiffness K_0 , the gap size D_0, and the reloading degradation index α, is represented in Eq. 5.6.

$$\begin{cases} K_{UL} = K_0 & \text{if } D_0 \le D_y \\ K_{UL} = (D_y / D_0)^{\alpha\gamma} K_0 & \text{if } D_0 > D_y \end{cases} \qquad \text{(Eq. 5.6)}$$

where $D_y = Q_0 / (K_0 - Q_1)$, which corresponds to a yielding deformation given by the intersection of the original slope and the asymptote.

The embedment response in terms of *p(w)*, *dp/dw*, and *D* are expressed in Eq. 5.7. In the algorithms, *D* represents the residual gap at the current loading step while D_0, w_0, and P_0 represent the residual gap, displacement, and response from the previous step.

$$
\begin{cases}
p(w) = 0 \\
dp/dw = 0 \\
D = D_0
\end{cases}
\qquad if \quad w < \beta D_0
$$

$$
\begin{cases}
p(w) = 0 \\
dp/dw = K \\
D = D_0
\end{cases}
\qquad if \quad w = \beta D_0
$$

$$
\begin{cases}
p(w) = \begin{cases} P_0 + K_0(w - w_0) & if \;\; p(w) > 0 \\ 0 & if \;\; p(w) \le 0 \end{cases} \\
dp/dw = \begin{cases} K_0 & if \;\; p(w) > 0 \\ 0 & if \;\; p(w) \le 0 \end{cases} \qquad if \quad \beta D_0 < w < w_0 \\
D = w - p(w)/K_0
\end{cases}
$$

$$
\begin{cases}
p(w) = \min \begin{cases} P_1 = (Q_0 + Q_1 w)(1 - e^{-K_0 w/Q_0}) \\ P_2 = P_0 + (D_y / D_0)^{\alpha\gamma} K_0 (w - D_0) \end{cases} \\
dp/dw = \begin{cases} Q_1(1 - e^{-K_0 w/Q_0}) + \dfrac{K_0(Q_0 + Q_1 w)e^{-K_0 w/Q_0}}{Q_0} & if \;\; p(w) = P_1 \\ (D_y / D_0)^{\alpha\gamma} K_0 & if \;\; p(w) = P_2 \end{cases} \qquad if \quad w > \beta D_0 \;\; and \;\; w_0 < w < D_{\max} \\
D = w - p(w)/K_0
\end{cases}
$$

$$
\begin{cases}
p(w) = \min \begin{cases} P_1 = P_{\max} e^{Q_3 (w - D_{\max})^2} \\ P_2 = P_0 + (D_y / D_0)^{\alpha\gamma} K_0 (w - D_0) \end{cases} \\
dp/dw = \begin{cases} 2P_1 Q_3 (w - D_{\max}) & if \;\; p(w) = P_1 \\ (D_y / D_0)^{\alpha\gamma} K_0 & if \;\; p(w) = P_2 \end{cases} \qquad if \quad w > D_{\max} \\
D = w - p(w)/K_0
\end{cases}
$$

(Eq. 5.7)

5.2.5 Model construction

Each nail can be divided into up to 50 beam elements. The cross-section of the beam can be rectangular, circular or annular. Each beam element possesses two nodes which can displace and rotate in the x-y plane (Figure 5.10). The beam element is modelled based on the Euler-Bernoulli theory incorporating von Karman strains which account for the contribution of the slope of the deflected beam to the axial strains. The strains are still assumed to be unaffected by shear deformation while the cross-section of the beam remains perpendicular to its primary axis. Thus, the strain at a distance y from the beam axis is expressed as Eq. 5.8 which is composed of three terms: axial strain, bending strain, and the strain due to the large slope of the deflected beam.

$$\varepsilon = \partial u/\partial x - y\cdot\partial^2 w/\partial x^2 + 1/2\cdot(\partial w/\partial x)^2 \qquad \text{(Eq. 5.8)}$$

Three degrees of freedom (DOF) are assigned to each node to describe its deformation: transverse displacement *w* (w), rotation *w′* (∂w/∂x), and axial displacement *u* (u). Also, Gauss integration points are assigned along the element length in the x-direction and over the cross-section in the y-direction to approximate the integrals.

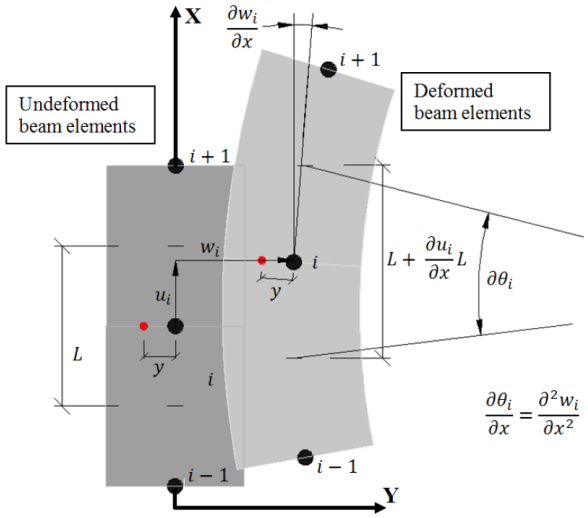

Figure 5.10 The deformations of two beam elements with three nodes (Lim et al., 2017)

The interaction between the nail elements and the wood medium springs under applied loads was formulated by applying the principle of virtual work. The total external work due to the applied lateral force *F* and virtual displacement at the location of the applied force is equal to the total work performed by the nail and the wood medium over the length (*L*), as shown in Eq. 5.9. The internal work of the nail is determined by the stress in the volume (*V*) over the virtual strain ($\delta\varepsilon$) while the internal work of the wood is determined by the response along the length (*L*) over the virtual displacement (δw).

$$\int_V \sigma(\varepsilon)\delta\varepsilon dv + \int_0^L p(|w|)(w/|w|)\delta w dx = F\delta w_{x=L} \quad \text{(Eq. 5.9)}$$

For each element with node *i* and node *j*, the vector of the DOFs matrix can be expressed as Eq. 5.10.

$$a = (w_i, w_i^{'}, u_i, w_j, w_j^{'}, u_j)^T \quad \text{(Eq. 5.10)}$$

High-order shape functions are used to approximate the displacements and their derivatives of the Gauss integration points along the element: for *u(x)*, C_1 continuity interpolation functions are used; for *w(x)*, and *w'(x)*, C_2 interpolation functions are used, which are written in Eq. 5.11.

$$w(x) = M_0 a, w'(x) = M_1^T a, u(x) = N_0 a, u'(x) = N_1^T a \quad \text{(Eq. 5.11)}$$

Thus, Eq. 5.9 can be written as Eq. 5.12:

$$\int_V \sigma(\varepsilon)(N_1 + M_1 M_1^T a)dv + \int_0^L p(|M_0^T a|)(M_0^T a/|M_0^T a|)M_0 dx = FM_{0|x=L} \quad \text{(Eq. 5.12)}$$

ψ is defined as the out-of-balance vector, which can be calculated with Eq. 5.13:

$$\psi = \int_V \sigma(\varepsilon)(N_1 + M_1 M_1^T a)dv + \int_0^L p(|M_0^T a|)(M_0^T a/|M_0^T a|)M_0 dx - FM_{0|x=L} \quad \text{(Eq. 5.13)}$$

And $\nabla\psi$ is the corresponding tangential stiffness matrix, which can be calculated with Eq. 5.14:

$$\nabla\psi = \partial\psi / \partial a = \int_V (d\sigma / d\varepsilon)(N_1 + M_1 M_1^T a)(N_1 + M_1 M_1^T a)^T + \int_V \sigma(\varepsilon) M_1 M_1^T + \int_0^L (dp / dw) M_0 M_0^T \quad \text{(Eq. 5.14)}$$

Thus, the global displacement vector *a* can be solved through Newton-Raphson iterations as Eq. 5.15:

$$a = a^* + [\nabla\psi^*]^{-1}[-\psi^*] \quad \text{(Eq. 5.15)}$$

where a^*, ψ^*, and $\nabla\psi^*$ are the global displacement vector, out-of-balance vector, and corresponding tangential stiffness matrix from the previous step.

The displacement and force convergence criteria are expressed in Eq. 5.16 at the i^{th} iteration.

$$\| a_{i+1} - a_i \| / \| a_i \| \leq Tol_{displacement}, \| \psi \| \leq Tol_{force} \quad \text{(Eq. 5.16)}$$

where $Tol_{displacement}$ and Tol_{force} are the values of tolerant displacement and force set by the user.

For any given displacement history, the response of the model can be calculated through the process illustrated in the flow chart in Figure 5.11.

In the first module, the variables are defined, the input information and displacement history are imported, and the program obtains the shape functions and initializes the variables based on build-in codes.

In the second module, the stress, strain, and stiffness of each nail element and the response, gap, and stiffness of the wood embedment at each node are calculated. The global tangential stiffness matrix $\nabla\psi$ and the out-of-balance vector ψ are constructed. After the boundary conditions are introduced. The global tangential stiffness matrix $\nabla\psi$ is decomposed through Cholesky decomposition. For alterations in the displacement vector Δa, if the convergence is

reached and the searching displacement is equal to the current displacement, the data will be recorded for the variables.

In the checking module, several procedures are added to improve the robustness of the program. If the global tangential stiffness matrix $\nabla\psi$ fails to be decomposed, the displacement and gap information will be set as previously converged values. If the convergence is not arrived at, additional iterations will be carried out. At the end of each step, the displacement vector, stress, strain, and gap information will be updated before the next step.

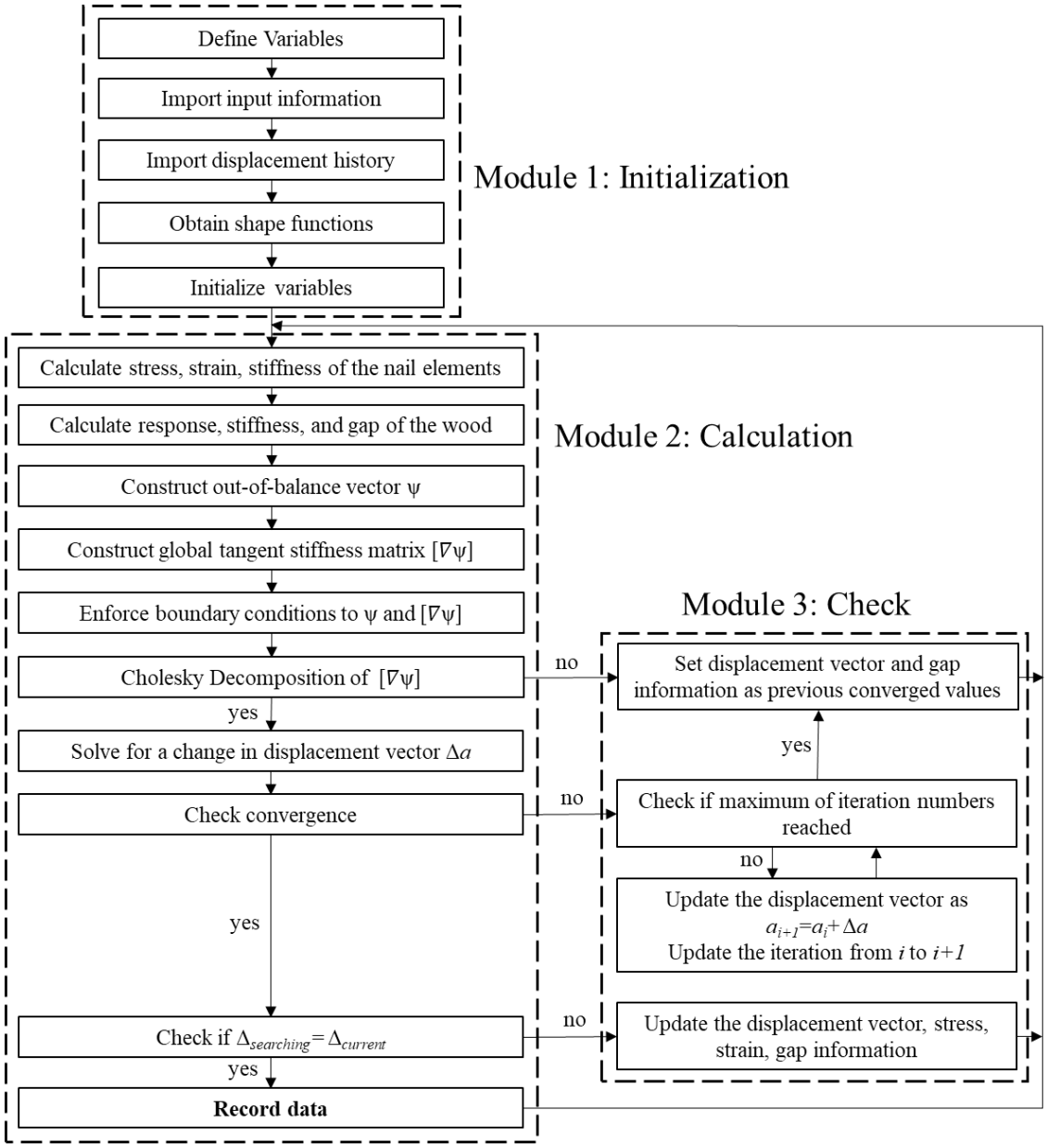

Figure 5.11 A flow chart of the model procedures

The proposed algorithm has been compiled using the Fortran compiler in Intel Parallel Studio XE 2018. The longest duration of the test protocol, which is the shear cyclic test of the hold-down connections under the co-existent tension force, requires approximately 20 seconds to run on a computer with a quad-core CPU and 8 GBs of memory.

5.3 Parameter discussion

Nine key parameters are presented in this model, specifically, the nail diameter (D_N), Q_0, Q_1, Q_2, K_0, D_{max}, α, β, and γ; these determine the hysteresis loops and are discussed in this section to assess their influence on the model.

The initial parameters for the "standard" model were 8 mm (D_N), 0.16 kN/mm (Q_0), 0.20 kN/mm^2 (Q_1), 1.3 (Q_2), 0.31 kN/mm^2 (K_0), 35 mm (D_{max}), 0.2 (α), 1.0 (β), and 0 (γ), which are the parameters for the angle bracket pure shear test. A cyclic protocol shown in Figure 5.12 was applied to this model. The hysteresis loop curves from the model is shown in Figure 5.13.

Cyclic Loading Phase	Displacement rate 0.8 mm/s
No. of Cycle	Peak displacement (mm)
1	2
1	4
3	6
3	8
3	16
3	32

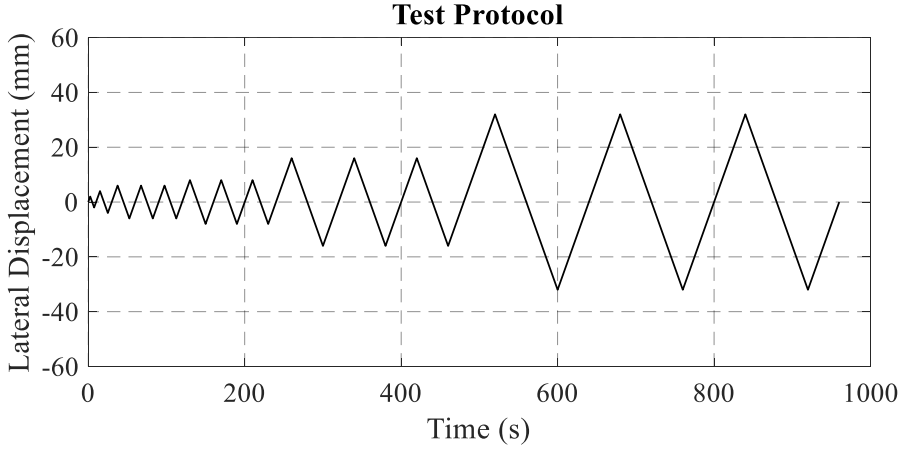

Figure 5.12 Protocol for the parameter discussion

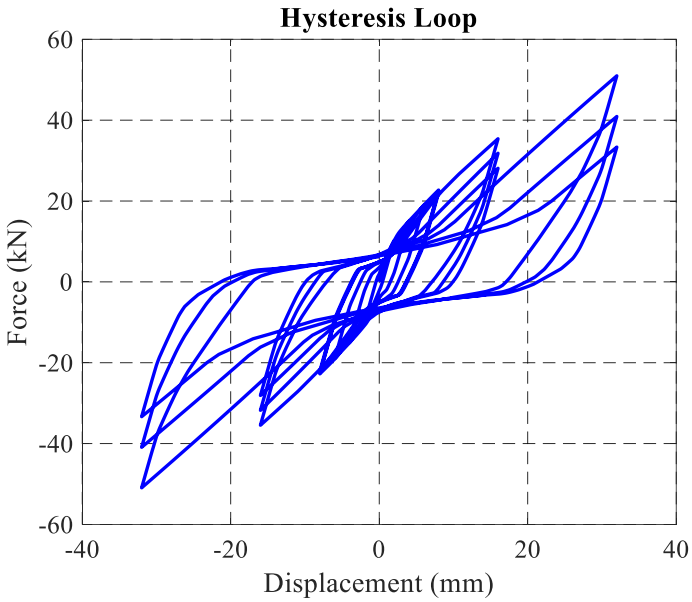

Figure 5.13 Hysteresis loop curves from the "standard" model

5.3.1 Nail diameter D_N

Four different values of nail diameter D_N, 6 mm, 8 mm, 10 mm, and 12 mm, were input into the model while the remaining parameters were retained as their initial values. The hysteresis loops are shown in Figure 5.14. It can be observed that the influence of the nail diameter was mostly on the amplitudes of the force values. Larger diameters caused greater forces, which follows the common sense schema that stronger nails can undertake greater loads.

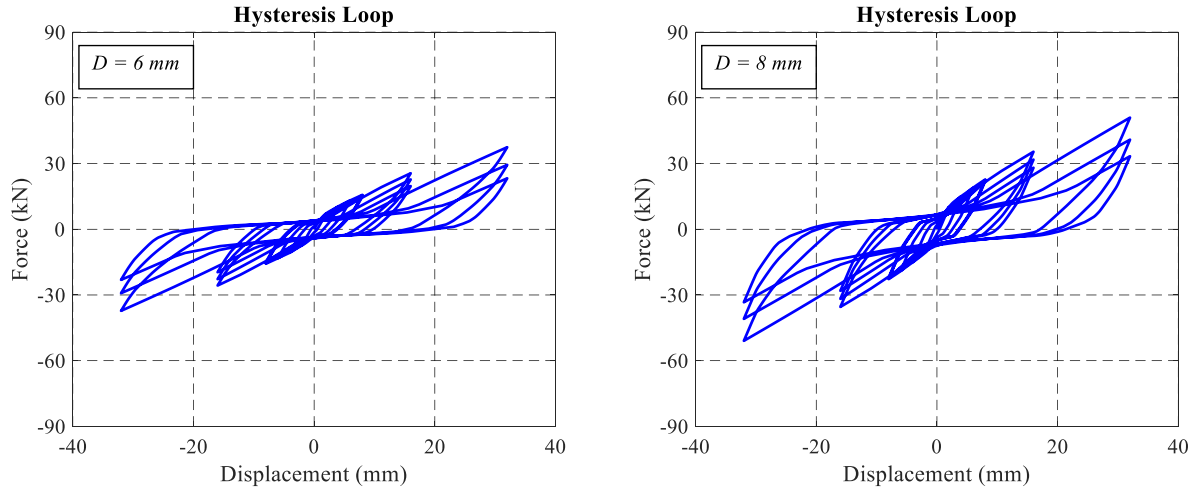

(a) (b)

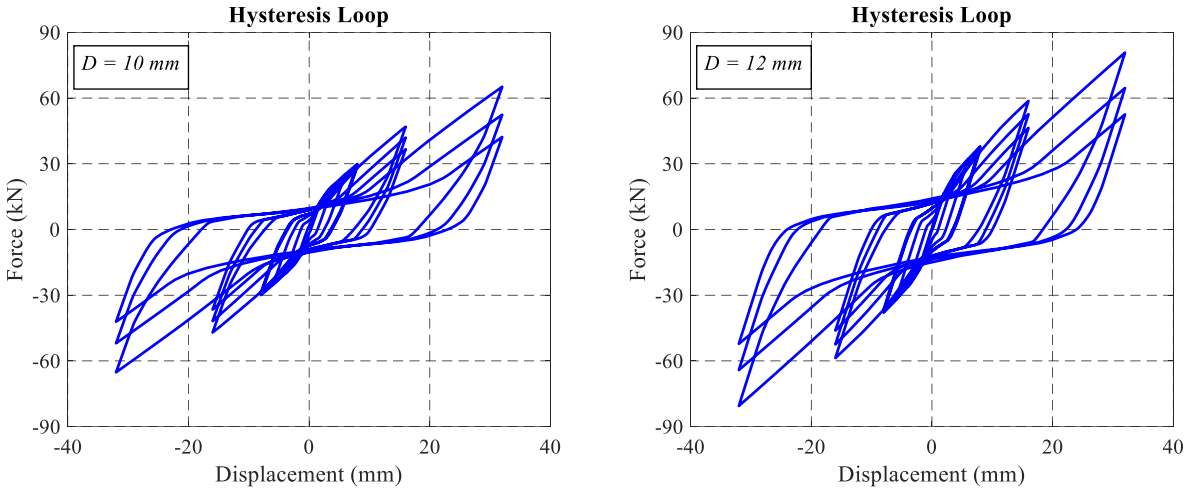

(c) (d)

Figure 5.14 Hysteresis Loops with diverse nail diameters: (a) 6 mm; (b) 8 mm; (c) 10 mm; (d) 12 mm

5.3.2 Intercept of the asymptote at the maximum compressive response Q_0

Four different values for the intercepts of the asymptote at the maximum compressive response Q_0, 0.04 kN/mm, 0.16 kN/mm, 0.64 kN/mm, and 2.56 kN/mm, were input into the model while the remaining parameters were remained as initially established. The hysteresis loops are shown in Figure 5.15. The figures imply a trend in which the hysteresis curves were "stretched" in the diagonal direction as Q_0 increased. A large Q_0 reduced the degradation and made the model more "elastic and stiff".

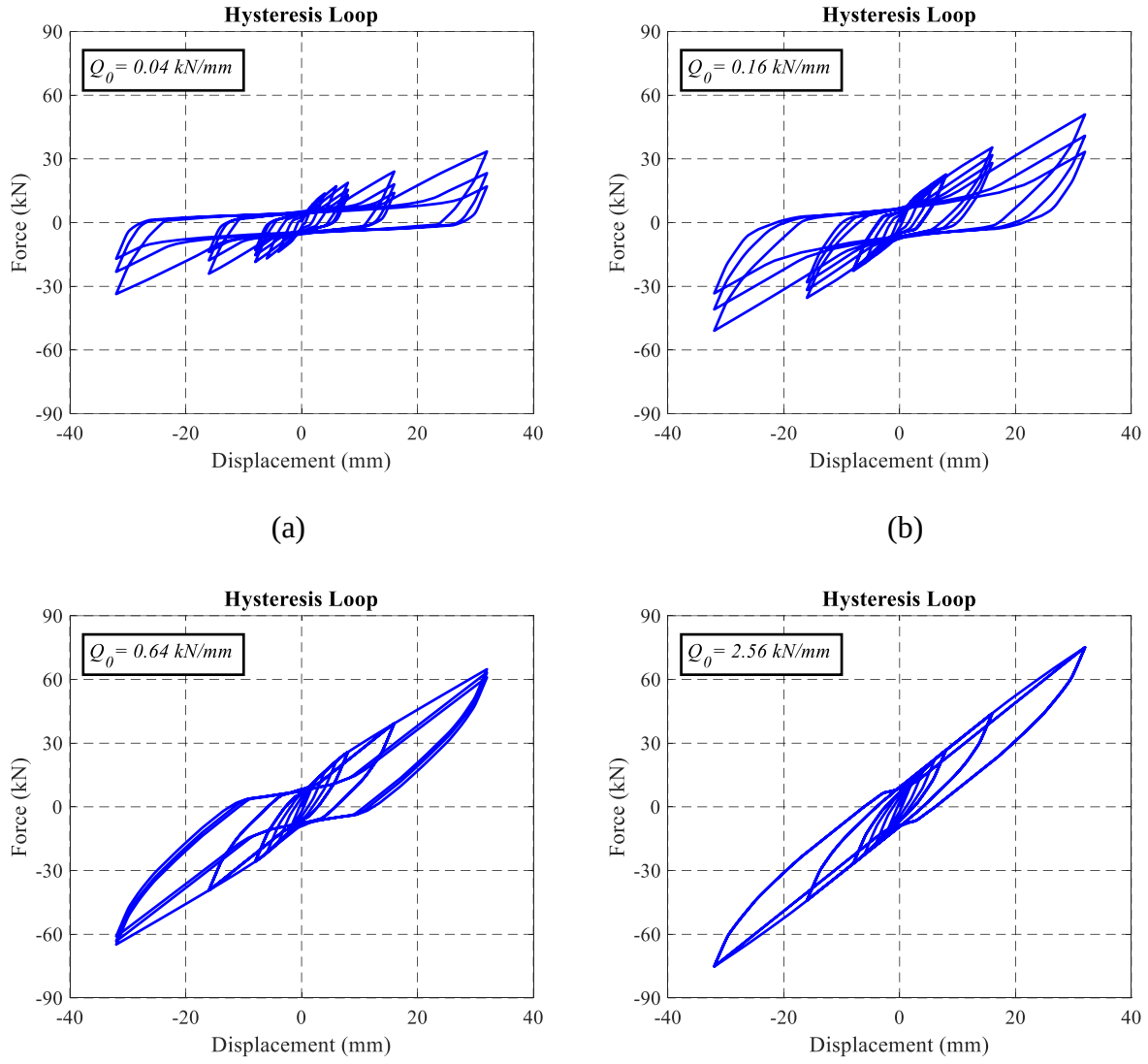

Figure 5.15 Hysteresis Loops with diverse intercepts of the asymptote at the maximum compressive response: (a) 0.04 kN/mm; (b) 0.16 kN/mm; (c) 0.64 kN/mm; (d) 2.56 kN/mm

5.3.3 Slope of the asymptote at the maximum compressive response Q_1

Five different values for the slopes of the asymptote at the maximum compressive response Q_1, 0.05 kN/mm^2, 0.10 kN/mm^2, 0.20 kN/mm^2, 0.25 kN/mm^2, and 0.30 kN/mm^2, were input into the model while the remained parameters were retained as initialized. The hysteresis loops are shown in Figure 5.16. As Q_1 increased, the force values increased and the strength degradation

decreased, which is similar to the effects of Q_0. It was found that, in the calculation, the model was very sensitive to this parameter. Slight value changes made significant difference to the shape of the hysteresis loops. By comparing these five figures, it can be observed that there was an accelerating trend of dramatic change in the hysteresis loops at larger Q_1. In Figure 5.16 (a), it was noticed that, for small Q_1 (0.05 kN/mm^2), the loading curve demonstrated softening at the regions of greater displacements (16 mm and 32 mm).

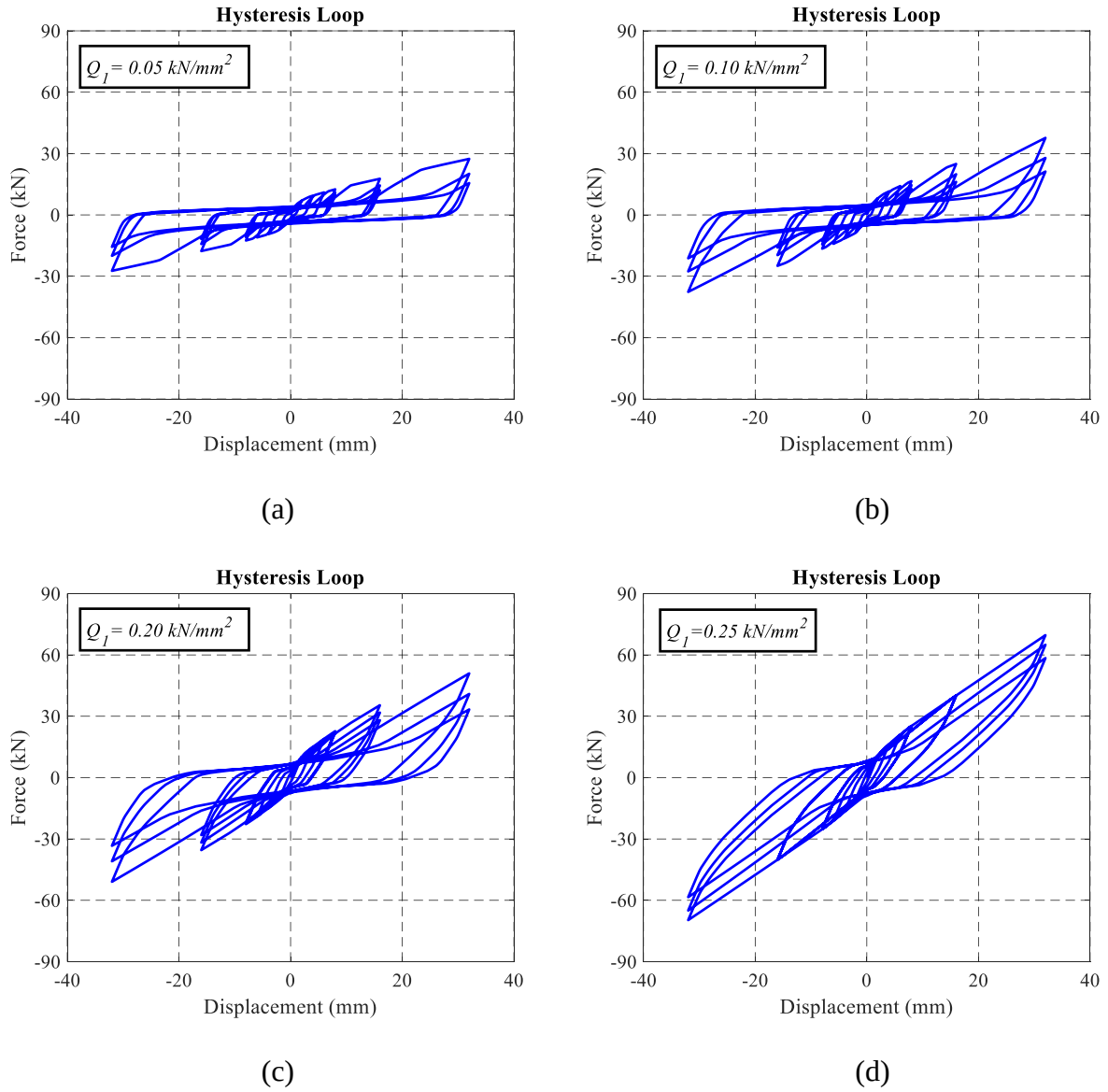

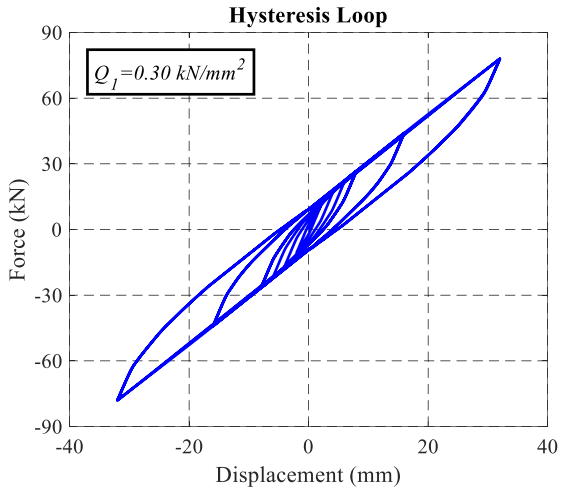

(e)

Figure 5.16 Hysteresis loops with different slopes of the asymptote at the maximum compressive response: (a) 0.05 kN/mm^2; (b) 0.10 kN/mm^2; (c) 0.20 kN/mm^2; (d) 0.25 kN/mm^2; (e) 0.30 kN/mm^2

5.3.4 Postpeak decay factor Q_2

Four different values of postpeak decay factor Q_2, namely, 1.05, 1.3, 1.5, and 2, were input into the model while the remaining parameters were retained as initialized, except that D_{max} was set to 20 mm to observe the postpeak stage. The hysteresis loops are shown in Figure 5.17. It was clear that, in cyclic protocols, Q_2 only affected the curves following the peak and determined the displacement for the peak value. For a small Q_2 value (1.05) which is close to 1, the model showed oscillations after the peak. As Q_2 increased, the displacement for the peak value increased while its influence declined.

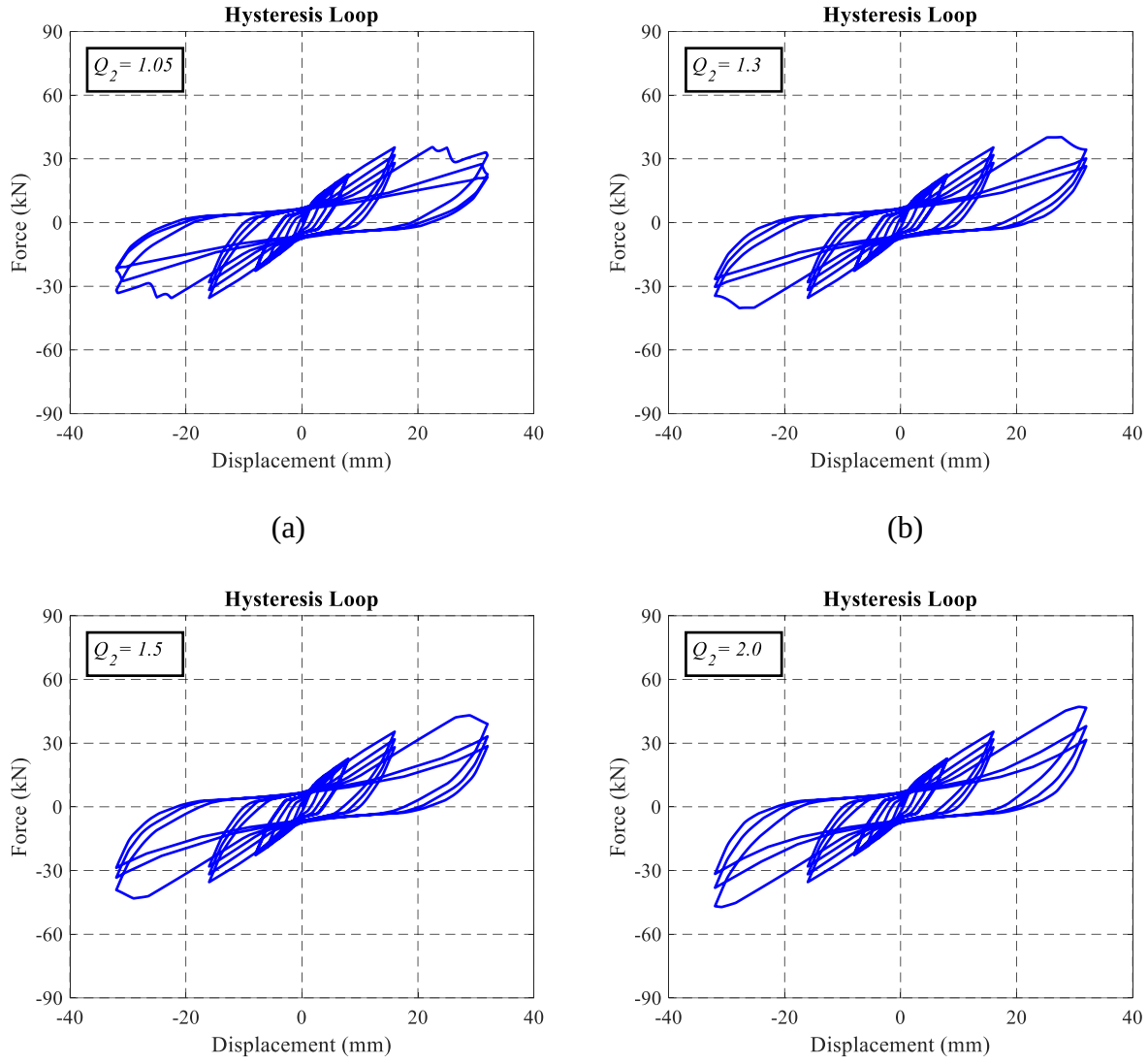

Figure 5.17 Hysteresis loops with different postpeak decay factors: (a) 1.05; (b) 1.3; (c) 1.5; (d) 2

5.3.5 Initial stiffness K_0

Four different values of initial stiffness K_0, namely, 0.10 kN/mm^2, 0.31 kN/mm^2, 0.50 kN/mm^2, and 1.0 kN/mm^2, were input into the model while the remaining parameters were retained as initialized. The hysteresis loops are shown in Figure 5.18. At small displacements (under 8 mm), K_0 is very effective in controlling the stiffness of the entire model. Larger K_0 values improved the

loading capacity of the model, especially at greater displacement (32 mm). As well, as K_0 increased, the unloading curve steepened and the pinching effect strengthened.

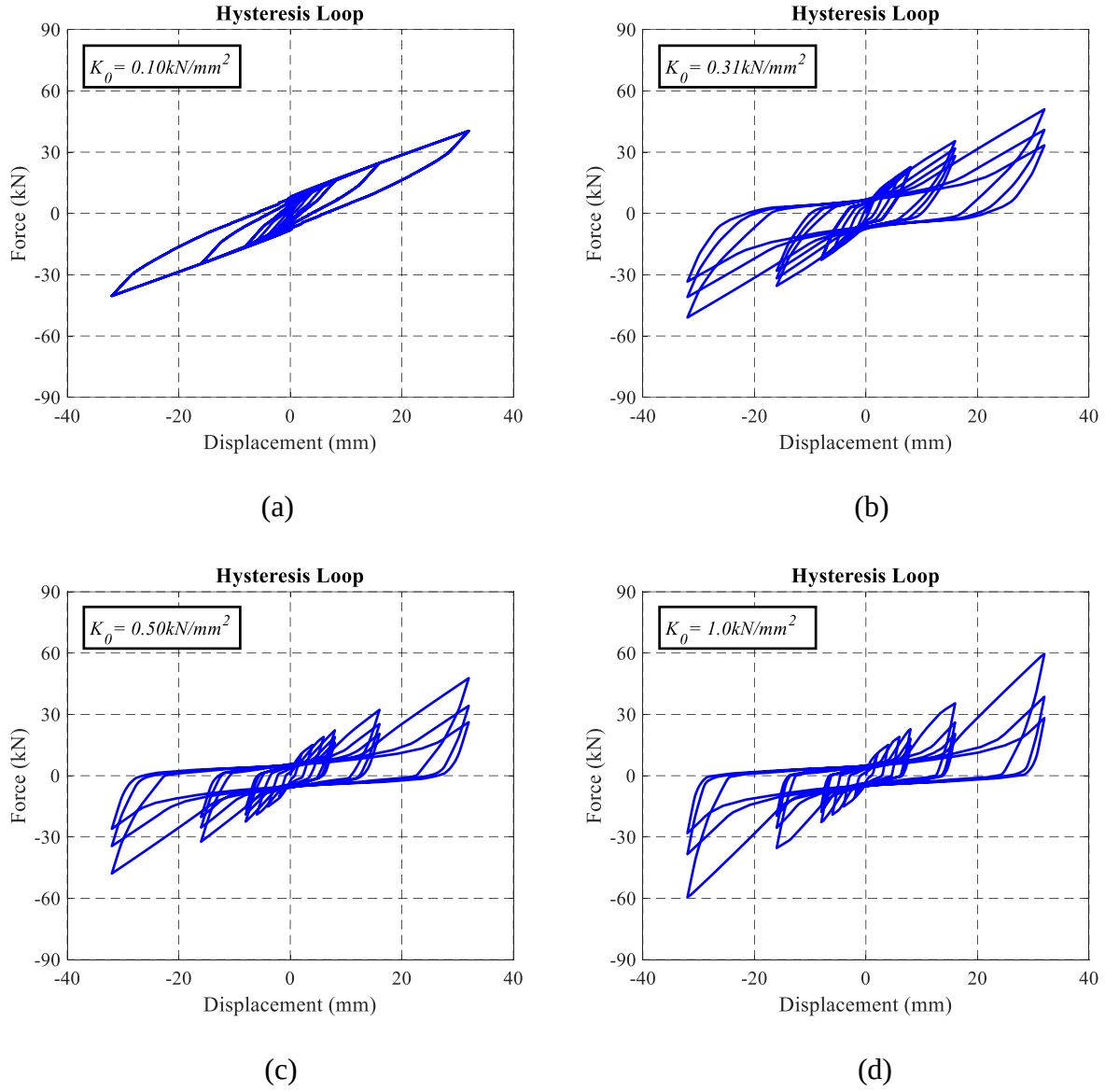

Figure 5.18 Hysteresis loops with different initial stiffness values: (a) 0.10 kN/mm^2; (b) 0.31 kN/mm^2; (c) 0.50 kN/mm^2; (d) 1.0 kN/mm^2

5.3.6 Displacement at the maximum compressive response D_{max}

Six different values of displacement at the maximum compressive response D_{max}, specifically, 10 mm, 15 mm, 20 mm, 25 mm, 35 mm, and 45 mm, were input into the model while

the remainder of the parameters were retained as initially established. The hysteresis loops are shown in Figure 5.19. D_{max} influenced almost all the characteristics of the hysteresis loops, including their force value, displacement at peak value, shape of the curves, degradation, and pinching. It was observed that a smaller D_{max} had a greater impact.

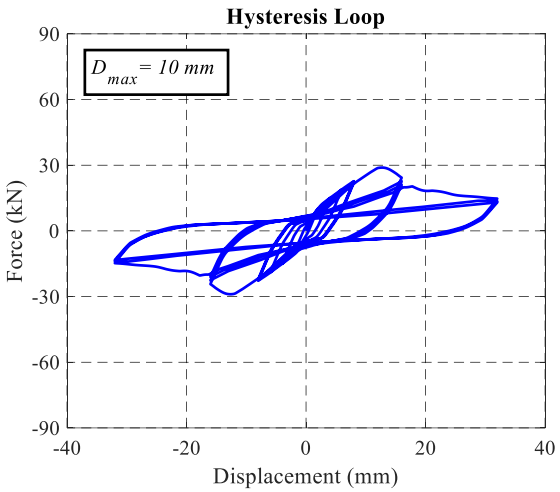

(a)

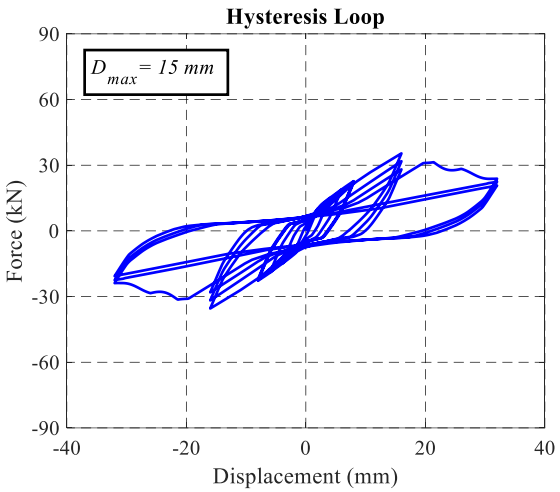

(b)

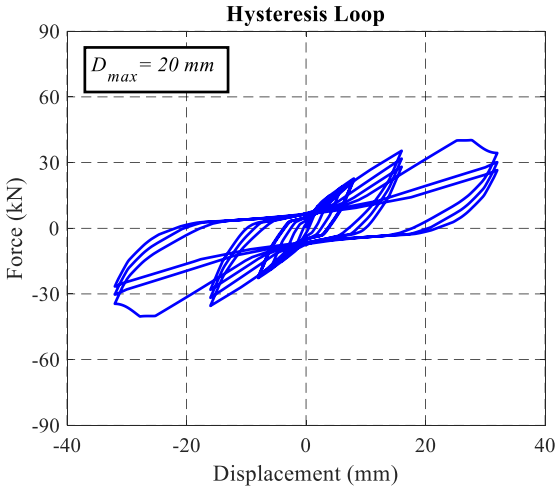

(c)

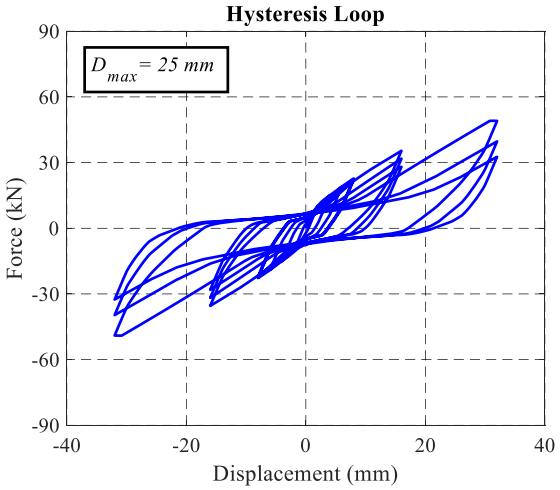

(d)

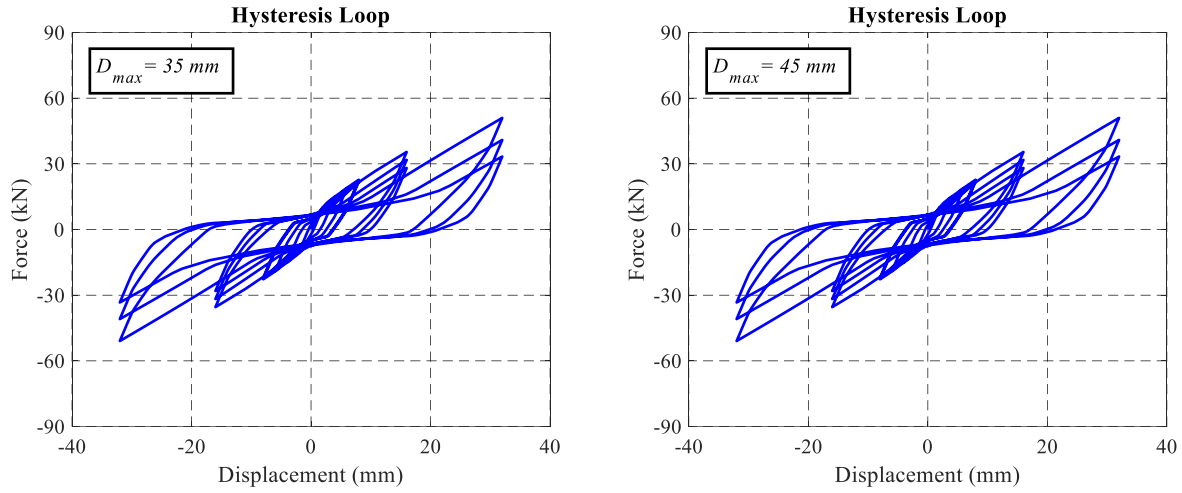

(e) (f)

Figure 5.19 Hysteresis loops with different displacements at the maximum compressive response level: (a) 10 mm; (b) 15 mm; (c) 20 mm; (d) 25 mm; (e) 35 mm; (f) 45 mm

5.3.7 Reloading degradation index α

Four different values of the reloading degradation index α, including 0, 0.2, 0.5, and 1.0, were input into the model while the remaining parameters were retained as initiated. The hysteresis loops are shown in Figure 5.20. The loading capacity dropped as α increased. For each amplitude, the peak values of the three cycles decreased due to α.

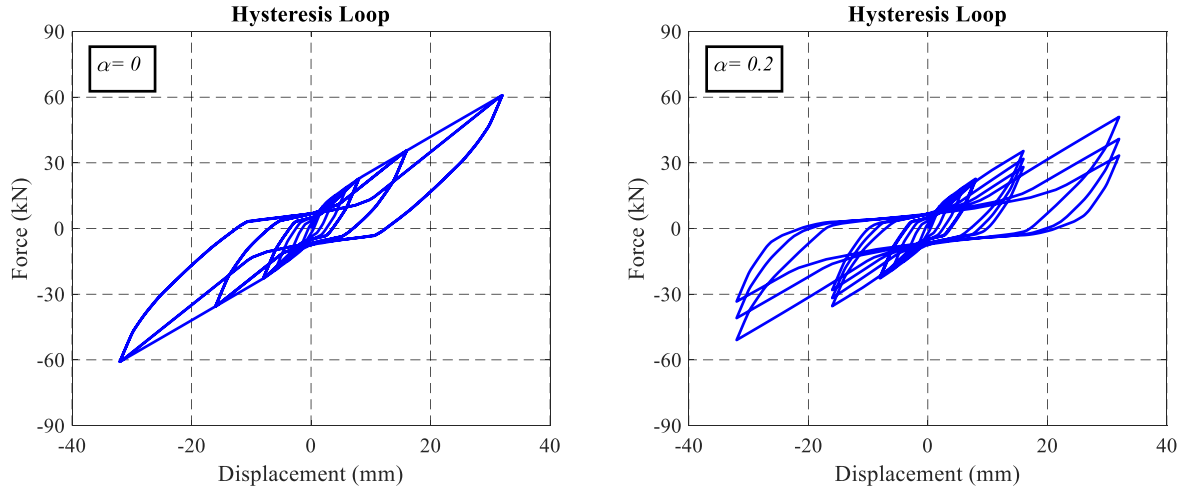

(a) (b)

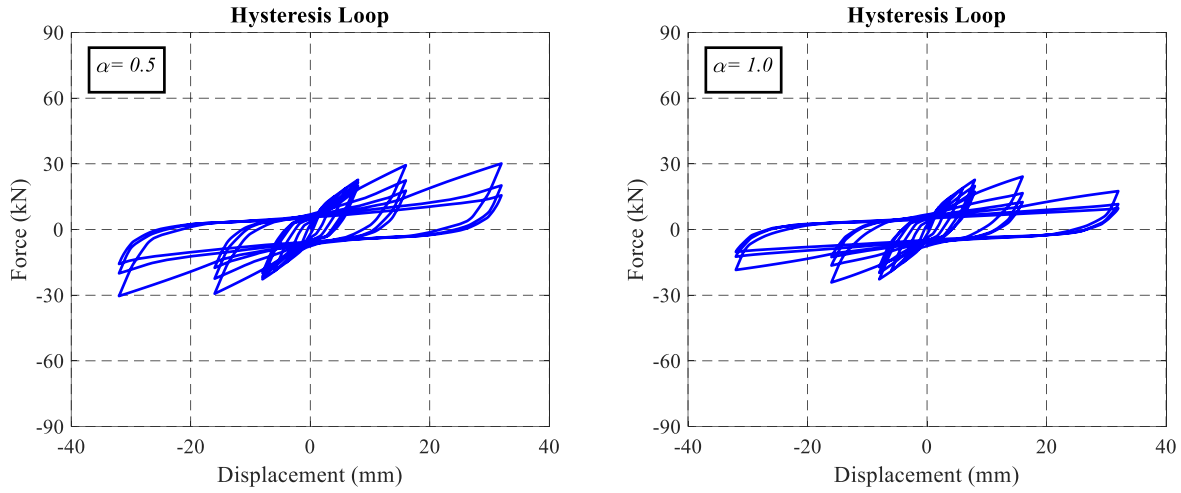

(c) (d)

Figure 5.20 Hysteresis loops with different reloading degradation indices: (a) 0; (b) 0.2; (c) 0.5; (d) 1.0

5.3.8 Gap size factor β

Five different values of gap size factor β, namely, 1, 0.8, 0.5, 0.3, and 0, were input into the model while the remaining parameters were retained as initialed. The hysteresis loops are shown in Figure 5.21. It was observed that, as the gap size factor decreased, the loading capacity slightly increased. The most significant effect is that the unloading strength increased and the degradation weakened as β decreased.

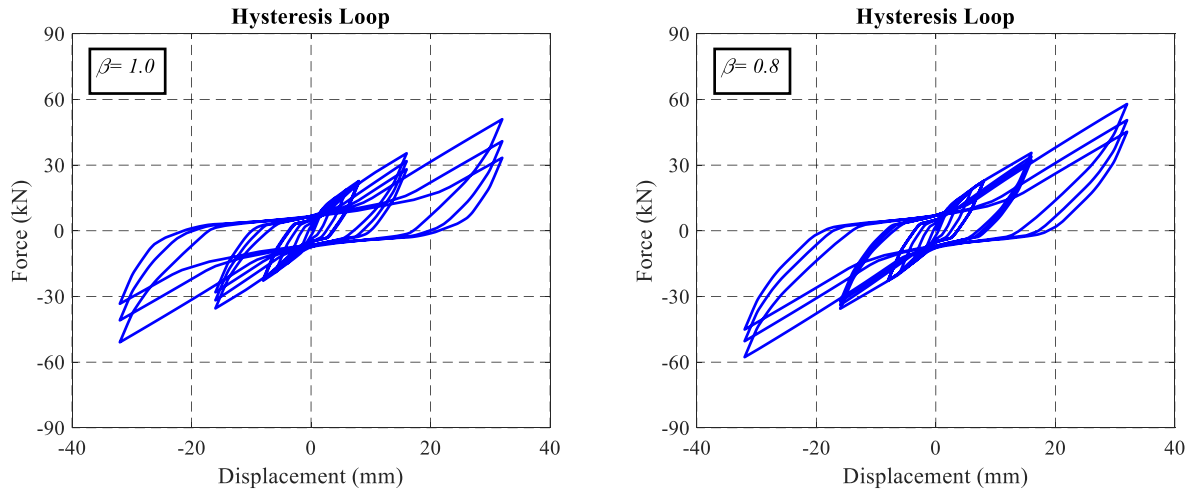

(a) (b)

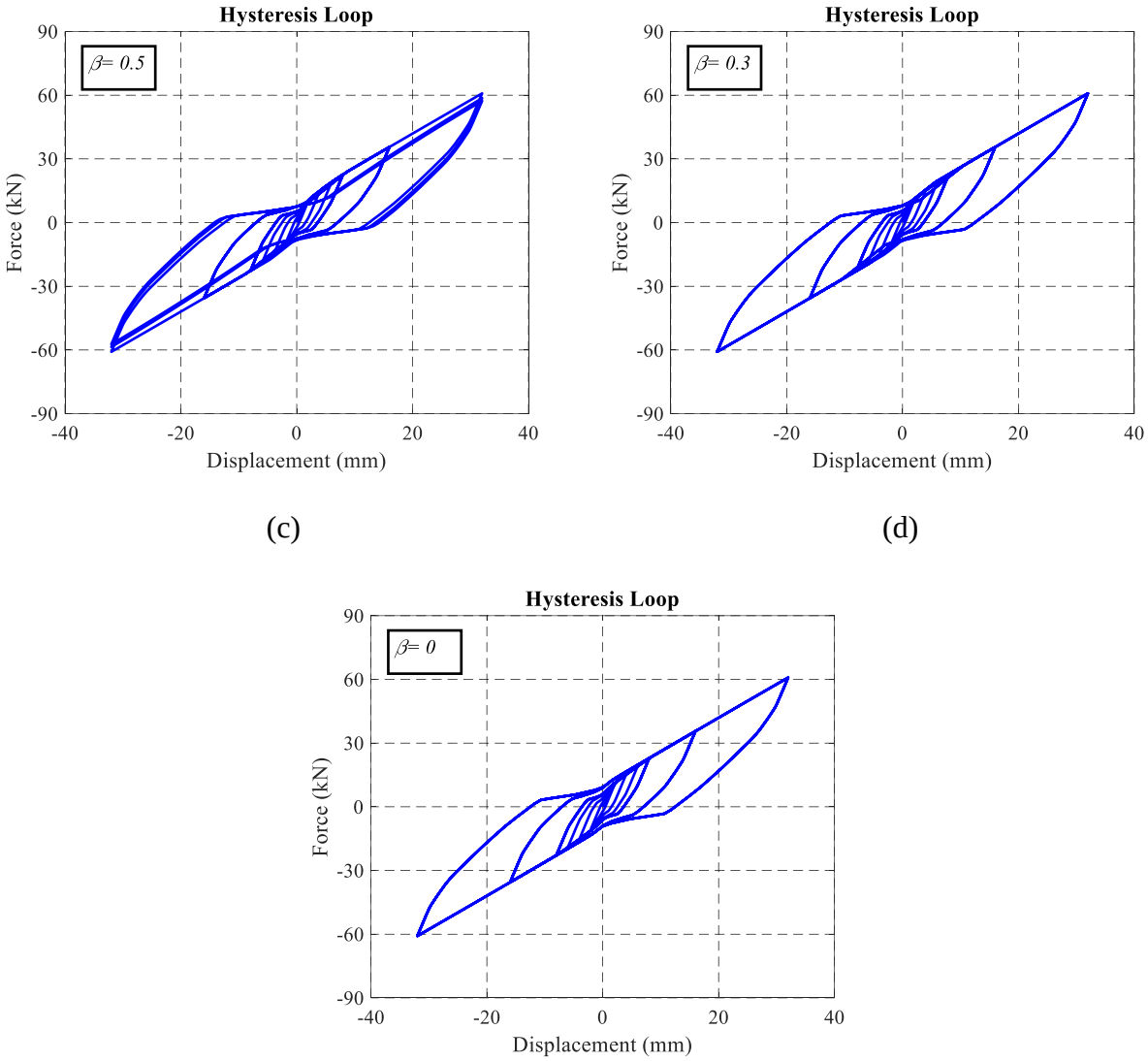

Figure 5.21 Hysteresis loops with different gap size factors: (a) 0; (b) 0.3; (c) 0.5; (d) 0.8; (e) 1.0

5.3.9 Unloading degradation index γ

Five different values of unloading degradation index γ, namely, 0, 0.2, 0.5, 0.8, and 1.0, were input into the model while the remaining parameters were retained as initialed, with the exception that the gap size factor β was set at 0.3 to observe the unloading behaviour. The hysteresis loops are shown in Figure 5.22. This parameter had little influence on the overall hysteresis loops. Its key contribution was that it controlled the unloading stiffness and range of

slippage. Larger values of γ increased the unloading stiffness and reduced the distance of the slipping.

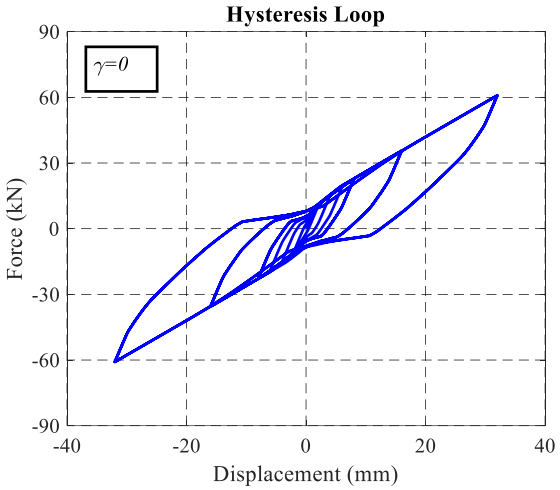

(a)

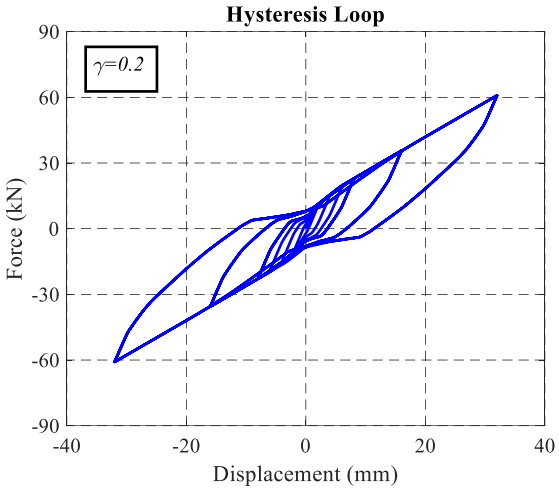

(b)

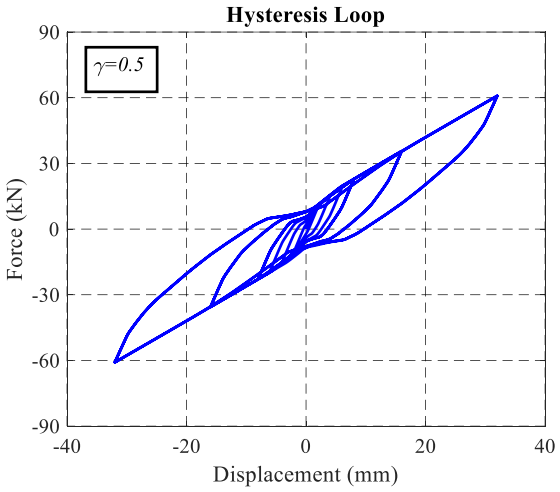

(a)

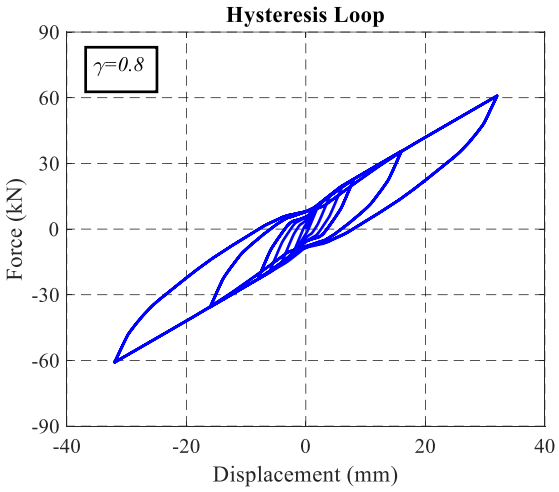

(b)

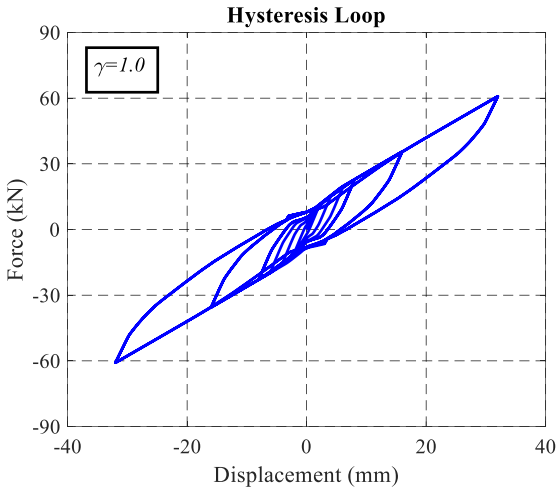

(e)

Figure 5.22 Hysteresis loops with different unloading degradation indices: (a) 0; (b) 0.3; (c) 0.5; (d) 0.8; (e) 1.0

5.4 Summary

In this chapter, the mechanisms for the CLT connections under bi-axial loading were presented. The difference in unloading for bi-axial loading as compared to uniaxial loading was explained. To better simulate the new characteristics found in the experiments, a pseudo-nail model was constructed using a proposed algorithm based on the protocol-independent nail connection algorithm HYST. The proposed HYST algorithm added an unloading stiffness degradation feature to the original algorithms, extending its sufficient application to nail-based timber connections, which require taking into consideration strength degradation, unloading/reloading stiffness degradation, the pinching effect, and the coupling effect.

The principle of the new algorithm is that the nails received resistance in the residual gap of the wood embedment when co-existent force is applied in the perpendicular direction. Accordingly, a gap size factor β and an unloading stiffness degradation index γ were introduced into the HYST algorithm. In the wood embedment, before unloading to zero, the wood medium

had a stiffness of $(D_y / D_0)^{\alpha\gamma} K_0$ when the nail was travelling from w_0 to βD_0. The construction of the model was then based on the principle of virtual work.

A parameter study was carried out for nine key parameters in this model, including the nail diameter D_N, intercept of the asymptote at the maximum compressive response Q_0, slope of the asymptote at the maximum compressive response Q_1, postpeak decay factor Q_2, initial stiffness K_0, displacement at the maximum compressive response D_{max}, reloading degradation index α, gap size factor β, and unloading degradation index γ. The results show that: 1) a larger D lead to higher capacity; 2) a large Q_0 reduced the degradation and made the model more "elastic and stiff"; 3) Q_1 is a very sensitive parameter to the model. As it increased, the force values augmented and strength degradation decreased; 4) as Q_2 increased, the peak value displacement became larger and its influence declined; 5) a larger K_0 improved the loading capacity of the model, especially at larger displacements; 6) D_{max} influenced all the characteristics of the hysteresis loops and a smaller D_{max} had a greater impact; 7) as α increased, the loading capacity dropped. For each amplitude, the peak values of the three cycles decreased due to α; 8) as β decreased, the unloading strength increased and the degradation was weakened; 9) larger values of γ increased the unloading stiffness and reduced the distance of the slip. The parameter study provides a guideline in understanding this model and the foundation for further modelling calibrations.

It should be noted that, this model can not only be used for the studied connections, but is also suitable for all types of hysteresis behaviour in combination with strength degradation, reloading/unloading stiffness, pinching effect, and coupling effect.

Chapter 6: Model Validation for CLT Connections under Bi-axial Loading

The CLT connections were simulated using the pseudo-nail model with the proposed HYST algorithm. For each configuration, one representative specimen was modelled. In total, 32 pseudo nail models were calibrated to cover all configurations. The models were validated against the test results; their parameters are discussed in this section.

6.1 Model validation

The results from the HYST model and test results are presented first to demonstrate the efficiency of the proposed algorithm.

6.1.1 Modelling angle bracket tension tests with a co-existent shear force

For Set A, as is shown in Figure 6.1, the co-existent shear force weakened the axial loading capacity and energy dissipation capacity at large vertical displacements. The backbones deteriorated more severely. At the 40 kN co-existent shear force, the tension capacity dropped by 25% as compared to that at the 0 kN co-existent shear force. This was simulated by changing the five parameters of equivalent wood embedment, Q_0, Q_1, Q_2, K_0, and D_{max}, that influenced the backbone of the pseudo-nail model. The setup of the tests, involving loading tension through a steel cable, limited the unloading and reloading. However, the model still performed well in capturing the hysteresis loops with the real protocol recorded from the cyclic tests.

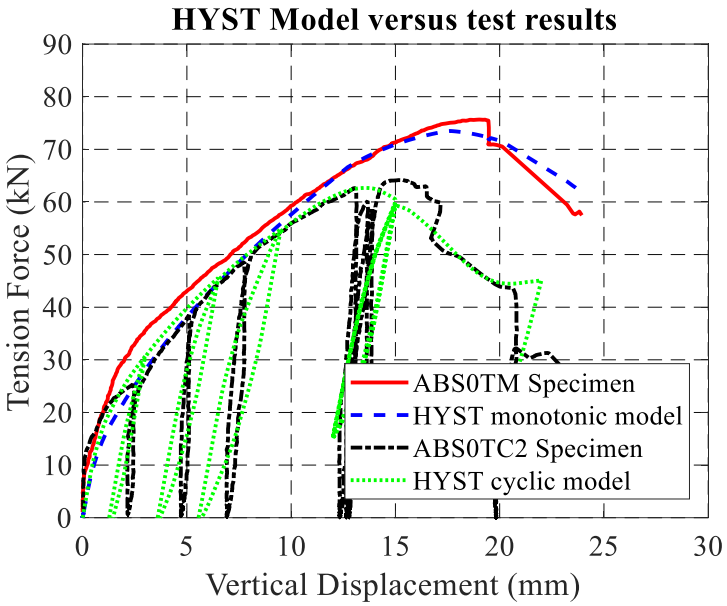
HYST Model versus test results
Tension Force (kN)
Vertical Displacement (mm)
ABS0TM Specimen
HYST monotonic model
ABS0TC2 Specimen
HYST cyclic model

(a)

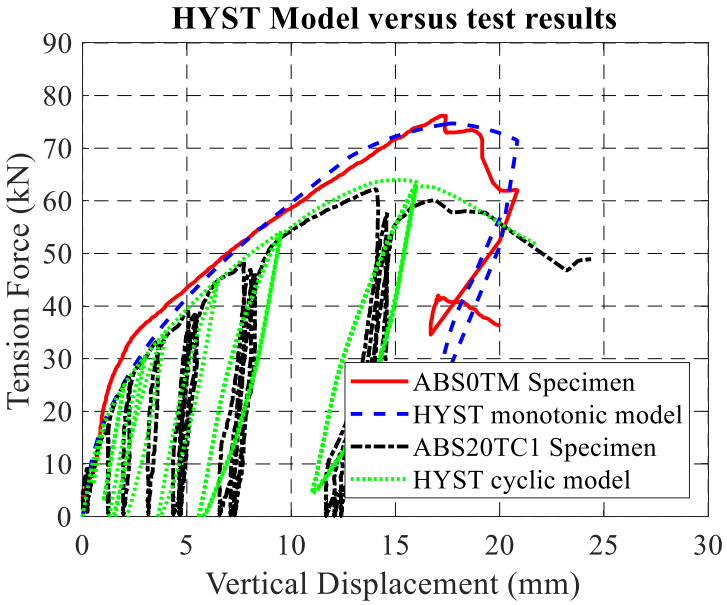
HYST Model versus test results
Tension Force (kN)
Vertical Displacement (mm)
ABS0TM Specimen
HYST monotonic model
ABS20TC1 Specimen
HYST cyclic model

(b)

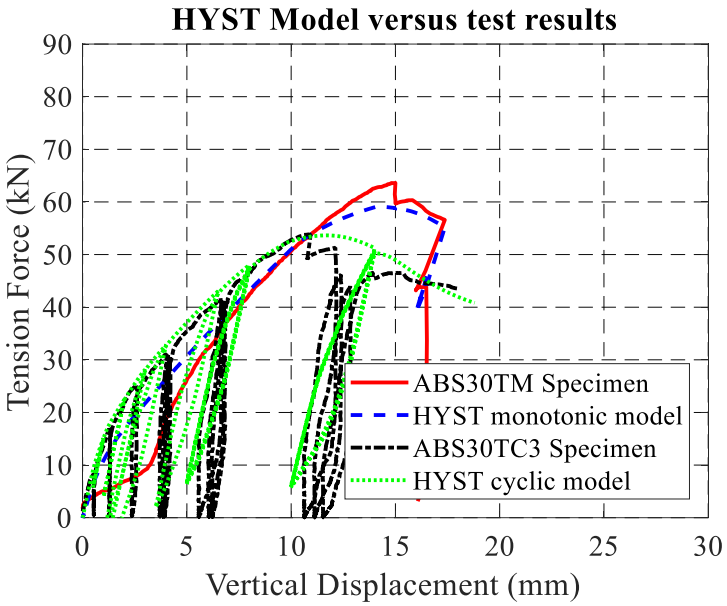

(c)

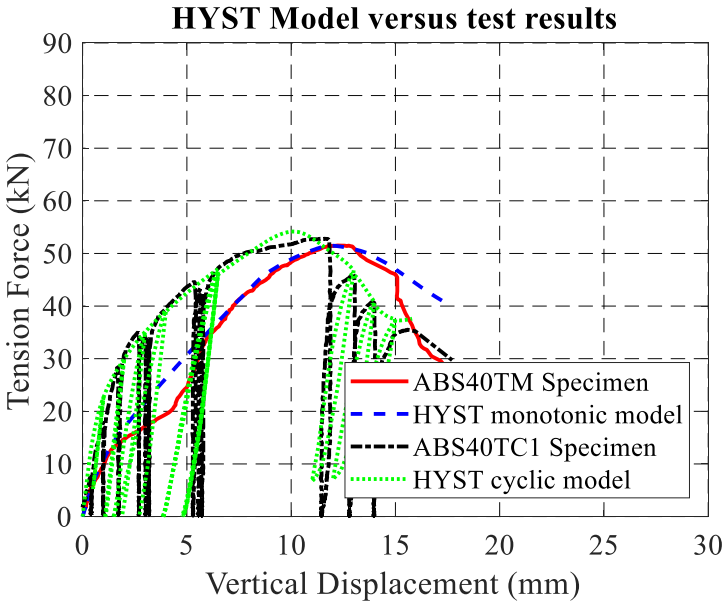

(d)

Figure 6.1 The HYST model versus the test results for energy dissipation in Set A: (a) 0 kN; (b) 20 kN; (c) 30 kN; (d) 40 kN

6.1.2 Modelling angle bracket shear tests with a co-existent tension force

Figure 6.2 presents the HYST model results versus the test results for Set B, which are the angle bracket shear tests with a co-existent tension force. From those figures, it is first noticed that the proposed HYST algorithm exhibited high consistency in modelling the monotonic behaviour of the connections under the four conditions. As shown in Figure 6.2 (a) to (d), with the introduction of the co-existent tension force, the hysteresis behaviour changed dramatically. As the co-existent tension load increased, the shear performance of the connectors was weakened, especially the strength, unloading stiffness, energy dissipation capacity and stability. The model showed satisfying adaptability in capturing those features. By comparing the curves in the red boxes in Figure 6.2 (a) and (b), the changes in unloading were captured by this model. This could not be modelled with the original modified HYST algorithm (Li and Lam, 2015). In Figure 6.2 (d), due to the instability of the connections under high co-existent tension loads, the modelling results differed from the test results in the last cycle as pointed by the arrows.

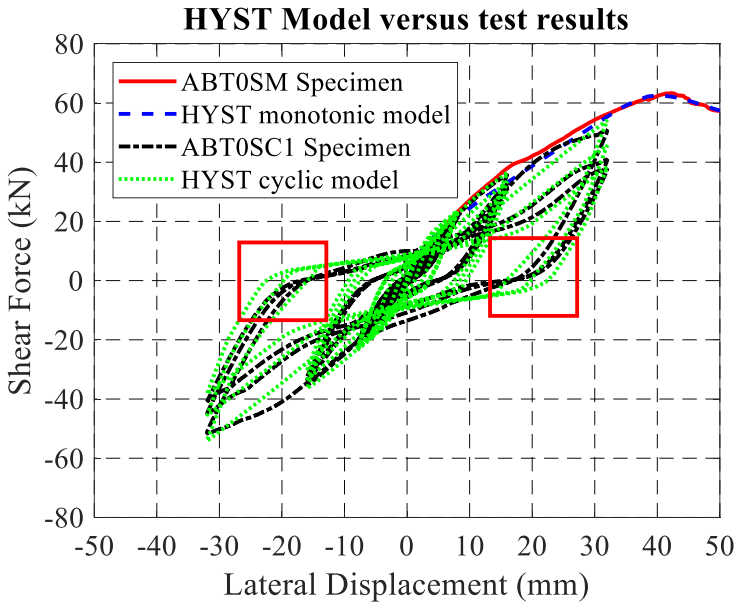

(a)

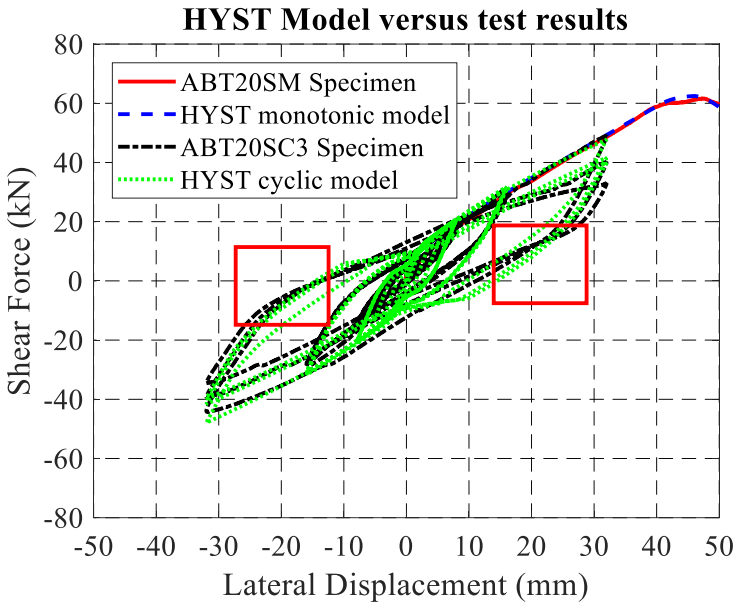
HYST Model versus test results
ABT20SM Specimen
HYST monotonic model
ABT20SC3 Specimen
HYST cyclic model
Shear Force (kN)
Lateral Displacement (mm)
80
60
40
20
0
-20
-40
-60
-80
-50 -40 -30 -20 -10 0 10 20 30 40 50

(b)

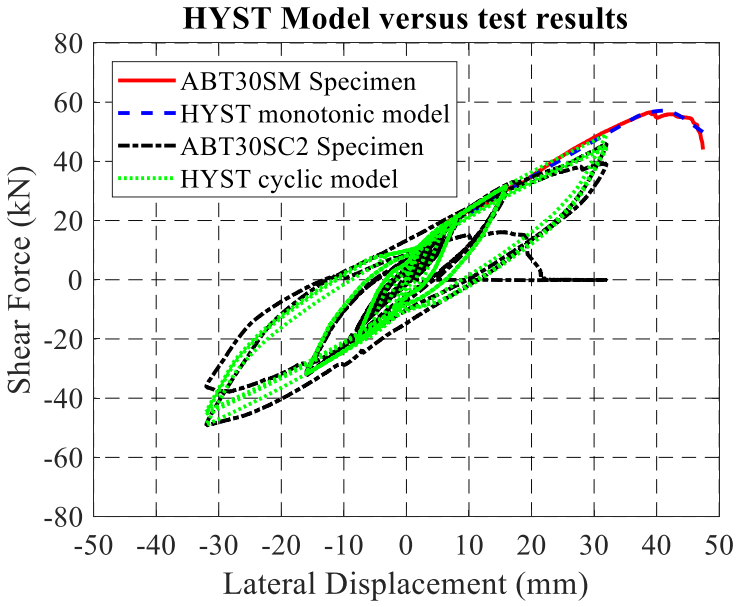
HYST Model versus test results
ABT30SM Specimen
HYST monotonic model
ABT30SC2 Specimen
HYST cyclic model
Shear Force (kN)
Lateral Displacement (mm)
80
60
40
20
0
-20
-40
-60
-80
-50 -40 -30 -20 -10 0 10 20 30 40 50

(c)

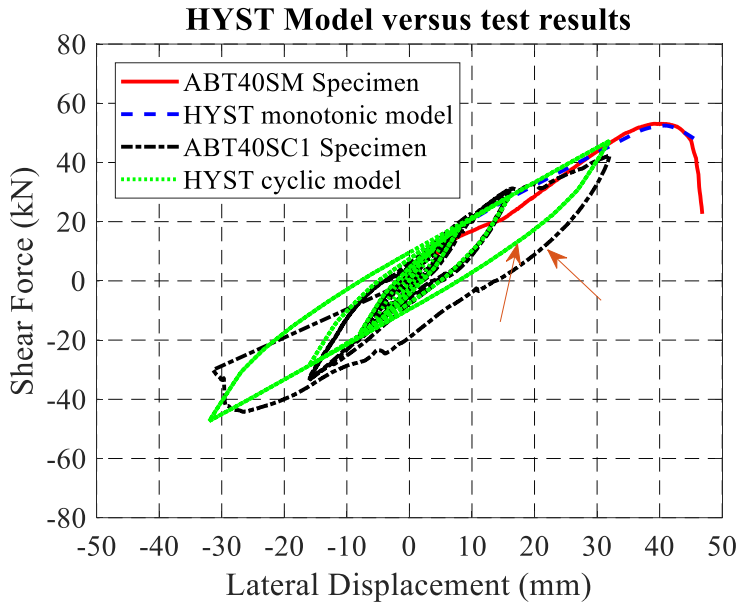

(d)

Figure 6.2 The HYST model versus the test results for the force-displacement curves of Set B: (a) 0 kN ; (b) 20 kN; (c) 30 kN; (d) 40 kN

Figure 6.3 compares the energy dissipation in the cyclic tests for Set B. Good agreement can be observed, which also validates the accuracy of the proposed method in modelling hysteresis behaviour.

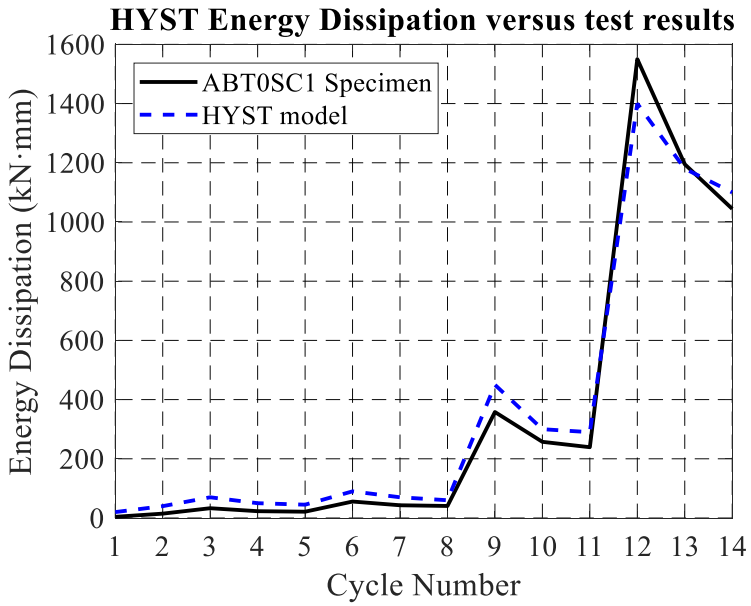

(a)

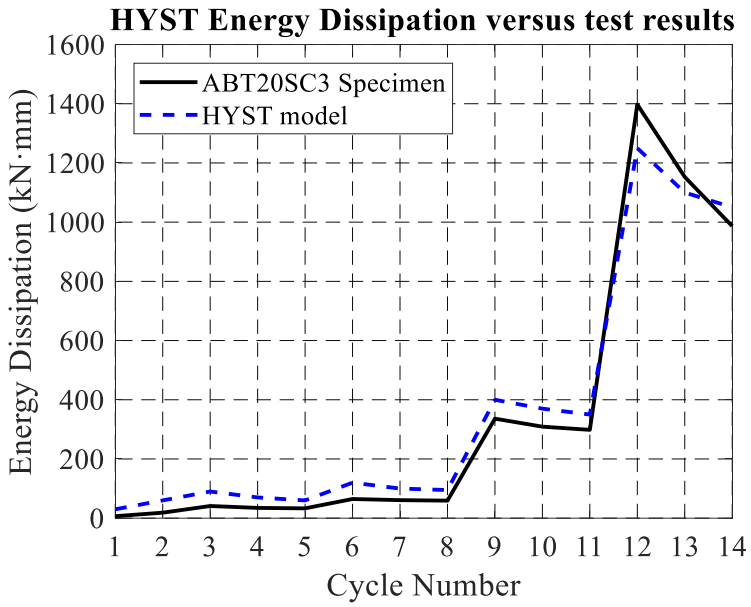
HYST Energy Dissipation versus test results
ABT20SC3 Specimen
HYST model
Energy Dissipation (kN·mm)
Cycle Number
0
200
400
600
800
1000
1200
1400
1600
1 2 3 4 5 6 7 8 9 10 11 12 13 14

(b)

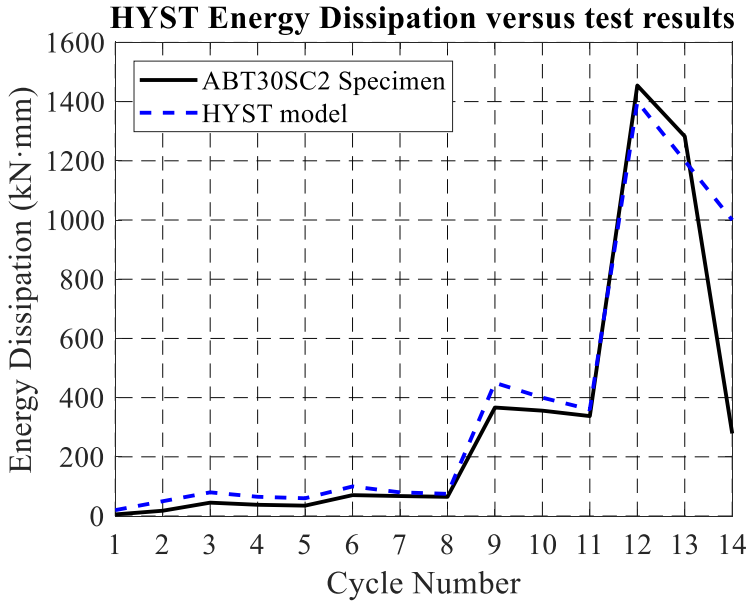
HYST Energy Dissipation versus test results
ABT30SC2 Specimen
HYST model
Energy Dissipation (kN·mm)
Cycle Number
0
200
400
600
800
1000
1200
1400
1600
1 2 3 4 5 6 7 8 9 10 11 12 13 14

(c)

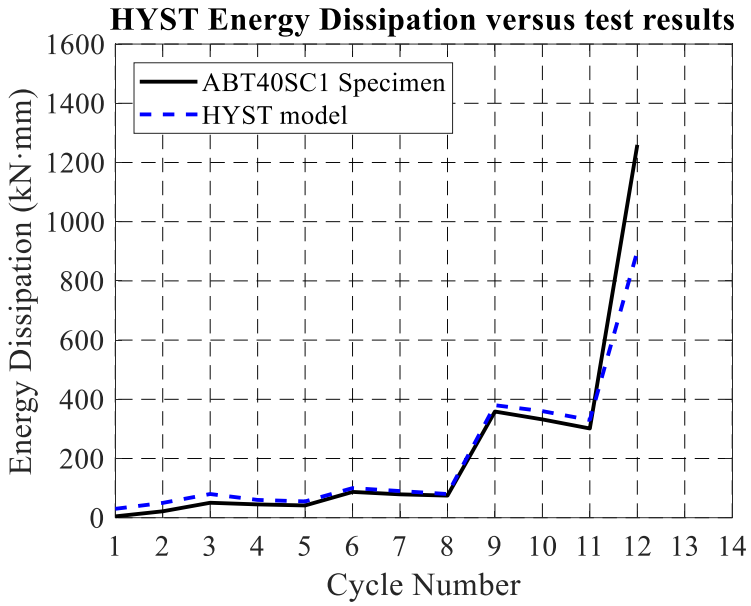

(d)

Figure 6.3 The HYST model versus the test results for energy dissipation of Set B: (a) 0 kN ; (b) 20 kN; (c) 30 kN; (d) 40 kN

6.1.3 Modelling hold-down tension test with a co-existent shear force

In Set C, similar characteristics were observed in hold-down tests with a co-existent shear force as those in Set A for angle brackets, as shown in Figure 6.4. Difference between the model and test results in terms of unloading is due to the relaxation of the loading cable. Otherwise, the accuracy of the model compares well with the test results.

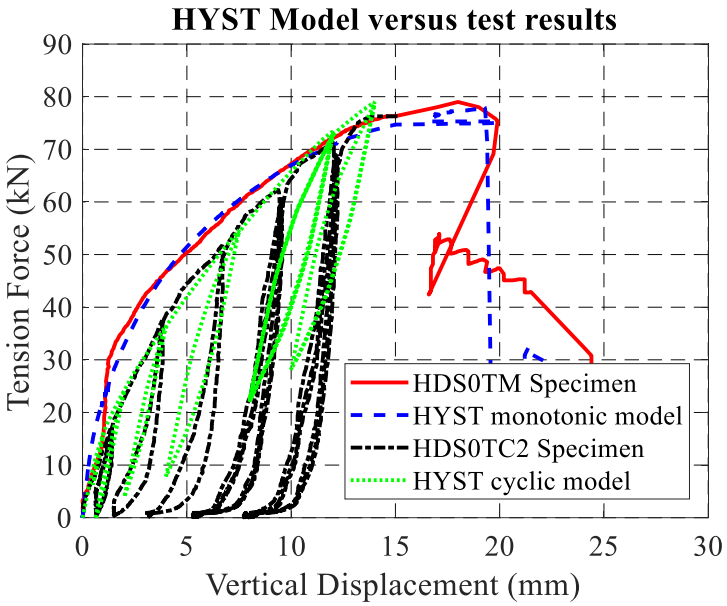
HYST Model versus test results
Tension Force (kN)
Vertical Displacement (mm)
HDS0TM Specimen
HYST monotonic model
HDS0TC2 Specimen
HYST cyclic model

(a)

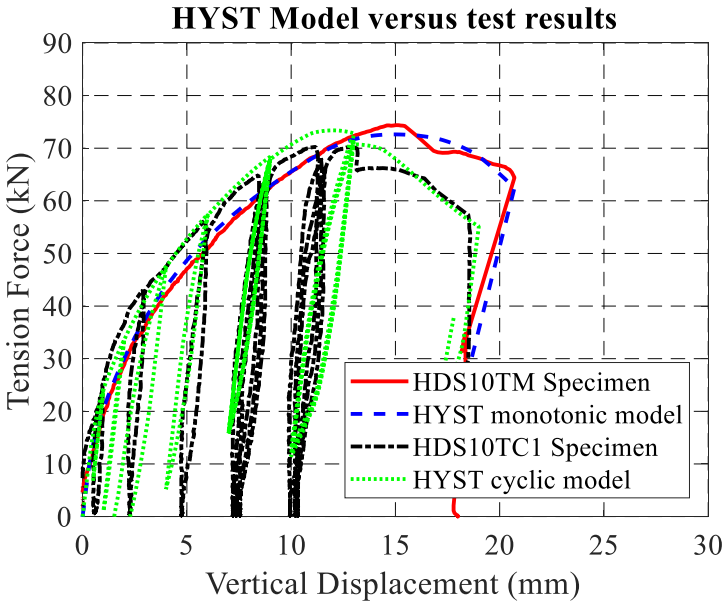
HYST Model versus test results
Tension Force (kN)
Vertical Displacement (mm)
HDS10TM Specimen
HYST monotonic model
HDS10TC1 Specimen
HYST cyclic model

(b)

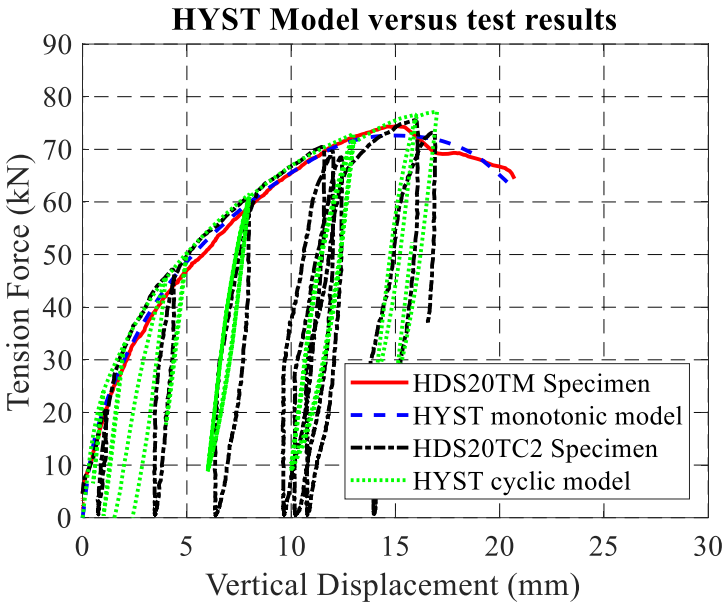

(c)

Figure 6.4 The HYST model versus the test results for the force-displacement curves of Set C: (a) 0 kN; (b) 10 kN; (c) 20 kN

6.1.4 Modelling hold-down shear tests with a co-existent tension force

The HYST model results versus the test results for Set D, the hold-down shear tests with a co-existent tension force, are shown in Figure 6.5. The results present similar features as those for Set B. The changes in unloading, highlighted in the red boxes, and the weakening of the pinching effect, indicated by the arrows, were even more apparent under these five conditions when compared with Set B. The reloading stiffness degradation was more obvious, as shown in the circles in Figure 6.5 (a) and (c). These features were captured with high accuracy by the current proposed model.

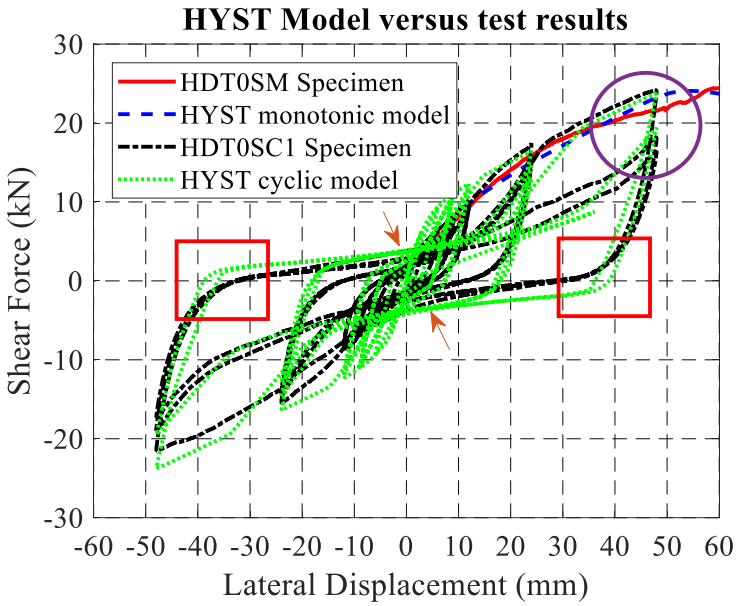
HYST Model versus test results
HDT0SM Specimen
HYST monotonic model
HDT0SC1 Specimen
HYST cyclic model
Shear Force (kN)
Lateral Displacement (mm)
30
20
10
0
-10
-20
-30
-60 -50 -40 -30 -20 -10 0 10 20 30 40 50 60

(a)

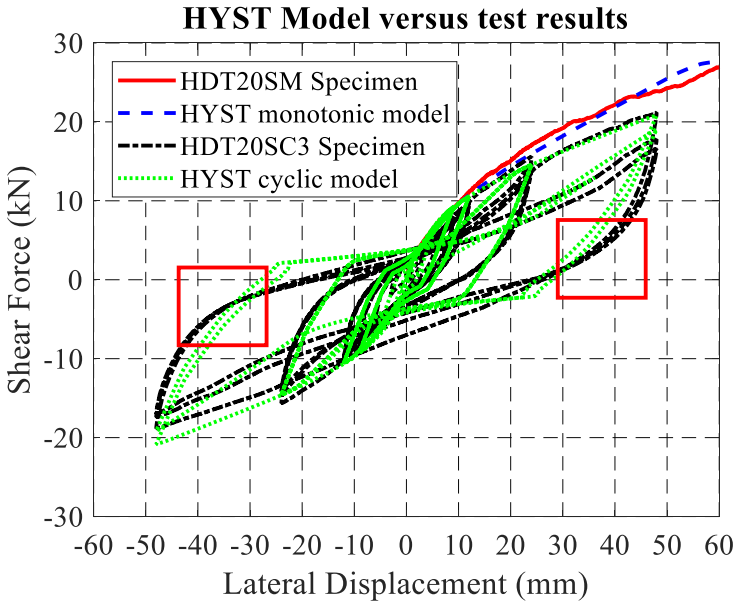
HYST Model versus test results
HDT20SM Specimen
HYST monotonic model
HDT20SC3 Specimen
HYST cyclic model
Shear Force (kN)
Lateral Displacement (mm)
30
20
10
0
-10
-20
-30
-60 -50 -40 -30 -20 -10 0 10 20 30 40 50 60

(b)

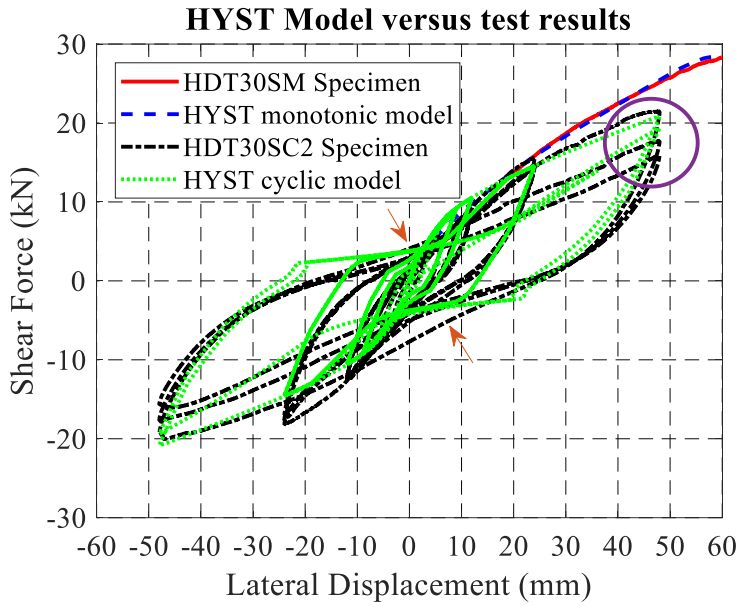
HYST Model versus test results
HDT30SM Specimen
HYST monotonic model
HDT30SC2 Specimen
HYST cyclic model
Shear Force (kN)
Lateral Displacement (mm)
30
20
10
0
-10
-20
-30
-60 -50 -40 -30 -20 -10 0 10 20 30 40 50 60

(c)

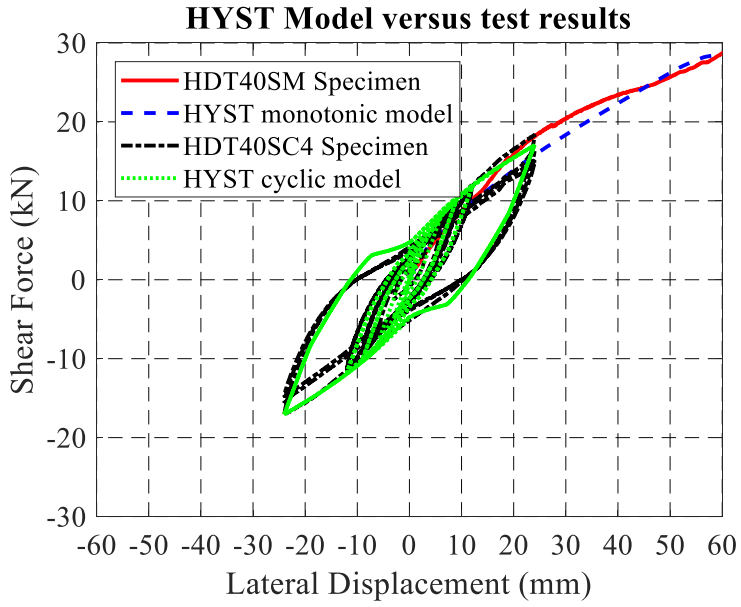
HYST Model versus test results
HDT40SM Specimen
HYST monotonic model
HDT40SC4 Specimen
HYST cyclic model
Shear Force (kN)
Lateral Displacement (mm)
30
20
10
0
-10
-20
-30
-60 -50 -40 -30 -20 -10 0 10 20 30 40 50 60

(d)

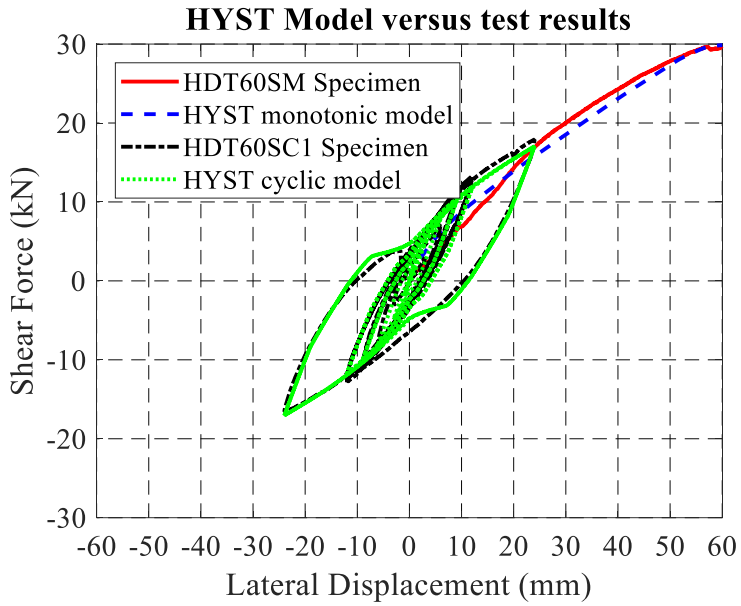

(e)

Figure 6.5 The HYST model versus the test results for the force-displacement curves of Set D: (a) 0 kN; (b) 20 kN; (c) 30 kN; (d) 40 kN; (e) 60 kN

The energy dissipated by the hysteresis loops using the models indicated satisfying consistency with that of the tests, as shown in Figure 6.6.

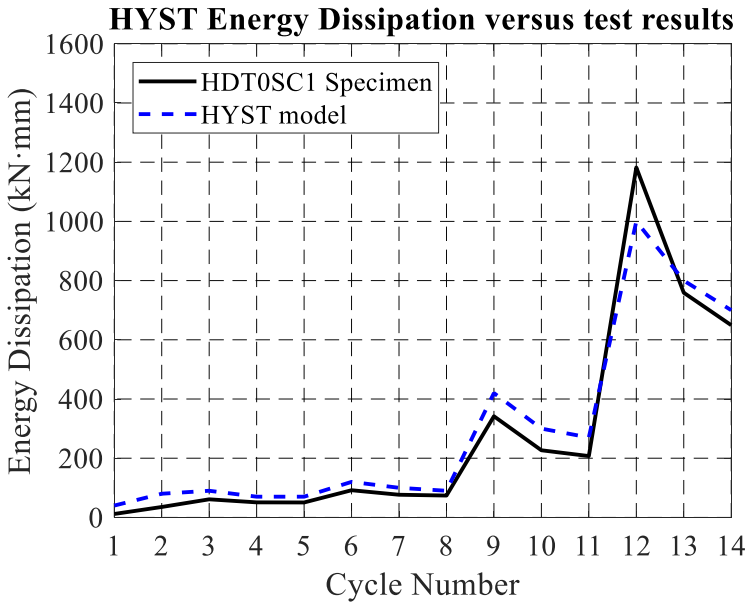

(a)

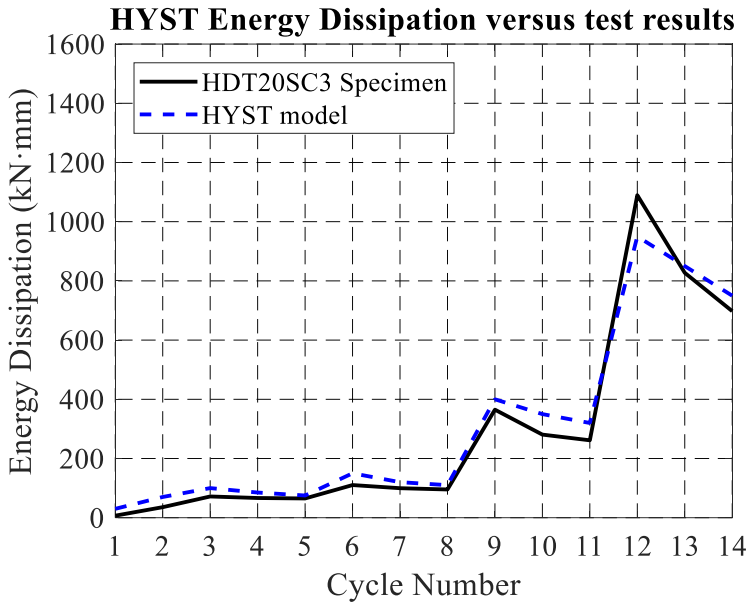
HYST Energy Dissipation versus test results
HDT20SC3 Specimen
HYST model
Energy Dissipation (kN·mm)
Cycle Number
0
200
400
600
800
1000
1200
1400
1600
1 2 3 4 5 6 7 8 9 10 11 12 13 14

(b)

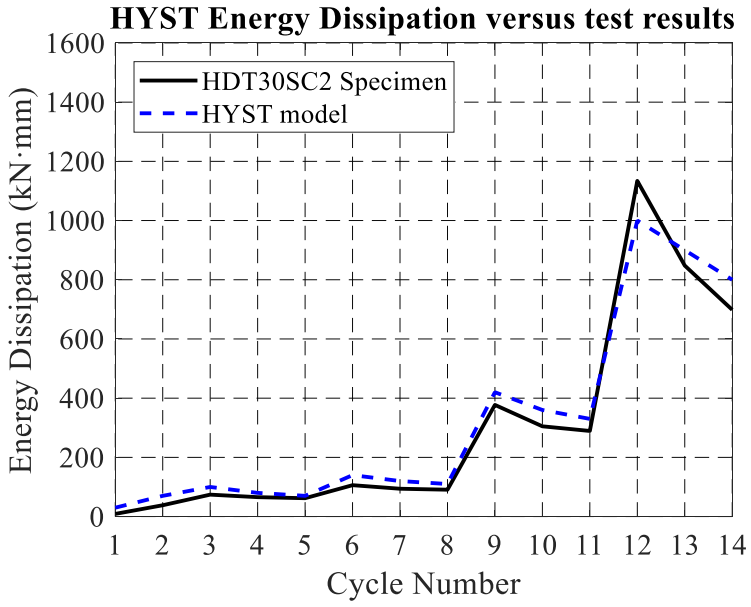
HYST Energy Dissipation versus test results
HDT30SC2 Specimen
HYST model
Energy Dissipation (kN·mm)
Cycle Number
0
200
400
600
800
1000
1200
1400
1600
1 2 3 4 5 6 7 8 9 10 11 12 13 14

(c)

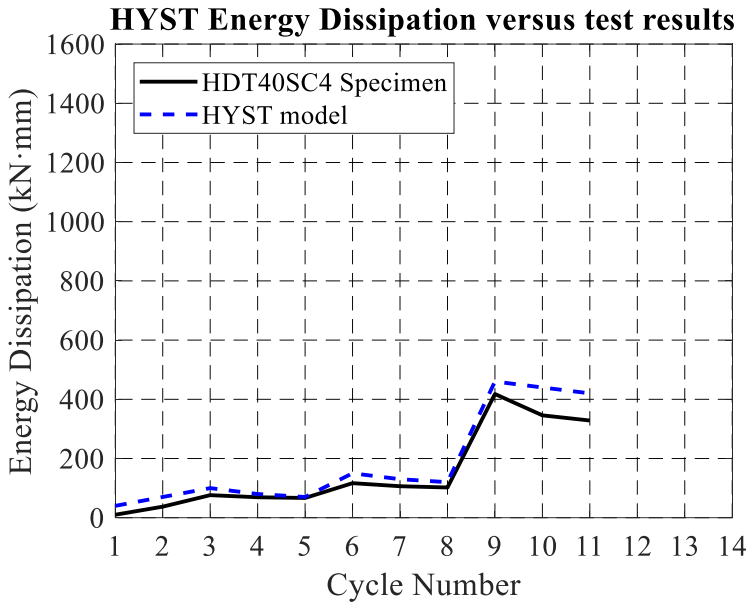

(d)

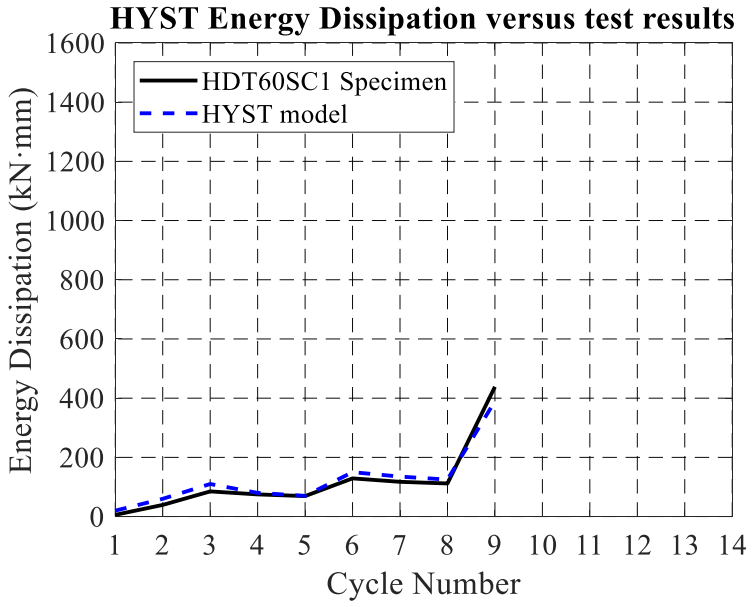

(e)

Figure 6.6 The HYST model versus the test results for energy dissipation of Set D: (a) 0 kN; (b) 20 kN; (c) 30 kN; (d) 40 kN; (e) 60 kN

Based on the above validations, it can be concluded that the pseudo-nail model with the proposed HYST algorithm is a powerful finite-element based method in simulating CLT

connections under bi-axial loading, and more generally, nail-based wood connections under different loading protocols.

6.2 Parameter discussion for CLT connections under bi-axial loading

The parameters used to calculate force-displacement curves are presented and discussed as below.

One feature of the proposed methodology is that it helps explain and comprehend the structural mechanisms of nail-based wood connections under complex loading.

In all models, the pseudo-nail had the same length (L_N) of 150 mm, diameter (D_N) of 8 mm, Elastic Modulus (E) of 200 GPa, and yield strength (E_y) of 0.01 kN/mm^2. All angle bracket and hold-down connections were considered to be stiff steel plate sheaths with a thickness of 5 mm, and large embedment property parameters of Q_0 (100 kN/mm), Q_1 (100 kN/mm^2), Q_2 (200), K_0 (200 kN/mm^2), and D_{max} (200 mm). The α, β, and γ of the sheath had little influence on their performance.

The major differences between the models were the embedment property parameters of the equivalent wood embedment. Table 6.1 presents these parameters for each test configuration. For all monotonic tests, only the first five parameters, Q_0, Q_1, Q_2, K_0, and D_{max}, were needed for the models. For Set A and Set C, where the tension cyclic tests were conducted, loading the vertical force through a steel cable limited the accuracy of unloading and reloading. Thus, the models only adopted the first five parameters targeting the backbones. For the shear cyclic tests in Set B and Set D, the hysteresis behaviour of the CLT connections were well captured. Subsequently, all eight parameters played their roles in depicting the characteristics of the CLT connections under bi-axial loading. In each set, the parameters of the pure shear or tension tests were first calibrated. After

that, the parameters of the remaining tests with different co-existent forces were calibrated based on these parameters, and with the principle of modifying the least numbers of parameters.

Table 6.1 Property parameters for the equivalent wood embedment for each test configuration

Set	Configuration	Q_0 (kN/mm)	Q_1 (kN/mm^2)	Q_2	K_0 (kN/mm^2)	D_{max} (mm)	α	β	γ
A	ABS0TM	4	0.5	1.35	2	11	-	-	-
	ABS0TC	4	0.3	1.35	2	10	-	-	-
	ABS20TM	4	0.5	1.35	3	11	-	-	-
	ABS20TC	4	0.28	1.8	2	10	-	-	-
	ABS30TM	4	0.5	1.35	1	9	-	-	-
	ABS30TC	4	0.3	2	1.5	7	-	-	-
	ABS40TM	4	0.5	1.35	1	7.5	-	-	-
	ABS40TC	4	0.2	1.2	4	8	-	-	-
B	ABT0SM	0.16	0.22	1.2	0.31	32	-	-	-
	ABT0SC	0.16	0.20	1.3	0.31	35	0.15	1	0.2
	ABT20SM	0.16	0.18	1.1	0.31	39	-	-	-
	ABT20SC	0.16	0.16	1.3	0.31	35	0.2	0.3	0.7
	ABT30SM	0.16	0.18	1.1	0.31	35	-	-	-
	ABT30SC	0.16	0.16	1.3	0.31	35	0.2	0.2	0.7
	ABT40SM	0.16	0.16	1.1	0.31	35	-	-	-
	ABT40SC	0.16	0.16	1.3	0.16	35	0.2	0.1	1
C	HDS0TM	7.5	0.15	2.3	5	8	-	-	-
	HDS0TC	8	0.15	2.3	4.5	10	-	-	-
	HDS10TM	7.5	0.15	1.3	4	10	-	-	-
	HDS10TC	8	0.12	2	4	7	-	-	-
	HDS20TM	7.5	0.15	1.3	4	10	-	-	-
	HDS20TC	7	0.1	2.8	4	10	-	-	-
D	HDT0SM	0.26	0.025	1.2	0.04	45	-	-	-
	HDT0SC	0.26	0.02	1.2	0.1	45	0.15	1	0
	HDT20SM	0.26	0.028	1.2	0.05	50	-	-	-
	HDT20SC	0.26	0.015	1.2	0.05	45	0.4	0.8	0.8
	HDT30SM	0.26	0.03	1.2	0.04	50	-	-	-
	HDT30SC	0.26	0.015	1.2	0.05	45	0.5	0.7	0.9
	HDT40SM	0.26	0.03	1.2	0.04	50	-	-	-
	HDT40SC	0.26	0.024	1.2	0.05	45	0.5	0.3	0.5
	HDT60SM	0.26	0.033	1.2	0.04	50	-	-	-
	HDT60SC	0.26	0.024	1.2	0.05	45	0.5	0.1	0.5

Since the parameters in nail shank and steel plate sheath are the same in all sets, the parameters of the equivalent wood embedment are comparable. Furthermore, they provided a clear explanation for the phenomena in the tests.

Co-existent forces weakened the loading and unloading in the cyclic tests, which can be observed from the decreasing trend in the values Setof Q_0, Q_1, Q_2, K_0, and D_{max} in each set. The

observation that the CLT connections can hold strength following the peak values for a longer period for tension than for shear conformed to the variations in the parameter Q_2, specifically, 1.1 ~ 1.3 for shear, and 1.35 ~ 2.8 for tension. The fact that angle brackets have greater shear stiffness than hold-downs was reflected in the initial stiffness parameter K_0, 0.31 kN/mm^2 for angle brackets and 0.04 kN/mm^2 for hold-downs. The weak shear stiffness and strong tension stiffness of the hold-downs were also identical with the values of the initial stiffness parameter K_0, 0.04 kN/mm^2 and 4 kN/mm^2, respectively. The fact that the CLT connections exhibited greater deformation capacity in shear than in tension was demonstrated through the parameter D_{max}, specifically, 35 mm ~ 50 mm for shear, and 7 mm ~ 11 mm for tension.

As for the degradation parameters, the strength/reloading stiffness degradation factor α has been discussed in detail by Li. *et al.* (2011). Larger values of α lead to more severe strength degradation and reloading stiffness degradation. The unloading degradation requires two parameters to be captured. First, an exponential index γ was used to calculate the unloading stiffness value. The similar definition form as α guaranteed the continuity and stability of the algorithm. Second, the algorithm needed a definition for the force interval in the gap during unloading. Thus, the gap size factor β was introduced to demonstrate the interval between βD_0 and D_0. Table 2 reveals that β became smaller under larger co-existent forces. This confirms the fact that larger co-existent forces caused greater resistance in the gap.

Figure 6.7 is a representative curve showing the properties of the equivalent wood embedment of HDT30SC in the modified HYST algorithm generated from the parameters in Table 6.1.

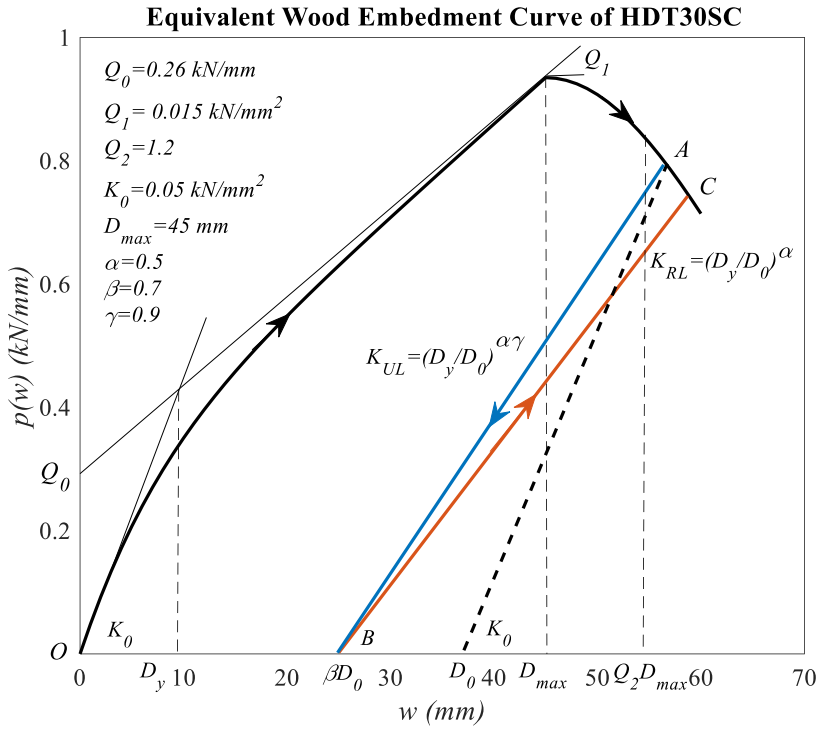

Figure 6.7 The embedment property curve for the equivalent wood embedment of HDT30SC

The figure and Eq. (1) in Section 2.4 show that the values of the left curve are mostly contributed by Q_0 and Q_1, and weakly influenced by K_0, until D_{max} is reached. K_0 and Q_0 control its shape. Q_2 controls the shape of the right curve after D_{max}. The equivalent wood embedment provided resistance within the gap from D_0 to $0.7D_0$. This gap size factor β and the unloading stiffness index γ are the keys to capture the coupling effects under bi-axial loading.

6.3 Summary

In this chapter, the expansion of an existing protocol-independent nail connection algorithm was presented and applied to simulate the coupling effects of the CLT connections under bi-axial loading. The proposed HYST an algorithm added unloading stiffness degradation feature to the original algorithms, which extended its sufficient application to the nail-based timber connections that needed to consider strength degradation, unloading/reloading stiffness

degradation, pinching effect, and coupling effect. Using the pseudo-nail model with this proposed HYST algorithm, four sets of CLT connection tests were modelled, including: Set A) monotonic/cyclic tension tests of angle bracket connections with four levels of co-existent shear force, Set B) monotonic/cyclic shear tests of angle bracket connections with four levels of co-existent tension force, Set C) monotonic/cyclic tension tests of hold-down connections with three levels of co-existent shear force, and Set D) monotonic/cyclic shear tests of hold-down connections with five levels of co-existent tension force. The simulation provided a mechanism-based explanation for understanding the behaviour of CLT connections under bi-axial loading protocols.

The model results were compared with the test results for all 32 configurations through hysteresis loops and energy dissipations, which indicated the strong accuracy and efficiency of the pseudo-nail modelling method and the proposed HYST algorithm. The newly observed unloading stiffness degradation phenomenon in CLT connections, caused by the co-existent force, was captured by the two introduced parameters in the equivalent wood embedment properties, gap size factor β, and unloading stiffness degradation index γ. Based on the simulation results, the parameters of the proposed HYST algorithm were discussed to explaining the mechanisms of the structural behaviour of CLT connections. The observations in the tests were identical with the variations in the model parameters. The key feature in the coupling effect of bi-axial loading, that nails undertake loads in the gaps in wood embedment, was explained and quantified by the gap size factor β and the unloading stiffness degradation index γ.

The pseudo-nail methodology and the proposed HYST model provided a powerful tool for nail-based timber connections. As for this research, the modelling of bi-axial loading effects of the CLT connections with constant loading in one direction and dynamic loading in the perpendicular

direction has reached its goal. Still, further research on the dynamic bi-axial loading of the CLT connections is required.

Chapter 7: Conclusions and Recommendations for Future Work

7.1 Conclusions

In CLT structures, most deformation occurs at the metal connectors rather than the wood, and is dominated by rocking and slip mechanisms. Current design has assumed that, for conventional connectors, angle brackets slip under loading and only take the shear force along the CLT wall, while hold-downs take all the tension forces to resist the overturning moment. Rocking and slip mechanisms are assumed to interact independently. Most existing experimental and numerical research has been conducted based on these assumptions. However, recent studies have proven that both the connectors undertake shear and tension force when the structures are under lateral loading, and that the shear behaviour and axial behaviour of those connectors are coupled. The presented work is the first to systematically examine the behaviour of CLT connections under bi-axial loading through robust experimental setup, mechanism-based model and detailed parameter study. It gives a more profound understanding of the structural behaviour of the CLT connecters through tests and numerical simulation of CLT connections under bi-axial loading.

The study contains four major components: experimental tests of angle bracket connections, experimental tests of hold-down connections, mechanism-based model development, and modelling of the coupling effect of CLT connections. First, experimental tests of typical angle bracket and hold-down connections were conducted under bi-axial loading. Then, from the findings of these tests, the coupling mechanism was explained. Based on this mechanism, a numerical model, the pseudo-nail model, which used a modified protocol-independent nail connection algorithm, was developed. Last, using the proposed model, numerical simulations of the coupling effects of CLT connections under bi-axial loading were carried out. The results reached a good match with the experimental tests under all 32 configurations. The model showed

high accuracy and efficiency in addressing the characteristics of the structural behaviour of CLT connections under bi-axial loading.

Two sets of experimental tests of angle bracket connections under bi-axial loading were performed: In Set A, the specimens were tested under monotonic/cyclic tension loading with four levels of co-existent shear loads (0 kN, 20 kN, 30 kN, and 40 kN). In Set B, the specimens were tested under monotonic/cyclic shear loading with four levels of co-existent tension loads (0 kN, 20 kN, 30 kN, and 40 kN). 44 specimens were tested in total.

From Set A, it was found that for angle brackets, greater co-existent shear loads caused more brittle failures. The mechanical properties of angle brackets were weakened by the co-existent shear loads. The average values of K_{el}, F_{yl}, F_{max}, v_{max}, F_u, and v_u in shear decreased by 13.1%,17.1%, 31.8%, 24.1%, 31.6%, and 24.0% from 0 kN to 40 kN, respectively. Co-existent axial loading made the hysteresis loops of cyclic shear loading less stable and the connections less ductile. Tension capacity was maintained within a 10% degree of change at small and moderate amplitudes (6 mm, 9 mm, and 12 mm) but was rapidly reduced to 0 at a large vertical amplitude (18 mm). The connections had smaller energy dissipation capacities in tension than in shear, so the energy dissipation was dominated by the constant co-existent shear force. Lager co-existent shear loads caused greater energy dissipation. However, for large amplitudes (18 mm), the energy dissipated by large shear loads (30 kN and 40 kN) was weakened due to damage from cyclic tension loading. Furthermore, the co-existent shear force causes deterioration in the energy dissipation capacity of the tension.

For Set B, it was found that a greater co-existent axial load lead to more severe stretch in the angle brackets, and more brittle failures for the connections. The co-existent axial load weakened the mechanical properties of the angle brackets. The average values of K_{el}, F_{yl}, v_{yd}, F_{max},

v_{max}, F_u, and v_u decreased by 13.1%, 17.2%, 10.6%, 16.2%, 7.1%, 16.2%, and 22.4% from 0 kN to 40 kN, respectively. The co-existent axial load reduced the stability and ductility, and weakened the pinching effect of the hysteresis behaviour of cyclic shear loading. As the tension force increased, the shear capacity and energy dissipation capacity of the connector dropped significantly. A large axial load level (40 kN) decreased the maximum shear capacity of the connections and initial stiffness of the connectors by 25% and 15%, respectively. Under a large lateral amplitude (32 mm), the co-existent axial load caused an over 60% reduction of the shear loading capacity of the connections, and around 25% reduction of its energy dissipation capacity. At relatively small amplitudes (6 mm, 8 mm, and 16 mm), the total energy dissipation had a growing trend with increases of the co-existent axial loads, while at a large amplitude (32 mm), it dropped by over 45%. The co-existent axial load had a severely negative influence on the energy dissipation capacity. While the co-existent tension load weakened the shear strength of the specimen at large amplitudes, it also pressed the nails into the surrounding wood embedment, which eliminated the gaps. Thus, under relatively small amplitudes, it helped the nails to carry greater shear loads.

The results showed that the shear behaviour and tension behaviour of the angle brackets were strongly coupled. The following explanation for the hysteresis behaviour of the angle bracket connections under bi-axial loading was proven: the nails in the CLT connections were pressed into the surrounding wood embedment in both the horizontal and vertical directions, causing different mechanisms from uniaxial loading.

There were likewise two sets of experimental tests for the hold-down connections under bi-axial loading: In Set C, the specimens were tested under monotonic/cyclic tension loading with three levels of co-existent shear loads (0 kN, 10 kN, and 20 kN). In Set D, the specimens were

tested under monotonic/cyclic shear loading with five levels of co-existent tension loads (0 kN, 20 kN, 30 kN, 40 kN and 60 kN). 44 specimens were tested in total.

For Set C, greater co-existent shear loads caused increased brittle failure modes for hold-down connections, especially steel plate torsion and nail pullout. Co-existent shear loads weakened the axial loading capacity. The average values of K_{el}, F_{yl}, v_{yd}, F_{max}, v_{max}, F_u, and v_u decreased by 19.7%, 5.8%, 2.9%, 5.4%, 11.6%, 12.9%, and 4.0% from 0 kN to 20 kN, respectively. A small co-existent shear load (10 kN) showed a minor influence on the tension capacity. Conversely, the shear capacity in the cyclic tests on a large co-existent shear load (20 kN) dropped significantly, especially for the last few cycles at the maximum vertical displacement of 16 mm (17.5%). At small displacements (below 16 mm), a small co-existent shear load (10 kN) increased the energy dissipation from the tension force since it mitigated the gap between the nails and wood embedment to help the tension load dissipate energy; a high co-existent shear load (20 kN) had little influence on the energy dissipation capacity from the tension force. At a larger amplitude (24 mm) when the hold-downs were about to fail, the co-existent shear load changed to weaken the energy dissipation capacity from the tension force since it accelerated the failure of the connections.

For Set D, a greater co-existent tension load caused more brittle failures from nail breakage. The co-existent axial load strengthened the shear loading capacity at small displacements (below 24 mm). The average values of K_{el} and F_{yl} in shear increased by 55.2% and 43.4% from 0 kN to 60 kN, respectively. The average values of F_{max} and F_u increased by 25.3% and 20.3% from 0 kN to 30 kN, and then decreased by 12.1% and 16.6% from 30 kN to 60 kN. Small co-existent forces (20 kN and 30 kN) improved the contact between the nails and surrounding wood embedment whereas large co-existent forces (40 kN and 60 kN) crushed the surrounding wood embedment, causing the load capacity to decrease. At large displacements (24 mm and 48 mm), shear capacity

dropped rapidly as co-existent tension increased. The co-existent tension force helped increase the energy dissipation at small displacements (below 24 mm). Large co-existent tension forces (40 kN and 60 kN) decreased the energy dissipation at large displacements (24 mm and 48 mm).

An insightful finding is that, in the hold-down connections, the nails travelling in the gap within the wood embedment received resistance due to the co-existent force in the perpendicular direction under bi-axial loading, which changed the hysteresis behaviour and caused the coupling effect, including strength degradation, reloading stiffness degradation, and unloading stiffness degradation.

Those four sets of bi-axial loading tests of CLT connections provided a more realistic way than uniaxial tests to understand the behaviour of hold-down connections in CLT structures under dynamic loading. It was found that the nails received resistance in the residual gap in the wood embedment when co-existent force was applied in the perpendicular direction. Based on this principle, a finite-element based numerical model, called pseudo-nail model, which employed a protocol-independent nail connection algorithm HYST, has been constructed. The model can fully address the characteristics of CLT connections, including strength degradation, unloading and reloading stiffness degradation, pinching effect and coupling effect.

The key contribution of the presented work in numerical simulations is its adding unloading stiffness degradation features to the original HYST algorithm by introducing two parameters, a gap size factor β and an unloading stiffness degradation index γ, to take the coupling effect into consideration. In the wood embedment, before unloading to zero, the wood medium exhibits stiffness when the nail travels from w_0 to βD_0.

A parameter study was carried out for nine key parameters in this model, including the nail diameter D, intercept of the asymptote at the maximum compressive response Q_0, slope of the

asymptote at the maximum compressive response Q_1, postpeak decay factor Q_2, initial stiffness K_0, displacement at the maximum compressive response D_{max}, reloading degradation index α, gap size factor β, and unloading degradation index γ. The results show that: 1) larger D values lead to higher capacity; 2) large Q_0 values reduced the degradation and made the model more "elastic and stiff"; 3) Q_1 is a very sensitive parameter to the model. As it increased, the force values increased and the strength degradation decreased; 4) as Q_2 increased, the displacement for the peak value became larger and the influence declined; 5) larger K_0 values improved the loading capacity of the model, especially at larger displacements; 6) D_{max} influenced all the characteristics of the hysteresis loops and a smaller D_{max} had a greater impact; 7) as α increased, the loading capacity dropped. For each amplitude, the peak values of the three cycles decreased due to α; 8) as β decreased, the unloading strength increased and the degradation was weakened; 9) larger values of γ increased the unloading stiffness and reduced the distance of the slip. The parameter study provides a guideline in understanding this model and the foundations for modelling calibrations.

It should be noted that, this model can not only be used for the studied connections, but it is also suitable for all types of hysteresis behaviour associated with strength degradation, reloading/unloading stiffness, pinching effect and coupling effect.

Using this model, the four sets of CLT connection tests were simulated. The model results were compared with test results for all 32 configurations through hysteresis loops and energy dissipations, which indicated strong accuracy and efficiency of the pseudo nail modeling method and the proposed HYST algorithm. The newly observed unloading stiffness degradation phenomenon in CLT connections, caused by co-existent forces, was captured by the two introduced parameters in equivalent wood embedment properties, the gap size factor β and unloading stiffness degradation index γ. The parameters of the proposed HYST algorithm showed

the mechanisms to explain the connection behaviour. The observations in the tests were identical with the variations in the model parameters. The key features of the coupling effect of bi-axial loading, that nails undertake loads in the gaps in wood embedment, was explained and quantified by the parameters.

The research explained the complex behaviour of CLT connections under bi-axial loading and provided a sufficient modelling tool. The pseudo-nail methodology and the proposed HYST model not only applies to this research, but can also be employed in other nail-based connections.

7.2 Recommendations for Future Work

Considering its similarity to the real case and feasibility of the tests, bi-axial loading was conducted in the research in the form of constant loading in one direction, and dynamic loading in the perpendicular direction, to reach a good match. While in real structures, CLT connections undertakes dynamic loads in both directions. Further efforts are needed for the creation of more precise testing and modelling methods.

Only two typical commercialized CLT connectors, AE116 and HTT5, were examined in this study. Increasingly more innovative nail-based CLT connectors have been invented within the past decade and therefore, these connectors also need to consider the coupling effect of complex loading. Variations of nail parameters for CLT connectors should be examined. Experimental tests and modelling should be conducted to understand their structural behaviour based on more accurate mechanism-based assumptions.

In the research, the influence of tension and shear on CLT connections has been studies in depth. However, a computational means for considering this coupling effect has not been established yet. The mathematical relationship between tension and shear, which can be input into the model, needs to be constructed for more precise modeling to be pursued. The dynamic changes

of backbone curves and degradations due to co-existent loads in the perpendicular direction are difficult to capture and model. A simplified method, such as the linear approximation of parameters, can be considered as more practical for application to real cases.

The developed model was run as an independent program. To study a CLT wall or structure, the model should be embedded into either existing structural analysis software or self-developed structural analysis programs. For instance, ABAQUS provides an interface for secondary development in FORTRAN. OpenSees similarly has an API for embedding new materials or elements in FORTRAN. As for self-developed programs, the UBC research group, Timber Engineering and Applied Mechanics, has developed the WALL2D and CLTWALL2D programs, which are specific for the dynamic analysis of nail-based and CLT walls. The algorithm presented in this research can be incorporated into those programs to conduct future CLT wall analyses involving the coupling effect. The CLT wall simulation can be compared with existing CLT wall test data from the group to further develop this model.

The model has exhibited sufficient computational efficiency and, thanks to the rapid development of computing power, more precise and complex structural models for analysis have become practical. It is highly recommended that, after embedding this model into structural analysis programs and performing calibrations, the seismic analysis of CLT walls, and later of 3D CLT structures, should be conducted. These can be compared with sufficiently accessible CLT structure shaking table test data. Additionally, as a timber product, CLT requires reliability studies, despite its relatively high property stability. A rational and feasible seismic reliability method is essential to the accuracy of reliability estimations of engineering structures. Practical methodology, including but not limited to the response surface method, local interpolation method or neural network method with designed experiments, might be considered later on.

Finally, to obtain more reliable guidelines for CLT structural design, performance-based assessment is encouraged; substantial computational efforts would thus be required to establish a broad associated database from the computer simulations.

As a micro-level study, this research has fulfilled its goal of improved understanding of the mechanisms of some common CLT connections. Having such solid knowledge, we can proceed in increments to carry on the further research possibilities mentioned above.

Bibliography

ANSI, A. (2012). "ANSI/APA PRG 320–2012 Standards for performance-rated Cross-laminated timber." Tacoma, US.

Benedetti, F., Rosales, V., and Opazo, A. (2016). "Cyclic testing and simulation of hold-down connections in radiata pine clt shear walls." *2016 World Conference on Timber Engineering, WCTE 2016*, University of Vienna, Austria.

CSA (Canadian Standard Association). (2014). "CSA O86-14: Engineering Design in Wood." CSA O86-14. Toronto, ON, Canada: CSA.

Casagrande, D., Doudak, G., Mauro, L., and Polastri, A. (2017). "Analytical approach to establishing the elastic behavior of multipanel CLT shear walls subjected to lateral loads." *J.Struct.Eng.*, 144(2), 04017193.

Ceccotti, A. (2008). "New technologies for construction of medium-rise buildings in seismic regions: the XLAM case." *Struct.Eng.Int.*, 18(2), 156-165.

Ceccotti, A., and Follesa, M. (2006). "Seismic behaviour of multi-storey X-lam buildings." *Proc. International Workshop on" Earthquake Engineering on Timber Structures"* Coimbra, Portugal.

Ceccotti, A., Sandhaas, C., Okabe, M., Yasumura, M., Minowa, C., and Kawai, N. (2013). "SOFIE project–3D shaking table test on a seven-storey full-scale cross-laminated timber building." *Earthquake Eng.Struct.Dyn.,* 42(13), 2003-2021.

Demirci, C., Málaga-Chuquitaype, C., and Macorini, L. "Seismic drift demands in multi-storey cross-laminated timber buildings." *Earthquake Eng.Struct.Dyn.*, 47(4), 1014-1031.

Diego, U. S. (2017). "Earthquake shake tests at UC San Diego toward 20-story earthquake-safe buildings made from wood." UC San Diego News Center.

Dujic, B., and Zarnic, R. (2005). "Report on evaluation of racking strength of KLH system." University of Ljubljana, Faculty of Civil and Geodetical Engineering, Slovenia.

Dujic, B., Aicher, S., and Zarnic, R. (2006). "Testing of wooden wall panels applying realistic boundary conditions." *Proceedings of the 9th World Conference on Timber Engineering*, Portland, Oregon, USA.

Dujic, B., Klobcar, S., and Zarnic, R. (2008). "Shear capacity of cross-laminated wooden walls." *Proceedings of the 10th World Conference on Timber Engineering*, Miyazaki, Japan.

Dujič, B., Pucelj, J., and Žarnić, R. (2004). "Testing of racking behaviour of massive wooden wall panels."

Dujič, B., and Žarnić, R. (2006). "Study of lateral resistance of massive X-Lam wooden wall system subjected to horizontal loads." Coimbra, Portugal.

Flatscher, G., and Schickhofer, G. (2011). "Verbindungstechnik in BSP bei monotoner und zyklischer Beanspruchung–Statusbericht TU Graz." *9. Grazer Holzbau-Fachtagung'11*.

Follesa, M., Christovasilis, I. P., Vassallo, D., Fragiacomo, M., and Ceccotti, A. (2013). "Seismic design of multi-storey cross laminated timber buildings according to Eurocode 8." *Ingegneria Sismica, 4*.

Folz, B., and Filiatrault, A. (2001). "Cyclic analysis of wood shear walls." *J.Struct.Eng.*, 127(4), 433-441.

Folz, B., and Filiatrault, A. (2002). "A computer program for seismic analysis of woodframe structures." *Consortium of Universities for Research in Earthquake Engineering*.

Foschi, R. O., Yao, F., and Rogerson, D. (2000). "Determining embedment response parameters from connector tests." *World Conference on Timber engineering*, Whistler, BC, Canada.

Fragiacomo, M., and Rinaldin, G. (2011). "Advanced models for seismic analyses of timber buildings." Holzbau Forschungs Gmbh.

Fragiacomo, M., Dujic, B., and Sustersic, I. (2011). "Elastic and ductile design of multi-storey crosslam massive wooden buildings under seismic actions." *Eng.Struct.*, 33(11), 3043-3053.

Ganey, R. S. (2015). "Seismic design and testing of rocking cross laminated timber walls". Doctoral dissertation, University of Washington, US.

Gavric, I. (2013). "Seismic behaviour of cross-laminated timber buildings". Doctoral dissertation, University of Trieste, Italy.

Gavric, I., Ceccotti, I., and Fragiacomo, M. (2011). "Experimental cyclic tests on cross-laminated timber panels and typical connections." Holz. bau Forschungs Gmbh.

Gavric, I., Fragiacomo, M., and Ceccotti, A. (2015). "Cyclic behaviour of typical metal connectors for cross-laminated (CLT) structures." *Mater.Struct.*, 48(6), 1841-1857.

Gavric, I., Fragiacomo, M., Popovski, M., and Ceccotti, A. (2014). "Behaviour of cross-laminated timber panels under cyclic loads." *Materials and Joints in Timber Structures*, Springer, 689-702.

Gavric, I., and Popovski, M. (2014). "Design models for CLT shearwalls and assemblies based on connection properties." *Proceedings of the International Network on Timber Engineering Research.*

Gu, J., and Lam, F. (2004). "Simplified mechanics-based wood frame shear wall model." *Proc., 13th World Conf. on Earthquake Engineering*, Vancouver Canada.

Hassanieh, A., Valipour, H. R., and Bradford, M. A. (2016). "Load-slip behaviour of steel-cross laminated timber (CLT) composite connections." *Journal of Constructional Steel Research*, 122 110-121.

Hristovski, V., Dujic, B., Stojmanovska, M., and Mircevska, V. (2012). "Full-scale shaking-table tests of XLam panel systems and numerical verification: Specimen 1." *J.Struct.Eng.*, 139(11), 2010-2018.

Izzi, M., Polastri, A., and Fragiacomo, M. (2018). "Investigating the hysteretic behavior of Cross-Laminated Timber wall systems due to connections." *J.Struct.Eng.*, 144(5), 04018035.

Jacquier, N., and Girhammar, U. A. (2012). "Tests on shear connections in prefabricated composite cross-laminated-timber and concrete elements." *World Conference on Timber Engineering: 15/07/2012-19/07/2012*, New Zealand Timber Design Society, 441-450.

Kraler, A., Kögl, J., Maderebner, R. and Flach, M., (2014). "Sherpa-CLT-Connector for cross laminated timber (CLT) elements." *13th World Conference on Timber Engineering (WCTE 2014)*, Quebec City, Canada.

Kramer, A., Barbosa, A. R., and Sinha, A. (2015). "Performance of steel energy dissipaters connected to cross-laminated timber wall panels subjected to tension and cyclic loading." *J.Struct.Eng.*, 142(4), E4015013.

Krätzig, W. B., Meyer, I. F., and Meskouris, K. (1989). "Damage evolution in reinforced concrete members under cyclic loading." *Structural Safety and Reliability*, ASCE, 795-804.

Latour, M., and Rizzano, G. (2015). "Cyclic behavior and modeling of a dissipative connector for cross-laminated timber panel buildings." *J.Earthquake Eng.,* 19(1), 137-171.

Lauriola, M. P., and Sandhaas, C. (2006). "Quasi-static and pseudo-dynamic tests on XLAM walls and buildings." *COST E29 International Workshop on Earthquake Engineering on Timber Structures*, Coimbra, Portugal.

Li, M., Foschi, R. O., and Lam, F. (2011). "Modeling hysteretic behavior of wood shear walls with a protocol-independent nail connection algorithm." *J.Struct.Eng.*, 138(1), 99-108.

Li, M., and Lam, F. (2009). "Lateral performance of nonsymmetric diagonal-braced wood shear walls." *J.Struct.Eng.*, 135(2), 178-186.

Li, M., and Lam, F. (2015). "Lateral behaviour of cross laminated timber shear walls under reversed cyclic loads." *Proc., 10th Pacific Conf. on Earthquake Engineering*, Seismology Research Centre, VIC, Australia.

Li, M., Lam, F., and Foschi, R. O. (2009). "Seismic reliability analysis of diagonal-braced and structural-panel-sheathed wood shear walls." *J.Struct.Eng.*, 135(5), 587-596.

Li, Z., He, M., Lam, F., Li, M., Ma, R., and Ma, Z. (2014). "Finite element modeling and parametric analysis of timber–steel hybrid structures." *The Structural Design of Tall and Special Buildings*, 23(14), 1045-1063.

Lim, H., Lam, F., Foschi, R., and Li, M.. "Modeling load-displacement hysteresis relationship of a single-shear nail connection." *Journal of Engineering Mechanics*, 143, no. 6 (2017): 04017015.

Liu, J., and Lam, F. (2014). "Numerical simulation for the seismic behaviour of mid-rise CLT shear walls with coupling beams." *13th World Conference on Timber Engineering (WCTE 2014)*, Quebec City, Canada.

Liu, J., and Lam, F. (2016). "Experimental test of cross laminated timber connections under bi-directional loading." *2016 World Conference on Timber Engineering, WCTE 2016*, University of Vienna, Austria.

Liu, J., and Lam, F. (2018). "Experimental test of coupling effect on CLT angle bracket connections." *Eng.Struct.*, 171 862-873.

Liu, J., Lam, F. (2019). "Experimental test of coupling effect on CLT hold-down connections." *Eng.Struct.*, 178 586-602.

Lowes, L. N., Mitra, N., and Altoontash, A. (2003). "A beam-column joint model for simulating the earthquake response of reinforced concrete frames." University of California, Berkeley.

NBCC, N. (2005). "National building code of Canada." National Research Council of Canada (NRCC), Ottawa, Canada.

Nolet, V. (2017). "Analytical Methodology to Predict the Behaviour of Multi-Panel CLT Shearwalls Subjected to Lateral Loads." Doctoral dissertation, University of Ottawa, Canada.

Okabe, M., Kawai, N., and Takada, S. (2000). "Experimental analysis for estimating strength and stiffness of shear walls in wood-framed construction." *Proc.of the WCTE 2000*, Whistler, Canada.

Okabe, M., Yasumura, M., Kobayashi, K., Haramiishi, T., Nakashima, Y., and Fujita, K. (2012). "Effect of vertical load under cyclic lateral load test for evaluating Sugi CLT wall panel." *World Conference on Timber Engineering*, Auckland, New Zealand.

Pei, S., Berman, J., Dolan, D., van de Lindt, J., Ricles, J., Sause, R., Blomgren, H., Popovski, M., and Rammer, D. (2014). "Progress on the development of seismic resilient Tall CLT Buildings in the Pacific Northwest." *13th World Conference on Timber Engineering (WCTE 2014)*, Quebec City, Canada.

Pei, S., Popovski, M., and van de Lindt, John W. (2013). "Analytical study on seismic force modification factors for cross-laminated timber buildings." *Canadian Journal of Civil Engineering*, 40(9), 887-896.

Pei, S., Rammer, D., Popovski, M., Williamson, T., Line, P., and van de Lindt, John W. (2016). "An Overview of CLT Research and Implementation in North America." *2016 World Conference on Timber Engineering, WCTE 2016*, University of Vienna, Austria.

Pei, S., Van De Lindt, J W, Popovski, M., Berman, J. W., Dolan, J. D., Ricles, J., Sause, R., Blomgren, H., and Rammer, D. R. (2014). "Cross-laminated timber for seismic regions: Progress and challenges for research and implementation." *J.Struct.Eng.*, 142(4), E2514001.

Pei, S., van de Lindt, John W, and Popovski, M. (2012). "Approximate R-factor for cross-laminated timber walls in multistory buildings." *J.Archit.Eng.*, 19(4), 245-255.

Piazza, M., Tomasi, R., Grossi, P., Costa, A. C., and Candeias, P. X. (2015). "Seismic performance of timber buildings: the Series project." *Proceedings of the Institution of Civil Engineers-Structures and Buildings*, 168(11), 788-802.

Polastri, A., Giongo, I., Angeli, A., and Brandner, R. (2017). "Mechanical characterization of a pre-fabricated connection system for cross laminated timber structures in seismic regions." *Eng.Struct.*, 167 705-715.

Popovski, M., and Gavric, I. (2015). "Performance of a 2-story CLT house subjected to lateral loads." *J.Struct.Eng.*, 142(4), E4015006.

Popovski, M., Gavric, I., and Schneider, J. (2014). "Performance of two-storey CLT house subjected to lateral loads." FP Innovations Research Rep., FPIPRODUCT-1-6896, Vancouver, BC, Canada.

Popovski, M., Schneider, J., and Schweinsteiger, M. (2010). "Lateral load resistance of cross-laminated wood panels." *In Proceedings of 11th World Conference on Timber Engineering*, Riva del Garda, Trentino, Italy.

Pozza, L., Scotta, R., and Vitaliani, R. (2009). "A non linear numerical model for the assessment of the seismic behaviour and ductility factor of X-lam timber structures." *Proceeding of international Symposium on Timber Structures*, Istanbul, Turkey.

Pozza, L., Ferracuti, B., Massari, M., and Savoia, M. (2018). "Axial–Shear interaction on CLT hold-down connections–Experimental investigation." *Eng.Struct.*, 160 95-110.

Pozza, L., Saetta, A., Savoia, M., and Talledo, D. (2017). "Coupled axial-shear numerical model for CLT connections." *Construction and Building Materials*, 150 568-582.

Pozza, L., Scotta, R., Trutalli, D., Pinna, M., Polastri, A., and Bertoni, P. (2014). "Experimental and numerical analyses of new massive wooden shear-wall systems." *Buildings*, 4(3), 355-374.

Reynolds, T., Foster, R., Bregulla, J., Chang, W., Harris, R., and Ramage, M. (2017). "Lateral-load resistance of cross-laminated timber shear walls." *J.Struct.Eng.*, 143(12), 06017006.

Rinaldin, G., and Fragiacomo, M. (2016). "Non-linear simulation of shaking-table tests on 3-and 7-storey X-Lam timber buildings." *Eng.Struct.*, 113 133-148.

Rinaldin, G., Amadio, C., and Fragiacomo, M. (2013). "A component approach for the hysteretic behaviour of connections in cross-laminated wooden structures." *Earthquake Eng.Struct.Dyn.*, 42(13), 2023-2042.

Rinaldin, G., Amadio, C., and Fragiacomo, M. (2011). "A component approach for non-linear behavior of cross-laminated solid timber panels." *XIV Convegno ANIDIS "L'Ingegneria Sismica in Italia",* Franco Braga e Mauro Mezzina, .

Schneider, J., Karacabeyli, E., Popovski, M., Stiemer, S. F., and Tesfamariam, S. (2013). "Damage assessment of connections used in cross-laminated timber subject to cyclic loads." *J.Perform.Constr.Facil.*, 28(6), A4014008.

Schneider, J., Shen, Y., Stiemer, S. F., and Tesfamariam, S. (2015). "Assessment and comparison of experimental and numerical model studies of cross-laminated timber mechanical connections under cyclic loading." *Construction and Building Materials*, 77 197-212.

Schneider, J., Stiemer, S. F., Tesfamariam, S., Karacabeyli, E., and Popovski, M. (2012). "Damage assessment of cross laminated timber connections subjected to simulated earthquake loads." *Proceedings of the 12th world conference on timber engineering*, Auckland, New Zealand.

Scotta, R., Marchi, L., Trutalli, D., and Pozza, L. (2016). "A dissipative connector for CLT buildings: concept, design and testing." *Materials*, 9(3), 139.

Shahnewaz, M., Tannert, T., Alam, M. S., and Popovski, M. (2017a). "Performance of Cross Laminated Timber Shear Walls under Cyclic Loading." *6th International Conference on Engineering Mechanics and Materials, CSCE*, Vancouver, BC, Canada.

Shahnewaz, M., Tannert, T., Alam, M. S., and Popovski, M. (2017b). "In-plane stiffness of cross-laminated timber panels with openings." *Struct.Eng.Int.*, 27(2), 217-223.

Shen, Y. L., Schneider, J., Tesfamariam, S., Stiemer, S. F., and Mu, Z. G. (2013). "Hysteresis behavior of bracket connection in cross-laminated-timber shear walls." *Construction and Building Materials*, 48, 980-991.

Tamagnone, G., Rinaldin, G., and Fragiacomo, M. (2016). "A simplified non− linear procedure for seismic design of clt wall systems" *2016 World Conference on Timber Engineering, WCTE 2016*, University of Vienna.

Tamagnone, G., Rinaldin, G., and Fragiacomo, M. (2018). "A novel method for non-linear design of CLT wall systems." *Eng.Struct.*, 167 760-771.

Tavoussi, K., Winter, W., and Pixner, T. (2008). "Development of earthquake bracing systems for multi-storey buildings using slender shear wall elements in cross-laminated timber (CLT)." Vienna University of Technology, Austria.

Tomasi, R., and Smith, I. (2014). "Experimental characterization of monotonic and cyclic loading responses of CLT panel-to-foundation angle bracket connections." *J.Mater.Civ.Eng.*, 27(6), 04014189.

UNI, E. N. (2006). "12512: 2006, Timber structures. Test methods. Cyclic testing of joints made with mechanical fasteners.", UNI, Milano, Italy.

Appendices

Appendix A Drawings

Wood Specimen

The 4’x8’ 5 layer CLT panels were processed to 70 Type A specimens and 70 Type B specimens.

The dimensions are shown in Figure A.1 as below (in mm).

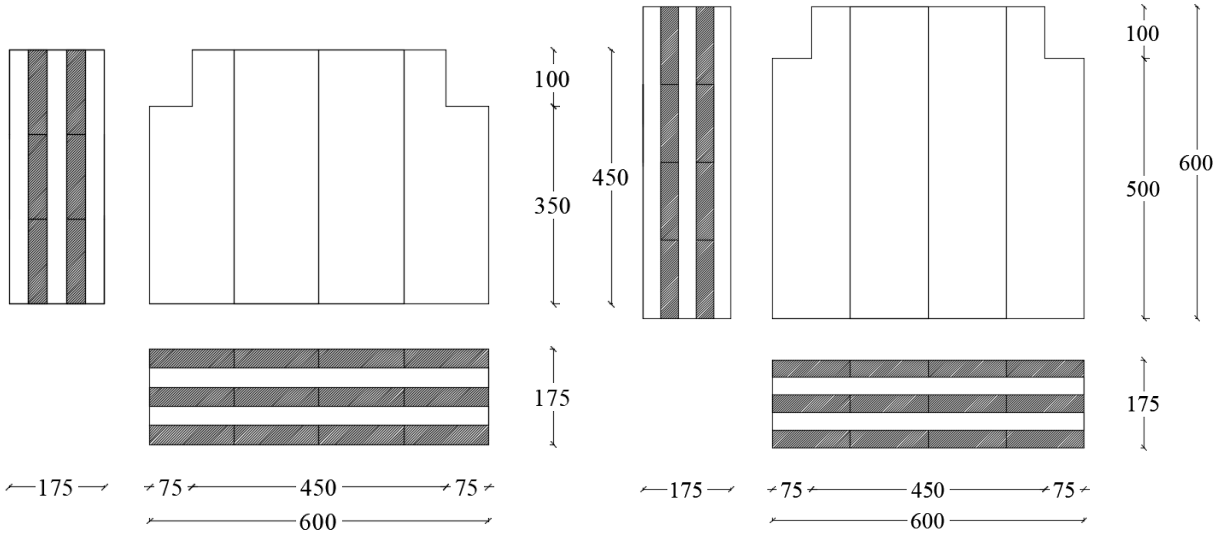

(a) (b)

Figure A.1 two specimen dimensions, (a)Type A; (b) Type B

Each panel produced 10 Type A specimens or 6 Type B specimens by the layout in Figure A.2. 7 panels were processed to Type A and 9 panels were processed to Type B.

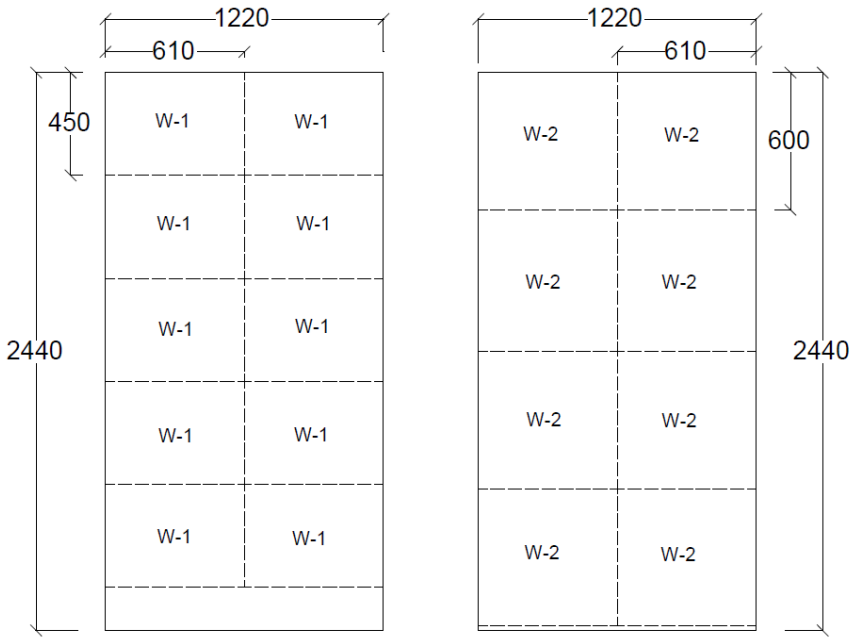

Fig. A.2 CLT panel cut plan

Steel parts

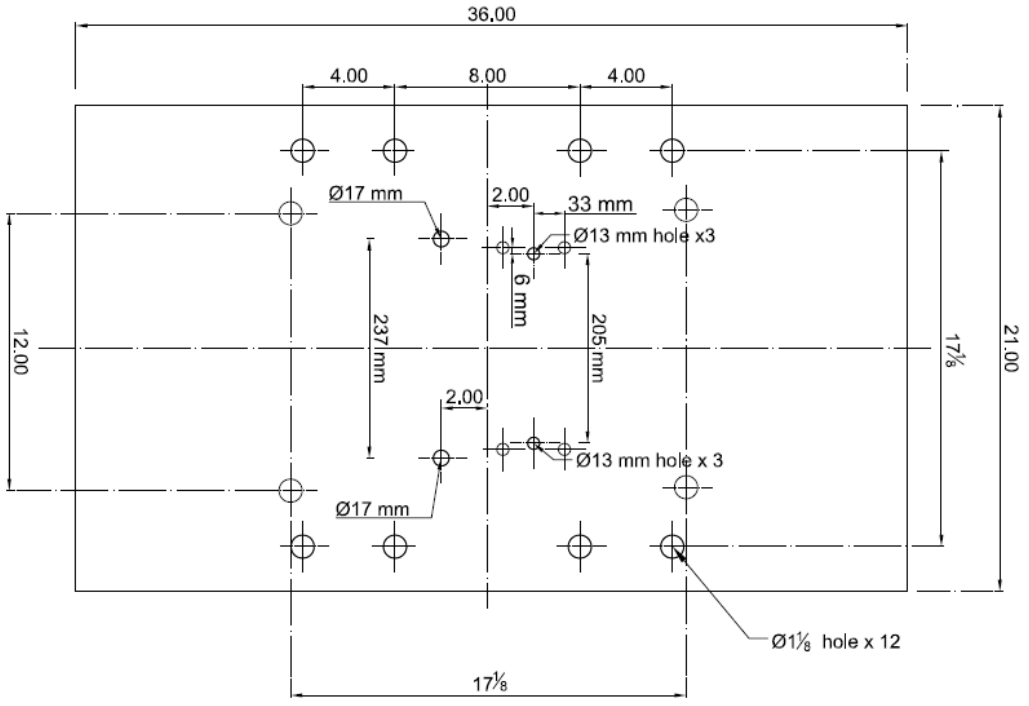

Figure A.3 Steel plate support I1, thickness 1.00 in., unit (in.)

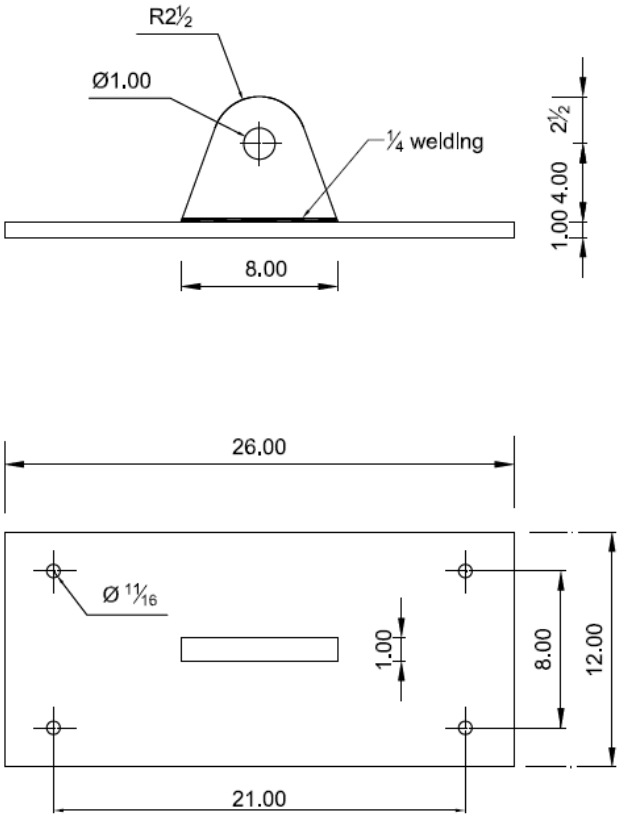

Figure A.4 Loading steel plate support P1, unit (in.)

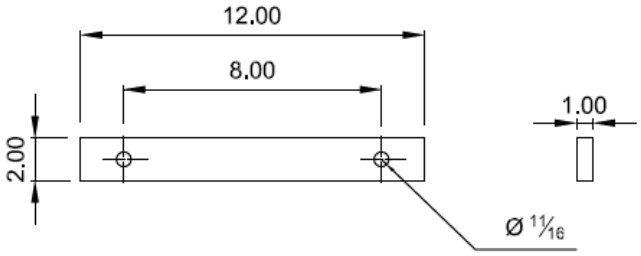

Figure A.5 Steel support B1, unit (in.)

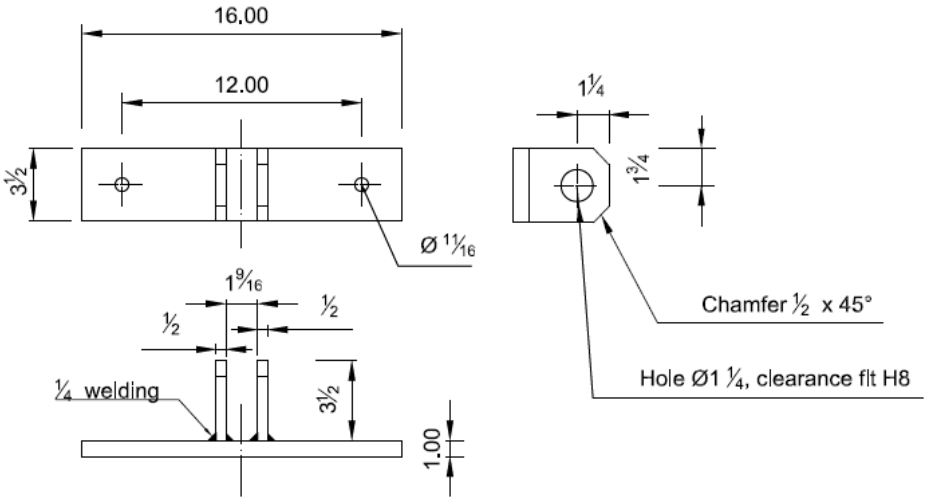

Figure A.6 Steel plate with predrilled holes B2, unit (in.)

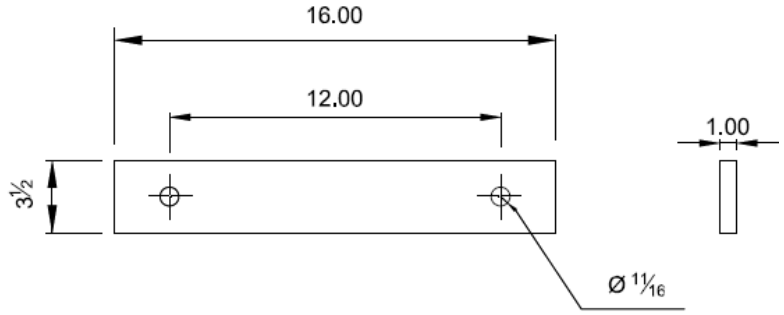

Fig. A.7 Steel support B4, unit (in.)

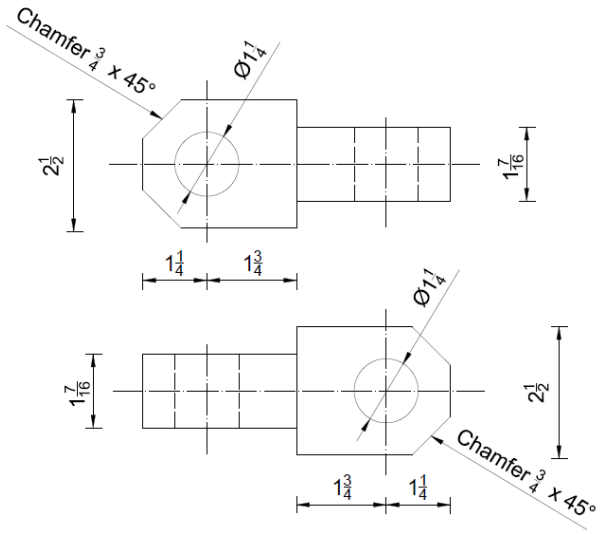

Figure A.8 Steel adopter 1, unit (in.)

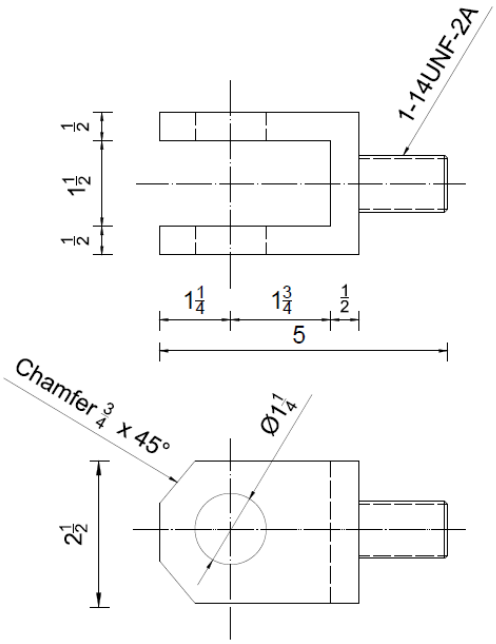

Figure A.9 Steel adopter 2, unit (in.)